uOttawa

L'Université canadienne
Canada's university

FACULTÉ DES ÉTUDES SUPÉRIEURES ET POSTOCTORALES

uOttawa

L'Université canadienne
Canada's university

FACULTY OF GRADUATE AND POSDOCTORAL STUDIES

Katherine McGilvray
AUTEUR DE LA THÈSE / AUTHOR OF THESIS

Ph.D. (Chemistry)
GRADE / DEGREE

Department of Chemistry
FACULTÉ, ÉCOLE, DÉPARTEMENT / FACULTY, SCHOOL, DEPARTMENT

Photochemical Strategies for the Synthesis of Gold Nanoparticles

TITRE DE LA THÈSE / TITLE OF THESIS

Juan C. Scaiano
DIRECTEUR (DIRECTRICE) DE LA THÈSE / THESIS SUPERVISOR

CO-DIRECTEUR (CO-DIRECTRICE) DE LA THÈSE / THESIS CO-SUPERVISOR

Maria De Rosa

Janvier Girogi

Muralee Murugesu

Mark Workentin
University of Western Ontario

Gary W. Slater
Le Doyen de la Faculté des études supérieures et postdoctorales / Dean of the Faculty of Graduate and Postdoctoral Studies

Photochemical Strategies for the Synthesis of Gold Nanoparticles

Katherine L. McGilvray

A thesis submitted to the

Faculty of Graduate and Postdoctoral Studies

In partial fulfillment of the requirements for the degree of

Doctor of Philosophy

in the Ottawa-Carleton Chemistry Institute

Center for Catalysis Research and Innovation

Department of Chemistry, University of Ottawa

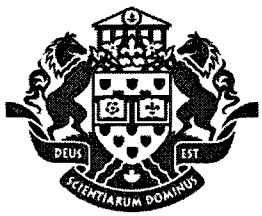

Université d'Ottawa • University of Ottawa

Candidate	Supervisor
Katherine L. McGilvray	Professor J. C. Scaiano

Your file Votre référence
ISBN: 978-0-494-73931-0
Our file Notre référence
ISBN: 978-0-494-73931-0

He who would learn to fly one day

Must learn to stand and walk and run and climb;

One cannot fly into flying.

Friedrich Nietzsche

Abstract

The synthesis of nanomaterials has received considerable attention in the past few decades owing to the enhanced physical and chemical properties of the particles upon approaching dimensions on the order of the Bohr radius. Several routes have been established for the synthesis of colloidal nanoparticles, where selection of reducing agent and stabilizer along with manipulation of reaction conditions dictate the outcome of the synthetic efficacy. In this work, a number of tactics have been examined in the synthesis of gold nanoparticles, which as a whole can serve as a guideline for the photochemical preparation of various aqueous metal colloids.

Aqueous gold nanoparticles have been synthesized with a variety of photoinitiators such as α-hydroxy ketones and α-amino ketones through the unimolecular photo-release of free radicals with reducing character. A water-soluble benzoin operated as an excellent precursor and subsequent stabilizer of colloidal gold by its photoproducts. A second technique has operated *via* an intermolecular pathway for the generation of reducing ketyl radicals from hydrogen atom abstraction involving aromatic ketones with a number of hydrogen donors. Selecting ketones with low-lying triplet states and reactive hydrogen donors led to the facile formation of AuNP in micellar media. Other syntheses of gold nanoparticles have focused on the reactivity of the metal salt itself, such that photolysis of the coordination complex in the vicinity of hydrogen donors has also resulted in efficient gold nanoparticle synthesis. These approaches have been optimized by manipulation of reagent concentrations and photolysis conditions to yield stable colloids with control over particle diameter as well as morphology.

With these strategies in place, the growth of nanoparticles and their surface reactivity were investigated through various methods. In particular, seed-mediated growth and kinetics were established to resolve an autocatalytic mechanism for particle formation. In addition, a novel photochemical seed-mediated growth technique was established for size selective synthesis.

Gold nanoparticles were also derivatized with a series of functional groups to evaluate ligand-nanoparticle interactions, leading the way to possible applications for the materials as optical sensors. Additionally, the photo-releasing synthetic approach has been applied to the design of gold on inorganic supports for heterogeneous catalysis, where preliminary research has revealed their catalytic activity.

Acknowledgements

As I look back on the person I was five years ago and reflect on the person I have become, a warm smile flourishes as a stream of rich memories take colour in my mind. Above all, Tito Scaiano has been a monumental and influential supervisor. His curiosity and creativity are refreshing and industrious, from his puzzlement of gold "climbing the walls" to MacIver-ing a sample-turner from a hotdog cooker bought off of eBay! His persistence to explore new frontiers in science and to steer into the rapid currents of nanoscience; dropping the photochemistry anchor and diving head-first into the murkiest of unfamiliar waters has been truly inspiring, and has shown me the pools of knowledge I can absorb when I swim outside of my comfort zone. I am certainly not the first, nor will I be the last, to realize that my graduate research experience with Tito has been 'incomparable'. Simply put. Thank you for all of the opportunities over the years. Thank you for teaching me the importance of a squeaky wheel and the "used car salesman" approach to communicating science.

The love and support from my family has been my security blanket over the years, holding me together when research pulled me apart. Cindy will always be an endless source of sisterly advice, karmic wisdom, and laughter. I must thank my parents for nurturing my restless and inquisitive mind, all the while instilling perception, patience, and persistence. My mother has provided many words of encouragement and skills for organization, while my dad, from his workshop to my benchtop, has catalyzed my need to design and play with materials. My grandfather has taught me that hard work gets the job done, and that networking pays off, but primarily that life is about family and the people you share it with. You are forever in my heart, Grampy. Rest in peace. Thank you for all believing in me.

I have shared a "lab life" with several wonderful people over the years, making my graduate experience truly exciting and memorable. A close network of coworkers has easily evolved into wonderful friendships with a true feeling of family, from the

lab bench and the group meetings, to ski weekends, BBQs, camping and conference travels. Michelle Chrétien, Kathy-Sarah Focseanu, Mathieu Frenette, Matt Lukeman, Belinda Heyne and Colleen Sutton have set the research chemist bar high, and have each been unique and remarkable leaders to follow. Mark Perry, Johanna Blacquiere, Jessie Blake, Paul Billone, Laetitia Rene-Boisneuf, Rob Godin, Matt Decan, Matt Yorke, Eve Heafey, Andrea Pardoe and Kevin Stamplecoskie have been amazing labmates, deskmates, squashmates, housemates, and friends over the years. "Fresh" lunch conversations, morning gym rituals, countless evenings out, Yeehah, and sushi parties have often left me in stitches and sometimes tears (read: surprise squid birthday party!); providing a wonderful balance to the work component of research. Maria Gonzalez Béjar has been a great labmate, roommate, friend and true inspiration to me. Also a great therapist, she has helped me cope with temporary bipolar symptoms of "thesis".

Working with Marius Ivan, Matt Decan, Nathan Yuan, Marisa Marin, Rachel Schwartz-Narbonne, Rochelle Kerluke, Mihaela Ceausu, Geniece Hallet-Tapley, Natalia Pacioni, Emilio Alarcon, and Charles Oneil-Crites, and many others in the Scaiano lab over the years have given me invaluable learning experiences and insight into scientific passion and communication. Keith Ingold has taught me to think critically, experiment fanatically and water-ski with vigor. Alexis Aspée has taught me to relax. Betty Yakimenko and Michel Grenier have been saviors on many occasions, where their organizational skills, logic and colourful sense of humour have rescued more than just a weak laser signal or a malfunctioning mac.

I also need to thank Tito, Hermenegildo Garcia and Avelino Corma for giving me the opportunity to study abroad at the Universidad Politécnica de Valencia, where I learned the ropes of nanomaterials catalysis. I thank Marisa Marin, Raquel Galian, and Pedro Montes Navajas for their kindness and generosity in treating me like family during my brief time abroad.

My graduate experience would never have been the same without the creative and social outlet of the CGSA. My experiences with Joseph Moran, Nathalie Lavoie,

Joffré Bourgeois, Jessie Blake, Becky Chapman, Paul Billone, and Alex Bush were true highlights to the years in D'Iorio, from annual photo-scavenger hunts and summer BBQs, to Chemistry Olympics and musical festivities with the Accommodators.

I extend my arms and my heart for the rich friendships and unconditional love of Jade Lachance, Yamile Wasslen, Hanna Bielawska and Jelena Trifkovic throughout my undergrad and grad school experience. Finally, I am grateful for the colour, cheer and clarity that Steven Turner has brought into my life. Your ability to recover hard drive failures and crack unknowingly-set passwords on thesis chapters (!) are truly timely assets, but it's your energy, your warmth, and your wit that keep me on my toes and happily by your side.

Thank you all

Table of Contents

List of Figures

List of Schemes

List of Tables

List of Abbreviations

2-prop	2-propanol
4-NH_2	*n*-butylamine
6-SH	*n*-hexanethiol
16-NH_2	*n*-hexadecylamine
16-SH	*n*-hexadecanethiol
AgNP	silver nanoparticle
APTES	3-aminopropyltriethoxysilane
AuNP	gold nanoparticle
AZX	1-axaxanthone
BN	benzoin
BODIPY	boron-dipyrromethene
BP	benzophenone
BPK	benzophenone ketyl radical
1,3-CHD	1,3-cyclohexadiene
1,4-CHD	1,4-cyclohexadiene
CTAB	cetyltrimethylammonium bromide
CTAC	cetytrimethylammonium chloride
CuNP	copper nanoparticle
CW	continuous wave
CYS	cysteine
ddH_2O	distilled, deionized water
DMSO	dimethylsulfoxide
DNA	deoxyribonucleic acid
DTBA	4,4'-dithiodibutyric acid

ΔE_{ST}	singlet-triplet energy gap
ETHA	ethanolamine
EtOH	ethanol
EXAFS	extended X-ray absorption fine structure
fcc	face-centered cubic unit cell
FT-IR	Fournier transform infrared spectroscopy
GC-MS	gas chromatography mass spectroscopy
4-HEBA	4-hydroxyethoxy benzoic acid
HOMO	highest occupied molecular orbital
HPLC	high pressure liquid chromatography
HT	hydrotalcite
IC	internal conversion
IEP	isoelectric point
ISC	inter-system crossing
I-127	2-hydroxy-1-{4-[4-(2-hydroxy-2-methyl-propionyl)-benzyl]-phenyl} -2- methyl-propan-1-one
I-184	1-hydroxy-cyclohexyl-phenyl-ketone
I-2959	1-[4-(2-hydroxyethoxy)phenyl]-2-hydroxy-2-methyl-1-propane-1-one, or Irgacure-2959
I-907	2-metyl-1-[4=(methylthio)phenyl]-2-(morpholinyl)phenyl-1-butanone, or Irgacure-907
k	rate constant
LED	light emitting diode
LFP	laser flash photolysis
LMCT	ligand-to-metal charge transfer
LUMO	lowest unoccupied molecular orbital
MB	methylene blue
MeCN	acetonitrile

MHDA	16-mercaptohexadecanoic acid
MPEG-SH	methoxy-poly (ethylene glycol) thiol
MPSA	3-mercaptopropane sulfonic acid sodium salt
MTHZ	2-mercaptothiazoline
NHE	normal hydrogen electrode
NMR	nuclear magnetic resonance
P25 TiO_2	commercial TiO_2, ~80% anatase, 20% rutile
PBN	α-phenyl benzoin
PEG	poly (ethylene glycol)
PMMA	poly (methylmethacrylate)
PNIPAAm	poly (*N*-isopropylacrylamide)
PTFE	Polytetrafluoroethylene (Teflon)
PtNP	platinum nanoparticle
PVA	poly (vinyl alcohol)
PVAc	poly (vinyl acetate)
PVP	poly (vinyl pyrrolidone)
pyrr	pyrrolidine
SBA-15	ordered mesoporous silicate support
SCE	standard calomel electrode
SDS	sodium dodecylsulfate
SEM	scanning electron microscopy/micrograph
SERS	surface-enhanced Raman scattering
SPB	surface plasmon resonance band
TEM	transmission electron microscope/micrograph
THF	tetrahydrofuran
TXAN	thioxanthone
TX-100	Triton-X 100

UVA	ultraviolet irradiation ranging from 315-400 nm
UVB	ultraviolet irradiation ranging from 280-315 nm
UVC	ultraviolet irradiation ranging from 100- 280 nm
v	rate of reaction
XAN	xanthone
XRD	X-ray Diffraction
XPS	X-ray Photoelectron Spectroscopy

Chapter 1

Introduction

1.1 From Noble to Nano

In the course of technological evolution, we are currently at the forefront of a scientific paradigm wherein nanotechnology has been speculated to be at the heart of the next industrial revolution.[1] In the same fashion that iron, the engine and transistors have developed to transform our culture by way of challenging classical and fundamental assumptions, the development of nanotechnology is also forecasted to push the limit of industrial design on a global scale and provide solutions to many economic, environmental and health matters.

Significant attention has been devoted to the study of nanotechnology and nanochemistry in particular in recent decades, where interest in the physical and chemical properties of metallic nanoparticles has been driven not only by a passion for understanding scientific marvels, but has also allowed for the development of numerous materials with diverse applications. The formation of nanomaterials has arisen through a multitude of methods which can be divided into top-down approaches, where high-energy techniques such as e-beam lithography or laser ablation are utilized to obliterate bulk materials into nanometer components, as well as bottom-up techniques where nanoparticles self-assemble from their atomic components in solution and gas-phase reactions.

Profound interest in metal nanotechnology results from an enhancement of chemical, catalytic, electrical, optical and magnetic properties, which are uniquely different from a metal's bulk components.[2] The physical and chemical properties of colloids and clusters have been studied for centuries, but new advances in technology now allow for further investigation down to a molecular level and thus allow for a better understanding for chemical reactivity at smaller dimensions. These recently discovered qualities arise from an increase in the surface area as well as considerable confinement of high-energy electrons to the particle surface.

Specific interest in gold nanoparticles (AuNP) has developed over the past few decades owing to their high stability under ambient conditions, as well as their

strong optical properties and rather recent revelation of catalytic properties. Gold nanoparticles have in fact been in use for centuries. The bright ruby reds, magentas, and deep blues in stained glass and ceramics have been displayed in cathedrals and churches since the middle ages. Colloidal gold was also exploited for its curative properties with heart and venereal diseases as well as epilepsy and arthritis.[2] Their healing properties are still marketed to this day in droplets for oral consumption for a variety of ailments, for treatment from Parkinson's disease and even Attention Deficit Disorder, where the efficiency of the treatment is skeptically left to the consumer!

Modern applications of colloidal gold nanoparticles have progressed toward biological diagnostic tools, where AuNP are tested as sensors for the detection of cancer cells to cancer prevention.[3, 4] Catalytic properties of gold nanoparticles have also been discovered and exploited in the past two decades, as contrary to the innertness of bulk gold towards numerous reactions, small AuNP on the nanoscale displayed catalytic activity towards CO oxidation when stabilized on metal oxide supports.[5, 6] Since this unearthing, gold nanoparticles have found fruitful facilitation in various oxidation reaction for alcohols and olefin epoxidation, as well as reduction reactions for nitroarenes and others.[6-10]

1.2 Optical Properties of Gold Nanoparticles

Nanometer-sized metal particles possess strong optical properties that have been employed in a number of esthetic, technological, sensor, and drug-delivery applications. The brilliant colours result from addition of inorganic metal complexes to materials, although the reason behind the colourful transformation remained unknown until the nineteenth century. Particle physical and chemical properties are becoming understood for a wealth of applications in optical and diagnostic imaging, drug delivery, batericides, magnetic storage, energy harvesting and catalysis.[2, 11, 12]

Noble metal nanoparticles, such as copper, silver and gold possess strong collective oscillations of surface electrons in their conduction band, whose resonating frequencies absorb strongly in the visible range of the electromagnetic spectrum. An example of the various colours achieved for gold nanoparticles is depicted in Figure 1.1, below. As AuNP become larger or as the interparticle distance decreases, the absorbance redshifts to lower energies, display purple and blue tones. These characteristic plasmon resonance absorbances are referred to as a metal's surface plasmon band, or SPB. The frequency of oscillations is a function of the metal, the particle size and shape, the interparticle distance, as well as temperature, dielectric constant and viscosity of the medium.[13]

Figure 1 . 1 - Aqueous colloidal gold with decreasing interparticle distance from left to right, depicting the colour range observed when AuNP were in the presence of varied concentrations of 3-mercaptopropane sulfonic acid sodium salt.

The electric field of a light wave polarizes electrons in the conduction band of surface atoms to generate a net charge, with which the resulting electronic motion in the plasmon resonates to produce a vivid colour. Noble metals display an intense resonance as a result of strong coupling between the plasmon transition and interband excitation, as well as a greater polarizability of mobile conduction band electrons. Surface plasmon resonance theory was first explained by Gustav Mie, who identified the dependence of the optical properties of spherical nanoparticles with their size.[14] The surface plasmon band is the summation of absorption and scattering modes, and shifts to lower frequencies with increased surface polarizability. Higher order modes, as a result of inhomogeneous polarization, dominate with an increase in particle size as well as redshifting and bandwidth broadening. The absorption modes also depend on particle size, such that only the

translational dipole oscillation contributes to absorption for particles of dimensions less than one tenth the incoming wavelength of excitation. The variation in absorption maximum of the translational SPB with particle size is illustrated with gold nanoparticles in Figure 1.2, below. The decreased intensity for larger particles is merely a consequence of lower concentrations of particles as prepared *via* seed-mediated growth, as described in detail in Chapter 6.

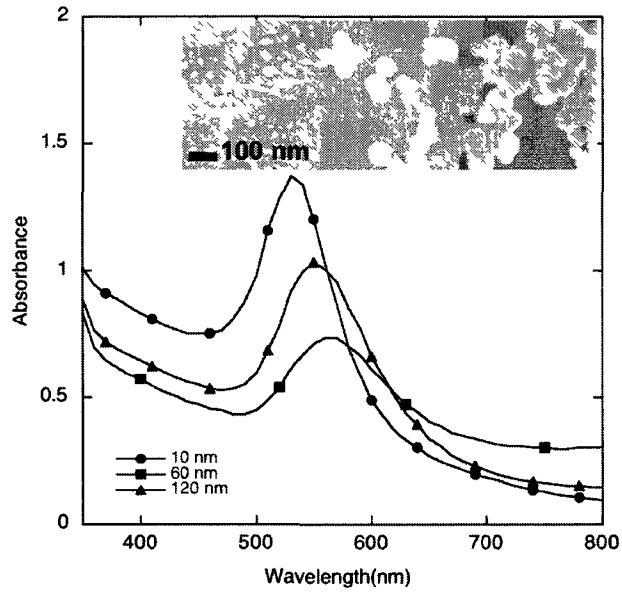

Figure 1 . 2 - UV-Vis absortion spectrum of gold nanoparticles of different sizes in water, as prepared in this research under various conditions. Inset: SEM images of the respective particles, where the scale bar represents 100 nm for all three images.

Mie particle theory predicts that particles below 20 nm possess an absorbance band dominated by a dipole term whose position and width is independent of size with the following approximation, where σ(ω) is the absorbance cross section given by

$$\sigma_{ext} = \frac{9V\varepsilon_m^{3/2}}{c} \bullet \frac{\omega\varepsilon_2(\omega)}{[\varepsilon_1(\omega) + 2\varepsilon_m]^2 + \varepsilon_2(\omega)^2} \qquad (1.1)$$

where V is the particle volume, ω is the angular frequency of excitation, and c is the speed of light. ε_m and $\varepsilon(\omega) = \varepsilon_1(\omega) + i\varepsilon_2(\omega)$ represent the dielectric functions of the medium and metal, respectively. In recent years, however, several reports have acknowledged a lack of sensitivity to the theorem, and deviance in size dependence for particles below 10 nm. Importantly, particles smaller than 2 nm do not possess an absorbance band as clusters possess independent electronic states contrary to collective oscillations. Essentially, the dielectric function within Mie theory is derived for a bulk metal and has since been modified by decomposing the dielectric function into an interband transition to account for the behaviour of the 5d-electrons, and a free-electron surface-scattering component for the mobile conduction electrons. As a result, the dielectric function obeys a size dependence and follows a $1/r$ size dependence with the plasmon bandwidth; emphasizing the limited mean free path of electrons as a consequence of the particle dimensions.[15]

Further modifications of the model have accounted for the observed optical properties of asymmetrical rod-shaped and platelet morphologies by incorporating a longitudinal dipole into the absorption coefficient.[13, 16]

$$\sigma_{ext} = \frac{\omega}{3c}\varepsilon_m^{3/2} V \sum_j \frac{(1/P_j^2)\varepsilon_2}{\{\varepsilon_1 + [(1-P_j)/P_j]\varepsilon_m\}^2 + \varepsilon_2^2} \qquad (1.2)$$

where P_j are depolarization factors along the three axes A, B and C of a prism where $A > B = C$, defined as

$$P_A = \frac{1-e^2}{e^2}\left[\frac{1}{2e}\ln\left(\frac{1+e}{1-e}\right) - 1\right] \qquad (1.3)$$

$$P_B = P_C = \frac{1-P_A}{2} \qquad (1.4)$$

with the aspect ratio between length and width included in the term e with

$$e = \left[1 - \left(\frac{B}{A}\right)^2\right]^{1/2} = \left(1 - \frac{1}{R^2}\right)^{1/2} \qquad (1.5)$$

With such structures, the absorption is characterized by two bands; a band representing the translational dipole perpendicular to the incoming electric field as well as a peak for the longitudinal dipole in the direction of the electric field, which also redshifts with increasing length of the *A* dimension. Anisotropic particles such as rods, large prisms and platelets are easily characterized by the increased scatter and absorption at longer wavelength, and display a greater sensitivity in diagnostics with interparticle distance relative to spherical particles.[17]

1.3 Catalytic Properties of Gold Nanoparticles

A decrease in size to the nanoscale results in a greater surface to volume ratio for particles relative to bulk metal counterparts. This increase in surface area as well as increase in surface energy account for an increase in chemical reactivity. For centuries, atomic gold was thought to be inert towards various chemical reactions, but recent pivotal work by Haruta *et al.* revealed the high catalytic activity for small gold nanoparticles supported on metal oxides.[18, 19] Gold nanoparticles have demonstrated successful catalytic activity in terms of high conversion and high selectivity for a variety of reactions, notably oxidation of carbon monoxide in the presence of H_2, as well as oxidation of olefins and hydrogenation of ketones and aldehydes, along with reduction of nitroaromatics.[20] While several chemical catalysis investigations have proceeded with gold nanoparticles embedded on mesoporous or metal oxide inorganic supports, valueable research has been realized in solution with unsupported 3 nm colloidal gold particles. Comotti *et al.* observed a significant increase in the rate of glucose oxidation over other unsupported metal particles.[21]

In general, the reasoning behind the catalytic activity of gold nanoparticles has not been adequately understood to date. The catalytic properties have frequently been attributed to the increase in surface energy and surface defects of the crystal lattice common to many nanomaterials, where the energy of the d states on a (111)

surface is so low that other atoms such as O bind poorly. Au atoms at steps and corners on a particle surface, on the other hand, possess d electrons closer in energy to the Fermi level and consequentially stronger interactions and a lower coordination number To account for the reactivity of gold nanoparticles, one must first account for the way that gold interacts with other elements. For years, gold has been considered a noble metal, forming weak bonds at best with elements such as H, C, N, and O as a result of short bond lengths owing to its high ionization potential. Hammer *et al.* investigated the chemical dissociation of H_2 on the surface of gold by computational methods, and identified gold as having the highest barrier to dissociation and the least stable chemisorption state relative to other noble metals such as Pt, Cu and Ni.[22] This was essentially attributed to highly filled metal d orbitals for late transition metals such as gold, and strong coupling to the close lying anti-bonding orbital of the *1s/6s* interaction. A molecular orbital energy diagram is presented in Figure 1.3.

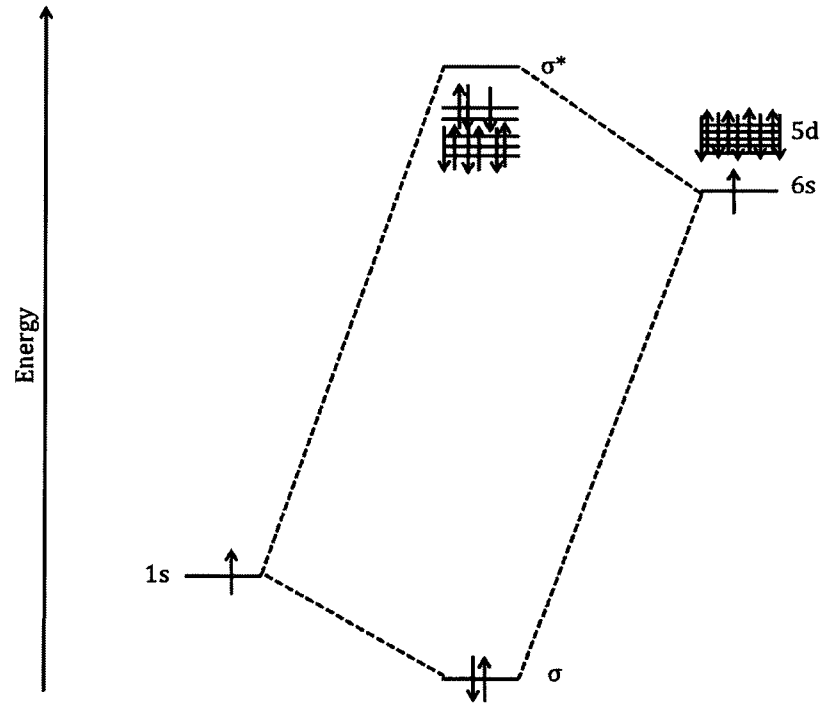

Figure 1 . 3 - Molecular orbital diagram representing the interaction between the 1s orbital of Hydrogen with the 5d and 6s orbitals of Gold.

While the interaction of the 1s orbital for H with the 6s orbital for Au results in the deep-lying filled bonding state and an empty anti-bonding state, the coupling of the anti-bonding interaction of the metal 5d states with the anti-bonding *s* orbital is only marginally higher in energy than the d electrons, and remains filled for Au. The interaction of the filled *d* bands with the anti-bonding orbitals is defined as a coupling matrix element, V_{sd}, and has one of the largest coupling matrix elements. The gap between the *5d* electrons and the Fermi level is smaller for gold than many other elements as a result of relativistic stabilization of the *6s* level. This renders the *5d* electrons more easily activated. As a consequence, the yellow luster of gold is the result of electrons of the metallic gold plasmon resonating at relativistic energies edging into the visible spectrum. Furthermore, the nobleness of gold is also attributed to the degree of orbital overlap between the d orbitals on gold and the orbitals of the adsorbates, such that a small overlap results in long, unstable bonds. While gold is rather noble in reactivity with several adsorbates composed of the elements mentioned above, its energy couples well with that of other metals, explaining the ability of gold to form alloy blends.

1.4 Particle growth

As the optical, electric and catalytic properties are principally dependent on particle size and shape, strong effort has been made to determine mechanisms for particle growth. Nanoparticles can be formed by a top-down approach through laser ablation[23, 24] or other destructive high energy techniques, as well as bottom-up wet chemical approaches via particle growth, electrodeposition, and self-assembly.[1, 25]

In the latter cases, metal ions are reduced to their atomic state at which nucleation of clusters can ensue above a threshold supersaturated concentration of nuclei.[13] Due to the challenge of observing nucleation and growth processes, the process for nanoparticle growth is not thoroughly understood. The currently accepted

mechanism will be discussed. Nucleation occurs at a point when a thermodynamically unstable solution possesses a positive free energy change, and this change is the driving force for the formation of a new volume and the free energy relating to its surface. The rate of particle nucleation in a homogeneous system has been expressed as

$$R_N = A\exp\left(\frac{-16\pi\sigma_{SL}^3 v^2}{3k^3T^3\ln^2 S}\right) \quad (1.6)$$

where R_N is the number of nuclei formed per unit time per unit volume, A is the pre-exponential factor in the range of 10^{25}-10^{56} $s^{-1}m^{-3}$,[26] σ_{SL} is the surface tension at the solid-liquid interface, ν is the atomic volume of the solute, k and T represent Boltzmann's constant and temperature, respectively, and S is the supersaturation of the solute given by

$$S = \frac{C}{C_{eq}} \quad (1.7)$$

where C and C_{eq} are the solute concentrations at saturation and at equilibrium, respectively. Additionally, the driving force for precipitation can be considered the difference in solute concentrations.

$$\Delta C = C - C_{eq} \quad (1.8)$$

The maximum positive free energy represents the activation energy for nucleation and is dependent on a critical nuclei radius, R*, where

$$R^* = \frac{\alpha}{\Delta C} \quad (1.9)$$

And α represents a collective term equivalent to

$$\alpha = \left(\frac{2\sigma_{SL}}{kT\ln S}\right)\nu C_\infty \quad (1.10)$$

Above the critical radius, R>R*, the free energy of particle growth will diminish allowing nuclei to stabilize via particle growth, yet below the critical radius, R<R*, particles will dissolve.[27] The free energy is defined as

$$\Delta G^* = \frac{4\pi\sigma_{SL}R^{*2}}{3} = \frac{16\pi\sigma_{SL}^3 v^2}{3k^2T^2\ln^2 S} \qquad (1.11)$$

and the rate of nuclei formation is thus expressed as a function of the free energy of the system as described above.

$$R_N = A\exp\left[\frac{-(\Delta G^*)}{kT}\right] \qquad (1.12)$$

The growth of metal nanoparticles from individual nuclei is also a non-trivial process, which can be either diffusion-controlled or reaction-limited. A recent review by Cushing *et al.* has concluded that previous studies allude to the former, where concentration gradients of nuclei and temperature of the system play pivotal rolls in governing the growth process.[26]

Others have expressed that metal nanoparticles do not form from simple reduction of ions to atoms, colliding to form by flocculation, a stable nucleus. Rather, a polymerization step is understood to take place where the unimolecular redox decomposition of an organic metal polymer occurs once a critical mass of metal polymer is reached.[28] Polymerization to form stable nuclei occurs when a particle's cohesive lattice energy is greater than its disruptive surface energy. Once a threshold mass of stable nuclei has formed, nanoparticle growth ensues in an autocatalytic mechanism.[29] Particles grow to reach a certain size dependent on the surface energy of the metal. Additional processes such as agglomeration and Ostwald ripening can occur if the particle surfaces are insufficiently stabilized.[30] As such, small particles dissolve and are consumed by larger particles.

Herein, metallic atoms are stabilized in the presence of aqueous counterions, where the growth mechanism has been found to depend on the concentration of stabilizer. Nanoparticles are thermodynamically stable when their kinetic growth is abruptly arrested by the presence of adsorbed ligands, or physisorbed solvent molecules

functioning as a stabilizer. At low stabilizer concentration, the anions neutralize the positive charges on residual monovalent clusters, and encourage condensation as the clusters grow by addition; accumulating a negative charge of stabilizer throughout colloid growth. The reactivity towards condensation decreases with increasing particle size and decreased surface energy.

At higher stabilizer concentration, the counter ions function to inhibit surface reductions and limit growth. Smaller particles grow more quickly than larger ones due to their higher surface energy, which decreases with growth until a narrowed and homogeneous population of particles is produced. Under these conditions, nucleation and growth are well separated and small, monodisperse, crystalline particles result. At lower stabilizer concentration, particles continue to grow via molecular addition where nuclei deposit on the surfaces of growing clusters followed by coalescence. The latter plays a more dominant role in particle enlargement. These processes are depicted in Figure 1.4.

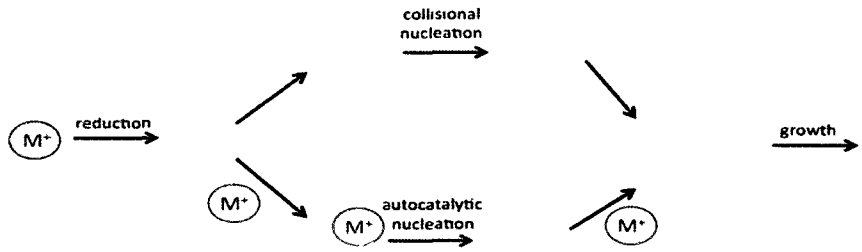

Figure 1 . 4 - Nucleation pathways towards nanoparticle growth.

Size broadening of a distribution can occur when larger particles continue to grow as a consequence of smaller ones dissolving below the critical nuclei radius. As the catalytic surface energy decreases with particle growth, remaining metal reductions occur to generate new nuclei, resulting in an overlap of nucleation and growth phenomena in the same stages. This leads to polydisperse and polycrystalline, multi-twinned particles. A summary of the competing routes is represented in Figure

1.5. Essentially, the rate of the two processes govern nanoparticle growth, and determine the size, morphology and distribution of the colloid. Fast nucleation followed by isolated growth leads to monodisperse particle sizes, while slow nucleation results in overlapping processes, Ostwald ripening, and agglomeration to yield larger and often polydisperse nanoparticulates.

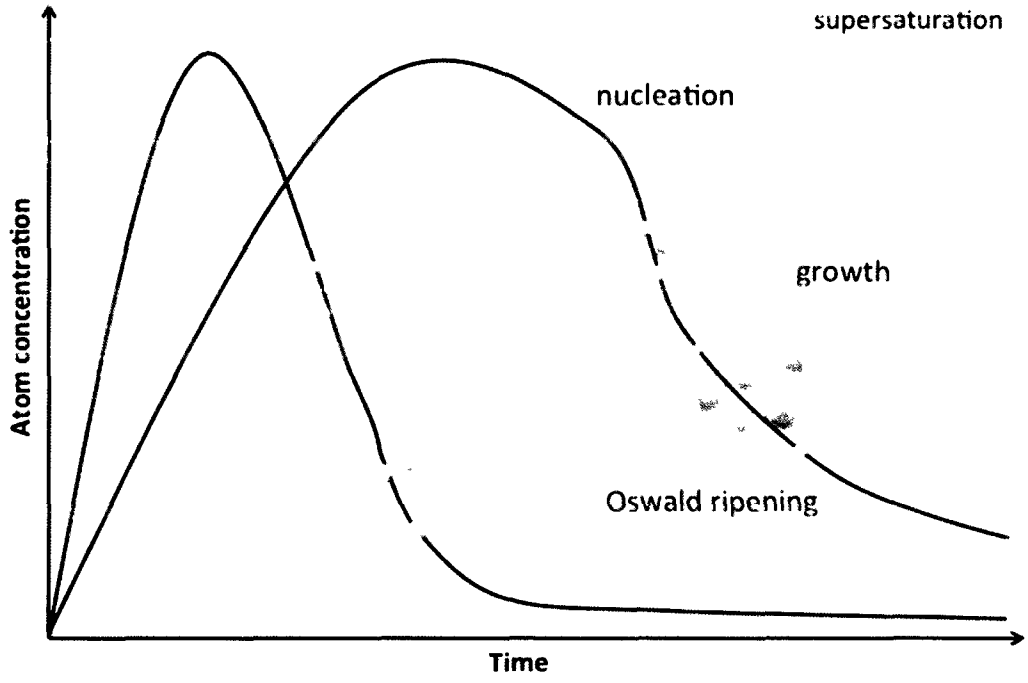

Figure 1 . 5 - Colloidal particle growth pathway

The rate of metal salt reduction and nanoparticle growth can be followed via analysis of the autocatalytic growth step. The autocatalytic growth of metal nanoparticles is characterized by an induction period and a signature sigmoidal growth curve to a concentration vs time plot. In the analyses in this research, the concentration was reported as the absorbance of the surface plasmon band, and converted to moles of AuNP formed, as presented in Chapter 6.

1.5 Particle Stabilization

The growth mechanism of nanomaterials implies that particles continue to grow to micron dimensions until an equilibrium between particle size and solute saturation is established, yet large prisms and aggregates precipitate easily and offer little difference from the bulk metal towards desirable applications. Stabilization of small nanoparticles is achieved through ligand attachment of self-assembled monolayers, polymer, dendrimer, surfactant, oligonucleotides, amino acids and other small biomolecules, films, glass or other solid supports. Essentially, the more stabilizer present during the synthetic steps, the smaller the particles can become.

1.5.1 Charge Stabilization

Colloidal particles can be considered to be in a metastable state in aqueous solutions, where attractive short range Van der Waals forces push towards the coagulation of dispersed particles, while adsorption of ions in solution cause sufficient repulsive forces at the particle surface. The presence of an electric field generated at the particle surface prevents ions from dissociating completely, forming a diffuse electrical double-layer surrounding the particle surface in which the first layer contains a high ionic concentration diffusing to the Debye length. The Debye length is defined as the distance at which the surface electrostatic potential decreases to $1/e$ of its initial value.[31] Maintaining a high electrostatic potential is critical to the stability of charge-stabilized colloids. Such colloids have been characterized by their zeta-potential, or electromobility, such that values approximating ± 30 mV or stronger indicate sufficient particle stabilization, while potentials in the 0 - ± 20 mV range reflect tendencies towards flocculation.[32] Flocculation occurs as a result of collisions of particles in solution when surface charges are neutralized, leading to precipitation. Flocculation is a broad term referring to the gathering of nanoparticles, and can result from agglomeration or

aggregation. Agglomeration is considered to be the loose and reversible dense assembly of particles, while aggregation refers to the irreversible morphological changes leading to precipitation.

1.6 Conventional Nanoparticle Synthesis

Nanoparticles have been successfully prepared in a number of methods. In regards to gold nanoparticles, the first scientific investigations into the synthesis of gold particles were reported by Michael Faraday in 1857, who produced the ruby-red films from reduction of gold chloride in a two phase system with phosphorus in CS_2.[33] He sought after proving that transparent thin films of gold were composed of non-particulate matter, but instead discovered the particulate nature of red aqueous solutions obtained after washing away excess chlorides from the gold films on his discarded glass slides. He also observed that these solutions could change colour to blue or purple, and appeared opalescent when a beam of sunlight passed through the solution. These serendipitous findings revealed the presence of matter in suspension, and Faraday later coined the term "colloid" to define such a fluid.

A classic synthesis of aqueous, colloidal gold nanoparticles was developed by Turkevich in 1951 whereby a dilute aqueous solution of $HAuCl_4$ was brought to boil followed by addition of sodium citrate.[34] The colour of the solution changed from pale yellow to grey to blue and violet before stabilizing to red. By varying the ratio of reducing agent to gold salt, the particle size of AuNP was varied from 10 to 20 nm. A simple modification of the synthesis was put forth by Frens *et al.,* which minimized the particle size down to 5 nm with improved monodispersity.[35] This citrate method has been used in numerous reports for studies involving gold nanoparticles and their applications in aqueous systems.[2, 11, 36-38]

Another groundbreaking synthesis arrived in 1994 when Brust and Schiffrin developed a method for preparing small 1-2 nm AuNP by functionalizing the surface

with long chain thiols.[39] A two-phase system with tetraoctylammonium bromide as a transfer agent for $HAuCl_4$ and dodecanethiol in the organic phase while fresh aqueous $NaBH_4$ was added slowly under vigorous stirring for three hours. The resulting particles were separated and dried to a powder; easily resuspendable in organic media. This method has been adopted in several practices where the terminal group has been varied with further functionality. This method succeeded in the preparation of small AuNP but with a decrease in monodispersity relative to the Turkevich method. Additionally, this method is essentially reserved for the generation of AuNP in non-polar media, as the long tail chains dictate the small particle's stability.[40-42]

An additional approach that has received significant attention has spanned the aqueous and organic diversity for nanoparticle preparation in what is termed the "polyol" synthesis. Herein, $HAuCl_4$ is reduced thermally by poly(ethylene glycol) in the presence of boiling poly(vinyl pyrrolidone) (PVP) as a stabilizer. In this preparation, the shape of the AuNP could be varied from spherical to dodecahedral or prismatic upon addition of silver ions.[43]

Other methods for synthesis have centered on the same principle of using different reducing agents in the presence of stabilizing media or adsorbing ligands. The majority of preparations occur via thermal mechanism, however some reductions have been induced by higher energy operations such as microwave synthesis,[44] sonication,[45] pulse radiolysis[46] or photochemical techniques. The photophysical methods have relied on excitation of species in solution to generate reactive transients capable of reducing metal salts.

1.7 Photochemical Principles Applied to Nanoparticle Synthesis

Prior to describing photochemical approaches for the synthesis of metal nanoparticles, a brief overview of photophysical processes is presented, where

these interactions will govern the efficacy of materials prepared in this doctoral research.

One of the fundamental requirements for the photochemical synthesis of nanomaterials is employ compounds which absorb light. Upon absorption of light, electrons in the highest occupied molecular orbitals of a particular chromophore will be excited to an upper excited singlet state. Once absorbed, the excess energy is dissipated through a number of possible pathways. The various photophysical deactivation pathways are presented in a Jablonski diagram in Figure 1.6. A molecule relaxes to the lowest singlet excited state, S_1, through vibrational relaxation and internal conversion (IC). From this level, molecules can continue to decay through non-radiative pathways via vibrational relaxation (VR) and dissipate energy as heat to the ground state, or through emission of a photon of lower energy relative the energy absorbed via fluorescence. Alternatively, electrons in the lowest excited singlet state can transition to a triplet state, T_1, close in energy to the singlet through the forbidden pathway of intersystem crossing (ISC), which becomes allowed upon vibronic coupling of molecular orbitals with an asymmetric nature. From the triplet state, energy can also be dissipated through thermal vibrational relaxation, or through radiative phosphorescence to the ground singlet state. In addition to radiative and non-radiative decay processes, molecules commonly release their energy through chemical reactions, where excited singlet and excited triplet states are common precursors to the formation of reactive intermediates in excited state chemistry.[47]

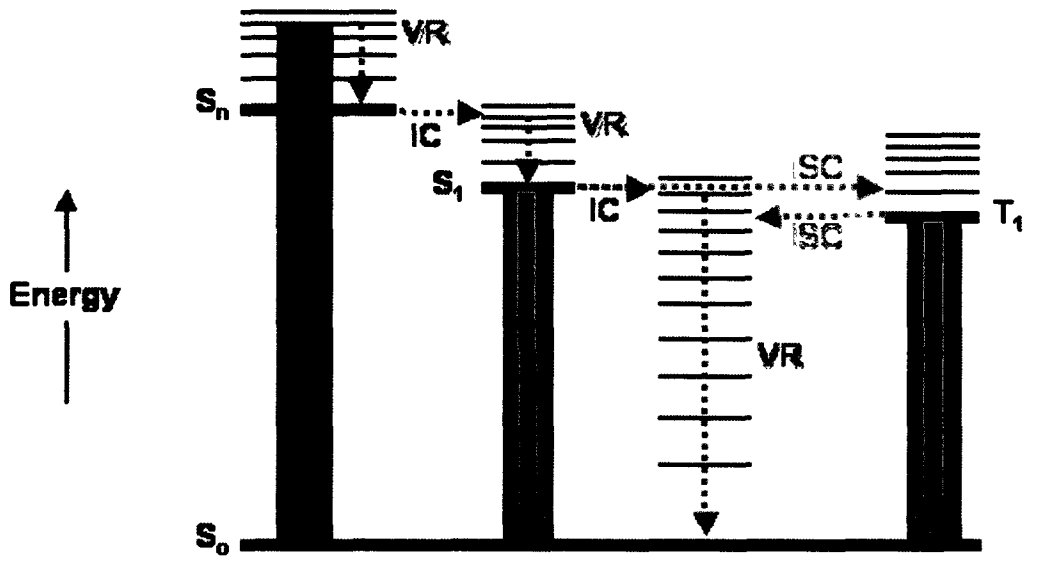

Figure 1 . 6 - Modified Jablonski diagram depicting different photophysical pathways

The generation of reactive intermediates with reducing character presented in this research has occurred from the triplet state of organic chromophores, and will be discussed in Chapters 3 and 4. Chemistry occurs from the triplet state as a consequence of the short excited singlet state lifetimes and favourable intersystem crossing, whereas free radical chemistry does not occur from the singlet state under these circumstances. Triplet species can be further described as having n,π* or π,π* character, which refer to the molecular orbital transitions of electrons from the ground to their excited states. Typically, molecular transitions with π,π* character possess high aromaticity and large singlet-triplet energy gaps, which strongly disfavour triplet formation. Such examples include symmetrical molecules pyrene, stillbene and xanthone. Structures with n,π* character possess asymmetry with non-bonding orbitals and smaller singlet-triplet gaps, which generally lead to a greater triplet population. Examples of molecules with n,π* character include ketones such as acetone and benzophenone. The character of the triplet states is also a useful classification of their reactivity in certain reactions. The research described in Chapters 4 and 5 results from hydrogen atom transfer reactions, where

chromophores with n,π* character are generalized to possess greater susceptibility toward abstraction over those with π,π* character.

Instead of productive chemical deactivation pathways, excited state species can also be deactivated through quenching by energy transfer or electron transfer processes. A common quencher of triplet species is oxygen, where molecular oxygen in the ground triplet state can interact with excited state triplets as well as reactive intermediates. Bimolecular rate constants for the quenching process occur on the order of 10^8-10^{10} $M^{-1}s^{-1}$.[48] Similarly, transition metal salts have also displayed strong tendencies to quench excited triplet states also on the order of diffusion control interactions, which is typically with rate constants on the order of 10^{10} $M^{-1}s^{-1}$.[49] These quenching pathways are present in the synthesis of metal nanoparticles described in this thesis and must be minimized through strategic preparatory methods.

1.8 Photochemistry of $HAuCl_4$

The majority of the research presented in this thesis has been conducted using one gold source; tetrachloroauric acid. $HAuCl_4$ possess a square planar coordination in the stable Au^{3+} oxidation state. This acidic, water-soluble salt displays strong absorption properties in the 200-400 nm UV-Visible region, which facilitates observation of reaction progress. The $AuCl_4^-$ complex displays an intense band at 320 nm (ε= 5800 $mol^{-1}L^{-1}cm$) and 227 nm representative of the ligand(π) to metal(σ*) charge transfer (LMCT) transitions from the filled molecular orbitals of chlorine to the empty d orbitals on gold.[50] Dissolution of $HAuCl_4$ into distilled water results in a blueshift of the LMCT band to approximately 300 nm, which is attributed to the sensitivity of speciation of the complex with pH.[51] The photochemistry of $HAuCl_4$ has been known for several decades, where excitation of the metal complex

leads to homolytic cleavage of a halide ligand, which can induce further reactivity and reduction.

1.9 Photochemical Nanoparticle Synthesis Routes

A photochemical method to generating nanoparticles offers several advantages over traditional thermal methods, such as cleaner synthesis with fewer byproducts, lower temperatures and often less overall energy required to drive the reaction.[52] Spatiotemporal control over the rate of the reaction, as well as the degree of reduction, are also included benefits. Additionally, photochemical nanomaterial syntheses can occur in a variety of different media such as aqueous and organic environments, polymers, micelles, films, semiconductor surfaces, and biological systems.[53]

There are several ways to reduce metal ions to atomic metals, and many ways to achieve this goal using photochemistry. From a wet chemical perspective, nanoparticles can be synthesized from a metal salt and a reducing agent. These methods are summarized in Scheme 1.1, and include the direct coordination complex reduction (CR), sensitized reduction (SR) and photoinitiator reduction (PI).

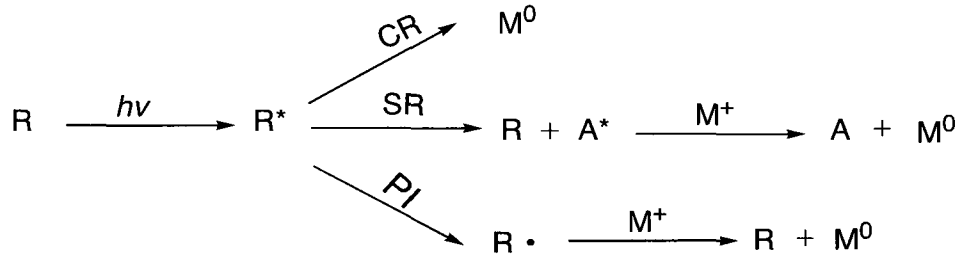

Scheme 1 . 1 - Photochemical pathways for reductions of metal salts. Photoinduced complex reduction, sensitized reduction, and photoinitiator reduction.

In some cases, the light-driven chemistry can be the result of excitation and reduction of the metal salt complex itself, as illustrated in the CR (complex reduction) pathway. Examples include the formation CuNP from the 254 nm photolysis of $Cu(acac)_2$ in ethanol or PVP.[54, 55] Formation of AuNPs has materialized from photolysis of (p-tosyl)CH_2NCAuCl or Au(CO)Cl, where the latter reduction was attributed to superior back-bonding as a result of its π-acceptance ability of ligands towards photochemical reactivity[56]. Therein, it was reasoned that RNCAuCl with greater π-acceptance character lead to stronger M-L bonds with consequential higher absorbance and a higher population of the π* ligand orbital (and decreased population of the metal *d* orbital), resulting in greater ligand dissociation. In another approach, a photochemical polythiol process was devised by Warren *et al.* by using the strong reducing potentials of photoexcited thiolates after complexation with a metal salt to form bismuth, copper, lead and antimony nanoparticles upon photolysis.[57]

1.9.1 Sensitized Photoreduction by Excited State Species

Nanoparticles can also be prepared via a sensitized reduction (SR) approach, as depicted in Scheme 1.1, where one excited state species transfers its energy to another molecule, where the latter acts as a reducing agent. The process is a consequence of either energy transfer or electron transfer process between a donor chromophore and an acceptor molecule. One approach for photochemical preparation of AgNP utilized the reduction potential of excited state species of pyrene or L-crown pyrene via 355 nm laser excitation of methanol solutions to reduce $AgClO_4$.[58] With fluorescence lifetimes of 296 and 51 ns for pyrene and L-crown-pyrene, respectively, addition of $AgClO_4$ resulted in singlet quenching with rate constants of 4.7×10^9 $M^{-1}s^{-1}$ and 3.7×10^9 $M^{-1}s^{-1}$, respectively. The reduction path from the pyrene moiety was attributed to electron transfer from the excited singlet state owing to a large ΔE_{ST}= 28.9 $kcalmol^{-1}$. The generation of colloidal silver

was evident from a SPB at 405 and 425 nm for pyrene and L-crown-pyrene treatments, respectively. The absorption intensity for L-crown pyrene was redshifted and more than twice as large as that for pyrene at equimolar pyrene moiety concentrations, indicating larger particles and a greater particle yield due to enhanced Ag^0 stabilization in the crown ether cavity. In the absence of additional stabilizer, the colloids were found to decompose overnight. Other reports by Gratzel *et al.* have identified similar Ag^0-chromophore-azo-crown ether complexes from photosensitized reduction of a cyanine dye in the presence of lipids, vesicles and micelles, and attributed the stability of the reduced species to the segregating function of the stabilizer.[59]

Another photochemical synthesis of metal nanoparticles was developed from singlet oxygen mediated photooxidation of amphiphilic dendrimers to generate reductive radicals upon photocleavage.[60] Oligo(*p*-phenylenevinylene) core branches and oligo(ethylene oxide) terminal chains were oxidized at the olefin center to generate the oxygen biradical, which photodegraded to yield the reductive α-hydroxymethyl radical as well as the aryl aldehyde product. 20 nm AuNP were prepared from the radical-induced reduction, and stabilized by the dendrimer or photodegraded dendrimer fragments.

1.9.2 Photoinitiator Reduction

Additionally, nanoparticles can be formed from the photolysis of photoinitiators, as outlined in the PI pathway in Scheme 1.1. This research deals with the latter approach, where a series of strategies and methods will be presented for photochemical synthesis of metal nanoparticles by the formation of reductive free radicals derived from photoinitiators. Photoinitiators are molecules that tend to have high absorbance in the 250-450 nm range, where their excited states form reactive intermediates such as free radicals. Photoinitiators (PI) can be described in two categories; those formed by intramolecular bond cleavage (PI_1) through a

unimolecular reaction, and those undergoing intermolecular hydrogen abstraction (PI_2) following bimolecular kinetics.[52]

1.10 Outline of Research Presented

The work presented in this doctoral thesis has centered on the synthesis of gold nanoparticles through the photoinitiator approach as well as analysis of their optical and catalytic properties. Synthetic approaches *via* a unimolecular photodissociation pathway for the generation of reducing transients are presented in Chapter 3, while different bimolecular strategies adopted are discussed in Chapter 4. The photochemical generation of reducing agents through hydrogen atom transfer is also carried through into the work in Chapter 5, where the research presented emphasizes the photochemical reactivity of the chloride metal salt. Modification of the surface of AuNP has been achieved with conventional seeded growth, a novel photochemical seeding technique, as well as various ligand attachments studies, which are all highlighted in Chapter 6. Finally, conclusions and future directions are presented in Chapter 7.

1.11 References

1. Ozin, G. A.; Arsenault, A. C., *Nanochemistry: A Chemical Approach to Nanomaterials*. Royal Society of Chemistry: London, UK 2005; p 628.

2. Daniel, M.-C., Arstruc, D., Gold Nanoparticles: Assembly, Supramolecular Chemistry, Quantum-Size-Related Properties, and Applications Toward Biology, Catalysis and Nanotechnology. *Chem. Rev.* **2004,** *104*, 293-346.

3. Kang, B., Mackey, M. A., El-Sayed, M. A., Nuclear Targeting of Gold Nanoparticles in Cancer Cells Induces DNA Damage, Causing Cytokinesis Arrest and Apoptosis. *J. Am .Chem. Soc.* **2010,** *132*, 1517-1519.

4. El-Sayed, I. H., Huang, X., El-Sayed, M. A., Surface Plasmon Resonance Scattering and Absorption of anit-EFGR Antibody Conjugated Gold Nanoparticles in Cancer Diagnostics: Applications in Oral Cancer. *Nano Lett.* **2005,** *5* (5), 829-834.

5. Haruta, M., Date, M., *Catal. Surv. Japan* **1997,** *1*, 61.

6. Haruta, M., Date, M., Advances in the Catalysis of Au Nanoparticles. *App. Catal. A: General* **2001,** *222*, 427-437.

7. Grisel, R., Weststrate, K.-J., Gluhoi, A., Nieuwenhuys, B. E., Catalysis by Gold Nanoparticles. *Gold Bull.* **2002,** *35*, 39-45.

8. Haruta, M., Catalysis of Gold Nanoparticles Deposited on Metal Oxides. *Cattech* **2002,** *6* (2), 102-115.

9. Sinha, A. K., Seelan, S., Tsubota, S., Haruta, M., Catalysis by Gold Nanoparticles: Epoxidation of Propene. *Top. Catal.* **2004,** *29*, 95-102.

10. Astruc, D., Lu, F., Aranzeas, J. R., Nanoparticles as Recyclable Catalysts: The Frontier Between Homogeneous and Heterogeneous Catalysis. *Angew. Chem. Int. Ed.* **2005,** *44*, 7852-7872.

11. Eustis, S.; El-Sayed, M. A., Why Gold Nanoparticles are More Precious than Pretty Gold: Noble Metal Surface Plasmon Resonance and its Enhancement of the Radiative and Nonradiative Properties of Nanocrystals of Different Shapes. *Chem. Soc. Rev.* **2006,** *35* (3), 209-217.

12. Wilson, R., The Use of Gold Nanoparticles in Diagnostics and Detection. *Chem. Soc. Rev.* **2008,** *2008* (37), 2028-2045.

13. Burda, C., Chen, X., Narayanan, R., El-Sayed, M. A., Chemistry and Properties of Nanocrystals of Different Shapes. *Chem. Rev.* **2005,** *105*, 1025-1102.

14. Mie, G., Beitrage zur Optik Truber Medien, Speziell Kolloidaler Metallosungen. *Ann. Phys.* **1908,** *330*, 377-445.

15. Alvarez, M. M., Khoury, J. T., Schaaf, G., Shafigullin, M. N., Vezmar, I., Whetten, R. L., Optical Absorption Spectra of Nanocrystal Gold Molecules. *J. Phys. Chem.B.* **1997,** *101*, 3706-3712.

16. Papavassiliou, G. C., Optical Properties of Small Inorganic and Organic Metal Particles. *Prog. Solid State Chem.* **1979,** *12* (3-4), 185-271.

17. Malinsky, M. D., Kelly, K. L., Schatz, G. C., Van Duyne, R. P., Chain Length Dependence and Sensing Capabilities of the Localized Surface Plasmon Resonance of Silver Nanoparticles Chemically Modified with Alkanethiol Self-Assembled Monolayers. *J. Am. Chem. Soc.* **2001,** *123*, 1471-1482.

18. Haruta, M., Yamada, N., Kobayashi, T., Iijima, S., Gold Catalysis Prepared by Coprecipitation for Low-Temperature Oxidation of Hydrogen and of Carbon Monoxide. *J. CAtal.* **1989,** *115*, 301-309.

19. Haruta, M., Tsubota, S., Kobayashi, T., Kageyama, H., Genet, M. J., Delmon, B., Low-Temperature Oxidation of CO over Gold Supported on TiO2, a-Fe2O3 and Co3O4. *J. Catal.* **1993,** *144*, 175-192.

20. Corma, A., Garcia, H., Supported Gold Nanoparticles as Catalysts for Organic Reactions. *Chem. Soc. Rev.* **2008,** *37*, 2096-2126.

21. Comotti, M., Della Pina, C., Matarrese, R., Rossi, M., The Catalytic Activity of "Naked" Gold Particles. *Angew. Chem. Int. Ed.* **2004,** *43*, 5812-5815.

22. Hammer, B., Norskov, J. K., Why Gold is the Noblest of All Metals. *Nature* **1995,** *376*, 238-240.

23. Kabashin, A. V., Meunier, M., Laser Ablation-Based Synthesis of Functionalized Colloidal Nanomaterials in Biocompatible Solutions. *J. Photochem. Photobiol. A* **2006,** *182*, 330-334.

24. Becker, M. F., Brock, J. R., Cai, H., Henneke, D. E., Keto, J. W., Lee, J., Nichols, W. T., Glicksman, H. D., Metal Nanoparticles Generated by Laser Ablation. *NanoStructured Mater.* **1998,** *10* (5), 853-863.

25. Mulvaey, P., Giersig, M., Henglein, A., Electrochemistry of Multilayer Colloids: Preparation and Absorption Spectrum of Gold-Coated Silver Particles. *J. Phys. Chem.* **1993,** *97*, 7061-7064.

26. Cushing, B. L., Kolesnichenko, V. L., O'Connor, C. J., Recent Advances in the Liquid-Phase Synthesis of Inorganic Nanoparticles. *Chem. Rev.* **2004,** *104*, 3893-3946.

27. Turkevich, J., Colloidal Gold Part I: Historical and Preparative Aspects, Morphology and Structure. *Gold. Bull.* **1985,** *18*, 86-91.

28. Turkevich, J., Colloidal Gold. Part II. Colour, Coagulation, Adhesion, Alloying and Catalytic Properties. *Gold Bull.* **1985,** *4*, 125-131.

29. Pashkey, R. M., Karaman, M. E., *App. Colloid Surf. Chem.* John Wiley & Sons: West Sussex, England, 2004; p 188.

30. Enustun, B. V., Turkevich, J., Coagulation of Colloidal Gold. *J. Am. Chem. Soc.* **1963,** *85* (21), 3317-3328.

31. Pashkey, R. M., Karaman, M. E., *Applied Colloid and Surface Chemistry.* John Wiley & Sons: West Sussex, England, 2004; p 188.

32. *Malvern Instruments Ltd. Zetasizer Nano Series User Manual.* Worcestershire, United Kingdom, 2004; Vol. MAN0317 Issue 2.1, p 288.

33. Faraday, M., Experimental Relation of Gold (and Other Metals) to Light. *Phil. Trans.* **1857,** *147*, 145-181.

34. Turkevich, J., Stevenson, P. C., Hillier, J., A Study of the Nucleation and Growth Processes in the Synthesis of Colloidal Gold. *Discuss. Faraday Soc.* **1951,** *11*, 55-75.

35. Frens, G., Controlled Nucleation for the Regulation of the Particle Size in Monodisperse Gold Suspensions. *Nature Phys. Sci.* **1973,** *241*, 20-23.

36. Li, P. Z., Duan, X. R., Liu, C. H., Du, B. A., Selective Determination of Cysteine by Resonanace Light Scattering Technique Based on Self-Assembly of Gold Nanoparticles. *Anal. Biochem.* **2006,** *351*, 18-25.

37. Liu, X., Atwater, M., Wang, J., Huo, Q., Extinction Coefficient of Gold Nanopartciels with Different Sizes and Different Capping Ligands. *Coll. Surf. B. Biointerfaces* **2006,** *58*, 3-7.

38. Jain, P. K., Lee, K. S., El-Sayed, I. H., El-Sayed, M. A., Calculated Absorption and Scattering Properties of Gold Nanoparticles of Different Size, Shape and Composition: Applications in Biological Imaging and Medicine. *J. Phys. Chem. B* **2006,** *110*, 7238-7248.

39. Brust, M. W., M., Bethell, D., Schiffrin, D. J., Whyman, R., Synthesis of Thiol-derivatized Gold Nanoparticles in a Two-phase Liquid-Liquid System. *J. Chem. Soc. Chem. Commun.* **1994**, 801-802.

40. Kamat, P. V., Photophysical, Photochemical and Photocatalytic Aspects of Metal Nanoparticles. *J. Phys. Chem. B.* **2002,** *106*, 7729-7744.

41. Brennan, J. L., Hatzakis, N. S., Tshikhudo, T. R., Dirvianskyte, N., Razamus, V., Patkar, S., Vind, J., Svendsen, A, Nolte, R J. M., Rowan, A. E., Brust, M., Bioconjugation via Click Chemistry: The Creation of Functional Hybrinds of Lipases and Gold Nanoparticles. *Bioconjugate Chem.* **2006,** *17*, 1373-1375.

42. Ingram, R. S., Hosteler, M. J., Murray, R. W., Poly-hetero-w-Functionalized Alkanethiolate-Stabilized Gold Cluster Compounds. *J. Am .Chem. Soc.* **1997,** *119*, 9175-9178.

43. Skrabalak, S. E., Chen, J., Sun. Y., Lu, X., Au, L., Cobley, C. M., Xia, Y., Gold Nanocages: Synthesis, Properties, and Applications. *Acc. Chem. Res.* **2008,** *41* (12), 1587-1595.

44. Tao, A. R.; Habas, S.; Yang, P. D., Shape Control of Colloidal Metal Nanocrystals. *Small* **2008,** *4* (3), 310-325.

45. Min, Z., Wang, Z.-S., Zhu, Y.-W., Praparation of Siliver Nanoparticle Via Active Template Under Ultrasonic. *Trans. Nonferrous Met. Soc. China* **2006,** *16*, 1348-1352.

46. Henglein, A., Meisel, D., Radiolytic Control of the Size of Colloidal Gold Nanoparticles. *Langmuir* **1998,** *14*, 7392-7396.

47. Turro, N. J.; Ramamurthy, V.; Scaiano, J. C., *Modern Molecular Photochemistry of Organic Molecules*. University Science Publishers: New York, N.Y., 2010; p 1100.

48. Maillard, B.; Ingold, K. U.; Scaiano, J. C., Rate Constants for the Reactions of Free Radicals with Oxygen in Solution. *J. Am. Chem. Soc.* **1983,** *105* (15), 5095-5099.

49. Wilkinson, F., Quenching of Triplet States of Organic Compounds by Coordination Complexes. *Pure Appl. Chem.* **1975**, 661-670.

50. Vogler, A., Kunkely, H., Photoreactivity of Gold Complexes. *Coordination Chemistry Reviews* **2001,** *219*, 489-507.

51. Wang, S., Quian, K., Bi, X., Huang, W., Influence of Speciation of Aqueous HAuCl4 on the Synthesis, Structure and Property of Au Colloids. *J. Phys. Chem. C.* **2009,** *113*, 6505-6510.

52. Pappas, P. S., Photoinitiators. In *Handbook of Organic Photochemistry* Scaiano, J. C., Ed. CRC Press: Boca Raton, 1989; Vol. II.

53. Sakamoto, M., Fujistuka, M., Majima, T., Light as a Construction Tool of Metal Nanoparticles: Synthesis and Mechanism. *J. Photochem. Photobiol. C.* **2009,** *10*, 33-56.

54. Condorelli, G. G.; Costanzo, L. L.; Fragala, I. L.; Giuffrida, S.; Ventimiglia, G., A Single Photochemical Route for the Formation of Both Copper Nanoparticles and Patterned Nanostructured Films. *J. Mater. Chem.* **2003,** *13*, 2409-2411.

55. Giuffrida, S.; Costanzo, L. L.; Ventimiglia, G.; Bongiorno, C., Photochemical Synthesis of Copper Nanoparticles Incorporated in Poly(vynil pyrrolidone). *J. Nanopart. Res.* **2008,** *10*, 1183-1192.

56. Elbeijirami, O., Omary, M. A., Photochemistry of Neutral Isonitrile Gold(I) Complexes: Modulation of Photoreactivity by Aurophilicity and π-Acceptance Ability. *J. Am. Chem. Soc.* **2007,** *129*, 11384-11393.

57. Warren, S. C., Jackson, A. C., Cater-Cyker, Z. D., DiSalvo, F. J., Wiesner, U., Nanoparticle Synthesis via the Photchemical Polythiol Process. *J. Am. Chem. Soc.* **2007,** *129*, 10072-10073.

58. Jao, T.-C., Beddard, G. S., Tundo, P., Fendler, J. H., Stabilization of Colloidal Silver Produced by Pyrene-Sensitized Photoreduction of Silver Ions in Methanol. *J. Phys. Chem.* **1981,** *85*, 1963-1966.

59. Monserrat, K., Gratzel, M., Tundo, P., Light-Induced Charge Injection in Functional Crown Ether Vescicles. *J. Am. Chem. Soc.* **1980,** *102*, 5527-5529.

60. Chang, D. W., Dai, L., Photo-Induced Formation and Self-Assembling of Gold Nanoparticles in Aqueous Solution of Amphiphilic Dendrimers with Oligo(p-phenylenevinylene) Core Branches and Oligo(ethyleneoxide Terminal Chains. *Nanotechnology* **2007,** *18* (36), 365605.

Chapter 2

Experimental Materials and Methods

2.1 Instrumentation

2.1.1 Photolysis

Photolysis experiments were conducted using a few different irradiation sources. Unless stated otherwise, a Luzchem LZC-4 photoreactor was used as the irradiation source, equipped with 14 UVA lamps giving a power dose of 35.9 Wm^{-2}. Different lamp combinations generated different power doses, which are summarized in Table 2.1. Experiments with I-907 and some results with I-2959 were conducted using a LZC-5 containing ten UVA lamps with a power dose of approximately 13.7 W/m^2.

LZC-4	Power Intensity (W/m^2)		
photoreactor	UVA	UVB	UVC
UVA lamps			
14	35.93	0.73	0.38
8 (side)	11.24	0.19	N/A
6 (top)	24.01	0.55	0.30
1 (top)	3.97	0.13	0.36
UVB lamps			
12 (6 top/6 side)	15.63	22.01	2.49
8 (side)	5.09	7.02	0.80
6 (side)	4.96	6.88	0.59
UVC lamps			
4 (side)	N/A	N/A	11.44
8 (side)	0.83	0.47	23.25

Table 2 . 1 - Power Intensity for photolysis reactions carried out in Luzchem photoreactors. Power measurements were determined using a Luzchem SPR-4001 Spectroradiometer.

Power measurements were taken using a Luzchem SPR-4001 spectroradiometer, where the reader was positioned center in the photoreactor and facing up for all measurements.

Samples prepared in quartz cuvettes were irradiated with a rotating carousel centered in the LZC-4 or LZC-5 photoreactor (Luzchem Research, Inc.). Samples were also photolyzed in a 24 well plate, also centered in the LZC-4. The temperature inside of the photoreactors was measured to be 31.4°C with 14 lamps in use. At times, samples were also photolyzed with 8 UVB lamps or 8 UVC lamps. Some early photolysis work was executed with a Xenon lamp (LZC-ICH1, Luzchem Research Inc.) and a 350 nm filter such that the sample was positioned 63 cm away from the light source. Finally, few samples were prepared by laser photolysis using a Surelite Nd:YAG laser at 355 nm (third harmonic) with an average power of ~20 mJ/pulse and an average pulse duration of ~ 6 ns.

2.1.2 UV-VIS Absorbance Spectroscopy

UV-Visible ground state absorption spectra were measured using a CARY 50 or CARY 100 spectrophotometer, or a Molecular Devices SpectraMax M5 well plate absorbance reader in cuvette or well plate mode. The latter instrument was a wonderful addition to the lab, as "high throughput screening" could be performed in analyzing the changes in absorbance of nanoparticles subjected to multiple variables. The instrument also functions as a fluorometer in the 200-800 nm range, however the function was not used in this research.

2.1.3 Laser Flash Photolysis

Nanosecond laser flash photolysis was employed to study the absorbance of new species formed as well as the disappearance of short-lived transients. The LFP system is a home-built apparatus described in detail in Michelle N. Chretien's Doctoral Thesis.[1] A Lumonics Excimer500 laser was operated at 308 nm as the excitation source, with a Xenon lamp as the monitoring light source focused on the sample and monochromator. The detector in our system is a photomultiplier tube (PMT) operating on six dynodes, connected to an oscilloscope. All components were controlled by Labview software developed by Luzchem Research Inc. The laser power was < 25 mJ/pulse with a pulse width of approximately 6 ns.

Samples were prepared in 7x7 mm quartz cuvettes cleaned with aqua regia and rigourously washed with distilled, deionized H_2O. Samples were deareated *via* Ar purging for 30 minutes in their respective solvent. Quenching experiments were performed by monitoring the signal upon addition of aliquots of quencher.

2.1.4 Oxygen Evolution

The quantity of molecular oxygen in the synthesis of AuNP using H_2O_2 (Chapter 5) was measured using an *in-house* instrument donated from Professor Ross Barkley (Mount Allison, NB). Essentially, the change in pressure in a sealed pyrex reaction vessel equilibrated in a water tank at 30 °C is measured over time relative to a reference cell containing the same consitutents, but wrapped in aluminum foil to prevent photolysis. The experimental theory behind the operation of the "Oxygen Uptake" apparatus is described in detail in the Master thesis of Vasilisa Filippenko.[2] Samples were irradiated using a Luzchem EXPO panel with five UVA lamps mounted against a glass window looking into the water tank. The setup of the instrument is presented in Figure 2.1, below.

The sample cell and reference cell were suspended in the water bath and attached to a shaker, ensuring fast diffusion of gas throughout the cell. A baseline measurement of the pressure in the reaction vessel was acquired for a minimum of five minutes prior to turning on the UVA panel. The electrical signal generated from the pressure changes in the vessel is transferred to a chart recorder pen, where the data was recorded on a paper feed. The output was also digitized using Labview v8.5 software. Initially, the sample cell and reference cell undergo a pressure check and baseline prior to sample loading, and each cell is specifically calibrated to its specific volume. Each reaction cell has been pre-calibrated with a known autooxidation reaction in order to convert the voltage detected to the concentration of oxygen generated. The reaction cell used in these experiments was engraved with the symbol "iii".

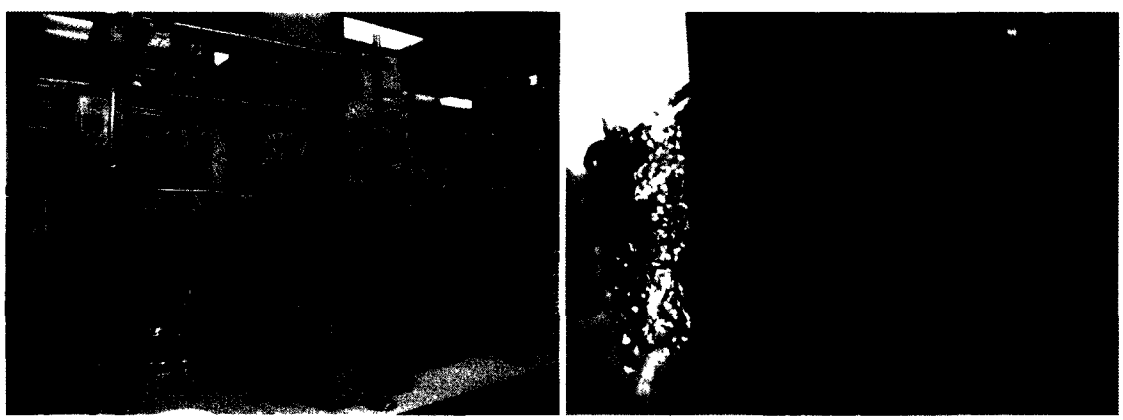

Figure 2 . 1 - (left) Benchtop view of the "Oxygen Uptake" apparatus mounted above an equilibrium water bath, and equipped with an EXPO panel positioned vertically against the left of the tank window. (right) View through the glass window, illustrating the foiled reference cell and the reaction vessel containing a pink solution of AuNP.

2.1.5 Electron Microscopy

Colloidal solutions were examined for particle size and distribution with both transmission electron microscopy (TEM) and scanning electron microscopy (SEM). Prior to examination, approximately 20 µL solution was deposited on copper grids coated with a carbon film (400 mesh), and placed in a dessicator under mild vacuum (~ 10^{-3} Pa). Dried grids prepared from AuNP samples in surfactants were subsequently rinsed with 50-100 µL methanol to remove the organic matter, and dried again. Some SEM images were obtained from AuNP deposited on silicon wafers, where the wafers were initially cleaned with a Piranha solution (1:1 concentrated HCl: 30%wt H_2O_2) for five minutes.

TEM images for samples of I-907-synthesized AuNP and some I-2959 AuNP were performed at the NRC (ICPET, Ottawa) with the help of Dashan Wang using a Philips CM20 STEM equipped with a Gatan Ultrascan 1000 CCD camera and an energy-dispersive X-ray spectrometer (EDS), INCA Energy TEM 200 operated at 200 kV. TEM images obtained for AuNP synthesized on solid supports TiO_2 (P25) and SBA-15 were acquired at Universidad Politécnica de Valencia on a Philips CM-10 microscope operating at 100 kV. All other TEM images were obtained at the University of Ottawa using a JEOL JEM-2100F field-emission TEM equipped with an ultrahigh-resolution pole piece operating at 200 kV. TEM images were occasionally obtained by Yun Liu, and the rest by personal acquision. SEM images were all obtained at the University of Ottawa using a JEOL JSM-7500F Field Emission SEM in either Transmission Electron Detector (TED) mode with a bright field (accelerating voltage 20 kV, emission current 20 µA, 7.9 mm working distance) or in Secondary Electron Imaging (SEI) mode with GB low mode (accelerating voltage 4.0 kV, emission current 20 µA, working distance 2-6 mm). To distinguish the difference between metallic particles and metal salt aggregates, backscattered-electron images were acquired by inserting the RBEI detector, where elastic scattering of electrons for the beam collide with atoms in a billiard-ball fashion. As such, larger atoms with higher atomic numbers, notably metals, possess a higher probability of elastic

collisions over non-metals, and result in a brighter intensity. Particle size was measured manually based on a minimum of 200 particles using Image J software or Image SXM software.

2.1.6 Dynamic Light Scattering and Zeta Potential

Particle size was also assessed using dynamic light scattering, or photon correlation spectroscopy, by measuring the fluctuations in scattered light of a sample from a laser light source. With this technique, particle size is determined based on the speed of random diffusion of particles such that smaller particles move more rapidly than larger ones, and this random movement of particles and colloisions with liquid solvent is known as Brownian motion. A fundamental size distribution is determined in terms of intensity of light fluctuated, which can be converted to a volume distribution using Mie theory, and then further manipulated to a number distribution to interpret particle size. Given the non-linear relationship between a particle's scattering intensity and its size, number distributions were trusted to be better representations for the determination of particle diameter. The metal particle diameter will be smaller than the value obtained for the hydrodynamic radius, which is obtained following the Stokes-Einstein equation:

$$D_H = \frac{kT}{3\pi\eta D} \qquad (2.1)$$

where k is Boltzmann's constant, T is the temperature of the system, η represents the solvent viscosity and D the diffusion coefficient. The Stokes-Einstein equation was developed for a hard sphere collision model.[3]

Zeta potential measurements were obtained by measuring the electrophoteric mobility through a type of "electrophoresis experiment" to determine particle velocity. The electric double layer of charge-stabilized particles consists of an inner charge layer where ions are strongly bound to the particle surface, called the Stern layer, and an outer layer, beyond which charges diffuse freely. Within the diffuse

layer is a boundary where ions move with a particle, but ions at further distances from the particle do not, and the electric potential at this boundary is known as the zeta potential.

DLS and ZP measurements were obtained using a Malvern Zetasizer Nano (ZEN3500) fitted with a 633 nm laser (DPSS, 50 mW). A 200 µL aliquot of gold nanoparticles was added to 1.5 mL of distilled deionized water in a plastic, disposable cuvette. 12-15 measurements were performed per samples to determine the hydrodynamic radius. Zeta potential measurements, on the other hand, were processed by rinsing disposable folded capillary cells with ethanol prior to loading with the colloid solution. An average of three consecutive measurements were performed to determine the average zeta potential for each sample.

2.1.7 Other Characterization Techniques

HPLC

High pressure liquid chromatography analysis of the decomposition of Irgacure-2959 was performed by analysis of aliquots of the irradiated sample via liquid chromatography using a HPLC-MS Integrity System from Waters, Inc. (2690 Reverse-Phase Separations Module, coupled to a 996 Photodiode Array and Integrity TMD).

GC-MS

Gas chromatography mass spectrometry analysis of Irgacure-2959 and its photoproducts was performed using a GC-MS from Agilent Technologies (6980 GC equipped with a 5973 MSD). Briefly, Aliquots of the aereated reaction mixture were removed from the vial during steady state photolysis over the course of the reaction, and added to vials of spectroscopic grade methanol.

FT-IR

For infrared spectroscopy analysis, large samples of AuNP were prepared (50 mL) by irradiating 50 mL of reagent solution in a 24 well plate in a photoreactor. Functionalized AuNP were subsequently centrifuged using a Sorvall Legend T centrifuge (Thermo Electron Corporation) equipped with either an F21-48X2 or F14-6x250 Fiberlite rotor. Following purification, samples were concentrated and dried under vacuum to afford a purple/blue/metallic film. Analytical grade KBr was combined, and the resulting solid was pressed into a pellet. IR was measured using a Nicolet Magna 550 IR spectrometer, Series II with chamber purging via N_2 flow.

XPS

X-Ray photoelectron spectroscopy was performed to assess the surface of gold nanoparticles, where aqueous AuNP were concentrated (50 mL batch to 100 µL), deposited onto a clean silicon wafer and dried under vacuum. The XPS was run using a Kratos analytical model Axis Ultra DLD, using monochromatic aluminum Kα X-rays at a power of 140 watts. The spectra were acquired by Alexander Mommers.

XRD

The crystal structure of gold nanoparticles was determined using an X-ray Diffractometer for powder samples. A 50 mL sample of AuNP was centrifuged and concentrated down to ~ 100 µL and deposited on a silicon disk prior to evaporation under vacuum. The resulting purple/metallic film was analyzed using a Siemens D5000 XRD diffractometer with Cu Kα X-rays (λ = 1.5418 Å). The spectra were recorded by Tara Kell.

NMR

All nuclear magnetic resonance imaging was performed using either the Bruker Advance 300 MHz, or 400 MHz Bruker equipped with an auto-sampler. Spectra were analyzed using TopSpin software.

Ion-Coupled Plasma Analysis

Experiments to determine the amount of Au in a sample were performed by fellow collaborator Marisa Marin and coworkers at the Universidad Politécnica de Valencia.

2.2 Materials and Methods Chapter 3

2.2.1 Materials and Sample Preparation

Distilled deionoized water was obtained from a Millipore MilliQ water filtration system with a measured resistivity of 18.2 mΩ. Acetonitrile (MeCN), tetrahydrofuran (THF) and methanol were either Omnisolv or Optima HPLC grade from Fisher Scientific. Cetyltrimethylammonium chloride (CTAC) and sodium dodecylsulfate (SDS) were purchased from Fluka Analytical (Seeize, Germany) and used as received. $HAuCl_4$, AuCl, polyethylene glycol (MW= 400), poly vinyl alcohol (MW= 10 000), poly vinylpyrrolidone (PVP) (MW= 29 000), dimethylsulfoxide (DMSO) (99.5%, spectroscopic grade), were purchased from Sigma-Aldrich (Oakville, Canada) and used as received without further purification. Special care was expressed to store the $HAuCl_4$ in a desiccator due to its hygroscopic nature, as well as using the wide end of a glass pasture pipette to dispense the material to avoid blackening of a stainless steel spatula. Fresh stock solutions of $HAuCl_4$ were prepared daily, for old stock solutions stored in amber vials (3 months +) were found to contain a small concentration of AuNP via SEM analysis. 2-methyl-1-[4-(methylthio)phenyl]-2-(morpholinyl)phenyl-1-butanone, or Irgacure-907 and 1-[4-(2-hydroxyethoxy)phenyl]-2-hydroxy-2-methyl-1-propane-1-one, or Irgacure-2959, were obtained as generous gifts from Ciba Chemicals (Basel, Switzerland). I-907 was recrystallized twice with ethanol, while Irgacure-2959 was recrystallized twice with ethyl acetate. 10 mM I-2959 did not dissolve in H_2O at room temperature, but dissolved upon heating to roughly 70°C. Stock solutions of I-2959 were prepared and used for weeks. Benzoin was obtained from Sigma-Aldrich and recrystallized twice in ethanol prior to

use. α-phenyl benzoin was synthesized by Marisa Marin and recrystallized in ethanol. Special care was taken to store photo-initiators in dark containers.

2.2.2 Photolysis in Cuvettes

Samples were prepared in static 10x10 mm quartz "home-blown" cuvettes (raw quartz tubing purchased from Freidrich & Dimmock, Inc. Millville, NJ, USA) and cleaned with aqua regia and rigourously washed with distilled, deionized H_2O. Aqua Regia was necessary to dissolve any AuNP that had plated onto the walls of the glassware. Cuvettes were typically left to clean with Aqua Regia for a minimum of three hours, or until effervescence had subsided. Cuvettes were carefully drained of concentrated the orange acid into beakers of water, and the cuvettes were flushed with running water for a minimum of five minutes and left to sit filled with water for a few hours prior to subsequent use.

Deareated samples were capped with a clean, new septum (purified and extracted in toluene prior to use). Samples containing surfactants were deareated via purging the headspace of the cuvette with Argon for 30 minutes, where the sample was briefly vortexed every ten minutes to remove dissolved oxygen from solution. Purging the headspace resolved the formation of bubbles when surfactant/micelle solutions were studied. Surfactant-free solutions were purged by fitting a 18 gauge stainless steel needle with a 5-10 cm long 20 gauge teflon tubing sleeve (where the sleeve is also pushed through the rubber septum such that only the Teflon tubing was in contact with the solution being purged. Samples were deareated via Ar purging for 30 minutes. Samples were placed on a merry-go-round sample holder (Luzchem Inc.) inside a Luzchem LZC-4 photoreactor operating with 14 UVA lamps. Samples were typically irradiated for 15-30 minutes on a timer.

2.2.3 Photolysis in Well Plates

In attempt to perform several post-synthesis modification on AuNP, aqueous, surfactant and polymer samples were prepared in 24-well plates. To simplify preparation and reduce particle size variance from well to well, large batches of the reagents solutions were prepared in a clean beaker prior to its distribution into a polypropylene BD Falcon non-tissue-culture-treated 24 well plate. 2.5 mL of solution was administered to each well. The well plate was placed in the center of a LZC-4 photoreactor operating with 14 UVA lamps. Samples were typically irradiated for 15-30 minutes on a timer. Samples of AuNP were generally left to ripen for a minimum of an hour prior to further modification. Particles were generally stored on the benchtop with exposure to ambient light. Negligible change in particle size or solution absorbance took place over prolonged periods. Gold nanoparticles that were prepared more than four years ago show excellent stability and minimal growth in particle size via TEM analysis were stored in a cupboard.

To validate photochemical mechanisms at play, certain dark experiments were performed. A volume of sample was placed in a polycarbonate centrifuge tube or quartz cuvette, wrapped in aluminium foil, and stored in a laboratory bench cupboard for a given period of time to simulate dark reaction conditions at room temperature.

2.2.4 AuNP Storage

Given the charge-stabilized nature of aqueous gold nanoparticles, changes in pH in a non-buffered solution were shown to affect the colloid stability. Results are further described in section 3.5.5. It is noted with caution that the absorbance of nanoparticles stored in generic glass vials will often redshift to develop a purple colour and at times precipitate in a matter of a few hours. The amorphous and basic

surface of the material varies from vial to vial, but has generally been known to induce flocculation through AuNP interaction with the vial surface. AuNP can be stored in cuvettes for hours to days, but also result in a smaller redshift. I quartz, particles have not generally precipitated from solution. Particles synthesized in polypropylene in sterilized, non-treated well plates are stable for long lengths of time as the particles have not been seen to interact with the plastic, however do succumb to solvent evaporation as the lids do not form a seal. Particles are best stored in polycarbonate centrifuge tubes or Nalgene bottles.

2.3 Materials and Methods Chapter 4

2.3.1 Materials and Sample Preparation

Samples were generally prepared in identical fashion as the techniques outlined in Sections 2.2.1. Materials were used, purified and processed in a similar manor. In addition, benzophenone and xanthone were obtained from Sigma-Aldrich (Oakville, Canada) and recrystallized twice with ethanol prior to use. 1-Azaxanthone was obtained from Maybridge and recrystallized with ethanol twice prior to use. 1,3-cyclohexadiene, 1,4-cyclohexadiene, thioxanthone, 2-propanol, and pyrrolidine were all obtained from Sigma-Aldrich and used as received.

Methods identical to those outlined in Sections 2.2.2 - 2.2.6 were followed for the experiments outlined in Chapter 4.

2.4 Materials and Methods Chapter 5

2.4.1 Materials and Sample Preparation

Samples were generally prepared in identical fashion as the techniques outlined in Sections 2.2.1 and Section 2.4.1. In addition, 35% wt H_2O_2 was obtained from Sigma-Aldrich and used as received. 4-hydroxyethoxy benzoic acid (HEBA) was synthesized by Natalia Paccioni, a postdoctoral fellow, and kindly donated. K_2PtCl_6, $RhCl_3$ and $RuCl_3$ were obtained from Sigma-Aldrich and used as received. Special care was taken to store the precious metal salts in a dessicator, and weighed with the larger end of a glass pasture pipette to avoid reactions with a metal spatula.

Methods identical to those outlined in sections 2.2.2 - 2.2.6 were followed for the experiments outlined in Chapter 5. In addition, experiments described in Section 5.2 were performed via direct photolysis of a cuvette stationed in a CARY 100 spectrophotometer, with a Luzchem EXPO panel mounted perpendicular to the monitoring light source. A removable door to the instrument housing had been removed such that the EXPO panel, the sample and the sample chamber were all covered with a opaque black cloth. Point absorbance measurements were taken at 530 nm every 30 s, at which time the EXPO panel was turned off for the 2-3 s required for spectum acquisition. This method was devised for a more accurate determination of the changes in absorbance of the sample over time, as opposed to 30-60 seconds of down time for each measurement for samples irradiated in a photoreactor and subject to a full spectrum sweep.

Samples were prepared for the oxygen evolution experiments such that two solutions of 0.33 mM $HAuCl_4$ for the sample and reference cells were brought to equilibrate in the water bath for approximately 30 minutes prior to injection of 3.0

mM H_2O_2 into both cells. The cells were then left to equilibrate for an additional five minutes prior to the commencement of irradiation. Hydrogen peroxide was added last as the reactivity of the oxidant can decrease with temperature and time. Initial efforts with the measurements were performed when H_2O_2 was left to thermally equilibrate, however a drastic reduction in the quantity of oxygen produced as well as the rate of oxygen production was observed.

2.5 Materials and Methods Chapter 6

2.5.1 Materials and Sample Preparation

Samples were generally prepared in identical fashion as the techniques outlined in Sections 2.2.1 with similar materials. In addition, 3-aminopropytriethoxysilane (APTES), Na_3SiO_2 (27% wt), hydroxylamine hydrochloride (99%), sodium ascorbate, KBr, KCN, KOH, NaOH, mercaptopropanesulfonate, mercaptohexadecanoic acid, L-cysteine HCl, 4,4-dithiodibutyric acid, mercaptothiazoline, ethanolamine, hexane thiol, hexadecanethiol, butylamine and hexadecylamine were all obtained from Sigma-Aldrich (Oakville, Canada) and used as received. Deoxyribonucleic acid, sodium salt Type I, "highly polymerized" from calf thymus was obtained from Sigma and used as received. Special care was taken to ensure that the DNA was stored in the freezer until needed.

Samples of AuNP were generally prepared in large batches via photolysis in a well plate, as described in Section 2.2.4.

2.5.2 Conventional Seeding

Early seeding experiments were prepared in quartz cuvettes such that varied volume of seed solution was added to 2.5 mL growth solution. These experiments include results obtained for non-functionalized AuNP, CYS, MPSA and MHDA-AuNP. Kinetics of seeded growth were also analyzed for samples prepared in cuvettes, where the changes in absorbance were monitored using the CARY-100. All other seeding experiments were performed in 24-well plates such that wells were filled with 2.5 mL of freshly prepared growth solution containing freshly prepared 0.25 mM $HAuCl_4$ and 0.4 mM NH_2OH-HCl. To maintain simplicity and reduce sample variance, a large batch of growth solution was prepared in a clean beaker prior to being decanted into the wells. Aliquots of gold nanoparticles or functionalized gold nanoparticles were added to the growth solutions, and the changes in absorbance were monitored over time with the SpectraMax M5 plate reader. As some seeded growth commenced immediately (especially for non-functionalized AuNP), the time required to fill wells was strictly minimized in comparative studies. Each plate experiment had a well reserved for monitoring changes in the growth solution without added seed to validate the reactivity of the mild reducing agent. Later experiments probed the order of addition of reagents such that equal aliquots of 0.4 mM NH_2OH-HCl were added to solutions of 0.25 mM $HAuCl_4$ and varied microlitre volumes of AuNP. The rate of NH_2OH-HCl addition was controlled by dropwise addition.

2.5.3 Photoseeding

In a similar fashion to conventional seeding, photolytic seeding experiments were performed in a well plate. Growth solutions were prepared containing 0.25 mM $HAuCl_4$ and varied concentrations of I-2959 or H_2O_2 (depending on the study). To

maintain simplicity and reduce sample variance, a large batch of growth solution was prepared in a clean beaker prior to decanting into the wells. Each plate experiment had a well reserved for monitoring changes in the growth solution without added seed to validate the reactivity of the mild reducing agent. An aliquot of AuNP synthesized from the I-2959 method under optimal conditions described in Section 3.5 was added to a well of growth solution, and placed center in the photoreactor for photolysis under 14 UVA lamps for 15 minutes. The sample was termed "A" for further seeding reactions, and the solution was left to ripen for 30 minutes. A 250 µL aliquot of A was then added to another well of 1.75 mL growth solution, and photolyzed for 15 minutes, followed by 30 minutes of ripening. This sample was termed "B". A 250 µL aliquot of B was subsequently added to another 1.75 mL of growth solution, photolyzed for 15 minutes and allowed to ripen for another 30 minutes. This sample was termed "C". Finally, a 250 µL aliquot of C was added to another 1.74 mL of growth solution, photolyzed for 15 minutes and left to ripen for 15 minutes. The wellplate was used as a reaction vessel, but seeded samples were removed and stored in centrifuge tubes to avoid repeated irradiation. The absorbance of all solutions was finally measured with the SpectraMax M5 plate reader. Each plate experiment had a well reserved for monitoring changes in the growth solution without added seed to validate the reactivity of the reducing agent.

2.5.4 Surface Functionalization

2.5.4.1 Addition of a Silica Shell

AuNP were synthesized from the I-2959 method under optimal conditions described in Section 3.5 with 0.33 mM $HAuCl_4$ and 1.0 mM I-2959, and left to ripen for approximately three hours. A 1 mM solution of APTES was combined with 50 mL AuNP solution and left to functionalize for a 30 minutes under mild stirring. A fresh aqueous solution of 0.54% wt Na_3SiO_2 was prepared, although no modification was

necessary to adjust the pH, contrary to previous reports, for the alkalinity was at a desired pH 10. 2 mL of a freshly prepared solution of 0.54 %wt Na_3SiO_2 solution was added to the reaction vessel with no modification to pH, and left to polymerize for 2-6 days. AuNP@SiO_2 were centrifuged at 6000 rpm for 60 minutes to remove SiO_2 NP which had also formed in solution. Particles were resuspended in distilled, deionized water or ethanol.

2.5.4.2 Functionalization with Organic Ligands

AuNP were synthesized from the I-2959 method under optimal conditions described in Section 3.5, and left to ripen for approximately three hours. AuNP were centrifuged at 2400 rpm for 45 minutes, and resuspended in 1.0 mM NaOH. Functionalization was conducted in 24 well plates or in polypropylene centrifuge tubes for larger batches established for further characterization. Essentially, aliquots of stock solutions of aqueous ligands were added to the wells. In comparative studies, stock solutions of MHDA, MTHZ and DTBA were prepared in ethanol. This procedure applied to studies involving MPSA, MHDA, CYS, DTBA, ETHA and MTHZ. Further studies with 6-SH, 16-SH, 4-NH_2 and 16-NH_2 were performed with ethanol stock solutions such that aliquots of the ligand were added to 1:1 solutions of non-centrifuged AuNP: ethanol. Samples were left to functionalize for a minimum of 24 hours prior to centrifugation, where some samples were placed in a Lab-Line Orbic Enviro-Shaker at room termperature for gentle and continuous shaking. AuNP were resuspended in water, ethanol or acetonitrile, depending on the ligand. Functionalized AuNP were more sensitive to centrifugation, and typical centrifugation speeds were 2000 rpm for 20 minutes.

2.5.4.3 Etching Experiments

Fresh solutions containing 0.1 M KCN and 1.0 KOH were prepared as a basic etching solution to decompose metallic gold to its auric state. To a 1x1 quartz cuvette containing 2.5 mL etchant solution, a 500 µL aliquot of AuNP or functionalized (and centrifuged) AuNP was added. The absorbance changes of the SPB were monitored over time to compare rates of etching among different surface-modified systems.

2.5.4.4 Functionalization with DNA

Double-stranded DNA solutions were prepared at 1.0 mg/mL concentrations in distilled, deionized water and shaken gently to dissolve the viscous biopolymer. DNA solutions were prepared fresh and stored at 4°C while other preparations took place. Single-stranded DNA was prepared by denaturing the double-stranded DNA through thermal modification. Samples of DNA were denatured by placing them in a boiling water bath for five minutes, after which were left to cool, and placed at 4°C with the double-stranded DNA. A typical AuNP precursor solution containing 0.33 mM $HAuCl_4$ and 1.0 mM I-2959 was placed in well plates, to which different volumes of single-stranded and double-stranded DNA were added. The ratio of AuNP precursor solution: DNA solution varied from 3:1 to 1:1. The well plate was placed in an icebath inside of the photoreactor operating with 14 UVA lamps, and the samples were photolyzed for 30 minutes. The ice bath was used to prevent denaturation of the double-stranded DNA. Later experiments were performed in a cuvette with 3:1 AuNP precursor solution: single-stranded or double-stranded DNA under ambient conditions.

2.6 References

1. Chretien, M. N. Photochemical, Photophysical, and Photobiological Studies of Zeolite Guest-Host Complexes. Doctoral, University of Ottawa, Ottawa, 2005.

2. Filippenko, V. Oxygen Uptake Studies of Organic and Inorganic Oxidations. Masters, Universiy of Ottawa, Ottawa, 2010.

3. *Malvern Instruments Ltd. Zetasizer Nano Series User Manual.* Worcestershire, United Kingdom, 2004; Vol. MAN0317 Issue 2.1, p 288.

Chapter 3

"Photo-Released" Synthesis of Gold Nanoparticles

3.1 Introduction

As mentioned in the introductory chapter, the synthesis of gold nanoparticles summarized in this doctoral thesis has occurred with the use of photoinitiators. One approach to the photochemical generation of metal nanoparticles is through an intramolecular bond cleavage of a photo-initiator in the triplet state to generate two radicals with via a Norrish type I mechanism. α-Cleavage of an excited triplet state results in the formation of an acyl-alkyl radical pair.[1, 2] While two radicals are formed, the benzoyl radical does not participate in reducing the metal salts, while the ketyl radical or the aminoalkyl radical are the active species. Significant work with photo-releasing reducing agents has succeeded with a series of benzoins, whose photodissociation is described in Scheme 3.1.

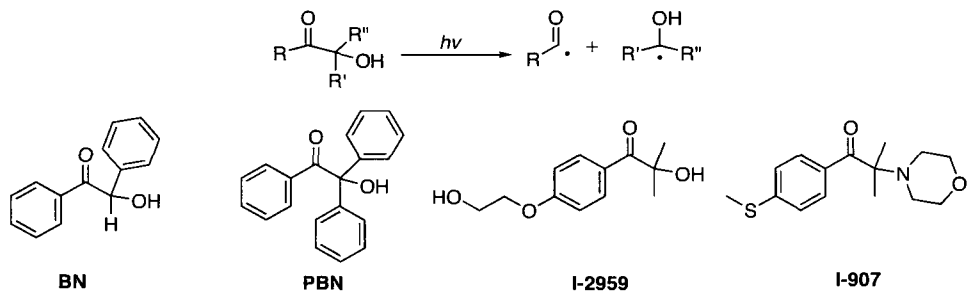

Scheme 3 . 1 - Intramolecular Norrish-I homolytic cleavage of α-hydroxy ketones and α-amino ketones investigated in this work.

The reduction of gold follows a series of reduction and disproportionation events as outlined in Scheme 3.2. Au(III) is reduced to Au(II), but its instability causes a fast disproportionation such that Au(III) is reformed along with Au(I) as outlined in Scheme 3.2. Au(I) is subsequently reduced to Au(0) in the presence of another ketyl radical, or by slow disproprotionation, as depicted in Reactions 3.5 and 3.6, respectively. Once a high concentration of atomic gold is formed in solution, nucleation ensues followed by growth.

$$HAuCl_4 \rightleftharpoons H^+ + AuCl_4^- \quad (3.1)$$

$$AuCl_4^- \xrightarrow{h\nu} AuCl_4^{-*} \quad (3.2)$$

$$Au^{III}Cl_4^{-*} + RC\dot{O}HR' \longrightarrow Au^{II}Cl_3^- + RCOR' + HCl \quad (3.3)$$

$$2\,Au^{II}Cl_3^- \xrightarrow{fast} Au^{I}Cl_2 + Au^{III}Cl_4^- \quad (3.4)$$

$$Au^{I}Cl_2^{-*} + RC\dot{O}HR' \xrightarrow{h\nu} Au^0 + 2Cl^- + H^+ + RCOR' \quad (3.5)$$

$$2\,AuCl_2^- \xrightarrow{slow} Au^{II}Cl_3^- + Au^0 + Cl^- \quad (3.6)$$

$$n\,Au^0 \longrightarrow AuNP \quad (3.7)$$

Scheme 3 . 2 - Reduction of hydrogen tetrachloroaurate by ketyl radicals.

Norrish-I α-cleavage of the ketones generates a benzoyl radical and a ketyl radical, or an α-amino alkyl radical in the case of I-907. The quantum yield for Norrish Type-I photodissociation for various α-hydroxy ketones is approximately 0.3, with a lifetime of the excited triplet state below 100 ns.[3] This substantially short triplet lifetime is a key requirement for successful nanoparticle formation, for the excited state species escapes both quenching from metal salts and oxygen on this timescale. Quenched ketone triplets mainly return to the singlet ground state, among other possible processes.

3.2 Irgacure-907

Gold nanoparticles were first realized using a commercial photoinitiator obtained as a generous gift from CIBA, 2-methyl-1-[4-(methylthio)phenyl]-2-(morpholinyl)phenyl-1-butanone, or Irgacure-907, (I-907). This photoinitiator undergoes Norrish-I α cleavage to yield a benzoyl as well as an α-amino alkyl radical, where the latter has a more negative reduction potential estimated around E^0= -1.47 vs. NHE.[4] The reaction is illustrated in Scheme 3.3.

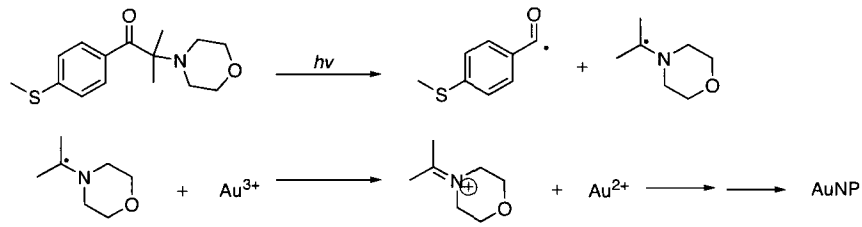

Scheme 3 . 3 - Synthesis of AuNP via I-907

Initial experiments utilized CW UVA (centered at 365 nm) photolysis of aqueous 0.1 M sodium dodecyl sulfate (SDS) solutions to solubilize the initiator in the presence of $HAuCl_4$. Experiments conducted in acetonitrile (MeCN) or tetrahydrofuran (THF) in the absence of a surfactant resulted in agglomerated, unstable particles that precipitated out of solution within hours. Alternatively, work was performed with a negatively charged surfactant such as SDS, and the concentration of $HAuCl_4$ was held at 0.33 mM and the concentration of I-907 was varied from 0.17-10.0 mM. Within this range, the maximum absorbance of the SPB blueshifted to shorter wavelength with increasing concentration. Initial studies were performed at 1.66 mM I-907 or a 5:1 I-907:Au(III) ratio. A TEM micrograph of a 5:1 I-907:Au ratio revealed an average particle size of approximately 4.78 ± 1.33 nm, as approximated for 200 nanoparticles, and is presented in Figure 3.1.

Due to the high concentration of SDS, however, imaging under high vacuum of the TEM led to a decrease in resolution and image quality in further images. For this reason, future surfactant-based samples were deposited and dried on copper grids followed by washing with methanol to dissolve and remove excess organic material. As a result of the post-treatment, however, images yielded particles of significant polydispersity, indicating the stabilizing role of the surfactant.

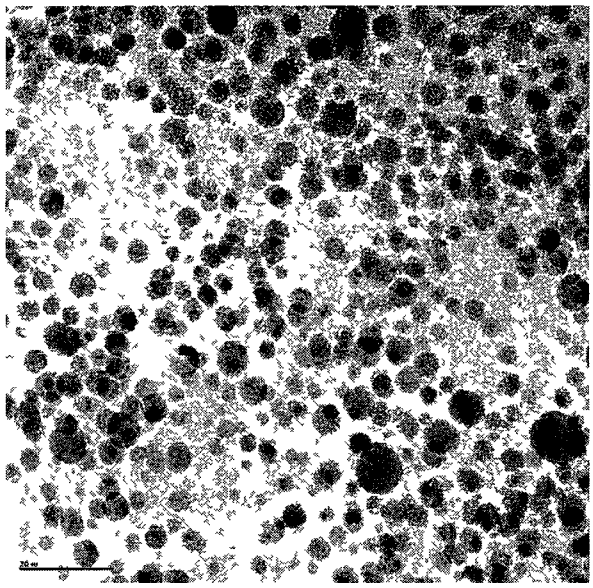

Figure 3 . 1 - TEM image of AuNP prepared from 0.33 mM $HAuCl_4$, 1.66 mM I-907 in deareated 0.1 M SDS via 30 minutes UVA photolysis. The scale bar represents 20 nm.

A concentration study was performed to establish the necessary molar ratio of photoinitiator to gold salt. Following 30 minutes of irradiation, the absorption spectra of different samples were recorded as depicted in Figure 3 2 Low ratios of I-907:Au(III) resulted in a broad surface plasmon band of low intensity, where increasing the ratio to 1:1 resulted in a blueshift, narrowing and increased SPB; suggestive of smaller and more monodisperse nanoparticles. A greater concentration of reducing agent accounted for a faster nucleation period and thus smaller nanoparticles. An optimal ratio was found to be 3:1, which correlates well with the stoichiometry of the electron transfer to form atomic gold. At concentrations above 3:1 I-907:Au(III), the SPB was seen to broaden again and increase at longer wavelength, where the latter is an indication of scattering from larger particles.

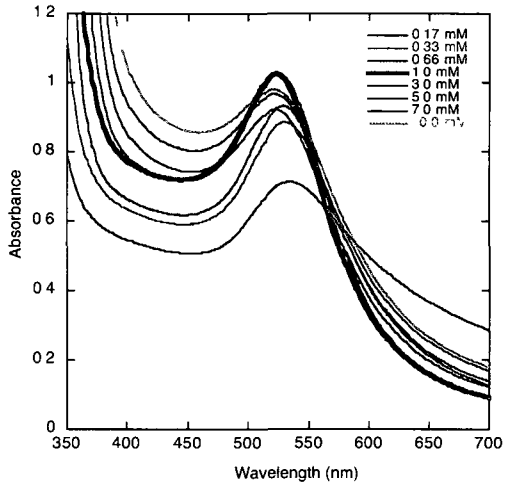

Figure 3 . 2 - UV-VIS Absorption spectra of gold nanoparticles prepared from aqueous, deareated 0.1 M SDS solutions of 0.33 mM HAuCl4 and varied concentration of I-907. Samples were subjected to 30 min UVA photolysis.

These larger particles could be the result of Oswald ripening processes incurred from insufficient amount of surfactant to stabilize an increased amount of particles prepared. Despite an apparent optimal SPB for a 3:1 ratio sample, initial exploratory research was conducted with 1.66 mM I-907 at a 5:1 I-907:Au ratio of reagents. This synthesis resulted in gold particles with long term stability, where no change in the surface plasmon band was observed for months.

The growth of gold nanoparticles using I-907 was further investigated to understand the mechanism for particle formation. The absorbance of a deareated nanoparticle solution was measured by quickly collecting an absorption spectrum at different time intervals during continuous irradiation of a Xenon lamp equipped with a 350 nm bandpass filter. The solution turned from clear, pale yellow to pink over the course of approximately ten minutes, before turning red with extended irradiation time of 30 minutes. The absorption changes are reflected in Figure 3.3 (left). The lamp was turned off after 30 minutes, but a small increase in absorption was observed over the following 14 hours. This increase in absorbance was an indication of continual growth or "ripening" and warranted further investigation.

To monitor the ripening, an identical solution was irradiated for one minute followed by monitoring the SPB using a UV-Vis spectrometer, and an increase in absorbance was in fact observed. The rate of increase of the SPB was significantly slower relative to the continually irradiated sample, and the absorbance maximum was also redshifted by 5 nm. Furthermore, the final absorbance of the 60 s sample after 300 minutes was 90% of the sample irradiated for 30 min and ripened. A comparison is presented in Figure 3.3 (right).

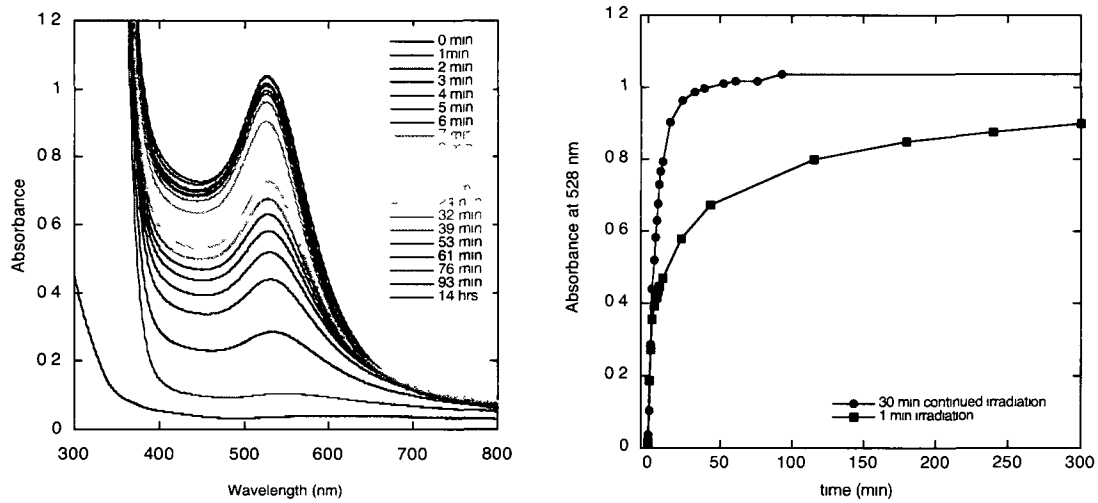

Figure 3 . 3 - (left) Growth of AuNP SPB over continuous irradiation time from an Xe lamp with a 350 nm fiter. Deareated sample contain 0.33 mM $HAuCl_4$, 1.66 mM I-907 in 0.1 M SDS. (right) Comparison of growth of AuNP monitored at 528 nm monitored over time for identical sample compositions; (●) photolysed for 30 minutes continuously and (■) for one minute.

These results indicate that the reduction of Au(III) to atomic gold is significantly progressed in as little as 60 s of Xe lamp photolysis, followed by a slower growth period. Interestingly, both samples showed the emergence of a plasmon band after 60 s irradiation time, but the experimental time spanning the walk from one lab to another and record the observed spectrum likely differed, and this accounts for the higher absorbance of the one minute sample compared to the equivalent irradiated time of the 30 min photolysis sample. Nevertheless, continued growth appears to

occur faster in the presence of light as continual generation of reducing radicals increases the rate and yield of nanoparticle growth.

These findings illustrate that both nucleation and growth processes are occurring at the same time for the three electron reduction in this system, particularly when irradiation is stopped momentarily but repeatedly during the initial stages of nucleation. On the other hand, 60 s of irradiation followed by the observed growth indicates an alternate growth mechanism whereby fast nucleation and formation of gold clusters within the short time-span resulted in surface-catalyzed growth of nanoparticles. As described in the introduction, the reduction of Au^{+} in the presence of small gold clusters is accelerated via particle-mediated electron transfer. In comparison to the continuously irradiated sample after three minutes, for example, the 60 s sample had a lower concentration of total atomic gold due to a shorter time of exposure to photogenerated radicals prior to their nanosecond decay. A longer nucleation period for the 60 s sample ensued to attain a threshold concentration of atoms prior to particle formation, and a slower growth process followed with a greater overlap of nucleation and growth phenomena.

From another perspective, the growth mechanism could result from a photochemical pathway as well as a thermal (dark) route. Continued growth after 60 s of irradiation was interesting and led to a series of control experiments with puzzling results. Dark reactions were performed to evaluate the ability of I-907 to reduce gold through a side reaction. It was observed that a deareated 0.1 M SDS solution containing 0.33 mM $HAuCl_4$ and 1.66 mM I-907 had turned purple after the sample was foiled and stored in a cupboard for two hours. Identical reagent concentrations prepared in THF in the absence of surfactant, however, remained clear and pale yellow. Further investigations indicated that solutions of 0.1 M SDS alone were capable of reducing $HAuCl_4$ upon photolysis, yet no AuNP were formed from a dark condition over equivalent time.

The quality of SDS was increased from reagent grade to analytical grade, yet photolysis in the absence of added photoinitiator still resulted in the appearance of a low and broad surface plasmon. The results of these control reactions are outlined in

Figure 3.4. In comparing AuNP formed with I-907 under irradiated and dark conditions, the bathochromic shift and higher intensity of particles prepared under light clearly illustrate the presence of smaller particles and hence the added benefit of photochemical control in this preparation

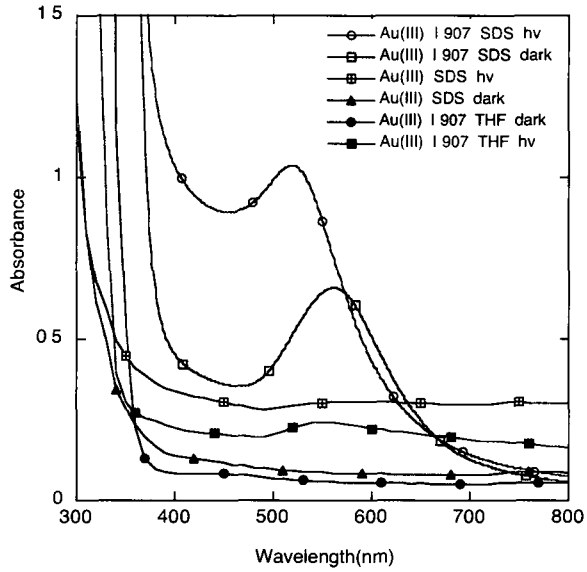

Figure 3 . 4 - Absorption of AuNP prepared for various control reactions. 0.33 mM $HAuCl_4$, 1.66 mM I-907, 0.1 M SDS, 30 minutes UVA photolysis.

Alternatively, synthesis was explored using different surfactants. Sodium decyl sulfate and sodium octyl sulfate were also used as negatively charged surfactants and gave similar results to those of sodium dodecyl sulfate A positively charged surfactant, cetyltrimethylammonium chloride (CTAC) was also tested. Interestingly, switching to a positively charged surfactant reduced the rate of nanoparticle growth but narrowed the bandwidth of the SPB under photolytic conditions. The growth of the SBP of AuNP at various times is illustrated in Figure 3.5 (left). The comparison of growth rate at the SPB maximum is presented in Figure 3 5 (right) Synthesis in CTAC resulted in an induction period to SPB formation of approximately 7 minutes, as well as a redshifted SPB maximum of 6 nm to 534 nm.

The growth of AuNP over time with both surfactants was also compared under deareated conditions, and it was apparent that SDS formed a SPB twice as fast in SDS relative to CTAC. The increased reactivity is hypothesized to be activated by a thermal reaction from impurities in the surfactant.

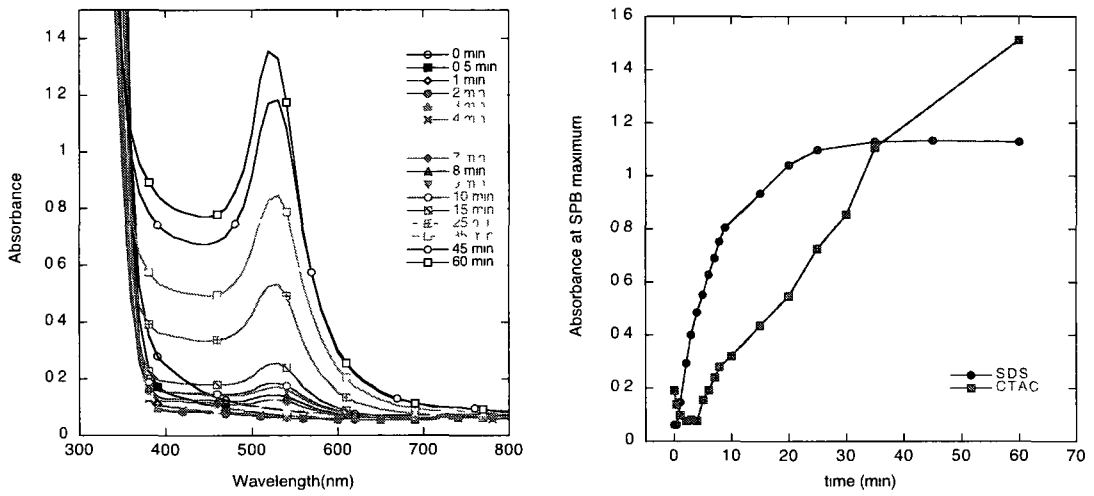

Figure 3 . 5 - (left) Absorption of AuNP prepared from 0.33 mM $HAuCl_4$, 1.0 mM I-907 in 17 mM CTAC during continuous UVA photolysis. (right) Comparison of growth at 530 nm between AuNP prepared by identical conditions in either 100 mM SDS or 17 mM CTAC.

Surfactant interference led to complications in deducing a mechanism, and the reasoning for the poor quality of the particles remains unclear. The reaction system employing I-907, nevertheless, is an effective way of generating small gold nanoparticles of approximately 4-5 nm. AuNP synthesis with I-907 in SDS was paused in search of a facile, aqueous preparation of AuNP with other photoinitiators.

3.3 Benzoin

Initial investigations reported by Itakura *et al.* used the photoinitiator benzoin, where UVB photolysis generated both the benzoyl radical as well as a hydroxybenzyl

radical in deareated ethanol solutions in the presence of metal salts with PVP as a stabilizer.[5] Silver nanoparticles were prepared as well from benzoin with $AgClO_4$ and PVP where an increase in the ratio of benzoin:Ag^+ from 1:1 to 10:1 resulted in a decrease in particle size from 17 to 7 nm, and the decrease in size was attributed to the stabilization by electron injection of benzoyl and benzyl radicals and strong surface repulsion forces. Furthermore, copper nanoparticles were prepared from $Cu(ClO_4)_2$ at a 5:1 photoinitiator:Cu^{2+} concentration ratio to afford 3 nm CuNP.

During the course of this doctoral research, gold nanoparticles were also prepared with benzoin. Experimentally, a sample was prepared by combining $HAuCl_4$, CTAC, and benzoin followed with irradiating samples in a photoreactor. While keeping the concentration of the gold precursor salt constant at 0.33 mM, variations in the surfactant and photoinitiator concentration were analyzed in order to optimize ideal conditions for synthesis. No increase in absorption resulted from irradiation times longer than ten minutes. Additionally, the concentration of CTAC was varied from 7 to 66 mM, showing negligible difference in the position and intensity of the SPB. On the other hand, increasing the concentration of BN from 0.66 mM to 1.0 mM increased the rate of the formation of the plasmon band, but only marginally increased the intensity of the peak. These results imply that the optimal conditions are obtained when a 3:1 ratio of Au(III): benzoin was present in deareated surfactant solutions above the critical micelle concentration of 1.1 mM for CTAC.[6] Additionally, there was no observed change in particle stability. The absorption spectra for these conditions are presented in Figure 3.6.

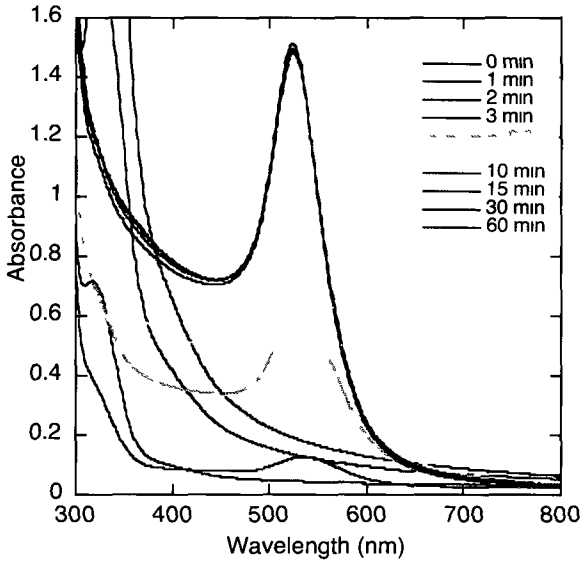

Figure 3 . 6 - UV-ViS Absorption spectrum of AuNP prepared from UVA photolysis of 1.0 mM benzoin, 0.3 mM $HAuCl_4$ in 17 mM deareated CTAC for 60 minutes.

To further understand the fast kinetics leading to AuNP formation, we sought after the ability to utilize a photo-releasing reducing transient that could be visualized spectroscopically. For this reason, a second benzoin was synthesized, which generates an observable ketyl radical; benzophenone.

3.4 α-phenyl benzoin

The substituted benzoin, α-phenyl benzoin (PBN) was synthesized according to a literature preparation[7] by Maria Luisa Marin, a visiting professor from the Universidad Politécnica Valencia (UPV). The synthesis is briefly outlined in Scheme 3.4, and involves the use of SmI_2 as a single electron transfer reagent for a ketone-nitrile reductive coupling reaction. SmI_2 chelates to the ketone to generate a ketyl

radical, rendering the carbon atom of the carbonyl more nucleophilic for attack of the carbon of the nitrile, followed by hydrolysis.

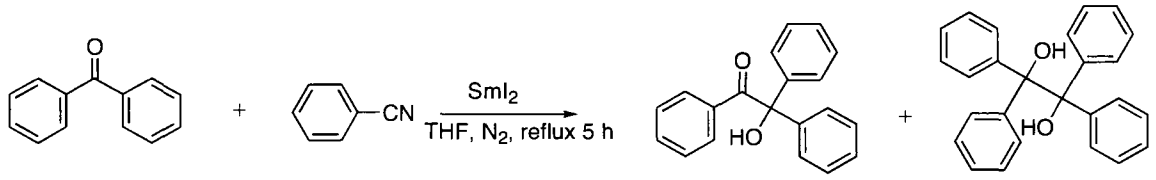

Scheme 3 . 4 - Synthesis of α-phenyl benzoin.

Upon similar experimental conditions employed using benzoin, PBN yielded AuNP in the same timeframe with an almost identical narrow bandwidth SPB. Upon 355 nm photolysis of PBN, a benzoyl radical and the benzophenone ketyl radical (BPK) are produced, where the latter was detected in laser flash photolysis studies to estimate the rate of initial gold reduction.

The short triplet lifetime of substituted benzoins (~1 ns)[8] prevents its transient absorption detection with nanosecond LFP, yet the generation of BPK is easily observed. The transient absorption spectrum of BPK generated from 5 mM PBN in acetonitrile is given in Figure 3.7.

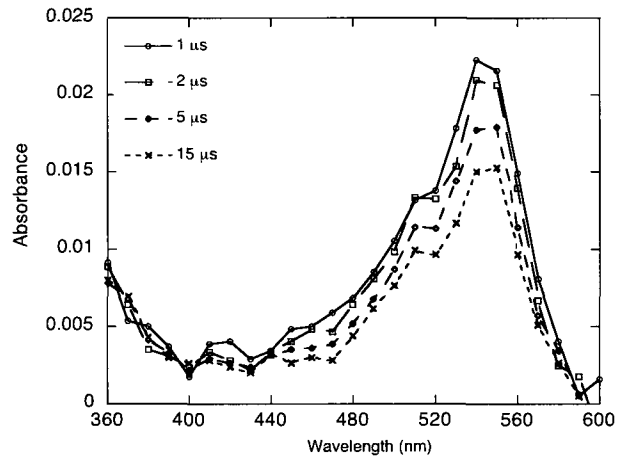

Figure 3 . 7 – Transient absorbance spectrum produced from 308 nm photolysis of deareated acetonitrile solutions of 5.0 x 10^{-3} M PBN. The absorbance peak at 540 nm is representative of the benzophenone ketyl radical.

The triplet lifetime of BPK was measured in deareated acetonitrile, and the quenching effects of adding increasing amounts of $HAuCl_4$ were determined by monitoring the decay of the triplet at 540 nm to evaluate the rate of initial reduction towards gold nanoparticle synthesis. The pseudo first order rate constant for radical decay (k_{obs}) was obtained at various quencher concentrations, and follows eq. 3.1:

$$k_{obs} = k_0 + k_{ET}[\text{Au ion}] \qquad (3.1)$$

where k_{ET} is the rate constant for electron transfer to the scavenger and k_0 is the rate constant for decay in the absence of gold ions. Plots of the pseudo-first-order rate constant for ketyl radical decay as a function of Au(III) concentration yielded a straight line whose slope gave k_{ET}= 9.9 x 10^8 $M^{-1}s^{-1}$ for the bimolecular process. This rate constant was measured to be representative of the rate of a one-electron transfer from BPK to Au^{3+}, yet a series of disproportionation steps and further subsequent reduction is prevalent for nanoparticles to develop. For simplicity, a comparative study was executed employing AuCl as the precursor salt to isolate the one-electron reduction process. An example of a decay trace monitored at 540 nm for the study is depicted in Figure 3.8, along with the kinetic analysis.

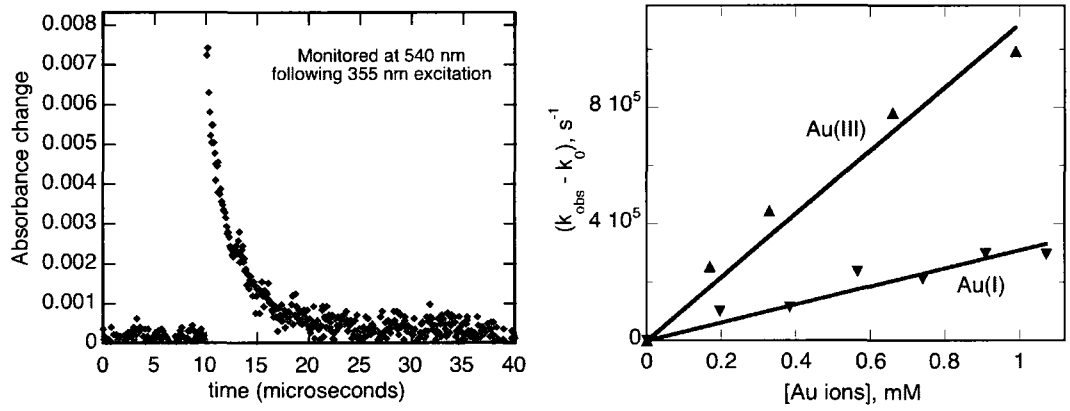

Figure 3 . 8 - (left) Transient absorption decay monitored at 540 nm upon 308 nm laser flash photolysis of deareated acetonitrile solutions of 4.0 x 10^{-3} M PBN in the presence of $HAuCl_4$. (right) Quenching plot of the changes in pseudo-first order decay rate constants upon additions of AuCl and $HAuCl_4$ as quenchers.

The limited solubility of the aurous salt in various solvents and its thermal reduction in others required the careful preparation of a fresh stock solution of AuCl for each experiment. A 10 mM stock solution of deareated AuCl was briefly sonicated in dimethylsulfoxide for five minutes prior to its addition as quencher to deareated 4.0 mM PBN in acetonitrile, where A_{355}= 0.51. In an identical kinetic approach to the samples containing the auric salt, the calculated rate constant for electron transfer with AuCl was determined to be 2.5 x 10^8 $M^{-1}s^{-1}$.[9] As a control, comparative LFP kinetics were measured with equivalent concentrations of DMSO added to $HAuCl_4$ samples to rule out any solvent effects with regards to differences in obtained rate constants.

The difference in rates of measured electron transfer can be understood by taking thermodynamics into consideration. The reduction potential for the three electron transfer for $AuCl_4^-$ is well known to be +0.99 V vs NHE, and +1.11 V vs NHE for the one electron transfer from AuCl,[10] which imply that the overall process of electron transfer and disproportionatioin for the three electron transfer is more challenging than to transfer one electron to AuCl to yield Au^0. Both processes, nevertheless, are extremely favourable as determined by the free energy rationale. The Nernst equation is presented in Equation 3.2, and was applied to the one electron and three electron processes for AuCl and $AuCl_4$, respectively to determine the free energy of the system. The concentration of the ketyl radical and its oxidation products were approximated given a quantum yield of 0.3 for the benzoin homolytic cleavage.

$$\Delta G = -zFE + RT\ln\left(\frac{[BP]^3[H^+]^3}{[Au^{3+}][BPK]^3}\right) \qquad (3.2)$$

The free energy for the three electron transfer with $HAuCl_4$ was calculated to be -841.6 kJ/mol, while the one electron transfer with AuCl equated to – 300.3 kJ/mol. Both processes are incredibly spontaneous, certifying that the synthesis of AuNP will be facile whether Au(III) or Au(I) are involved as demonstrated in the high rate constants. The free energy for the reduction of Au^{3+} is more than three times

greater than that for Au^{+}, and agrees with the kinetic analysis where the electron transfer to Au^{3+} is almost four times greater than the Au^{+} process. To our knowledge, the one electron transfer from Au^{3+} to unstable Au^{2+} has not been reported. Our measurements illustrate a rapid process for the one electron transfer, and emphasize that the primary electron transfer is more favourable from the stable $AuCl_4^-$ compared to an equivalent transaction from AuCl. The added difference of the kinetic investigation emphasizes the kinetic control of the reaction, but could also indicates other parameters involved, such as the reorganization energy consumed in reorganizing the chemical structures in electron transfer reactions.

The reduction of AuCl to gold nanoparticles employing PBN was also analyzed with UVA photolysis. Deareated samples were prepared in acetonitrile, however the stabilization of AuNP proved to be a challenge in the absence of additives, as shown by the broad and low absorption of the Au SPB in Figure 3.9, left. A substantial improvement in particle yield was obtained when the solvent was modified to 66 mM CTAC, and can be visualized in Figure 3.9, right.

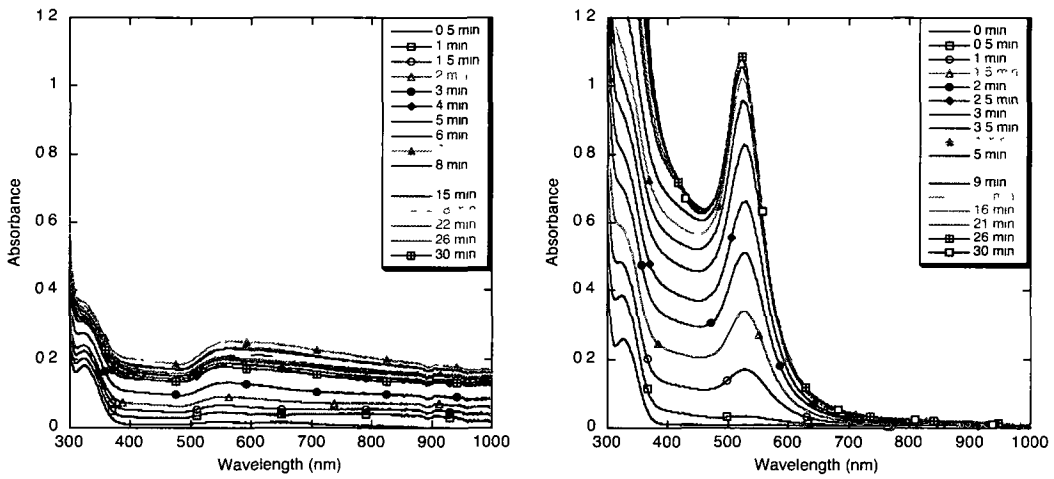

Figure 3 . 9 - UV-Vis Absorption of AuNP prepared from a deareated solution of 1.0 x 10^{-3}M PBZ and 3.0 x 10^{-4} M AuCl in (left) acetonitrile and (right) 6.6 x 10^{-2} M CTAC upon 30 minutes UVA photolysis.

Despite the smaller rate constant for electron transfer to AuCl, one clear observation is the faster generation of AuNP with the Au(I) salt. It is evident that no induction period (< 30 s) was observed in comparison with reduction of $HAuCl_4$. Secondly, the absorbance peak at 320 nm is of particular interest. The increase in absorption with irradiation time is attributed to both the characteristic absorption of AuNP at 530 nm as well as at higher wavelength, where the latter also overlaps with the production of light absorbing transients from benzophenone around 320 nm.[11] Slow disproportionation of the unstable AuCl in a chlorinated surfactant medium could also be cause for the absorbace. Ion-coupled plasma analysis of a 0.33 mM AuCl solution revealed a Au concentration measuring 33% less than samples containing the equivalent concentration of $HAuCl_4$, which underlines the precursor's delicate stability. When identical samples were prepared with similar concentrations of different gold precursor salts, notable differences were observed when their growth was monitored with time, as described in Figures 3.10 and 3.11. Particularly, the LMCT for Au(III) was easily monitored and its decay over the first five minutes of irradiation preceded SPB formation and growth after 15 minutes. With particle formation via PBN, the absorbance increased at 530 nm as well as an increase at higher wavelength, which was also characteristic for gold nanoparticles.[12-15]

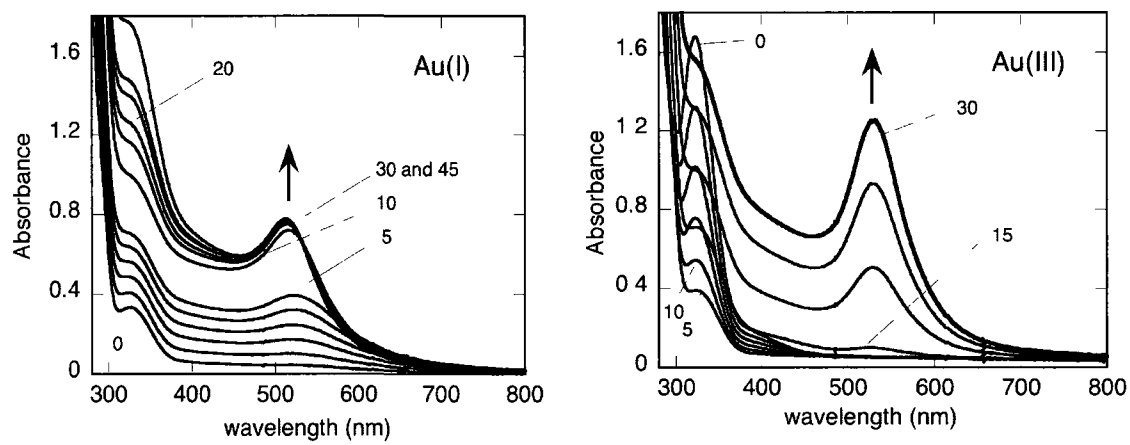

Figure 3 . 10 – UV-Vis Absorption of AuNP over time synthesized from 1.0 mM PBN in deareated 66 mM CTAC with 30 minutes UVA photolysis from (left) 0.33 mM AuCl and (right) 0.33 mM $HAuCl_4$. Time indications are given in minutes.

Conversely, no induction period was observed with Au(I) as the SPB grew at a slower rate at the stoichiometric concentration of PBN, but attained an intensity of roughly 66% relative to the Au^{3+} sample. This can be explained as the rate of electron transfer was measured to be faster than for Au^{+}. When the experiment was repeated at an excess concentration of PBN, that is 1:1 PBN:Au(I), the rate of AuNP formation increased but attained an overall identical absorption intensity as the 3:1 PBN:Au(I) sample. This lower absorption was again likely to result from the instability of the AuCl starting salt in solution.

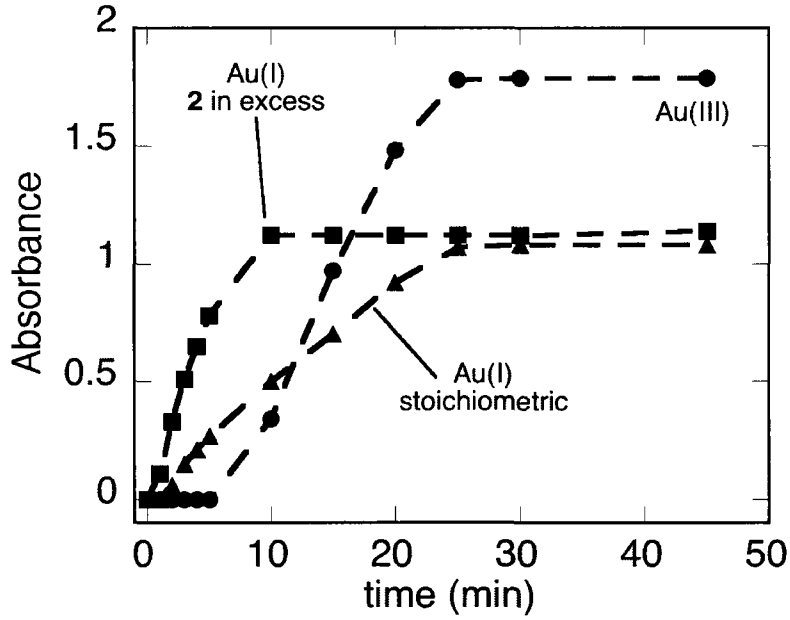

Figure 3 . 11 - Formation of AuNP from Au(I) and Au(III) over time with UVA photolysis. All three solutions were deareated and contained 0.33 mM $HAuCl_4$ or AuCl, 66 mM CTAC. The PBN concentration in Au(III) and excess Au(I) referred to a concentration of 1.0 mM while the stoicheometric amount was 0.33 mM PBN.

The absorption spectra for the different samples revealed a SPB of 512 nm for the NP prepared from AuCl, while a peak at 522 nm was attained for the AuNP prepared from the Au(III) salt. The size of the AuNP were also analyzed via TEM, and are depicted in Figure 3.12. Both samples show a predominance of spherical particles with significant polydispersity. The corresponding histograms disclose particle sizes of 7.5 ± 1.5 nm for Au(I) and 17.0 ± 7.8 nm for Au(III).

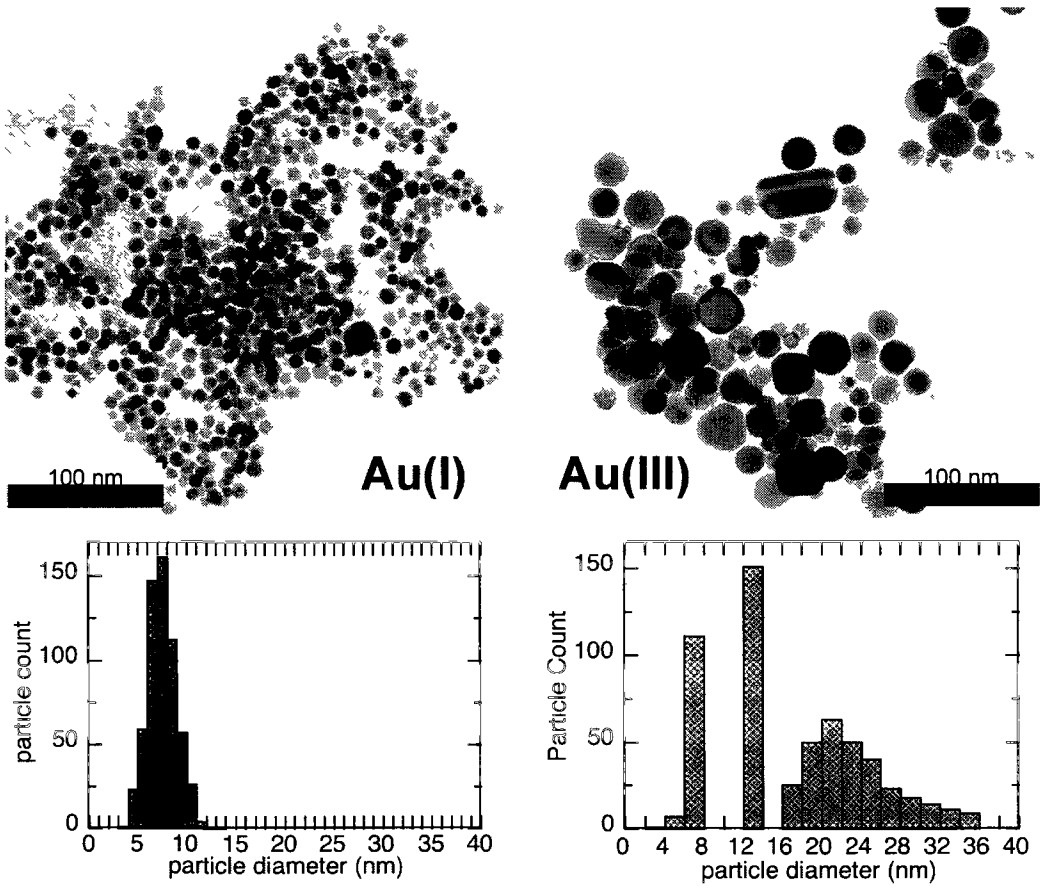

Figure 3 . 12 - Transmission electron micrographs and particle size distribution histograms for particles prepared as described in Figure 3.9: (left) Au(I); right Au(III).

In both cases, an increase in diameter of ~ 2 nm was observed within the first two weeks after particle synthesis that is indicative of particle ripening, where slow thermal reduction and disproportionation of surface Au^{+} leads to an increase in particle size. The particle size remained stable for six months thereafter.

3.5 Irgacure 2959

The most successful photo-releasing reducing agent has been 1-[4-(2-hydroxyethoxy)phenyl]-2-hydroxy-2-methyl-1-propane-1-one, or under the name of

Irgacure-2959™ (I-2959) as a commercial photoinitiator from Ciba Specialty Chemicals. Its rate of photolysis has been studied by measuring the decay in peak intensity at 272 nm by HPLC-MS to afford a first order decay characteristic of unimolecular reactions. The kinetic trace is plotted in Figure 3.13. The rate constant for the unimolecular decay was measured to be k= 0.0026 s^{-1} for photolysis with UVA photolysis of 35.9 Wm^{-2}. In the presence of an oxidizing agent such as $HAuCl_4$, the decay is presumed to occur much faster as evidenced by AuNP formation within minutes (*vide infra*).

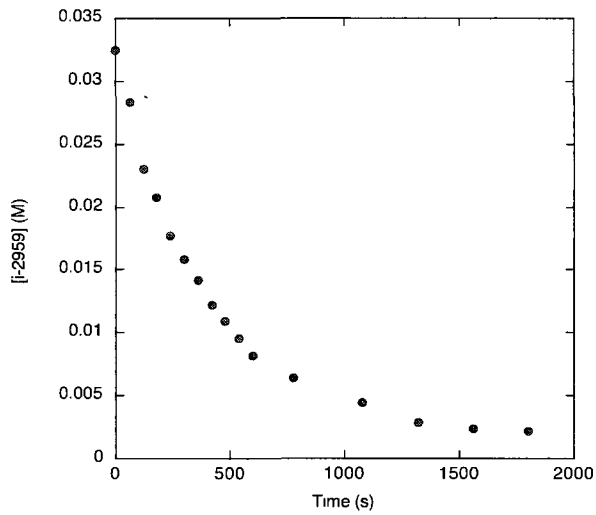

Figure 3 . 13 - HPLC analysis of the photodecay of I-2959 overtime, where the absorbance was monitored at 272 nm

This starting material has greatly facilitated colloidal gold nanoparticle synthesis owing to its hydrophilicity, and led to exciting exploratory research throughout this thesis. The lowest lying triplet state of the α-hydroxy ketone has a short lifetime of 11 ns, and the molecule dissociates to yield a benzoyl radical and the 2-hydroxy-2-propyl radical.[3]

The photolysis of Irgacure 2959 under ambient conditions in methanol was analyzed by GC-MS. Two peaks emerged at 28 min and 29 min, characteristic of the vinyl ether analogue (through facile loss of water under thermal GC conditions), and the

benzoic acid derivative (through oxidation of the benzoyl radical), respectively. The GC chromatograms and their MS analyses are provided in the Appendix in Figures 3.27- 3.29. In addition, ^1H NMR of I-2959 and its photoproducts have also been acquired in D_2O and DMSO, respectively, for the photoproducts were insoluble in D_2O at concentrations required for NMR (5 mM). The spectra can be found in the Appendix in Figures 3.31 and 3.32.

3.5.1 Nanoparticle Synthesis

For clarity, a comparison of the growth of gold nanoparticles with the three previously mentioned benzoins in CTAC is presented in Figure 3.14.

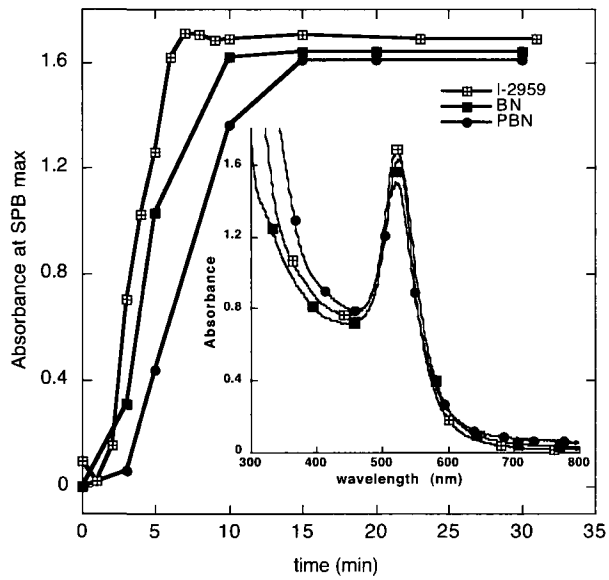

Figure 3 . 14 - Growth of SPB of AuNP over time for deareated solutions of I-2959, BN and PBN in CTAC solutions after 30 min UVA. (Inset) UV-Vis absorbance of AuNPs prepared from the three benzoins after 30 minutes photolysis. CTAC concentration varied from 66 mM for BN, and 17 mM for PBN and I-2959.

A comparative growth experiment at equimolar 1.0 mM benzoin revealed the formation of similar SPB within minutes, with I-2959 yielding AuNP faster than benzoin and α-phenyl benzoin. In a micellar solution, the trend is likely attributed to the transients with a greater dipole moment being located closer to the micellar Stern layer and therefore more readily accessible for reduction of aqueous species.[9] Also likely is the better mobility of the smaller 2-hydroxy-2-proply radical. The hydroxyethoxyl functional group of I-2959 facilitates water solubility, and the rapid photocleavage allows for ideal photoreduction in an aqueous environment. While the ketyl radicals are generated in the micelle, it is assumed that electron transfer occurs at the aqueous boundary of the Stern layer. Favourable growth conditions were studied for AuNPs in aqueous, ambient conditions by optimizing a number of factors through photochemical control.[9, 16]

A comparison was made between I-2959 and I-907 in both positive and negatively charged surfactants. Owing to the higher reduction potential for α-aminoalkyl radicals, faster rates and thus smaller particles were expected for I-907 over I-2959. The results showed a significant difference between the reaction rate for I-907 and I-2959 in CTAC, where I-907 led to a significantly slower reaction. The absorbance spectra after 60 minutes photolysis are displayed in Figure 3.15, left, and the absorbance at 530 nm compared in Figure 3.15, right. The slow growth of AuNP with I-907 could be attributed to its insoluble nature in water and is thus more likely to be located deeper in the micelle. Another difference included the lower absorbance for AuNP prepared from I-2959 in SDS relative to I-907 in SDS. Despite the difference in solubility, the reductions with both photoinitiators in SDS occurred almost instantaneously and with similar rates, however the SPB for I-2959 AuNP is broader and weaker in intensity relative to I-2959 AuNP in CTAC. Furthermore, the SPB for the I-2959/SDS sample was initially purple but shifted hypsochromically 20 nm to 530 nm. The kinetic similarities in SDS are likely due to accelerated reduction from surfactant impurities, as discussed previously in Section 3.2.

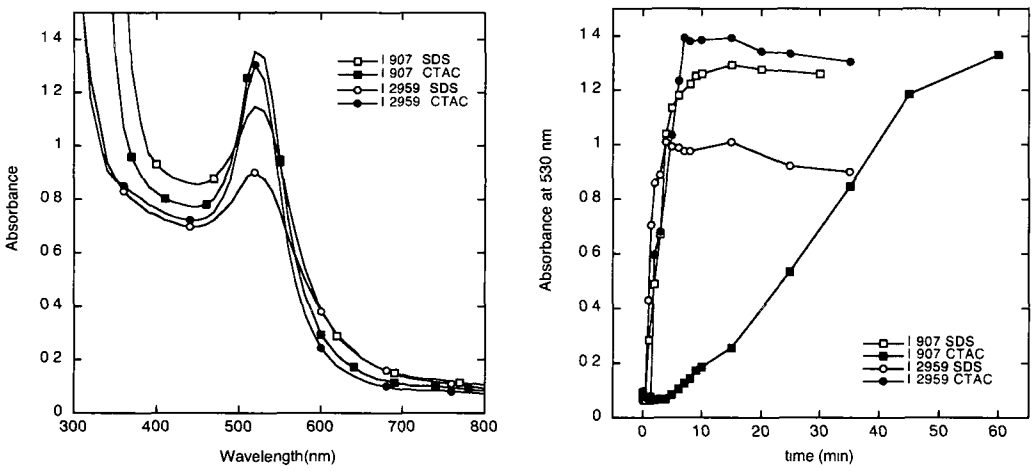

Figure 3 . 15 - (left) Absorbance of AuNP after 60 minutes photolysis in solutions of 0.33 mM $HAuCl_4$ with 1.0 mM photoinitiator in aereated 100 mM SDS or 17 mM CTAC throughout UVA photolysis, 14 lamps. (right) The Absorbance of the same four samples measured over time at the surface plasmon maximum.

With the interference in reduction brought forth by the presence of surfactant solutions, further work with I-2959 was realized in surfactant-free solutions. Typical absorption spectra of the starting materials and resulting AuNP in aqueous solution is presented in Figure 3.16.

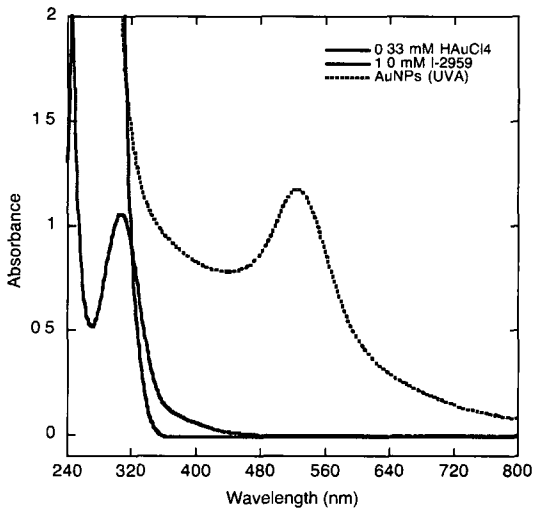

Figure 3 . 16 - Absorption spectrum of starting materials and resulting AuNP in aereated H_2O.

A concentration study on the starting materials was initialized in aqueous solutions, where the greater the concentration of I-2959, the better the yield of AuNP, in accordance with several reports with various reducing agents.[17] An optimal ratio of 3:1 I-2959:$AuCl_4$, was realized and carried over to several other systems presented in this thesis. Below the stoichiometric equivalence for reduction to the atomic state, slow growth was observed with the yield of larger, unstable anisotropic gold prisms and micron-sized plates similar to those in Figure 3.17A. At higher concentrations, however, the plasmon widened and red-shifted with increasing intensity. This observation is indicative of polydisperse or agglomerated particles, and can be attributed to insufficient stability of particles in solution as a result of acid photoproduct in solution beyond a 3:1-4:1 concentration. A comparison of absorbances at different concentrations is presented in Figure 3.17. With more I-2959, reduction occurred rapidly to yield small AuNP, but in the absence of substantial stabilizer, AuNP agglomerated as a result of more acid generated, for every mole of ketyl radical oxidized results in the generation of acetone and acid. AuNP typically precipitated within a few hours. These findings define a comfortable window at which nanoparticle synthesis can occur.

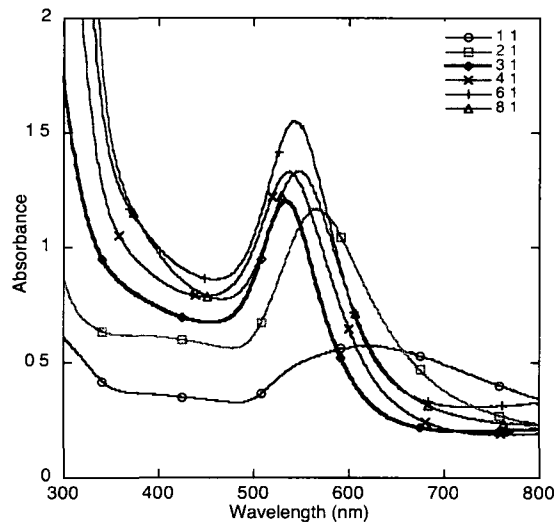

Figure 3 . 17 - Absorption of AuNP prepared from varied molar ratio of concentration of I-2959: $HAuCl_4$ with 0.33 mM $HAuCl_4$. Samples were prepared in quartz cuvettes and photolyzed via UVA light for 20 minutes.

3.5.2 Photolytic Control

Additionally, an effect on light intensity was explored to optimize particle growth. Conditions to yield small, monodisperse AuNP have also been optimized by controlling irradiation intensity and the wavelength of the light source.[9] [16] Higher irradiance under aereated conditions allowed for faster nucleation from a higher concentration of ketyl radicals under CW UVA. When the UVA light intensity was varied from ambient lab lighting (approximately 3% UVA) to 34 W/m^2 UVA (14 UVA lamps), particle size varied from 150 nm prisms to 8-10 nm particles. TEM images for the varied conditions are presented in Figure 3.18A-D.

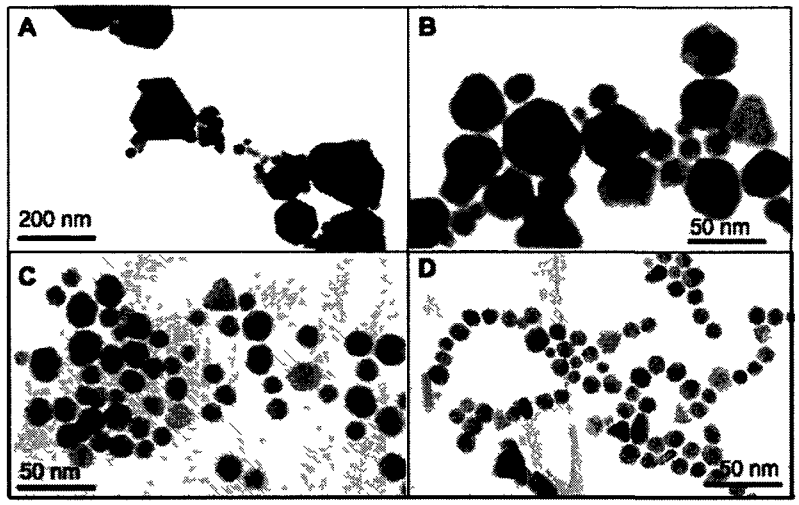

Figure 3 . 18 - TEM images of gold nanoparticles prepared with aereated 0.33 mM $HAuCl_4$ and 1.0 mM I-2959 under different irradiation conditions. A) VIS light (3% UVA), B) 4 W/m^2 UVA, C) 24 W/m^2 UVA and D) 34 W/m^2 UVA.

Irradiation with different wavelengths of light was also studied, as UVB or UVC light represents a region where the photoinitiator absorbs more photons. Nanoparticle synthesis was more rapid as a result of greater absorption and more ketyl radicals generated, yet a higher concentration of acid produced also led to particle agglomeration and yielded polydisperse particles from 3-15 nm. The differences are highlighted in Figure 3.19

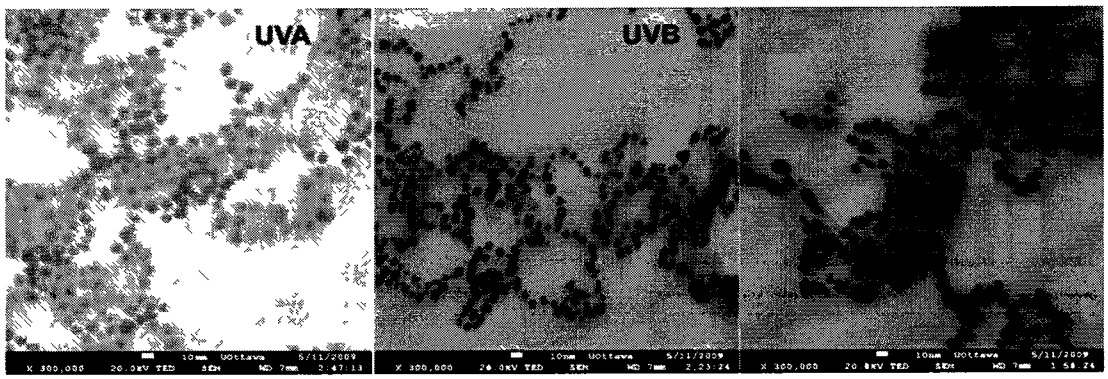

Figure 3 . 19 - SEM imaging of aqueous AuNP prepared from 0.33 mM HAuCl4, 1.0 mM I-2959 upon photolysis of different UV wavelengths, 8 lamps. The scale bars represent 10 nm.

In comparing AuNP that were synthesized with different light sources, the homogeneity of the irradiation source also affected the yield of nanoparticles, and illustrated the added control of photochemical reactions Samples were irradiated with a high power pulsed NdYAG laser operating at 355 nm, as well as with a Xenon lamp equipped with a 350 nm filiter, located 63 cm from the sample, or in a photoreactor where the sample was centered on a rotating merry-go-round. The duration of photolysis was 5 minutes for the laser experiment, and 30 minutes for the Xenon lamp and photoreactor trials; photolysis was arrested when absorbance intensities were relatively similar, however the laser-irradiated sample developed a bluish-purple colour unlike the other samples. It was essentially discovered that the more uniform the irradiation from the light source, the more uniform the nucleation for monodisperse particles. TEM images of the three samples are shown in Figure 3.20. The observed order of AuNP in TEM images is a characteristic of charge-stabilized AuNP, where attractive forces are present upon evaporation of the aqueous solvent.

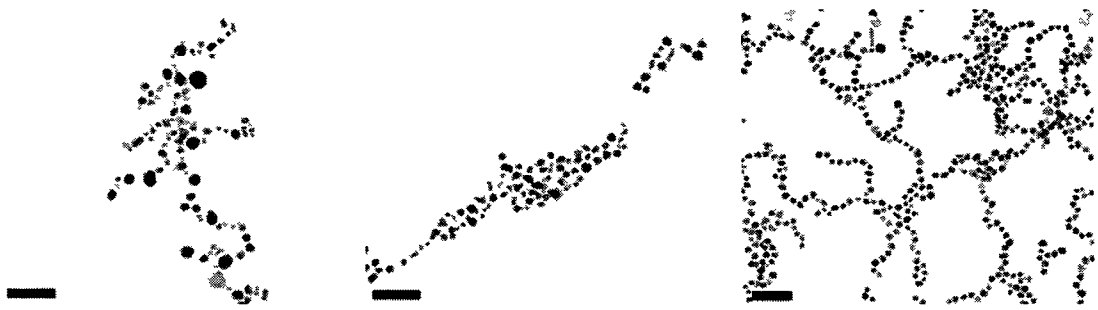

Figure 3 . 20 - TEM images of aqueous gold nanoparticles prepared from aereated 0.33 mM HAuCl4, 1.0 mM I-2959 under different irradiation conditions. (left) 355 nm NdYAG laser, (center) Xenon lamp, (right) Luzchem photoreactor, UVA, 35.9 W/m^2. The scale bars represent 50 nm.

Additionally, the variance in particle size and dispersity was also controlled by varying the photolysis time with optimal irradiation conditions in a photoreactor under UVA photolysis. At short irradiation times, solutions appeared pale violet and turbid with greater scatter at longer wavelength, while further photolysis resulted in a deeper red colour and a narrower plasmon band. Shorter irradiation times are synonymous with a weak reduction as a result of the low concentration of ketyl radicals generated at early times, and the results are indicative of the formation of large gold prisms.[13] The absorbance intensity was stabilized after approximately eight minutes. Longer irradiation times of generally 15-30 minutes have been used in many investigations in this work, where no change in the absorbance of AuNP from I-2959 was observed. Spectra for the different samples and their corresponding image are shown in Figure 3.21.

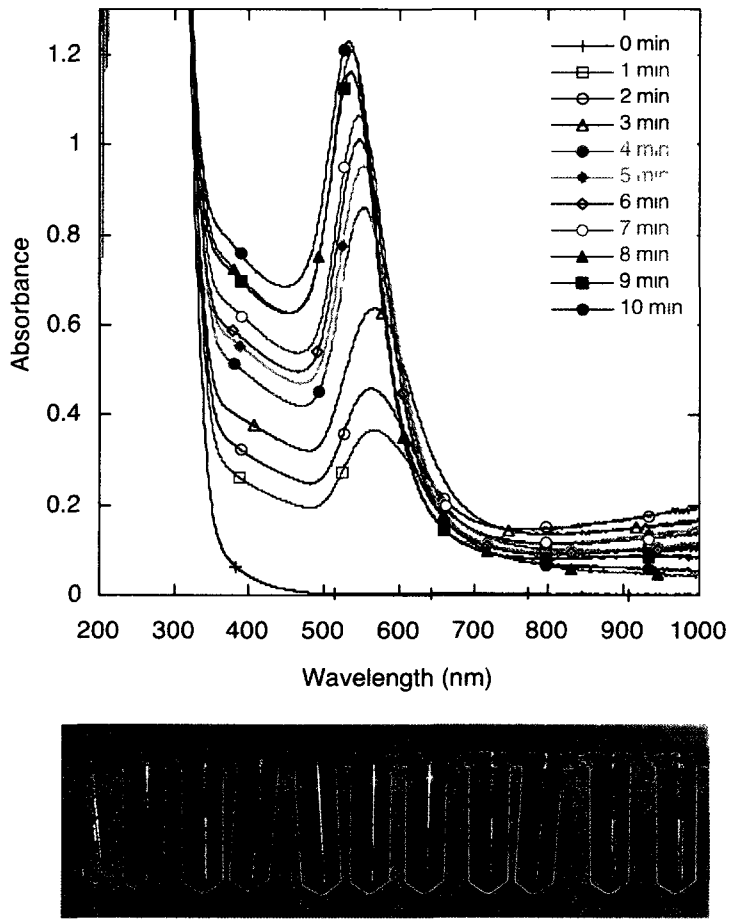

Figure 3 . 21 - Absorption spectra of AuNP prepared from 0.33 mM HAuCl4 and 1.0 mM and irradiated for different amounts of time under 14 lamps, UVA photolysis after 12 hours of ripening. Below, their corresponding sample image with increasing irradiation time from left to right.

The increased scatter at longer wavelength with shorter irradiation times is representative of anisotropic prism formation resulting from inadequate reducing agent. The photograph displayed in Figure 3.20 was taken after approximately 16 hours of AuNP synthesis, yet initial sample appearances were clear and colourless up until 8 minutes of irradiation where a pink solution was removed from the photoreactor. For short irradiation, $AuCl_4^-$ initially reduced by the low concentration of ketyl radicals during photolysis followed with the cascade of slow reduction through fast disproportionation of Au^{2+} followed by slow disproportionation of Au^+.

The above results have defined optimal irradiation conditions such that small, monodisperse particles are achieved via UVA photolysis in a photoreactor with 14 lamps. Furthermore, the number of photons reaching the sample plays a critical role in this reaction, since the photoproducts of the reaction screen the absorbance of the photoinitiator. I-2959 absorbs at 275 nm while the peak of its photoproduct shifts to 250 nm with a large tail into the UVA/UVB region. For this reason, it is paramount to maximize the amount of surface area of the solution for optimal photon absorption. This has been achieved by irradiating samples in quartz cuvettes as well as photolysis in 24 well plates. Since fewer photons reach the AuNP in well plates in comparison to cuvettes, the rate of AuNP formation is remarkably slower under these conditions. The induction period extended from 1-2 minutes for cuvette irradiation to approximately ten minutes for well plate photolysis. Once the induction period passed, the rate of growth appeared almost twice as fast for the quartz cuvette compared to the well plate. Nevertheless, AuNP synthesis has been carried out in well plates for several studies to make AuNP on a larger scale and to identify comparable variables in the work described in the following chapters.

3.5.3 Effects of Oxygen

Photochemistry involving triplet states is often hampered by the presence of oxygen, where purging samples with inert gas such as nitrogen or argon is necessary. While investigations with I-907, BN and PBN were performed under deareated conditions, it was later realized that this step was not necessary for the α-hydroxyketones, owing to their short triplet lifetimes (I-907 was also effective at AuNP synthesis under ambient conditions, as discovered in later studies). The presence of oxygen was studied with the I-2959 system and was found to be beneficial, for the formation of photoproducts eliminated the need for any additional stabilizer.[9, 16] Oxygen is known to quench the excited triplet state of many ketones and react with free radicals.[18, 19] The growth of AuNP with I-2959 under various conditions over time is

presented in Figure 3.22. Initially, O_2 is sacrificially consumed as residual oxygen reacts with the photocleaved radicals. Oxygen has been found to add to ketyl radicals with bimolecular rate constants of 6.6 x 10^9 $M^{-1}s^{-1}$, and to benzoyl radicals with a rate constant of 1.8 x 10^9 $M^{-1}s^{-1}$.[20, 21] The concentration of oxygen in ambient solutions can be approximated to 0.3 mM, which could react with 0.15 mM I-2959 photoproducts. Nevertheless, an excess of unquenched I-2959 remains to release ketyl and benzoyl radicals. Ketyl radicals reacted quickly at near diffusion control rates to reduce the aurous salt, as observed with BPK. The reaction pathway for the quenching reaction is illustrated in Scheme 3.5.

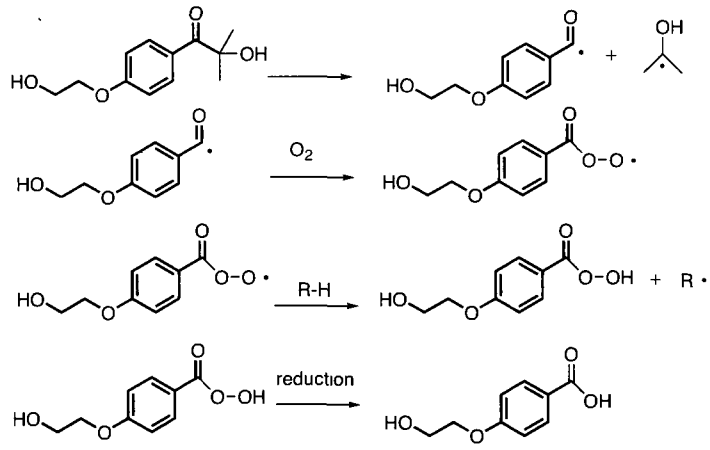

Scheme 3 . 5 – Oxidation of I-2959 benzoyl radical

Notably, the rate of electron transfer from a ketyl radical ($E^0(CH_3)_2CO,H^+/(CH_3)_2C•OH$ = -1.80 vs NHE) to the gold salt is faster than the rate of oxygen addition to the ketyl radical. As benzoyl radicals possess a less negative reduction potential (E^0= -1.18 vs NHE)[22] for the reduction of Au(III), the reactive intermediate succumbed to oxidation to yield 4-hydroxyethoxy benzoic acid (4-HEBA) as confirmed by GC-MS. The nanoparticle SPB formed within five minutes showing rapid AuNP growth, at which time growth was arrested by photo-generated stabilizers. The stabilization occurs via physisorption of the carboxylate moiety to surface Au^+ charges, along with residual chloride ions, in a similar mechanism as

trisodium citrate, and accounts for the negative charge of the electronic double layer on the particle surface, as detected by zeta potential measurements. ^{1}H NMR spectra of AuNP prepared from I-2959 before and after centrifugation are available in the Appendix in Figures 3.33 and 3.34, respectively. The non-centrifuged AuNP display peaks identical to those of I-2959 photoproducts, while centrifugation and resuspension of AuNP greatly reduced the concentration of the physisorbed 4-HEBA anion on the surface, making surface characterization via NMR a challenge.

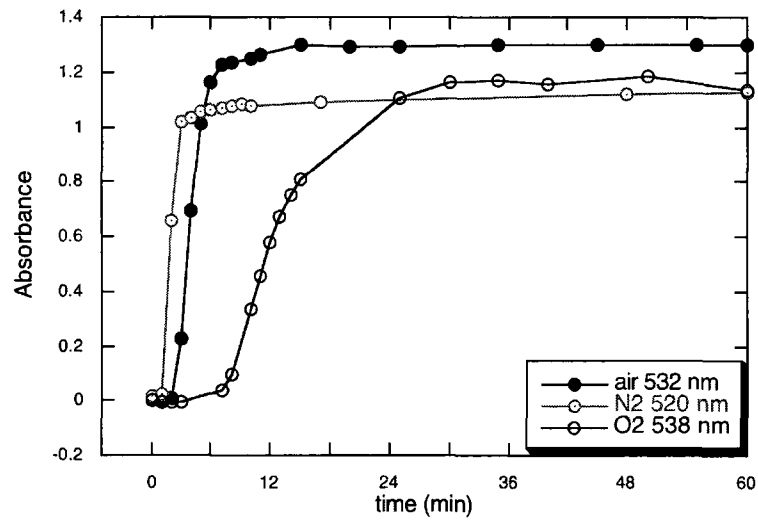

Figure 3 . 22 - Growth of I-2959-generated AuNPs over time under different O_2 environments; the lines are simply visual aids.

At higher oxygen concentration, where samples were purged with O_2 for 30 minutes, a longer induction period and a slower rate of growth were observed. Larger, prismatic particles were obtained owing to the overlap of slower nucleation and growth phenomena. Alternatively, in the absence of oxygen and any additional stabilizer, AuNP grew rapidly with a short induction period, yet coalesced into larger aggregates in the presence of excess acid generated.

3.5.4 Surface Characterization

Nanoparticles synthesized via I-2959 photo-released reduction have been studied extensively in this research, and their surface composition has been characterized using a number of techniques. Initially, gold nanoparticles were centrifuged at 3400 rpm for 40 minutes to separate excess photoproducts and unreacted $HAuCl_4$ from the nanoparticles.

Particles were also characterized via ^1H NMR from synthesis of AuNP in deuterated water. Spectra were taken of samples with and without a purification step, where centrifugation of the particles removed excess photoproducts and un-bound ligands. ^1H NMR revealed peaks that matched those of 4-HEBA. The spectrum of the irradiated I-2959 displayed an additional small peak of the aldehyde product at 9.8 ppm along with a strong peak at 2.1 ppm for the photogenerated acetone. The carboxylic acid proton typically found around 12 ppm was not present due to its rapid exchange. Additional peaks at 2.5 ppm, 1.4 and 1.1 are assigned to additional photoproducts or residual DMSO. Evidently, similar peaks were observed for AuNP samples prepared from the I-2959 reducing agent. Purification via centrifugation of the particles at 3500 rpm for 30 minutes resulted in a substantial removal of the photoproducts, which is further indication that the carboxylates are weakly physisorbed. The ^1H NMR spectra for I-2959 and AuNP are presented in the appendix, in Figures 3.31 - 3.34. The ^1H NMR for 4-HEBA is presented in Figure 3.35.

X-ray photoelectron spectroscopy was also employed to identify the oxidation state on the surface, where the characterization of a concentrated and dried nanoparticle sample revealed the 4f peaks at 83.9 eV and 87.9 eV, characteristic of Au^0 on the surface.[23] The spectrum is shown in the appendix in Figure 3.36.

Furthermore, powder X-ray diffraction was also performed on a concentrated sample dropcast onto a silicon wafer. The spectrum is presented in Figure 3.23 and

provided the characteristic (111), (200), (220) and (311) peaks for bulk gold. It should be noted that the broadening of the peaks is common for nanomaterial sized samples. Additionally, the width of the peaks was used to approximate the nanoparticle size according to the Scherrer equation,

$$t = \frac{0.9\lambda}{B\cos\theta} \qquad (3.3)$$

where t is the thickness, λ the X-ray (1.5418 Å for Cu Kα), B= the half width at half height in radians, and θ= the diffraction angle of the tallest peak; (111) for gold. The diameter of the I-2959 gold nanoparticles was calculated to be 14 nm, in close approximation to the average of 10-12 nm determined via particle counting of microscopy techniques.

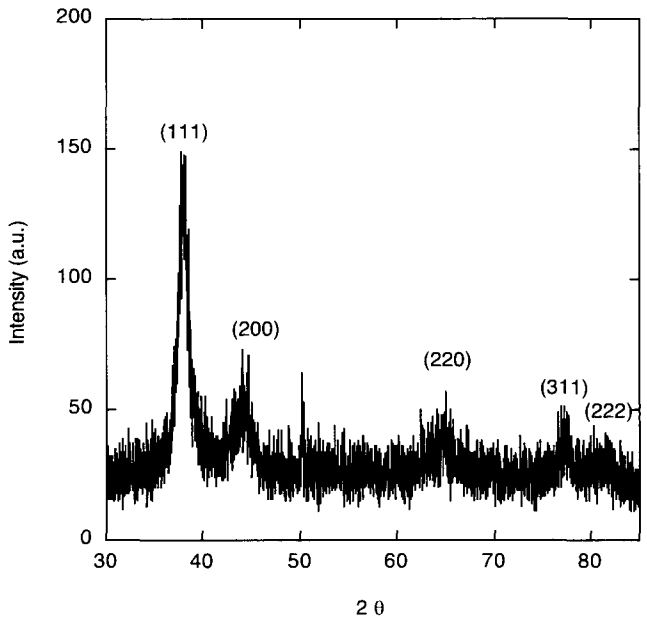

Figure 3 . 23 - Powder XRD spectrum of AuNP prepared from 0.33 mM $HAuCl_4$, 1.0 mM I-2959 following 30 min UVA photolysis.

Finally, charge-stabilized AuNP samples irradiated for different time durations were characterized by dynamic light scattering and zeta potential throughout the course of

irradiation, where the average hydrodynamic diameter was determined to be about 20 nm. The zeta potential was measured to be -30 mV, characteristic of charge-stabilized nanoparticles similar to those prepared via citrate reduction. An overlay of the change in both the hydrodynamic radius and the zeta potential with time is depicted is Figure 3.24.

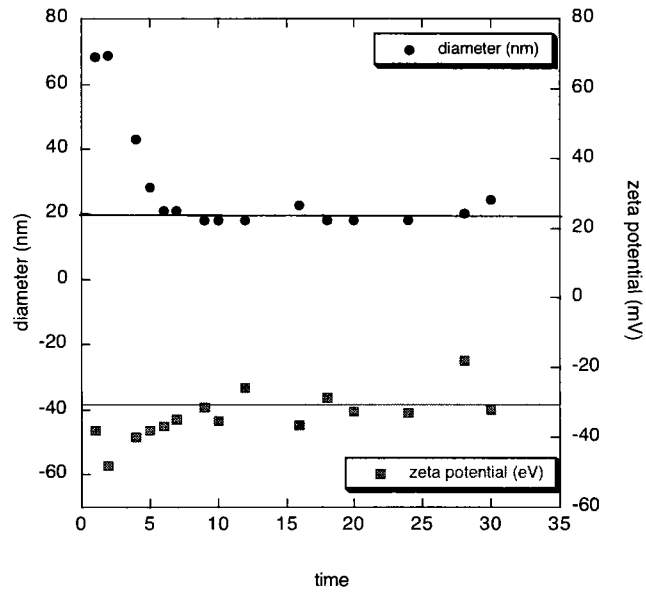

Figure 3 . 24 - Changes in the hydrodynamic radius and zeta potential with increasing irradiation time for separate samples prepared from UVA photolysis of 0.33 mM $HAuCl_4$ and 1.0 mM I-2959 under aereated conditions.

3.5.5 Stability

Aqueous AuNP prepared from 0.33 mM $HAuCl_4$ and 1.0 mM I-2959 are charge-stabilized via physisorbed photoproducts in solution, and have displayed remarkable stability for over four years. Particles did destabilize, however, as indicated by a redshift and broadening of the SPB when particles are stored in glass vials and occasionally quartz cuvettes and pyrex glassware. This destabilization is attributed to the hydroxyl surface of the silica in the glassware creating alkaline conditions.

Particles displayed a greater attraction to the walls of the glassware over the anions of the stabilizer. As such, the walls of cuvettes were often stained with gold particles, requiring cautious cleaning with Aqua Regia as is standard practice with colloidal gold. Fortunately, this destabilization was circumvented by storing particles in plastic containers, such that the samples remained stable. Over time, AuNP generally settle to the bottom of a container but resuspend easily upon shaking.

The physisorption of ions and ligands onto the surface of the particle results in a unprotected surface that is succeptible to changes in solvent, ligand attachment and pH. The pH of the resulting aqueous system has a value of approximately 5. Various pH studies have revealed that the particles are stable at pH 2-10, yet flocculate to precipitation outside of this range.

AuNP prepared from this aqueous, deareated technique employing I-2959 were sensitive to ionic strength of the surrounding media. At high ionic strength, the Debye length of the diffuse electric double layer is altered, and attractive forces lead to flocculation. Fortunately, the presence of a 7.5 mM phosphate buffer (pH 7.4) strengthened the double layer, and AuNP were stable to numerous chemical additions and resistant to flocculation onset by glassware. Synthesis of AuNP in buffer or solutions of high ionic strength, however, failed to yield stable nanoparticles.

Other methods have been undertaken to preserve nanoparticle stability, and include stabilization of particles in various media such as surfactant, polymer and chemisorbed ligands.

3.5.6 Synthesis in Polymers

Various polymers have been utilized in metal nanoparticle synthesis with the function of macromolecular stabilization. Careful selection of polymer, its molecular weight, and additives offer control over particle size and shape in solution and in thin

films.[5, 24-31] Interestingly, many polymers can partake in photochemical reduction owing to the presence of a ketone moiety and undergo hydrogen atom transfer (*vide infra*) between sensitizer and donor to form the reducing ketyl radical. In this research, AuNP have been prepared in hydrophilic polymers such as poly (ethylene glycol) (PEG), poly (vinyl alcohol) (PVA) and poly (vinyl pyrrolidone) (PVP), and studied briefly.

A concentration study was performed and revealed an optimal concentration of 3% wt PVA (MW = 10 000), where concentrations below this value generated lower intensity SPBs, and solutions above 3% wt displayed wider bandwidths. Five minutes of UVA irradiation yielded a pink/red solution with an absorption maximum at 533 nm, while a prolonged dark reaction (one day) yielded a pale purple and iridescent solution with a broad absorption centered at 600 nm. In the presence of 1.0 mM I-2959, however, a stronger SPB emerged with a maximum at 528 nm following 5 minutes UVA irradiation. The absorbance spectra of the reactions are compared in Figure 3.25.

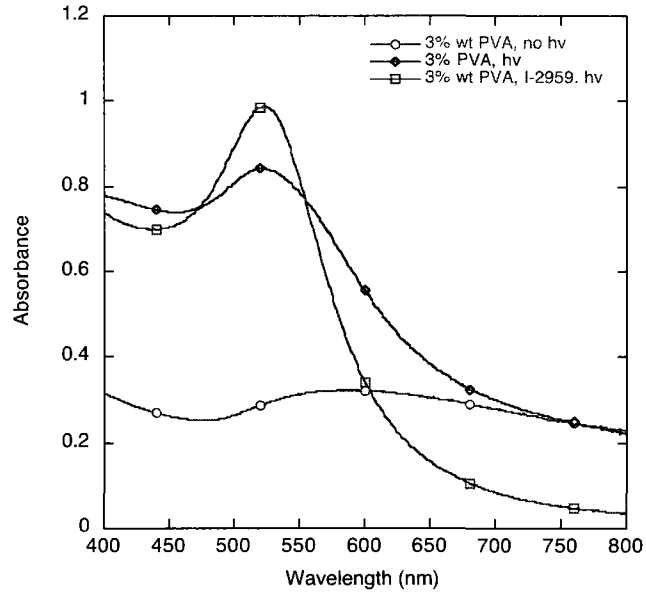

Figure 3 . 25 - Absorption of AuNP prepared at 3% wt PVA from 0.33 mM $HAuCl_4$ in the presence and absence of 1.0 mM I-2959 upon 5 min UVA photolysis.

Nanoparticles stabilized in PEG were found to be optimal at a 3% wt PEG (MW = 1000) concentration based on the similar observations. Nanoparticles prepared from PEG and I-2959 displayed a SPB centered at 522 nm, and formed a much broader peak at 533 nm in the absence of the photoinitiator, or at 563 nm for the dark control reaction (one day). Polyethylene glycol is known for its thermal reduction properties and is exploited in the polyol method.[32] A photochemical approach to generating the polyol reducing radical has been tested in previous reports as well.[31] The reduction capability of PEG thus added to the reduction by I-2959, as evidenced by the near doubling of absorption intensity. The results are presented in Figure 3.26, below.

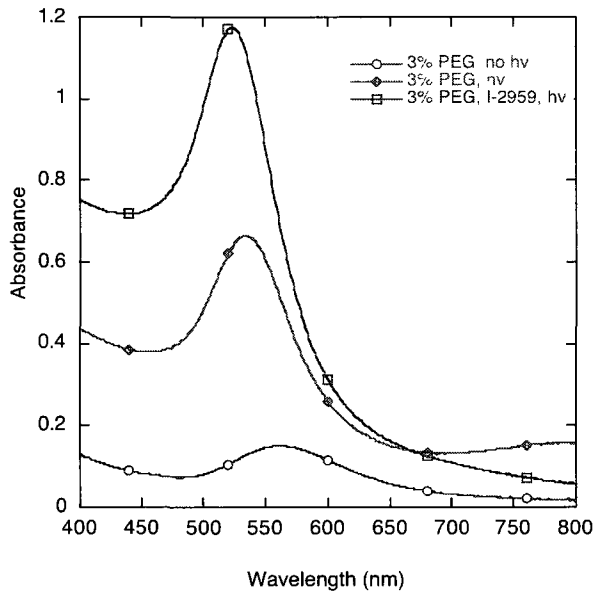

Figure 3 . 26 - Absorption of AuNP prepared at 3% wt PEG from 0.33 mM $HAuCl_4$ in the presence and absence of 1.0 mM I-2959 upon 30 min UVA photolysis.

Finally, PVP has also been investigated as a stabilizing agent for growth of nanopaticles *in situ.* Significant differences in absorption were observed with PVP that were not observed with the other two polymers. Specifically, a significant blueshift in the SPB was apparent at various polymer concentrations. A concentration study was also investigated for this polymer in the presence of I-2959,

where 1-2% wt PVP (MW = 23 000) generated an orange-brown solution with an absorption maximum at 502 nm. At concentrations of 3-5% wt PVP, the absorption centered closer to 520 nm with a red-pink colour. Above 5% wt, significant broadening of the peak occurred. Interestingly, the absorption intensity was much lower when the initiator was used and this could be attributed to smaller nanoparticles, which exhibit less scattering and smaller plasmon intensity according to Mie theory. The spectra are displayed in Figure 3.27.

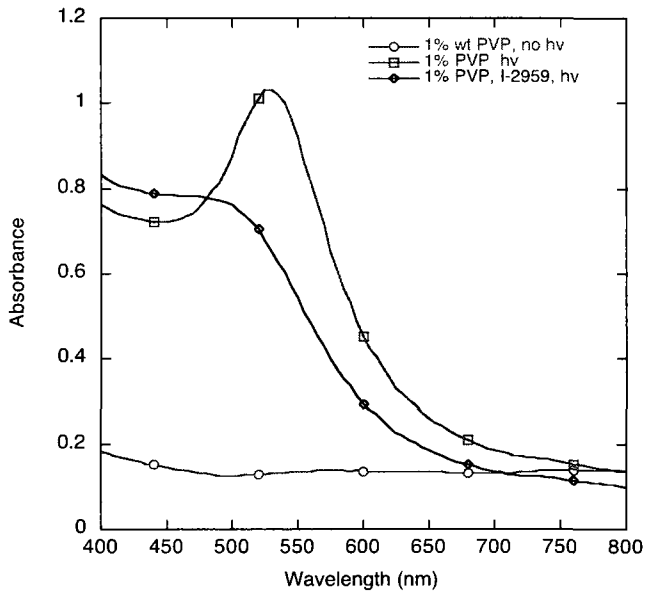

Figure 3 . 27 - Absorption of AuNP prepared at 1% wt PVP from 0.33 mM $HAuCl_4$ in the presence and absence of 1.0 mM I-2959 upon 30 min UVA photolysis.

Importantly, it was realized that photolysis of $HAuCl_4$ in the presence of the polymers with no additional hydrogen donor was sufficient to generate particles. The reduction of metal salts by PVP has been realized in other reports, where reduction of gold has been possible with its high reduction potential, yet challenging for $AgNO_3$ and negligible reduction occurred for $CuSO_4$.[5] The mechanism for reduction remains unclear, but is hypothesized herein to proceed through a Norrish-II mechanism to yield a ketyl radical. Nanoparticles have also been prepared from $HAuCl_4$ in the presence of polymer alone in the case of PVA,[10] where ketyl radicals

were easily formed upon abstraction of the α-hydrogen. Albeit, the SPB presented herein is broader and lower in intensity, affirming the need for an added reducing agent such as I-2959 for monodisperse, small nanoparticles. Unfortunately, electron microscopy imaging was not possible for the polymer-NP samples, as the excess of organic material led to significant contamination and burning, even when the sample was placed under vacuum for two days. Additionally, dynamic light scattering was unable to reliably determine the size of nanoparticles in the presence of the polymer, for only 130 nm or 1.0 μm+ agglomerates were detected.

3.6 Summary

The synthesis of gold nanoparticles from photolysis of α-hydroxy ketones and α-amino ketones presents a successful approach to colloid generation. Utilization of precursors with short lifetimes minimizes quenching of the precursor's excited triplet state by transition metal salts or oxygen. Selecting photoinitiators that generate observable transients via laser flash photolysis allows discovery of the electron transfer rates in nanoparticle synthesis. By varying the concentrations of reagents, the photolysis conditions, the irradiation time and the concentration of oxygen, finer tuning of optimal conditions can be realized as a result of the defined photochemical control. The presence of stabilizers such as positive and negatively charged surfactants and polymers further assist in the synthesis and stability of the colloid. Great success has been achieved with the synthesis of AuNP from I-2959 owing to their stability, the strong absorbance properties, and ease of derivitization. These features are explored further in Chapter 6.

3.7 Appendix

GC-MS

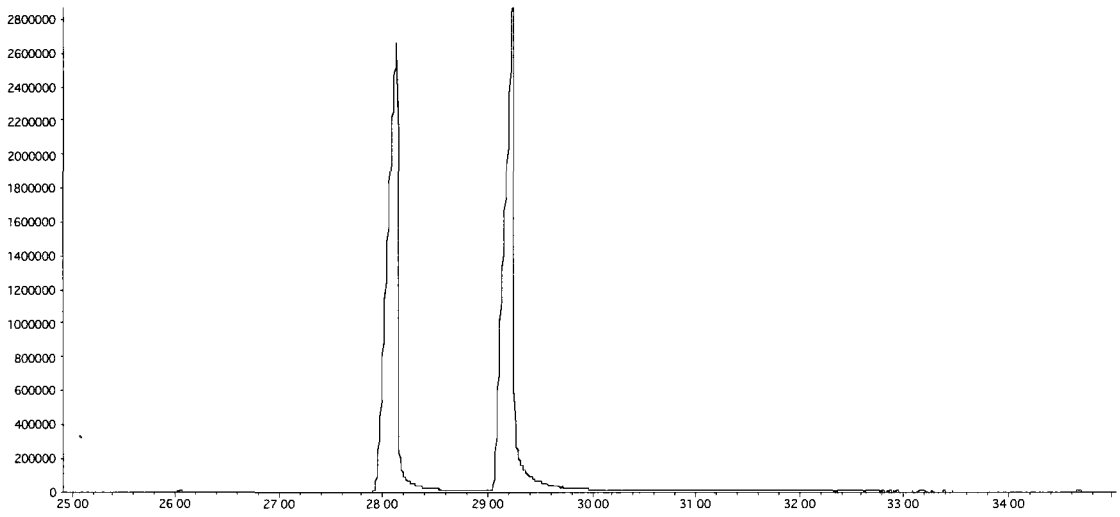

Figure 3 . 28 - GC-MS chromatogram of areated I-2959 in methanol after 30 minutes UVA photolysis.

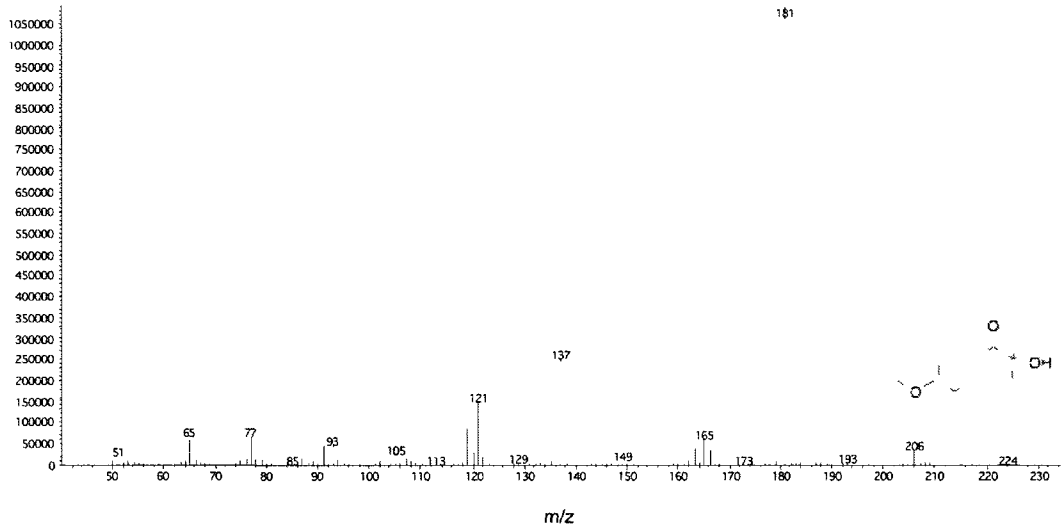

Figure 3 . 29 - GC-MS Mass spectrum taken at 28.124 minutes retention time for areated I-2959 in methanol after 30 minutes UVA photolysis.

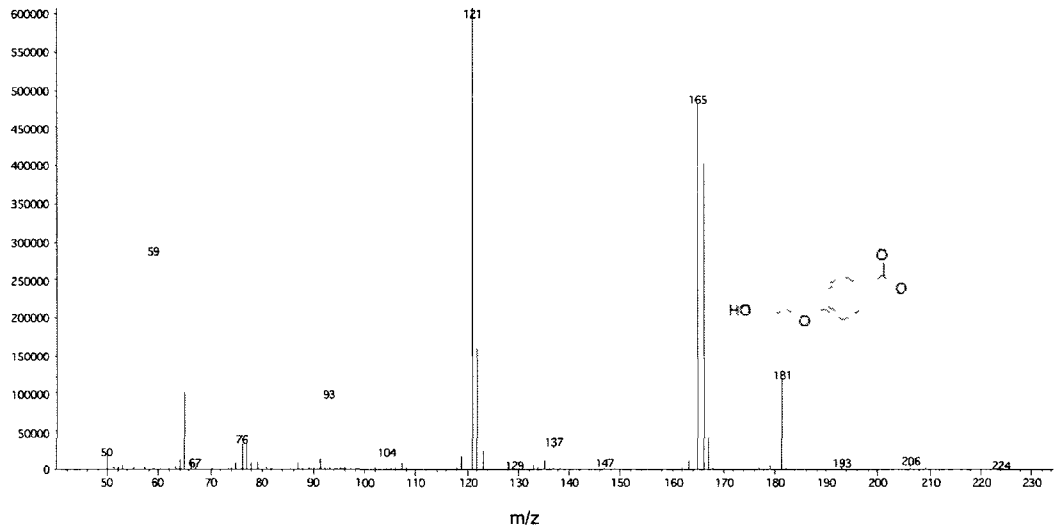

Figure 3 . 30 - GC-MS Mass spectrum taken at 29.23 minutes retention time for areated I-2959 in methanol after 30 minutes UVA photolysis.

^{1}H NMR

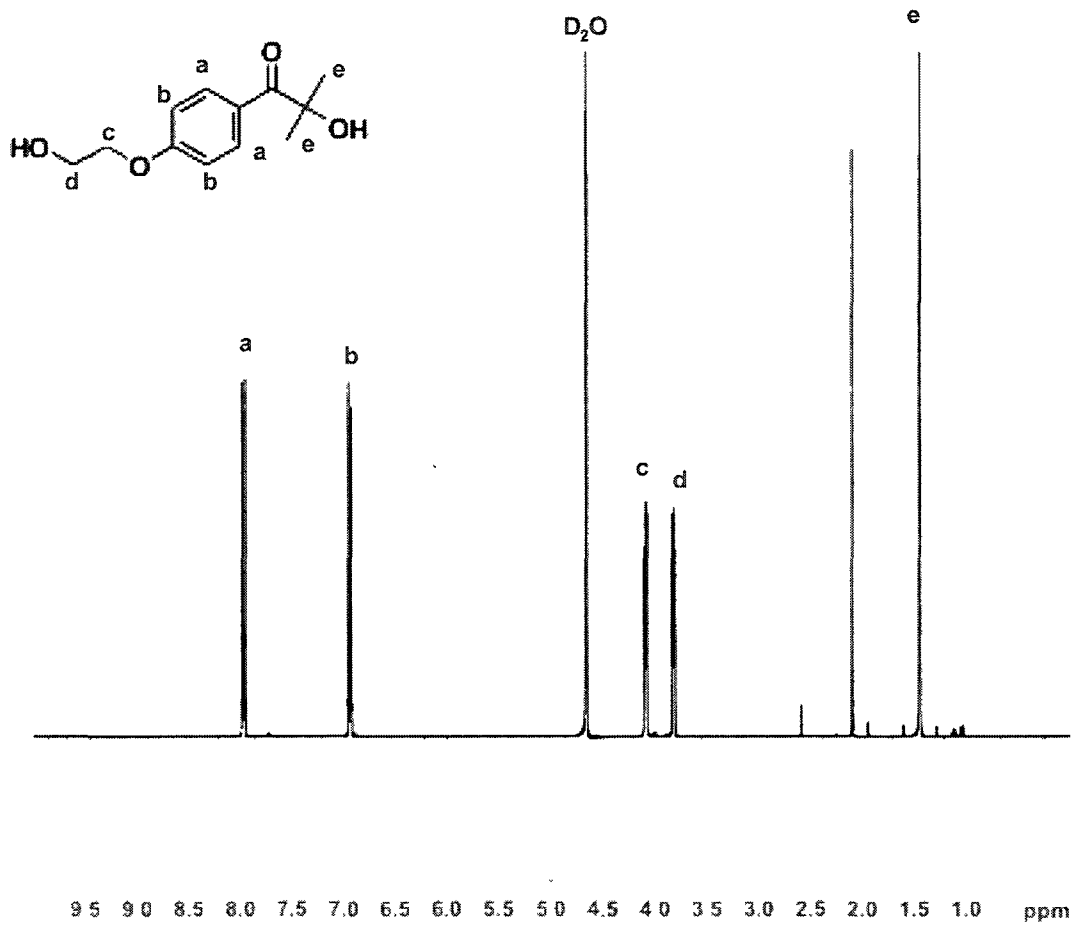

Figure 3 . 31 - ^{1}H (400 MHz) NMR of I-2959 in D_2O prior to photolysis

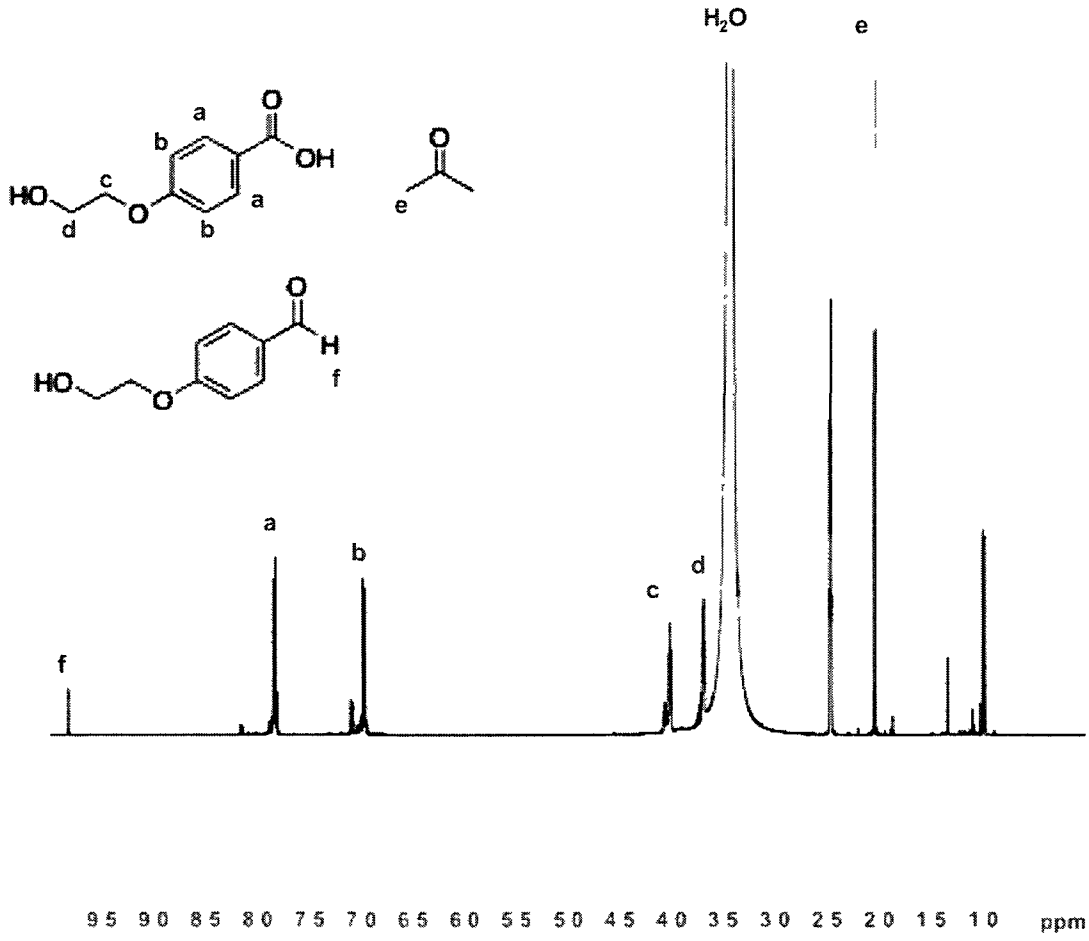

Figure 3 . 32 - ^{1}H NMR (400 MHz) of the crude products of UVA photolyzed I-2959 in deuterated DMSO

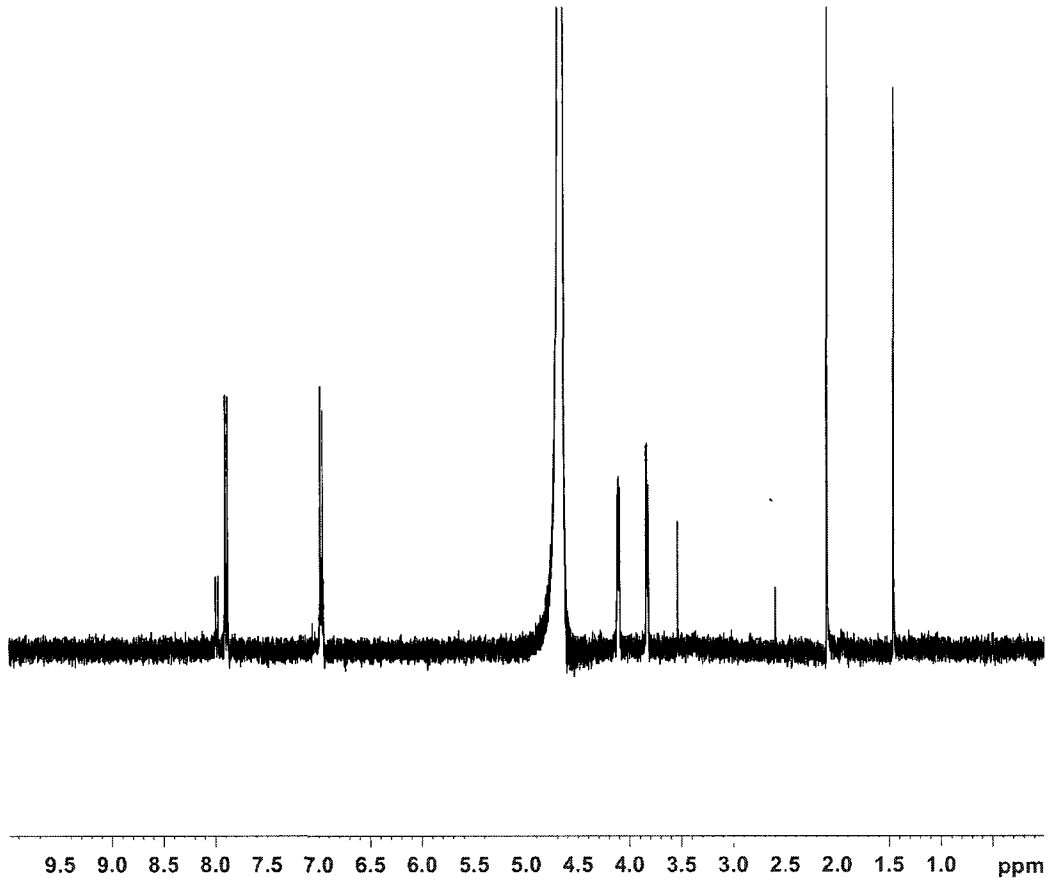

Figure 3 . 33 - ^{1}H NMR (400 MHz) of AuNP prepared from UVA photolysis of 0.33 mM $HAuCl_4$ and 1.0 mM I-2959 in D_2O. Sample not centrifuged prior to concentration.

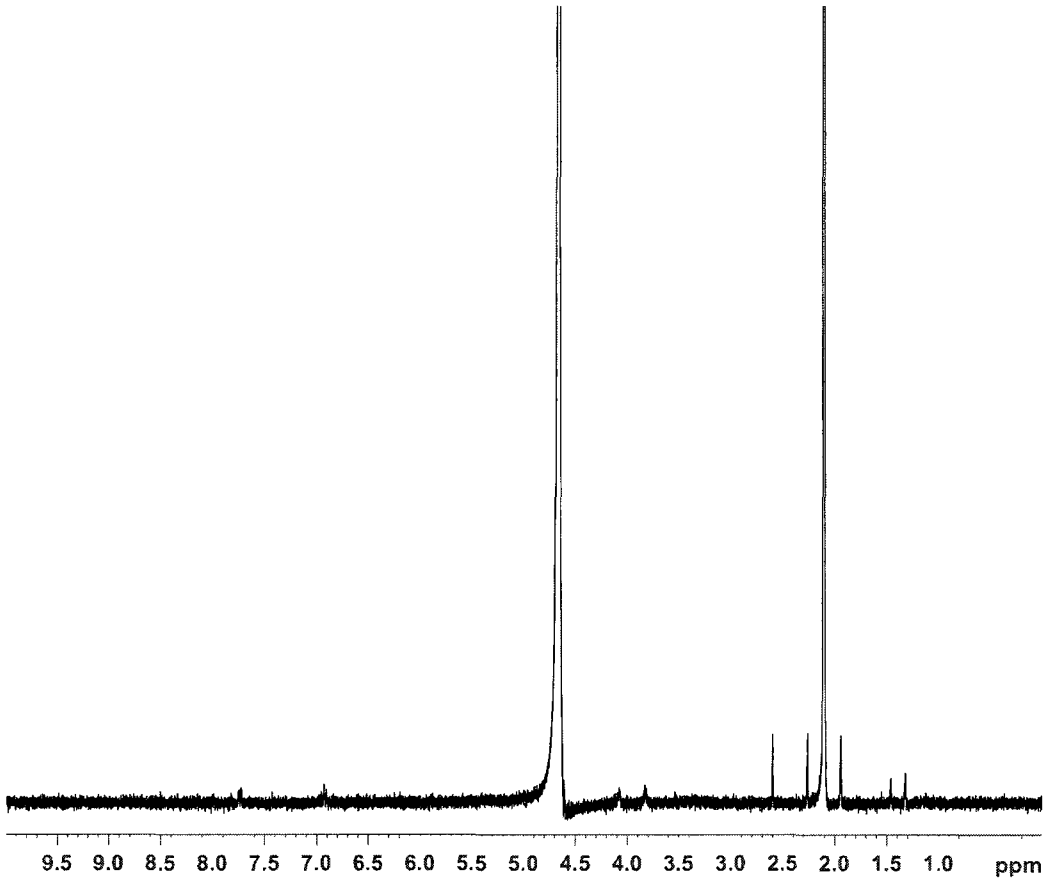

Figure 3 . 34 - ^{1}H NMR (400 MHz) of AuNP prepared from UVA photolysis of 0.33 mM $HAuCl_4$ and 1.0 mM I-2959 in D_2O. Sample centrifuged and resuspended prior to concentration, to remove non-bound photoproducts.

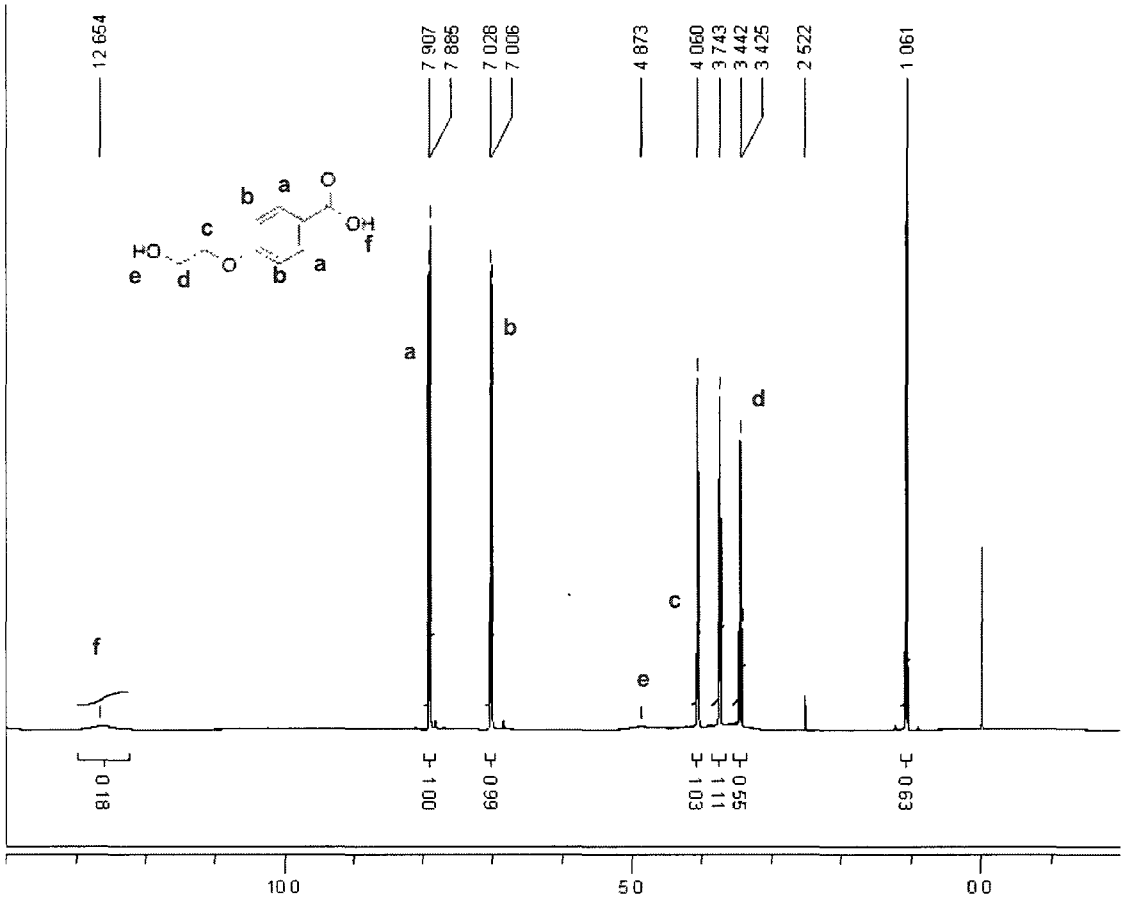

Figure 3 . 35 - ^{1}H NMR (400 MHz) of 4-hydroxyethoxy benzoic acid in deuterated DMSO. Additional peaks at 1.06 and 3.44 ppm are representative of residual ethanol in solution.

XPS

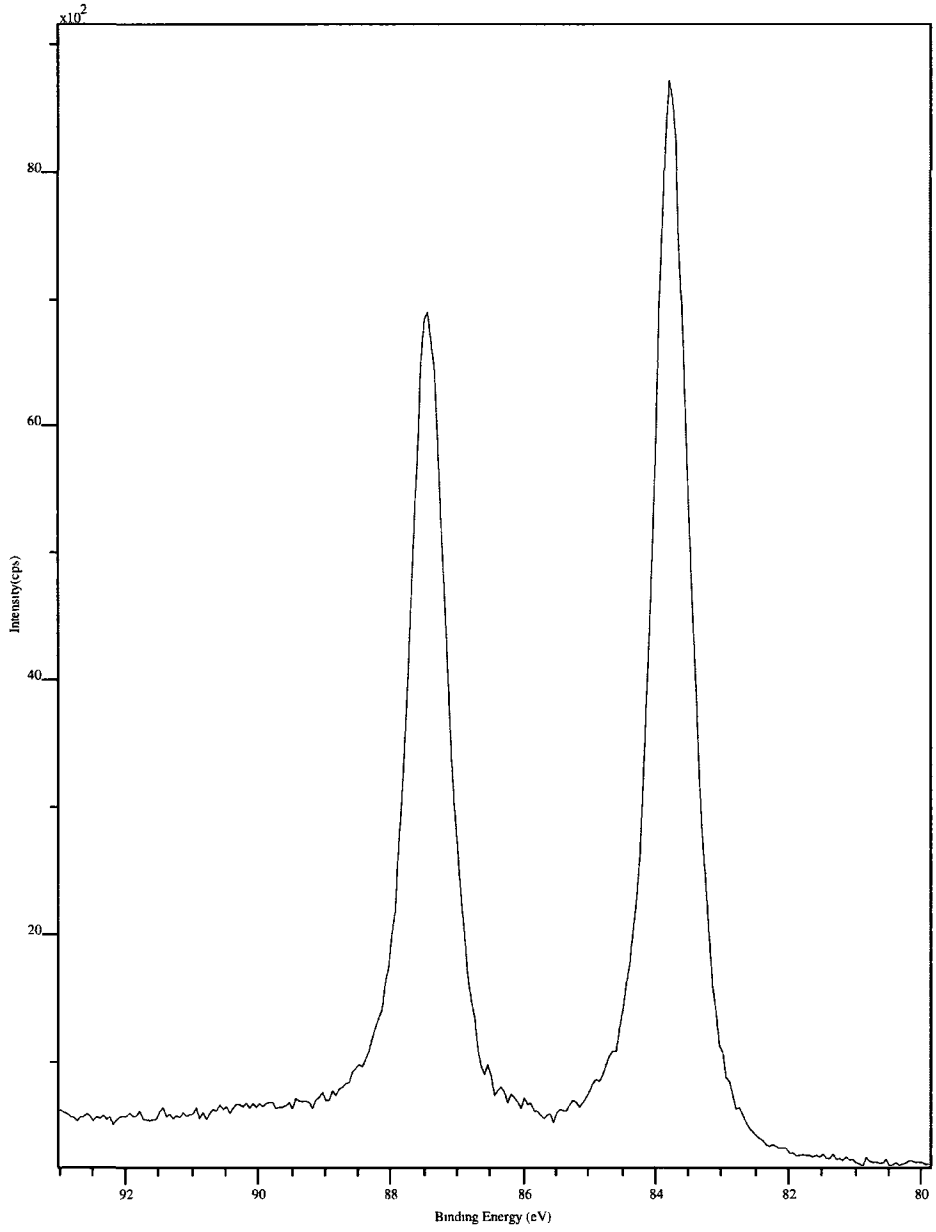

Figure 3 . 36 - XPS spectrum of gold nanoparticles prepared from deareated 0.33 mM $HAuCl_4$, 1.0 mM I-2959 in aqueous solution, following centrifugation, concentration and evaporation on a silicon disk. The two peaks represent the 4f peaks for gold.

3.8 References

1. Norrish, R. G. W., Appleyard, M. E. S., Primary Photochemical Reactions. Part IV. Decomposition of Methyl Ethyl Ketone and Methyl Butyl Ketone. *J. Chem. Soc.* **1934**, 874-880.

2. Bamford, C. H., Norrish, R. G. W., Primary Photochemical Reactions. Part X. The Photolysis of Cyclic Ketones in the Gas Phase. *J. Chem. Soc.* **1938**, 1521-1530.

3. Jockusch, S.; Landis, M. S.; Freiermuth, B.; Turro, N. J., Photochemistry and Photophysics of a-Hydroxy Ketones. *Macromolecules* **2001,** *34* (6), 1619-1626.

4. Fu, Y., Liu, H.-Z., Yu, Y.-M., Quantum-Mechanical Predictions of Absolute Standard Redox Potentials of Diverse Organic Molecules and Free Radicals in Acetonitrile. *J. Am. Chem. Soc.* **2005,** *127*, 7227-7234.

5. Itakura, T., Torigoe, K., Esumi, K., Preparation and Characterization of Ultrafine Metal Particles in Ethanol by UV Irradiation Using a Photoinitiator. *Langmuir* **1995,** *11*, 4129-4134.

6. Tofani, L., Freis, A., Snoke, R. E., Baglioni, P., Smulevich, G., Spectroscopic and Interfacial Properties of Myoglobin/Surfactant Complexes. *Biophys. J.* **2004,** *87*, 186.

7. Zhou, L., Zhang, Y., Shi, D. , Samarium (II) Iodide Promoted Novel Reductive Coupling Reaction of Ketones and Nitriles. *Tett Lett* **1998,** *39*, 8491-8494.

8. Lewis, F. D., Lauterbach, R. T., Heine, H.-G., Hartmann, W., Rudolph, H., Photochemical a-Cleavage of Benzoin Derivatives. Polar Transition States for Free-Radical Formation *J. Am .Chem. Soc.* **1974,** *97*, 1519-1525.

9. Marin, M. L., McGilvray, K. L., Scaiano, J. C., Photochemical Strategies for the Synthesis of Gold Nanoparticles from Au(III) and Au(I) Using Photoinduced Free Radical Generation. *J. Am. Chem. Soc.* **2008,** *130*, 16572-16585.

10. Gachard, E., Remita, H., Khatouri, J., Keita, B., Nadjo, L., Belloni, J., Radiation-induced and Chemical Formation of Gold Clusters. *New. J. Chem.* **1998**, 1257-1265.

11. Scaiano, J. C., Abuin, E. B., Stewart, L. C. , Photochemistry of Benzophenone in Micelles. Formation and Decay of Radical Pairs. *J. Am. Chem. Soc.* **1982,** *104*, 5673-5679.

12. Henglein, A., Meisel, D., Radiolytic Control of the Size of Colloidal Gold Nanoparticles. *Langmuir* **1998,** *14*, 7392-7396.

13. Millstone, J. E., Metraux, G. S., Mirkin, C. A. , Controlling the Edge Length of Gold Nanoprisms via a Seed-Mediated Approach. *Adv. Mater.* **2006,** *16*, 1209-1214.

14. Zhu, T., Vasilev, K., Kreiter, M., Mittler, S., Knoll, W., Surface Modification of Citrate-Reduced Colloidal Gold Nanoparticles with 2-Mercaptosuccinic Acid. *Langmuir* **2003,** *19*, 9518-9525.

15. Aslam, M., Fu, L., Su, M., Dravid, V. P., Novel One-step Synthesis of Amine-stabilized Aqueous Colloidal Gold Nanoparticles. *J. Mater. Chem.* **2004,** *14*, 1795-1797.

16. McGilvray, K. L., Decan, M. R., Wang, D., Scaiano, J. C., Facile Photochemical Synthesis of Unprotected Aqueous Gold Nanoparticles. *J. Am. Chem. Soc.* **2006,** *128*, 15980-15981.

17. Daniel, M.-C., Arstruc, D., Gold Nanoparticles: Assembly, Supramolecular Chemistry, Quantum-Size-Related Properties, and Applications toward Biology, Catalysis and Nanotechnology. *Chem. Rev.* **2004,** *104*, 293-346.

18. Maillard, B.; Ingold, K. U.; Scaiano, J. C., Rate Constants for the Reactions of Free Radicals with Oxygen in Solution. *J. Am. Chem. Soc.* **1983,** *105* (15), 5095-5099.

19. Turro, N. J.; Ramamurthy, V.; Scaiano, J. C., *Modern Molecular Photochemistry of Organic Molecules.* University Science Publishers: New York, N.Y., 2010; p 1100.

20. Hancock-Chen, T., Scaiano, J. C., Nonlinear Effects and a Cascade of Radical Events Leading to Laser-Specific Generation of Acitive Oxygen Species. *Photochem. Photobiol.* **1998,** *67* (2), 174-178.

21. Jockusch, S., Turro, N. J., Radical Addition Rate Constants to Acrylates and Oxygen: a-Hydroxy and a-Amino Radicals Produced by Photolysis of Photoinitiators. *J. Am. Chem. Soc.* **1999,** *121*, 3921-3925.

22. Occhialini, D., Daasbjerg, K., Lund, H., Estimation of Reduction and Standard Potentials of Acyl Radicals. *Acta. Chem. Scandinavica* **1993,** *47*, 1100-1106.

23. Karpenki, A., Leppelt, R., Plzak, V., Behm, R. J., The Role of Cationic Au3+ and Nonionic Au0 species in the Low-temperature Water-gas Shift Reaction on Au/CeO2 Catalysts. *J. Cat.* **2007,** *252*, 231-242.

24. Sakamoto, M., Tachikawa, T., Fujistuka, M., Majima, T., Two-color Two-laser Fabrication of Gold Nanoparticles in PVA Film. *Chem. Phys. Lett.* **2006,** *420*, 90-94.

25. Sakamoto, M., Tachikawa, T., Fujistuka, M., Majima, T., Photochemical Formation of Au/Cu Bimetallic Nanoparticles with Different Shapes and Sizes in a Poly(vinyl alcohol) Film. *Adv. Funct. Mater.* **2007,** *17*, 857-862.

26. Sakamoto, M., Tachikawa, T., Fujistuka, M., Majima, T., Two-Laser-Guided Three-Dimensional Microfabrication and Processing in a Flexible Matrix. *Adv. Mater.* **2008,** *20*, 3427-3432.

27. Korchev, A. S., Bozack, M. J., Slaten, B. L., Mills, G., Polymer-Initiated Photogeneration of Silver Nanoparticles in SPEEK/PVA Films: Direct Metal Photopatterning. *J. Am. Chem. Soc.* **2003,** *126*, 10-11.

28. Mallick, K., Witcomb, M. J., Scurrell, M. S., Polymer Stabilized Silver Nanoparticles: A Photochemical Synthesis Route. *J. Mater. Science* **2004**, 4459-4463.

29. Mallick, K., Witcomb, M. J., Scurrell, M. S., Self Assembly of Metal Nanoparticles: Formation of the Highly Oriented, Core-shell Type, Bimetallic Gold-silver Film. *J. Nanopart. Res.* **2007,** *9*, 323-330.

30. Kapoor, S., Mukherjee, T., Photochemical Formation of Copper Nanoparticles in Poly(N-vinylpyrrolidone). *Chem. Phys. Lett.* **2003,** *370*, 83-87.

31. Eustis, S., Hsu, S.-Y., El-Sayed, M. A., Gold Nanoparticle Formation from Photochemical Reduction of Au3+ by Continuous Excitation in Colloidal Solutions. A Proposed Molecular Mechanism. *J. Phys. Chem. B* **2005,** *109*, 4811-4815.

32. Skrabalak, S. E., Chen, J., Sun. Y., Lu, X., Au, L., Cobley, C. M., Xia, Y., Gold Nanocages: Synthesis, Properties, and Applications. *Acc. Chem. Res.* **2008,** *41* (12), 1587-1595.

Chapter 4

Synthesis of Gold Nanoparticles from Bimolecular Photoinitiators

4.1 Introduction

Nanoparticles have also been prepared by reduction by various ketyl radicals, where the radicals were generated through an intermolecular, bimolecular mechanism classified as a type II photoinitiation (PI_2) pathway. In this mechanism, free radicals are generated *via* one-step hydrogen atom abstraction from a donor. Significant research in the past two decades has looked into the generation of nanomaterials using a variety of chromophores coupled with reactive hydrogen donors for an alternate generation of reducing free radicals.[1-6]

Photo-induced hydrogen atom abstraction by ketones is one of the most important reactions in organic photochemistry.[7, 8] Excited triplet ketones abstract a hydrogen atom from a donor to yield two radicals or a biradical. Aryl ketones are common photochemical sensitizers owing to their low lying n,π* state and, thus, high reactivity for hydrogen abstraction.[8] A selection of chromophores studied in this doctoral work is presented in Scheme 4.1.

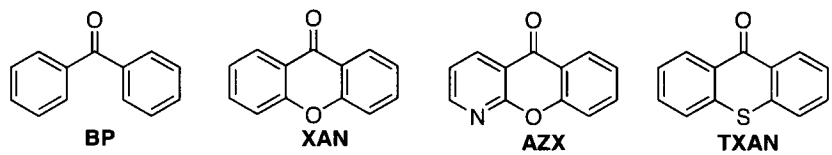

Scheme 4 . 1 - Schematic structures of the various aromatic ketones analyzed.

The rate of hydrogen abstraction is dependent on the electronic configuration of the ketone, where ketones with n,π* character have been reported to abstract hydrogen 100 times faster than carbonyls with π,π* character.[8, 9] Additionally, the rate of reaction also depends on the donor, where primary and secondary alcohols, ethers and alkyl benzenes induce faster reactivity with n,π* character over π,π* dominant ketones, yet phenolic hydrogen donors induce faster hydrogen transfer with π,π*

carbonyls.[10] An example of the hydrogen donors used in this work are presented in Scheme 4.2.

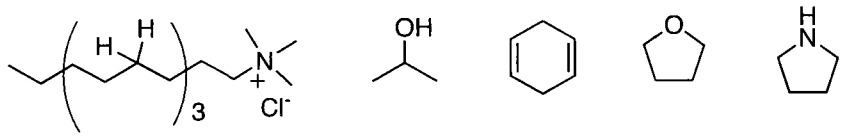

CTAC 2-prop 1,4-CHD THF pyrr

Scheme 4 . 2 - Schematic structures of hydrogen donors examined.

Hydrogen abstraction results in the formation of two radicals, which can undergo photoaddition, dimerization, further hydrogen abstraction, or chemical reduction (as is the case of ketyl radicals in the presence of many metal salts). Ketyl radicals reduce metal ions to metal atoms in the same manner as described in Chapter 3. Scheme 4.3 illustrates the process for M^+, where only one electron is needed.

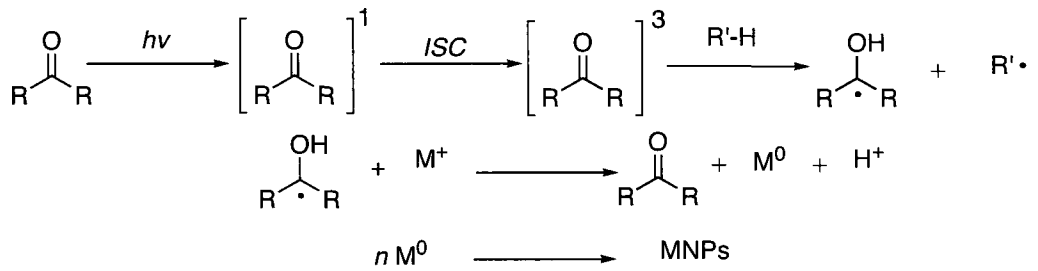

Scheme 4 . 3 - PI_2 pathway *via* intermolecular hydrogen atom transfer.

There has been abundant research into the generation of ketyl radical species through hydrogen abstraction from triplet ketones,[3, 7, 11-15] where the efficiency of the reaction is largely dependent on the lifetime of the reducing radical or its precursor. Notably, it has been widely observed that metal salts can quench the excited state triplets of many carbonyls with rates approaching diffusion control (*vide infra*). One way to maximize photochemical nanoparticle generation and avoid this competitive pathway has been to prepare the materials in the presence of stabilizers such as

polymers, dendrimers, or micelles. These supramolecular materials can sequester the excited state triplet species and enhance radical-pair generation *via* hydrogen abstraction,[16] as well as function to minimize quenching of triplet chromophores by transition metal salts. As a proof of concept, nanoparticle synthesis in the absence of micelles using benzophenone in acetonitrile, 2-propanol or tetrahydrofuran remains a challenge as a low yield of metal nanoparticle aggregates were obtained for experiments with silver or gold. *(vide infra)*

Many reports exist for the photochemical generation of nanoparticles and nanorods using a simple water-soluble ketone such as acetone.[13, 17-22] In many cases, particle formation required UVC (254 nm) photolysis and irradiation times on the order of several hours. Significant progress has been put forth by Dong *et al.* employing acetone to produce colloidal gold nanoparticles using a variety of different hydrogen donors, stabilizers, and photon energies.[21, 22] Solar irradiation of a Au(III)-sodium citrate solution produced 9-12 nm particles, and nanoparticles of approximately 7.5 nm in diameter were prepared by photolysis of a Au(III)-sodium dodecylsulfonate-acetone system, yet substitution with sodium dodecylbenzene sulfonate yielded smaller 6.7 nm particles with a narrower size distribution.

Bimetallic Au/Ag core/shell particles were also synthesized utilizing the photochemical seeding technique where 3 nm AuNP seeds were added to a PEG-acetone-$AgNO_3$ solution. Finally, gold nanorods were prepared from a Au(III)-DMF-CTAC-acetone system to yield monodisperse rods with high aspect ratios greater than 10:1. Other syntheses of nanorods from acetone have been reported, many of which require the addition of $AgNO_3$ for directed growth.[18-20] Interestingly, none of the reports cited here addressed deaeration during synthesis. With triplet lifetimes around 1-4 μs in aqueous systems,[23] significant quenching of the acetone triplet by oxygen or other metal species are likely contributors to the required long irradiation times. Working with aryl or biaryl ketones, on the other hand, for which the absorbances are shifted to lower energies and therefore with greater intensity in the UV region, allows for efficient triplet formation, followed by rapid hydrogen abstraction and minimized quenching as a result of shorter triplet lifetimes. As a

result, the time required for nanoparticle photochemical synthesis was significantly reduced. An example of such an aromatic chromophore is benzophenone.

4.2 Aromatic Ketones

4.2.1 Benzophenone

Benzophenone is an ideal candidate for generation of reducing species for the formation of nanoparticles due to its photophysical properties. The biarylketone possesses a strong absorption in the UV region with a peak at 350 nm representing the n,π* transition. While its absorption does screen the LMCT of $HAuCl_4$, BP possesses a higher extinction coefficient at the photolysis wavelength (the molar extinction coefficient for BP is 8400 $M^{-1}cm^{-1}$ at 319 nm while that of $AuCl_4^-$ is 5800 $M^{-1}cm^{-1}$).[24]

Benzophenone has been widely used as a sensitizer for the generation of colloidal nanoparticles.[1, 5, 11, 25, 26] In one example, Eustis *et al.* prepared colloidal AgNP from photolysis of benzophenone with 100 fs pulses at 265 nm and CW UVA light in the presence of $AgNO_3$ and CTAB as a stabilizer.[1] In another study, CuNP were prepared by Kapoor *et al.* using $CuSO_4$, benzophenone and poly vinylpyrrolidone (PVP) as a stabilizer in the presence of CW 253.7 nm light.[6] Laser flash photolysis studies were unable to detect the formation of the BP triplet between 470-600 nm in the time-resolved spectrum, implying that PVP must be responsible for the reduction. Moreover, LFP experiments revealed energy transfer from the benzophenone triplet to PVP, without hydrogen atom abstraction. Photolysis of PVP in the presence of $CuSO_4$ alone, however, did not yield nanoparticles. This preparation yielded polydisperse particles as small as 15 ± 4 nm. In later studies, the author succeeded in preparing 10-40 nm CuNP from benzophenone with gelatin as a hydrogen donor.[27]

While micelles can segregate photochemically generated intermediates from quenching events, their cage-like structure can also enhance geminal recombination of radical pairs and thus decrease micellar escape of reducing radicals. Previous studies *via* laser flash photolysis reported the triplet lifetime of benzophenone in CTAC or SDS to be approximate 320 ns.[28] The photophysics of the ketone have also been investigated in the presence of metal salts, where the rate of BP triplet quenching by silver salts in the presence of SDS has been reported as 4.3×10^{10} $M^{-1}s^{-1}$. Similarly, the quenching of the ketyl radical was also measured at 4.3×10^{9} $M^{-1}s^{-1}$.[29] The challenge of radical recombination or biradical formation was overcome by working in the presence of a magnetic field. Since geminal recombination of these reactive triplet transients requires a change in multiplicity, removing the degeneracy of the triplet states in the magnetic field significantly reduces probability for recombination and hence promotes micellar exit, which is not affected by magnetic fields, and subsequent nanoparticle formation. This concept was reflected in recent work carried out by Steven Maguire and described in his Master thesis.[30] AgNP were prepared in the presence of a 100 mT weak magnetic field *via* 320 nm photolysis of benzophenone with $AgNO_3$ in 0.1 M SDS in the presence of a strong hydrogen donor; 1,4-cyclohexadiene.[11] It was observed that the presence of the magnetic field increased nanoparticle yield by 67%, increased the rate of AgNP formation by 30% and an increased the particle size from 4 to 8 nm.

Benzophenone has also been used in this work as a sensitizer for the generation of AuNP. Initially, benzophenone was photolyzed in a variety of different solvents, as shown in Figure 4.1. The narrow SPB bandwidth for nanoparticles made in CTAC showed promise for an optimal micellar solvent system for further work, as was similarly observed for benzoins discussed in Chapter 3. It is clear from the analysis of SPB presented in Figure 4.1 that nanoparticle agglomeration occurred in the absence of stabilizer, where a grey/blue solution formed quickly and precipitated in the case of the water/isopropanol solvent system. Neither photoproducts, chloride ions, nor light absorbing transients effectively participated in charge stabilization. Isopropanol was present as a hydrogen donor in some experiments. It was observed that benzophenone in the presence of surfactants alone led to

nanoparticle formation, where the methylene hydrogens of the surfactant chain have been reported to donate a hydrogen in photoreduction of aromatic ketones.[28]

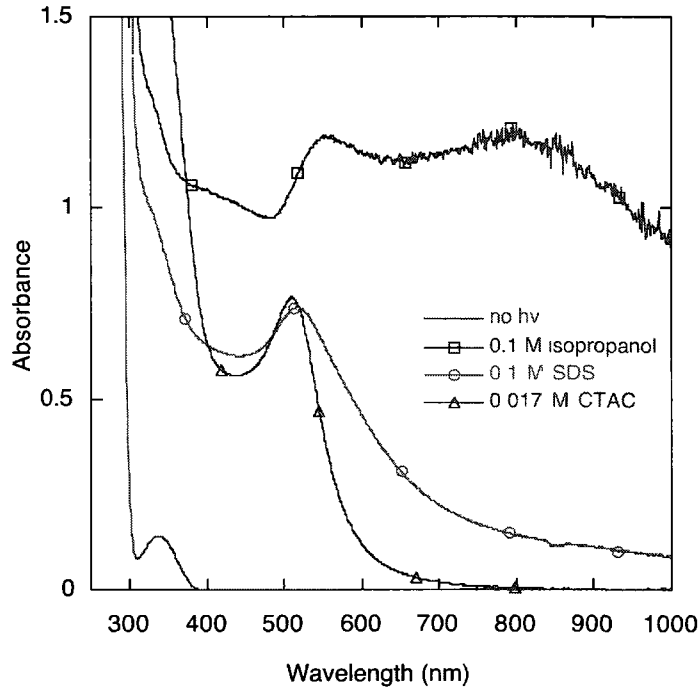

Figure 4 . 1 - Absorption of AuNP prepared from 0.33 mM $HAuCl_4$ and 1.0 mM benzophenone in the presence of 0.1 M isopropanol, 0.1 M SDS or 0.017 M CTAC upon 30 minutes UVA photolysis.

The formation of gold nanoparticles utilizing benzophenone as a sensitizer was investigated in the presence of various hydrogen donors in deareated CTAC micelle solutions. A concentration range from 0.33 to 5.0 mM benzophenone in the presence of CTAC stabilizer with 0.33 mM $HAuCl_4$ offered an increase in absorption intensity of the SPB with minimal (4 nm) peak shifting, confirming the stability provided by working in a surfactant system. The surfactant alone has been known to have hydrogen abstracted with rate constants approaching 3×10^6 $M^{-1}s^{-1}$,[28] while the rate constant has been measured to be 1.3×10^6 $M^{-1}s^{-1}$ for isopropanol,[31] and 2.9×10^8 $M^{-1}s^{-1}$ for 1,4-CHD.[28] A comparison of the absorption spectra for AuNP

generated from different hydrogen donors with benzophenone is presented in Figure 4.2.

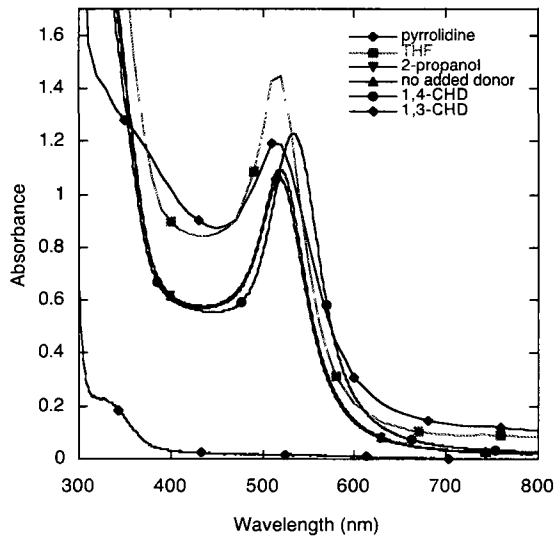

Figure 4 . 2 - Absorption of AuNP prepared from various hydrogen donors with 0.33 mM $HAuCl_4$, 1.0 mM benzophenone and 50 mM hydrogen donor with deareated 17 mM CTAC upon 30 minutes UVA photolysis.

The rate of hydrogen abstraction has a direct effect on the kinetics of nanoparticle synthesis. The appearance of some of the final solutions are depicted in a photograph in Figure 4.3, while the growth of AuNP over time with different hydrogen donors is presented in Figure 4.4. The shape of the growth curve is indicative of an autocatalytic growth mechanism, and can thus not simply be correlated with a bimolecular process as hydrogen abstraction. Alternatively, comparisons between hydrogen donors can be made by analysis of the induction period prior to SPB growth, the absorbance maximum, and the time at half of the absorbance. Generally, the longer the induction period, the slower the actual SPB growth and the lower the final absorption intensity, which could be interpreted as nanoparticle yield. The analysis is presented in Table 4.1.

Figure 4 . 3 - Photograph of AuNP synthesized from 1.0 mM BP in deareated 17 mM CTAC with different hydrogen donors (50 mM) with 30 min UVA. (left to right) THF, 1,4-CHD, no added donor, pyrrolidine.

The fastest growth was observed with pyrrolidine and correlates well with a reported rate of hydrogen transfer of 4.4 x 10^9 $M^{-1}s^{-1}$ to benzophenone.[32] Amines tend to be quite reactive hydrogen donors when the α-hydrogen is the species abstracted. The mechanism for ketyl radical formation occurs through an interaction between the excited state ketone and the ground state amine to form an exciplex, where the exciplex will decay to either yield a ketyl radical and an α-amino alkyl radical, or react through electron transfer to form the ketyl radical anion and α-amino alkyl radical cation. The pathways are illustrated in Scheme 4.4.

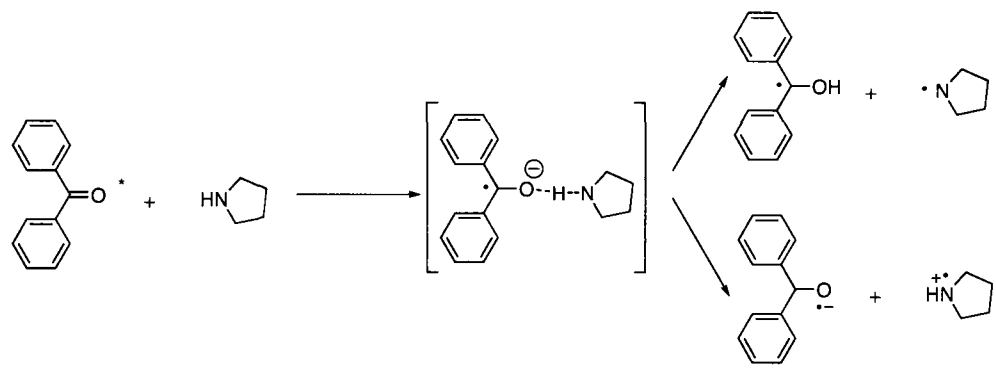

Scheme 4 . 4 - Hydrogen atom transfer pathways between benzophenone and pyrrolidine.

The latter is more likely in polar solvents, but studies by Cohen *et al.* have revealed that triplet quenching of benzophenone by aliphatic amines results in the formation of ketyl radicals. Furthermore, interaction of the α-amino alkyl radical with ground state benzophenone results in reduction of the ketone to form the ketyl. [33-35] If formed as in the polar condtions in this work, the α-amino alkyl radical possesses a more negative reduction potential than BPK and could result in greater thermodynamic control over nanoparticle yield relative to other donor-ketone systems. Hydrogen abstraction from a tertiary amine is generally faster than from a secondary amine,[35] and it is not simple kinetics of hydrogen abstraction that govern the rate of particle growth.

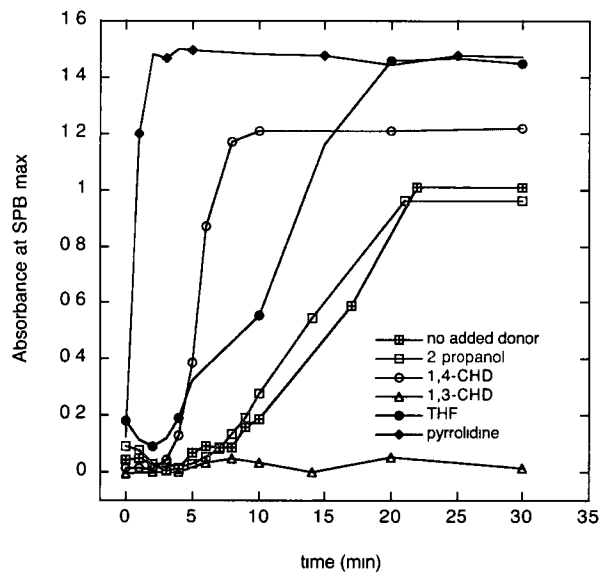

Figure 4 . 4 - Growth of AuNPs prepared from 0.33 mM $HAuCl_4$, 1.0 mM benzophenone and 17 mM CTAC over time, in the presence of various hydrogen donors. 0.1 M 2-propanol, 0.05 M 1,4-CHD, 0.05 M 1,3-CHD, 0.05 M tetrahydrofuran, and 0.05 M pyrollidine with 30 min UVA photolysis

LFP studies have measured a rate constant for hydrogen transfer to be 8.3×10^6 $M^{-1}s^{-1}$ for tetrahydrofuran with di-*tert*-butylperoxide.[31] In this work, THF was slower at AuNP generation than pyrrolidine and 1,4-CHD, but managed to generate an SPB with a rather high absorbance intensity. In the case of

1,3 cyclohexadiene, no nanoparticle growth was observed during photolysis and absorption measurements.

1,3-cyclohexadiene (1,3-CHD) is known as an excellent donor for a very fast rate of hydrogen abstraction, reported as 4.2 x 10^7 $M^{-1}s^{-1}$ for hydrogen abstraction from the *tert*-butoxyl radical from di-*tert*-butyl peroxide, in comparison with 5.4 x 10^7 $M^{-1}s^{-1}$ for 1,4-cyclohexadiene, or 0.18 x 10^7 $M^{-1}s^{-1}$ for 2-propanol in the same report.[31] Despite its high reactivity towards hydrogen abstraction, 1,3-CHD is also a powerful triplet ketone quencher *via* energy transfer,[8] thus decreasing its tendency to undergo excited state intermolecular hydrogen transfer. For example, 1,3-CHD has been reported to quench triplet xanthone with a rate constant of 9.9 x 10^9 $M^{-1}s^{-1}$, as measured by triplet triplet transient absorbance.[36] The correlation between reported rates of hydrogen transfer, as presented in Table 4.1, can act as a good predictor for synthesis of nanoparticles, where generally the faster the rate, the faster the rate of nanoparticle growth. Generally, the shorter wavelength of the SPB, the smaller the nanoparticle size.

H_{donor}	$k_{H\text{-}abs}$ (x 10^7 $M^{-1}s^{-1}$)	$t_{induction}$ (min)	$t_{half\text{-}max}$ (min)	Abs_{max}	λ_{max} (nm)
1,3-cyclohexadiene	4.20 [31]	>60	N/A	N/A	N/A
CTAC	0.30 [28]	3	17	1.09	519
2-propanol	0.13 [31]	5	14	1.06	518
Tetrahydrofuran	0.83 [31]	3	11	1.45	515
1,4-cyclohexadiene	29 [28]	4	5	1.23	534
Pyrrolidine	440 [32]	< 1	<1	1.46	514

Table 4 . 1 - Parameters governing nanoparticle growth upon measuring the growth of the SPB at λ_{max} over time from 0.33 mM $HAuCl_4$, 1.0 mM benzophenone and 50 mM various hydrogen donors in deareated CTAC.

The rapid growth of nanoparticles via 1,4-cyclohexadiene can be attributed to the ease of hydrogen abstraction and the resulting stability of the resonance stabilized cyclohexadienyl radical. Additionally, the regeneration of ketone highlights the photocatalytic appeal to this technique. The mechanism is given in Scheme 4.5.

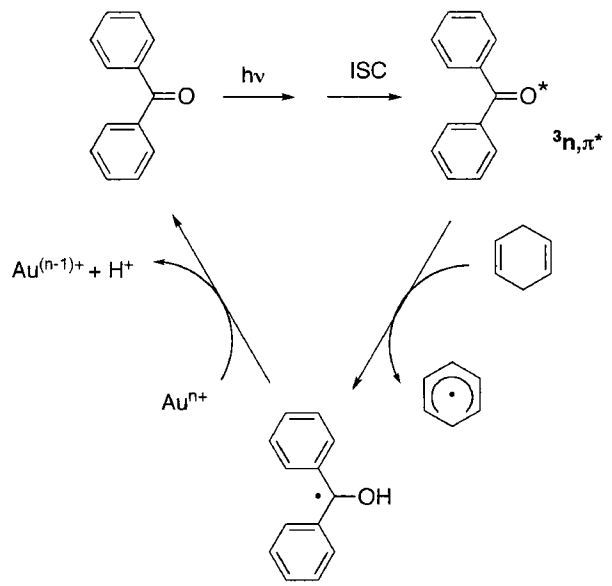

Scheme 4 . 5 - Photoreduction of benzophenone by 1,4-cyclohexadiene and reduction of Au ions, illustrating the photocatalytic nature of the process.

The size of gold nanoparticles prepared from benzophenone has been analyzed for selected samples, particularly in the absence of any hydrogen donor, as well as with 1,4-cyclohexadiene. Particle diameters were measured from analysis of transmission electron microscopy images to estimate a particle size of 7 nm and 17 nm for particles prepared in the absence and presence of 1,4-CHD, respectively. The TEM and corresponding histograms are presented in Figure 4.5. While 1,4-CHD significantly reduces the duration of the induction period from eight minutes to two minutes, there is an increase in the particle size as well as size distribution. This is counter-intuitive to the theory of small nanoparticles resulting from short nucleation times, but the photocatalytic regeneration of the ketone can extend the nucleation period and lead to larger particles.

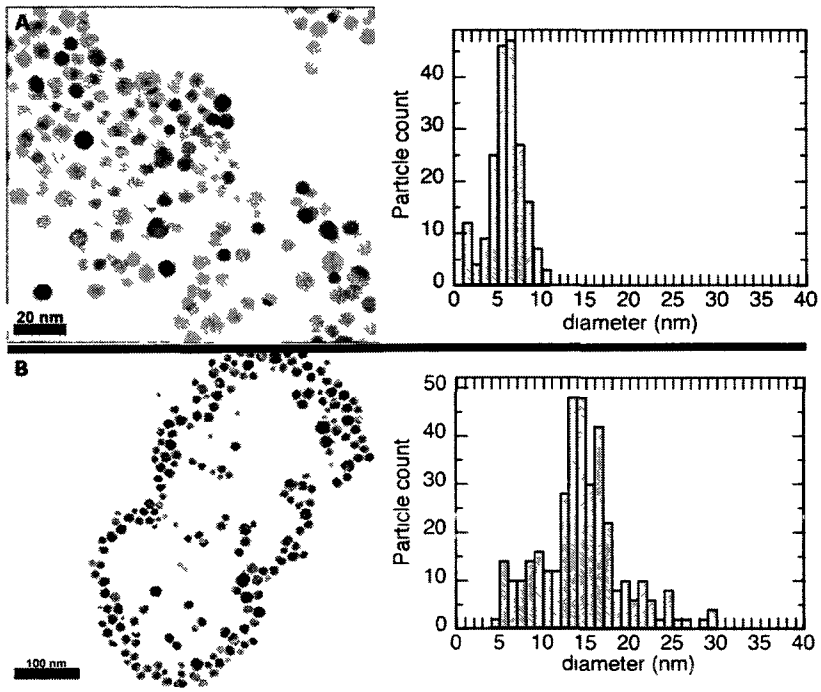

Figure 4 . 5 - TEM image and corresponding size distribution of AuNP prepared from photolysis of benzophenone in the presence of A) no added hydrogen donor and B) 50 mM CTAC.

The rate of nanoparticle synthesis was also studied in the presence and absence of dissolved oxygen, as the triplets states for these chromophores are longer lived than for the benzoins described in Chapter 3. Quenching should thus decrease the effectiveness of nanoparticle synthesis. A comparison of various conditions for making nanoparticles is depicted in Figure 4.6, and illustrates the span in the rate of particle growth that was established by working in the presence of a good hydrogen donor, or a good quencher. From the data, it is clear that the presence of 1,4-CHD has a greater role on the rate of particle growth and the yield of AuNP compared to oxygen

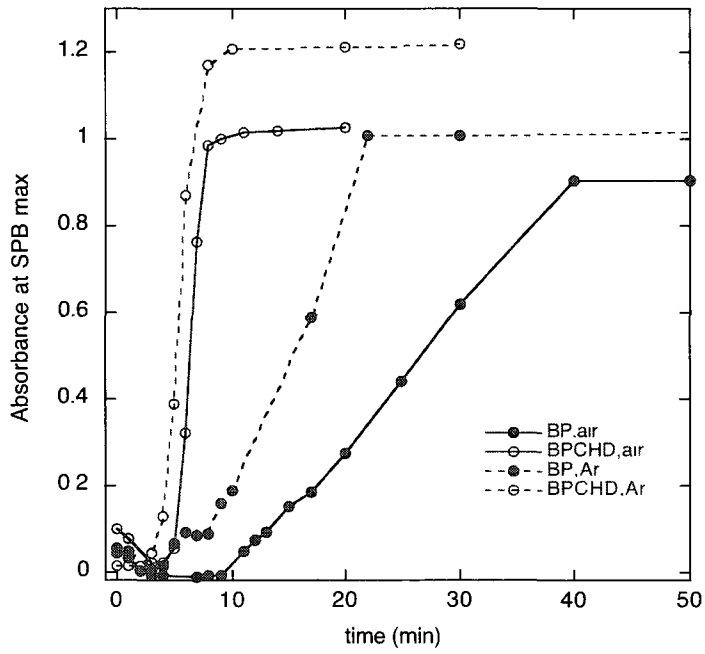

Figure 4 . 6 - Growth of AuNPs prepared from 0.33 mM $HAuCl_4$, 1.0 mM benzophenone and 17 mM CTAC over time with UVA photolysis, in the presence and/or absence of 1,4-cyclohexadiene and dissolved oxygen.

The synthesis of gold nanoparticles in the absence of a hydrogen donor and presence of oxygen was substantially slower, but nevertheless provides nanoparticles with an SPB maximum at 524 nm; approximately 6 nm redshifted from particles prepared under Argon-purged conditions.

4.2.2. Xanthones

4.2.2.1 Xanthone

While the photochemistry of unsubstituted benzophenone occurs from the n,π* state, the photophysical properties of xanthone are dependent on the polarity of the environment, and thus vary significantly in different solvents.[37] The variance in

polarity is a result of an inversion of states, where the triplet n,π* state, the LUMO in organic media, increases in energy in the presence of polar media, leaving the triplet π,π* state as the lowest energy triplet state. The absorption properties of the two aromatic ketones also differ such that xanthone possesses a much stronger absorption at the irradiation wavelength in the UVA region. Owing to this, there are greater differences between the absorption spectra of the ketone and ketyl radical for xanthone than there are for benzophenone.[15]

In aqueous media, the low lying ^{3}π,π* state of xanthone leads to poor reactivity towards hydrogen abstraction.[14, 15, 37, 38] In this work, gold nanoparticles were synthesized using xanthone, and results differed substantially in comparison to benzophenone. Following 30 minutes of photolysis, absorption spectra of the solutions were obtained, and are presented in Figure 4.7. When deareated 0.1 M SDS was used as a surfactant, the AuNP SPB was greater for xanthone than for benzophenone, and can likely be attributed to an alternative thermal reaction induced by a contamination assisting the photochemical reaction, similar to results presented in Chapter 3. For this reason, colloidal nanoparticle synthesis was continued in 17 mM CTAC.

With 17 mM CTAC, similar to reactions with benzophenone, the generation of AuNP in the presence of common hydrogen donors was investigated. In the absence of an additional donor (where hydrogen abstraction arose from CTAC and the ketone alone), results were comparable with 50 mM 2-propanol. Utilizing 1,4-CHD for hydrogen donation also proved to be quite effective. The absorption intensity of the surface plasmon band *via* 1,4-CHD was approximately three times larger relative to the use of other hydrogen donors. Noteworthy are dramatic differences in the yield of nanoparticles when the samples were deareated. With 1.0 mM xanthone in the presence of CTAC alone, the SPB intensity was almost halved relative to ambient dissolved-oxygen samples. The time-resolved spectra for growth of AuNP prepared from xanthone are presented in Figure 4.8.

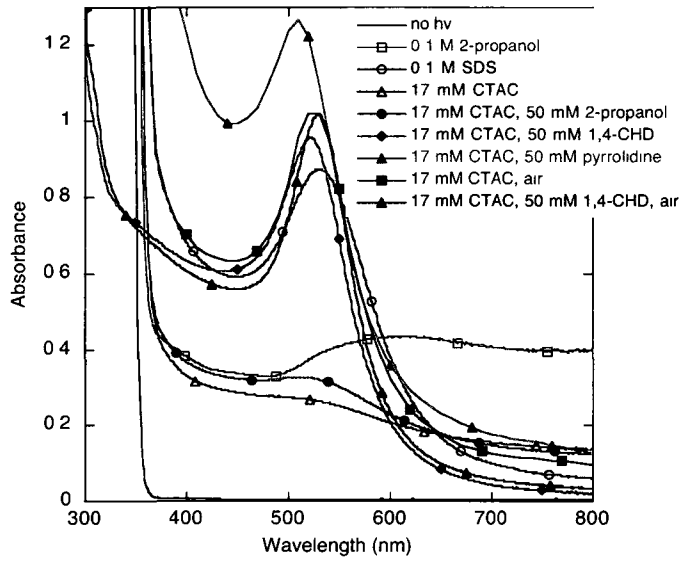

Figure 4 . 7 - Absorption spectra of AuNP prepared from 30 minute UVA photolysis of 0.33 mM, 1.0 mM xanthone in the presence of various surfactants and hydrogen donors. Samples were deareated unless specified.

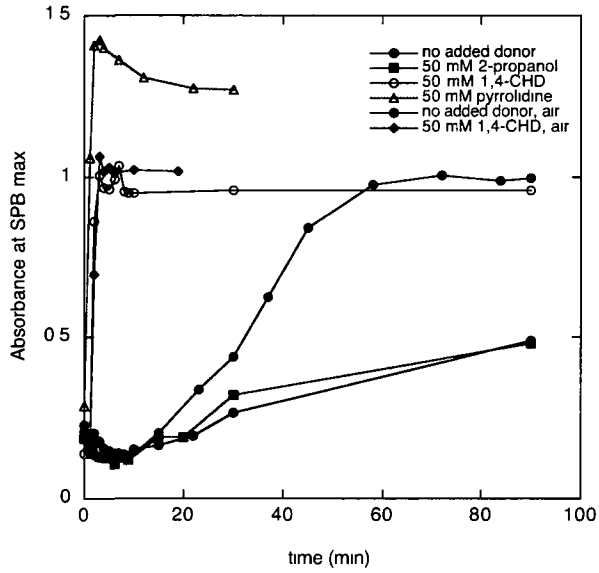

Figure 4 . 8 - Growth of AuNPs prepared from 0.33 mM $HAuCl_4$, 1.0 mM xanthone and 17 mM CTAC over time, in the presence of 50 mM various hydrogen donors after 30 min UVA photolysis.

The difference in reactivity could be related to the absorption of the starting solutions. There was an induction period of nine minutes for both "non-donor" samples. A greater scatter was observed at 350 nm in the purged sample, relative to the air-saturated sample whose scatter disappeared within three minutes of irradiation. The scatter diminished negligibly with irradiation time, and eventually the Au SPB formed constructively with the scatter. There could be a synergistic effect at play in this synthesis, for the control photolysis of $HAuCl_4$ in 17 mM CTAC led to no plasmon generation after 30 minutes irradiation, but a faint pink colour was obtained after prolonged irradiation for two hours.

Hydrogen Donor	O_2	$t_{induction}$ (min)	$t_{half\text{-}max}$ (min)	Abs_{max}	λ_{max} (nm)
17 mM CTAC	No	9	540	0.48	513, broad
17 mM CTAC	Yes	9	540	0.99	524
2-propanol	No	9	540	0.49	520, broad
1,4-cyclohexadiene	No	1	60	0.95	520
1,4-cyclohexadiene	Yes	1	60	1.02	529
pyrrolidine	No	<1	<1	1.42	509

Table 4 . 2 - Parameters governing nanoparticle growth with 1.0 mM Xanthone and 50 mM hydrogen donor in a 17 mM CTAC system.

The rate of nanoparticle growth was also investigated in a similar fashion to the analysis with benzophenone. Under deareated conditions, the relative order of rates of SPB growth agreed well with reported rates of hydrogen abstraction mentioned in Section 4.2.1, which had been measured in the absence of oxygen in various experiments. Two growth processes seem to be occurring in the xanthone system, depending on the hydrogen donor and the presence of dissolved oxygen.

A very slow growth arose from the presence of moderate hydrogen donors due to the inefficient hydrogen abstraction from triplet states with π,π* character. As depicted in Figure 4.8, a long induction period preceded the slow formation of an orange-brown solution with a small SPB positioned at approximately 510 nm amid scatter from insoluble organic/surfactant products when no additional hydrogen donor was present. Alternatively, a rapid growth occurred with 1,4-CHD where the rate of SPB formation was triple the rate observed when benzophenone was used as a sensitizer. In this case, the rapid formation of AuNP led to the formation of a red/pink colloid having a SPB centered at 530 nm. Scanning electron microscopy determined the average particle size to be 14.3 ± 3.7 nm, whereas smaller nanoparticles of approximately 6.9 ± 2.1 nm in diameter were obtained under slow growth conditions when only CTAC present as a hydrogen donor. Samples of the images are presented in Figures 4.9 and 4.10.

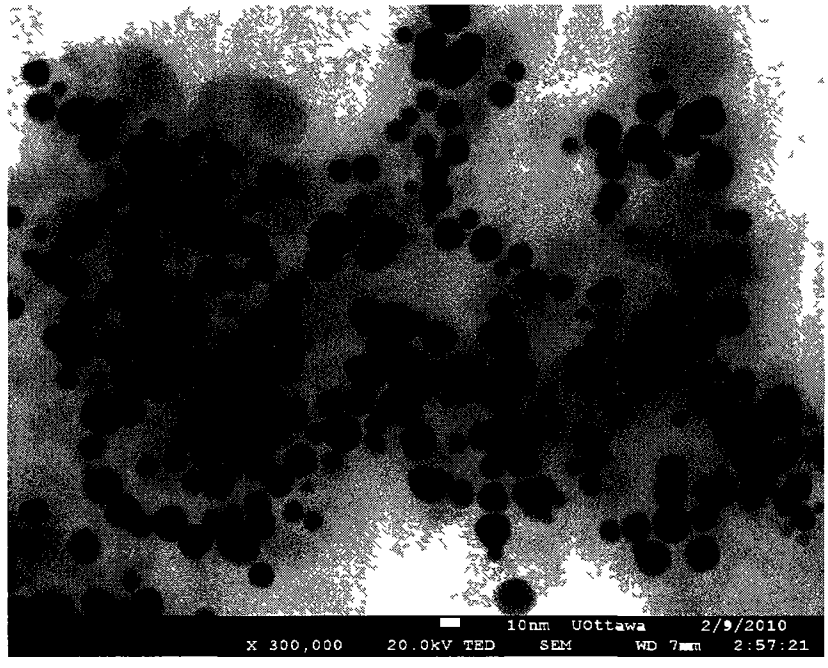

Figure 4 . 9 - SEM image of AuNP prepared from 30 minute UVA photolysis of 0.33 mM $HAuCl_4$, 1.0 mM xanthone and 50 mM 1,4-CHD in deareated 17 mM CTAC. The scale bar represents 10 nm.

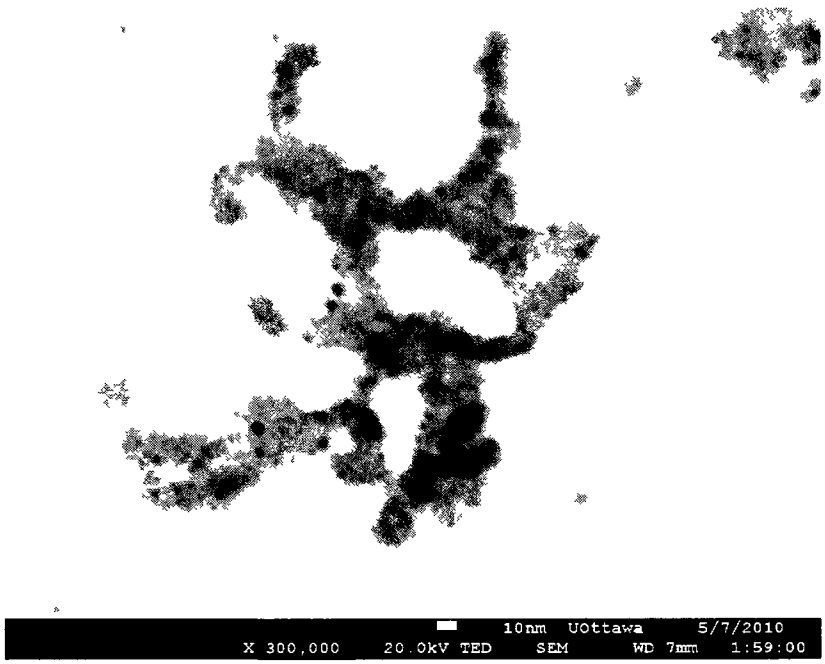

Figure 4 . 10 - SEM image of AuNP prepared from 30 minute UVA photolysis of 0.33 mM $HAuCl_4$, 1.0 mM xanthone in deareated 17 mM CTAC. The scale bar represents 10 nm.

These results are also contrary to principles for nanoparticle growth, which establish that long nucleation periods lead to large and polydisperse particles grown with effects of Oswald ripening, as discussed in Section 1.4. The long induction period and slow growth process could result in small nanoparticles if substantial surface functionalization was performed by xanthone and CTAC. Given that triplet π,π^* character is synonymous with poor hydrogen acceptance, this can then imply that these excited state species are better electron donors to a highly electron rich species such as the surface of gold nanoparticles, similar to olefins and their tendency to undergo oxidation on the particle surface.[39] Either the ether or the carbonyl moiety of the aromatic ketone could allow for preferential binding to the nanoparticle surface and assist in stabilizing small nanoparticles in the presence of CTAC. In the absence of any surfactant, photolysis of the gold salt/xanthone solution resulted in a grey solution with precipitation within a couple of hours. The absorbance spectrum is presented in Figure 4. 7.

For comparison, AuNP were also prepared with an alternative strong hydrogen donor, pyrrolidine. Gold nanoparticles were rapidly formed photochemically, and the mechanism is though to follow a proton-coupled electron transfer typical of many amines.[32] The fast reactivity is shown in Figure 4.11, and compared to the growth rate observed with benzophenone. Hydrogen transfer occurred at an essentially equivalent rate, irrespective of the triplet excited state character involved.

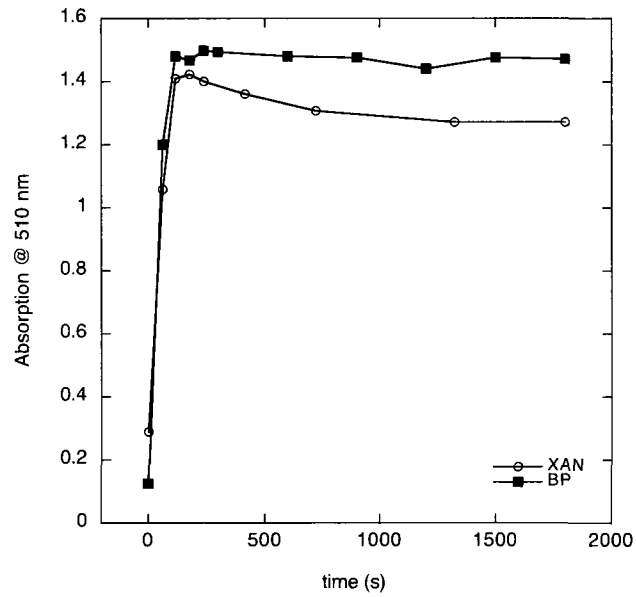

Figure 4 . 11 - Growth of AuNP over time with 0.33 mM $HAuCl_4$ and 50 mM pyrrolidine as a hydrogen donor in deareated 17 mM CTAC from UVA photolysis. A comparison is made between the two ketones BP and XAN.

In summary, the synthesis of gold nanoparticles from the ketyl radical of xanthone led to a very slow nanoparticle generation in the presence of a poor hydrogen donor to yield ~ 7 nm particles, but a very fast synthesis of larger particles when a strong hydrogen donor is employed. The slow reactivity is a consequence of the poor hydrogen abstraction ability of the triplet π,π^* state of xanthone. To determine if the similar small nanoparticles are the result of adsorption of the chromophore to the nanoparticle, an alternative xanthone was also tested.

4.2.2.2 1-Azaxanthone

When a pyridine ring is substituted into the xanthone framework, the excited triplet state has a low-lying triplet state with n,π* character, and is higher in energy than xanthone and also benzophenone.[14, 15] 1-Azaxanthone (AZX) also has a similar absorption spectrum to xanthone in the UV-Visible region. Owing to this, the generation of AuNP from the 1-azaxanthone system was studied in order to elucidate the nature of the excited state. With the same methodology administered for both benzophenone and xanthone, gold nanoparticles were prepared in 17 mM CTAC at identical starting material concentrations using AZX as the reducing agent. In the absence of surfactant, quenching of the triplet state is likely by oxygen or by the metal salt, and any particles that did form were not sufficiently stabilized as evidenced by a broad absorption band. Parallel gold nanoparticle syntheses were attempted under similar concentrations and different surfactants and hydrogen donors with the results of these experiments presented in Figure 4.12.

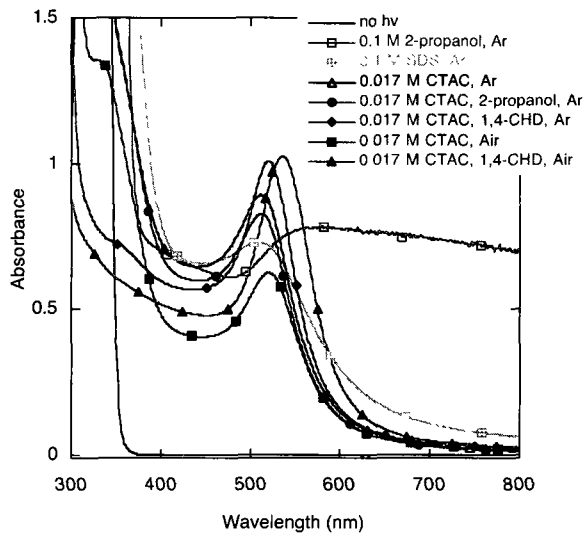

Figure 4 . 12 - Absorption spectra of AuNP prepared from 30 minute UVA photolysis of 1.0 mM 1-azaxanthone in the presence of various surfactants and 50 mM hydrogen donors.

As in the case with benzophenone, the particles formed in 0.1 M SDS displayed a broad SPB relative to identical conditions with 17 mM CTAC, potentially attributed to the photochemical reduction from SDS alone, as well as to the behaviour of n,π* triplets in polar negatively charged micelles (Future studies employ CTAC as the surfactant due to the narrower SPB). One marked difference between AZX and the other chromophores evaluated in this work was the blueshifted SPB relative to AuNP prepared by benzophenone or xanthone. Figure 4.13 illustrates the formation of the SPB over time when no hydrogen donor was added under deareated conditions. A high absorption at 511 nm was attained, giving rise to an orange solution.

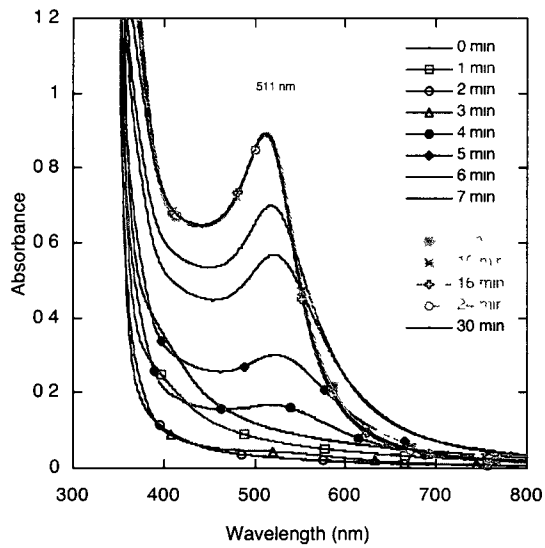

Figure 4 . 13 - Absorption of AuNP prepared from 0.33 mM $HAuCl_4$ and 1.0 mM 1-azaxanthone in deareated 17 mM CTAC after 30 min 350 nm photolysis.

Nanoparticles prepared in this fashion were measured to be 4.6 ± 1.6 nm in diameter as determined from TEM images as displayed in Figure 4.14. XPS was also performed on AuNP that were synthesized with no added donor under deareated conditions. The particles were then washed to remove residual surfactant and dried on a silicon wafer. XPS data analyzed the surface and found that the

particle surface contained Au^0 on the surface as indicated by the Au 4f peaks at 85 5 eV and 89 0 eV (corrected to 84.0 eV and 87 5 eV with the reference peak) Similar to AuNP prepared from I-2959, the peaks are indicative of Au^0 on the surface. The XPS spectrum for the Au peaks and the 1s reference peak for carbon are found in the appendix in Figures 4 25 and 4.26, respectively.

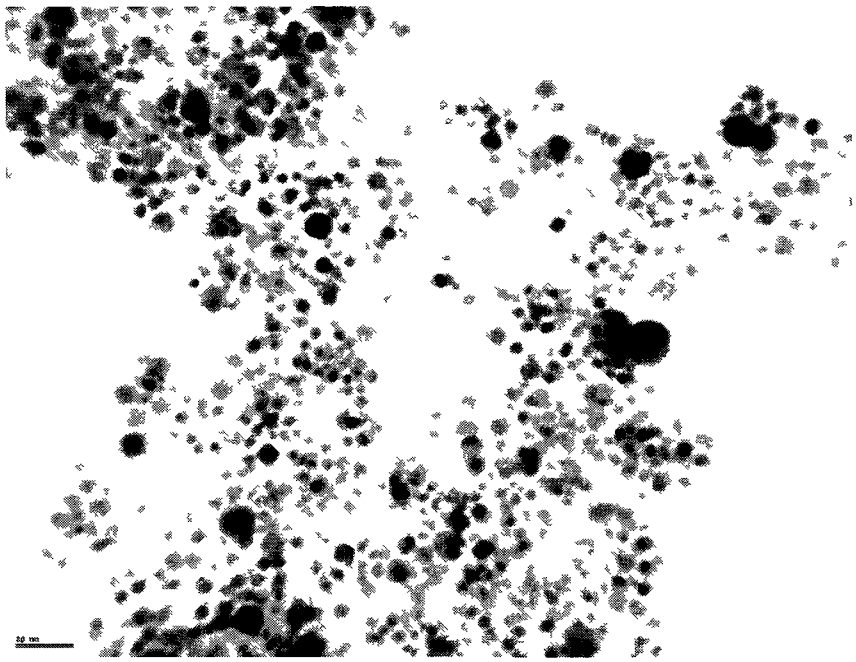

Figure 4 . 14 - TEM image of AuNP prepared from 0.33 mM $HAuCl_4$ and 1.0 mM 1-azaxanthone in deareated 17 mM CTAC following 30 minutes UVA photolysis. Scale bar represents 20 nm.

Time-resolved absorption measurements were performed for all samples with different hydrogen donors, and illustrated a faster generation of nanoparticles relative to xanthone and benzophenone. This can be directly attributed to faster hydrogen abstraction from the n,π^{3*} state. Just as with no added donor and 2-propanol with the other chromophores, both systems display similar rates. Either both systems coincidentally operate at similar kinetics, or the rate of hydrogen abstraction for 2-propanol is slower than that of CTAC, as one would expect given the rate constants of hydrogen abstraction for both donors discussed in Section

4.2.1. The time-resolved absorption spectra are compared in Figure 4.15. Unlike the chemistry occurring with xanthone, the presence of oxygen did not enhance the rate of nanoparticle growth, in the presence or absence of 1,4-CHD as a hydrogen donor.

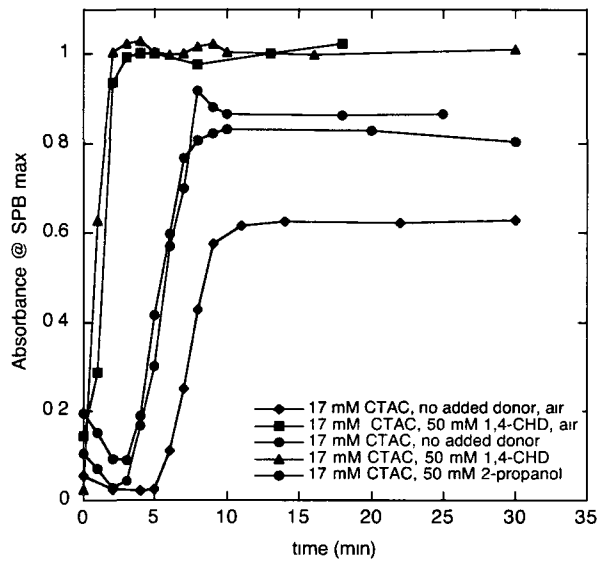

Figure 4 . 15 - Growth of AuNP monitored at the SPB maximum over time for AuNP prepared from 0.33 mM $HAuCl_4$ and 1.0 mM 1-azaxanthone in 17 mM CTAC with different hydrogen donors. Samples were deareated unless specified.

As the same observations were made with benzophenone, the peculiarity with xanthone could be simply because any reduction via the formation of superoxide occurs slower than the hydrogen abstraction from a triplet n,π* state, yet fast enough to out-perform intermolecular hydrogen atom abstraction from a π,π* state.

Hydrogen Donor	O_2	$t_{induction}$ (min)	$t_{half\text{-}max}$ (min)	Abs_{max}	λ_{max} (nm)
17 mM CTAC	No	3	6	0.86	513.4
17 mM CTAC	Yes	5	8	0.62	519.0
2-propanol	No	3	5	0.80	511.5
1,4-cyclohexadiene	No	<1	<1	1.01	519.8
1,4-cyclohexadiene	Yes	<1	<1	1.03	535.5

Table 4 . 3 - Parameters governing nanoparticle growth with 1.0 mM 1-azaxanthone in the presence 50 mM of various hydrogen donors in 17 mM CTAC.

The fast kinetics of the AZX system were further probed *via* laser flash photolysis. In the absence of a surfactant, the 1-azaxanthone triplet was easily quenched by metal center Au^{3+} through electron transfer. By exciting to the triplet state with a 355 nm NdYAG laser, quenching the signal upon addition of aliquots of Au salt allowed for the measurement of the one-electron transfer; the primary step in the photochemical reduction. Similar to studies performed with α-phenylbenzoin described in Section 3.4, both $HAuCl_4$ and AuCl were utilized as metal salts to compare rates of electron transfer. The rates of decay of AZX^3 over time at various $HAuCl_4$ concentrations are presented in Figure 4.16. The pseudo first-order approximation for the first-order rate constants, k_{obs}, were determined using a Kaleidagraph exponential decay fit, where the concentration of the quencher was assumed to significantly exceed the concentration of triplet formed.

The pseudo-first order rate constants for triplet decay were measured at different gold concentrations, and the bimolecular rate constants were derived from the slopes of the plots of (k_{obs} - k_0) versus gold concentration for the decay of the triplet signal at 600 nm following identical analysis as discussed for the determination of electron tranfer from BPK in Section 3.4. The values obtained are 1.03×10^{10} $M^{-1}s^{-1}$ for Au(III) and 2.8×10^9 $M^{-1}s^{-1}$ for Au(I) in acetonitrile, both determined at room temperature under a nitrogen atmosphere.

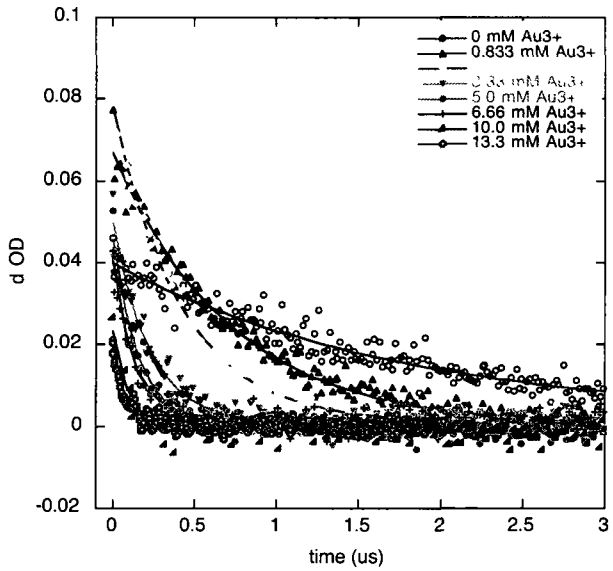

Figure 4 . 16 - Transient decay of triplet 1-azaxanthone at 600 nm upon 355 nm excitation of a deareated 4.0 mM 1-azaxanthone sample in 3:1 water:acetonitrile upon addition of $HAuCl_4$ via laser flash photolysis.

The data have been plotted as k_{obs}-k_0 because the lifetimes in the absence of quencher were different, reflecting the chromophore sensitivity to different solvents and concentrations in the two systems. These lifetimes were measured to be 5.3 μs for 0.4 mM azaxanthone in acetonitrile and 310 ns for 4 mM azaxanthone in 3:1 water:acetonitrile, where the short lifetime in the latter case was likely a reflection of the well-known rapid self-quenching of the aromatic ketone. Both values are indicative of efficient triplet quenching. The decay of 4.0 mM AZX is presented in Figure 4.16, and the normalized rates over different concentrations of gold quencher are summarized in Figure 4.17.

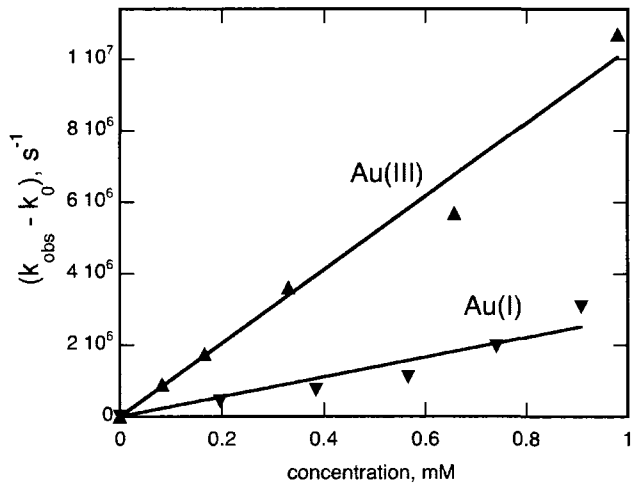

Figure 4 . 17 - Quenching of triplet 1-azaxanthone by addition of $HAuCl_4$ to a solution of 4.0 mM 1-azaxanthone in 3:1 water:acetonitrile, or 0.4 mM in AuCl to a solution of neat acetonitrile during 355 nm excitation, monitored at 600 nm.

The measured rate constants for triplet quenching indicate a faster electron transfer process by an order of magnitude in comparison with the quenching of ketyl radicals formed intramolecularly with α-phenylbenzoin. This order of magnitude difference is in agreement with other studies involving the measurement of the quenching of the benzophenone triplet and benzophenone ketyl radical.[29] Similar to the α-phenylbenzoin system, the rate constant for electron transfer for Au(III) was also measured to be approximately four times faster than electron transfer by the triplet to Au(I). It is worth emphasizing that despite the higher reduction potential for AuCl in the one electron process, the first electron transfer for $AuCl_4^-$ reduction is more facile. This LFP study signifies a novel way for determining the rate of electron transfer from a an excited triplet to give the first electron to Au^{3+}.

4.2.2.3 Thioxanthone

Another xanthone derivative was also investigated to explore its potential for reduction of gold salt *via* ketyl radical formation through hydrogen abstraction.

Thioxanthone (TXAN) exhibits strong solvent dependence with the triplet n,π* and π,π* lying close together, leaving confusion over the lowest lying excited state. A recent study found that the triplet lifetime of the substituted xanthone to be longer in hydroxylic solvents such as alcohols compared to aprotic solvents such as acetonitrile.[40] Additionally, hydrogen abstraction was observed in the alcohol solvents such as 2-propanol from the formation of ketyl radical in transient absorption spectroscopy. Ferreira *et al.* established hydrogen abstraction from the lowest lying π,π* state, but communicated the probability of a mixing of n,π* and π,π* states. Nevertheless, the intersystem crossing to an excited triplet state of thioxanthone is not a facile transition, but is allowed through vibronic coupling. The triplet energy is much lower and the single-triplet energy gap larger for thioxanthone than the other chromophores studied, making fluorescence a much more favourable transition for this substituted xanthone.[41]

In deareated solutions of 1.0 mM thioxanthone in 2-propanol with 17 mM CTAC, a small degree of nanoparticle formation was optimized, and challenging at best. Prolonged photolysis beyond 12 minutes led to further broadening of the SPB and aggregation. The absorption changes and corresponding SEM of the particles are presented in Figures 4.18 and 4.19, respectively. Within six minutes, a broad SPB had formed, yielding a pale purple/blue solution. This description is characteristic of agglomerated particles as evidenced in the corresponding SEM image. Populations of small particles, 11.8 ± 2.6 nm deposited on 55.8 ± 9.5 nm aggreagated particles are present. It is speculated that the smaller particles tether to the larger ones by the thioether of the thioxanthone, which then adhere to the larger aggregates through the carbonyl group.

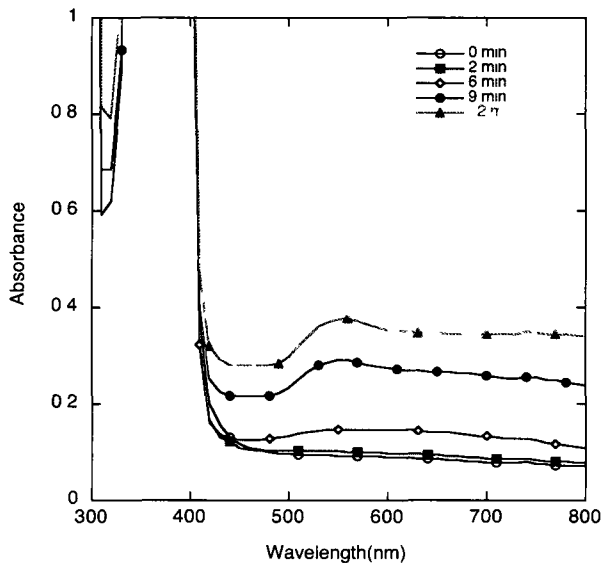

Figure 4 . 18 - Growth of AuNP prepared from 0.33 mM $HAuCl_4$, 1.0 mM thioxanthone in 17 mM CTAC in isopropanol upon 355 nm photolysis.

Other reports deny the ability of thioxanthone to abstract a hydrogen.[42] The lack of reactivity could be a consequence of the low lying triplet energy such that intersystem crossing is poor. The triplet of TXAN is significantly lower than the triplets of BP and AZX. Unlike thioxanthone, azaxanthone possesses a small S-T gap of approximately 6 kcal/mol, which accounts for the strong reactivity in the generation of ketyl radicals.[43] Importantly, a slow reduction with the inefficient generation of the ketyl radical from poor hydrogen abstraction from the π,π^* state.

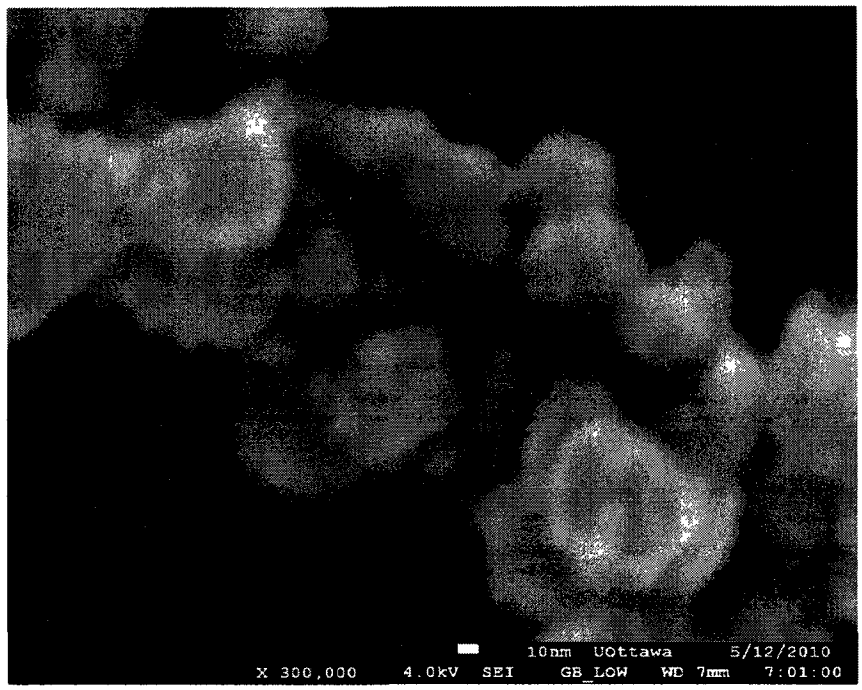

Figure 4 . 19 - SEM image of AuNP prepared from 350 nm photolysis of 0.33 mM $HAuCl_4$ 1.0 mM thioxanthone in 2-propanol with 17 mM CTAC. The scale bar represents 10 nm.

The structural differences between the different aromatic ketones highlight the ability to control the size and efficiency of nanoparticle generation by selection of a ketyl radical precursor with high hydrogen abstraction reactivity. This exploratory work with thioxanthone highlights syntheses that don't work well, underlining the importance of choosing chromophores with 1) small S-T energy gaps for facile intersystem crossing, and 2) chromophores with stable low-lying n,π* states.

Ketone	E^0_{red} (V) vs. SCE
Xanthone	-1.65 [42]
1-Azaxanthone	-1.48 [44]
Benzophenone	-1.72 [42]
Thioxanthone	-1.62 [42]

Table 4 . 4 - Reduction potentials for the studied aromatic ketones in acetonitrile.

The reduction potentials presented in Table 4.4 also contribute to the ease of nanoparticle generation when using the same hydrogen donor. (A greater comparison of all of the redox couples studied in this research is further described in Table 7.3.) For instance, with CTAC as a hydrogen donor the order the rate of particle growth is AZX > BP >> XAN > TXAN. On the other hand, the reactivity with 1,4-CHD as a donor is essentially AZX~XAN >> BP, where TXAN was neglected from the comparison. Aside from AZX, this order correlates with the more positive reduction potentials for the chromophores. The reduction potential for $AuCl_4^-$ is +0.99 V vs NHE, implying that the reactions are very thermodynamically favourable. If this system was solely under thermodynamic control, the yield of particles would be correlated with the relative order of reduction potentials. The feasibility of hydrogen atom transfer, however, is dependent on the energy of the $^3n,\pi^*$ state and its proximity to the $^3\pi,\pi^*$, as well as the difference in energy from the singlet state for efficient intersystem crossing.

4.3 The Peculiarity of 1,4-Cyclohexadiene

1,4-CHD is a very strong hydrogen donor and has indicated fast reactivity, but the peculiarity in the order of NP growth described in the previous section, as well as the size of the nanoparticles generated has led to further studies with 1,4-cyclohexadiene. Control experiments were conducted in the presence of 1,4-CHD and in the absence of a ketone, which revealed, to our surprise, the formation of AuNP after approximately twenty minutes with a higher absorption intensity and greater redshift, as compared to reactions with a ketone. No changes were observed when identical samples were left in dark conditions for an equivalent period of time. These results suggest that the formation of the cyclohexadienyl radical also plays a role in the reduction of metal salts. As many ketone triplets or their ketyl radicals can be quenched by molecular oxygen, these studies were

performed with deareated samples. Nevertheless, when the synthesis was performed under air, a similar relative reactivity among the three chromophores was still observed, but with longer induction periods. A comparison of the SPB generated with each chromophore is shown in Figure 4.20, and the kinetics of their generation under deareated conditions, for example, are highlighted in Figure 4.21.

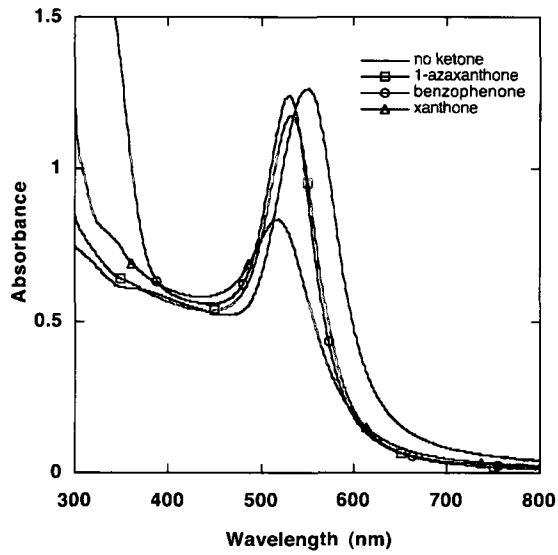

Figure 4 . 20 - Absorption spectrum comparing the SPB of AuNP prepared from 1.0 mM of various ketones with 50 mM 1,4-CHD as a hydrogen donor in deareated 17 mM CTAC from 30 minutes UVA photolyisis.

The data in Figure 4.21 shows that all of the reactions where 1,4-CHD is present with ketones led to faster AuNP generation, as has been suggested earlier in individual analyses of ketones. The order or reactivity as mentioned above, AZX~XAN > BP > 1,4-CHD alone, no longer correlates with hydrogen abstraction ability as do the results in the absence of a hydrogen donor.

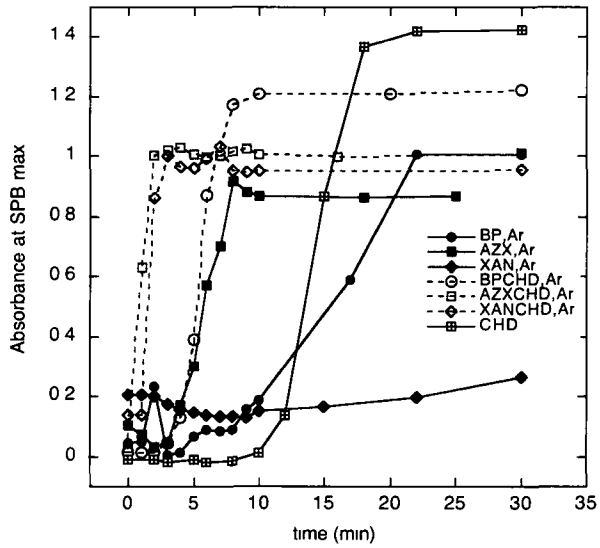

Figure 4 . 21 - Growth of AuNP over time for different 1.0 mM aromatic ketones in the presence of 50 mM 1,4-CHD under deareated conditions with 30 min UVA photolysis.

The most interesting results appear to be the generation of nanoparticles in the absence of a ketone. Several control reactions were performed, where photolysis of CTAC alone in the presence of $HAuCl_4$ alone did not lead to nanoparticle formation within 30 minutes UVA. Prolonged photolysis over 5-6 hours, however, did lead to a pale pink solution as mentioned in Chapter 3. 1,4-CHD has limited solubility in aqueous solutions, but photolysis of $HAuCl_4$ with 50 mM 1,4-CHD in water alone did generate an unstable, blue solution indicative of $HAuCl_4$ reduction. The absorption spectrum of the sample is presented in Figure 4.22.

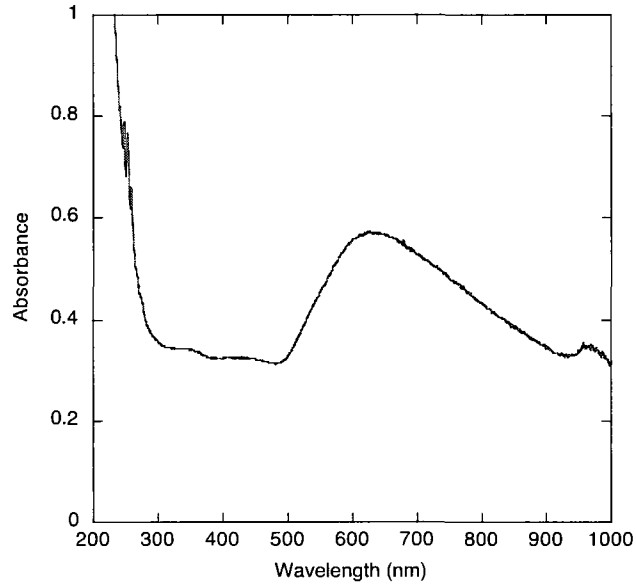

Figure 4 . 22 - Synthesis of AuNP from 0.33 mM $HAuCl_4$ and 50 mM 1,4-CHD in water under aerated conditions upon 30 minutes 350 nm irradiation.

Furthermore, as 1,4-CHD contains 0.1% hydroquinone as a stabilizer, 1,4-CHD was passed through a silica plug prior to repeating the experiment. In the absence of stabilizer, $HAuCl_4$ reduction proceeded with a stronger plasmon band. SEM images of the nanoparticles prepared with 1,4-CHD are presented in Figure 4.23, where the image on the left represents particles that were synthesized with 17 mM CTAC, while the particles on the right resulted from aggregates in water, largely due to the very low solubility of the cyclic diene in the solvent. There is almost a 10X difference in the magnification between the two images, but it is noted that particles prepared in the 1,4-CHD/CTAC system appeared to be cubic or dodecahedral in geometry, likely owing to the surface passivation of the surfactant. TEM Images of AuNP prepared from benzophenone are highlighted in Figure 4.5 also show a somewhat dodecahedral character, although two dimensional TEM images are less revealing in this domain.

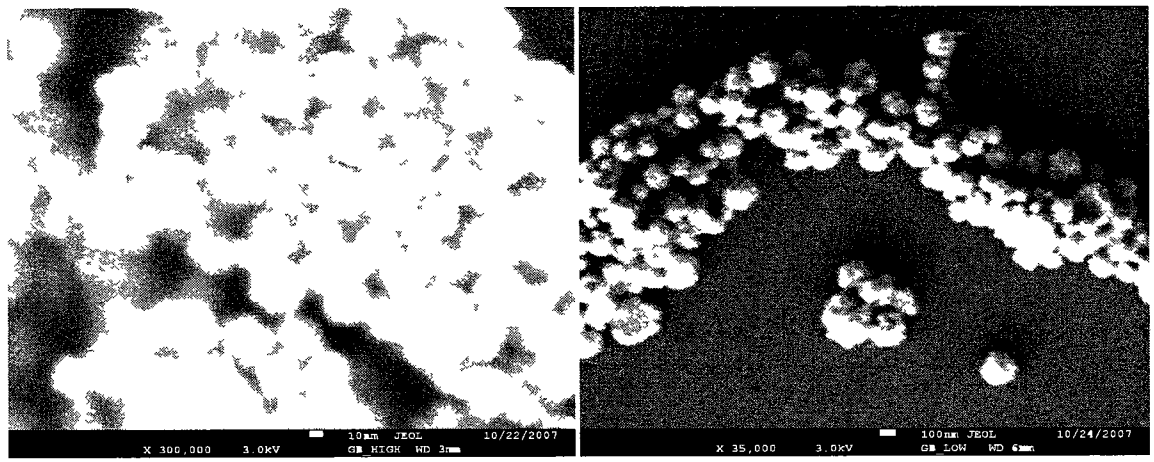

Figure 4 . 23 - SEM images of AuNP prepared from 0.33 mM $HAuCl_4$ in the presence of 50 mM 1,4-CHD in (left) 17 mM CTAC, and (right) water. The scale bars represent 10 nm and 100 nm for the images on the left and right, respectively.

One potential explanation was the possibility of a chlorine atom from $HAuCl_4$ reacting under photolysis to abstract a hydrogen from 1,4-CHD. An investigation was undertaken to see if another hydrogen donor could be probed for abstraction by the Cl atom of $HAuCl_4$. In this case, hydrogen peroxide was used as a hydrogen donor, with this work being presented in the following chapter.

4.4 Summary

The generation of gold nanoparticles from ketones through the bimolecular hydrogen atom abstraction mechanism has been explored with a variety of different hydrogen donors and hydrogen acceptors. In general, synthesis of metal nanoparticles is most effective using aromatic chromophore ketones with low lying triplet excited states possessing n,π^* character, as they are more reactive in hydrogen abstraction. Chromophores with π,π^* character, on the other hand, led to slow AuNP formation. In addition to the bonding character of the excited state, the triplet needs to be low enough for sensitizaion, yet high enough for intersystem crossing. This was the case when thioxanthone was used as a chromophore.

Optimal synthetic strategies were devised by minimizing quenching of the triplet chromophores *via* minimizing oxygen in sample preparation, as well as synthesizing NP in micelles. Donors synonymous with fast rates of hydrogen transfer displayed similar reactivity in the generation of AuNP, however several factors such as metal salt disproportionation and particle stability in the presence of stabilizers also play a role in determining successful synthesis. Finally, the role of a strong hydrogen donor, 1,4-CHD, was carefully analyzed to reveal additional pathways to metal nanoparticle synthesis.

4.5 Appendix

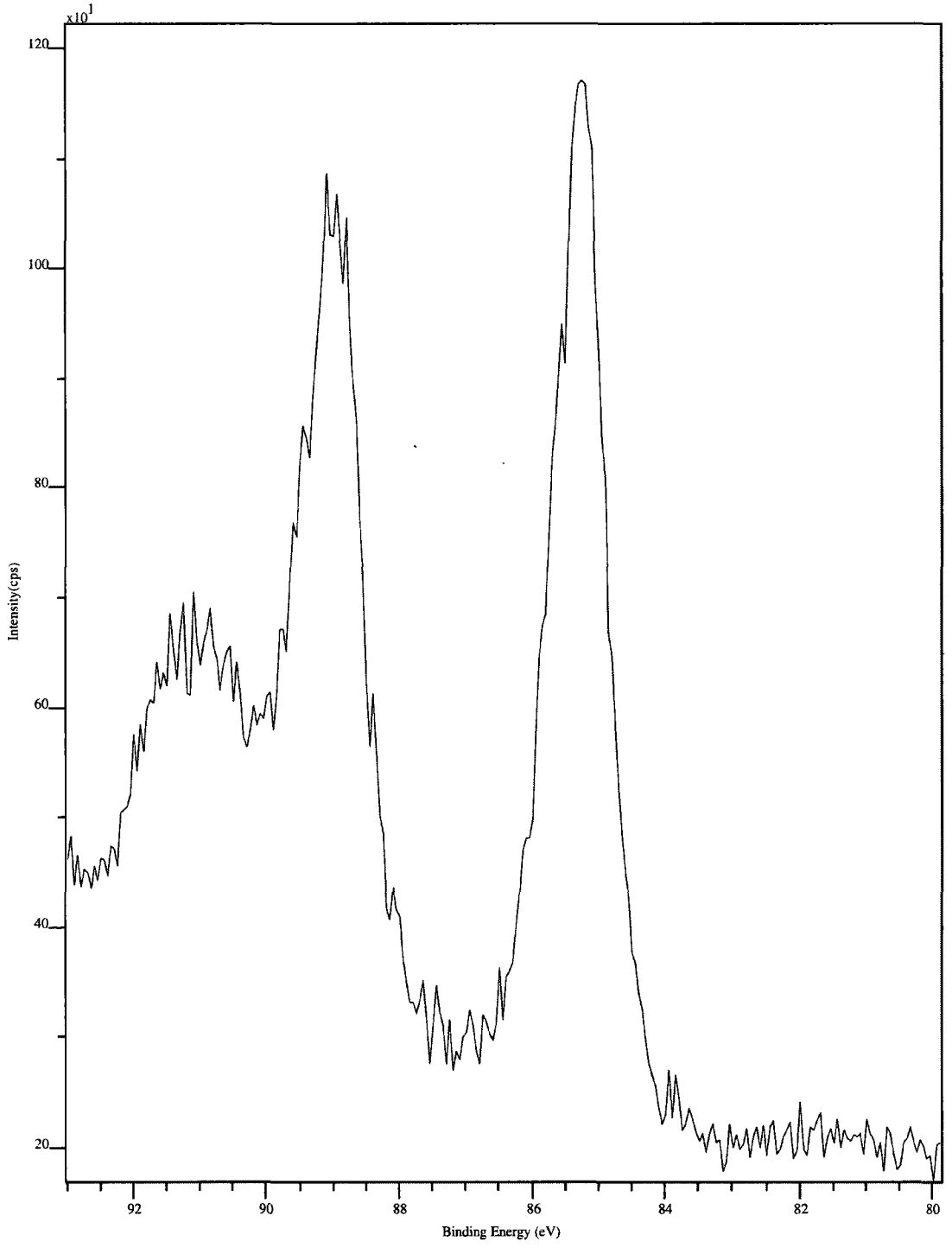

Figure 4 . 24 - XPS spectrum of the Au 4f peaks from AuNP prepared from 1.0 mM 1-azaxanthone in 17 mM CTAC.

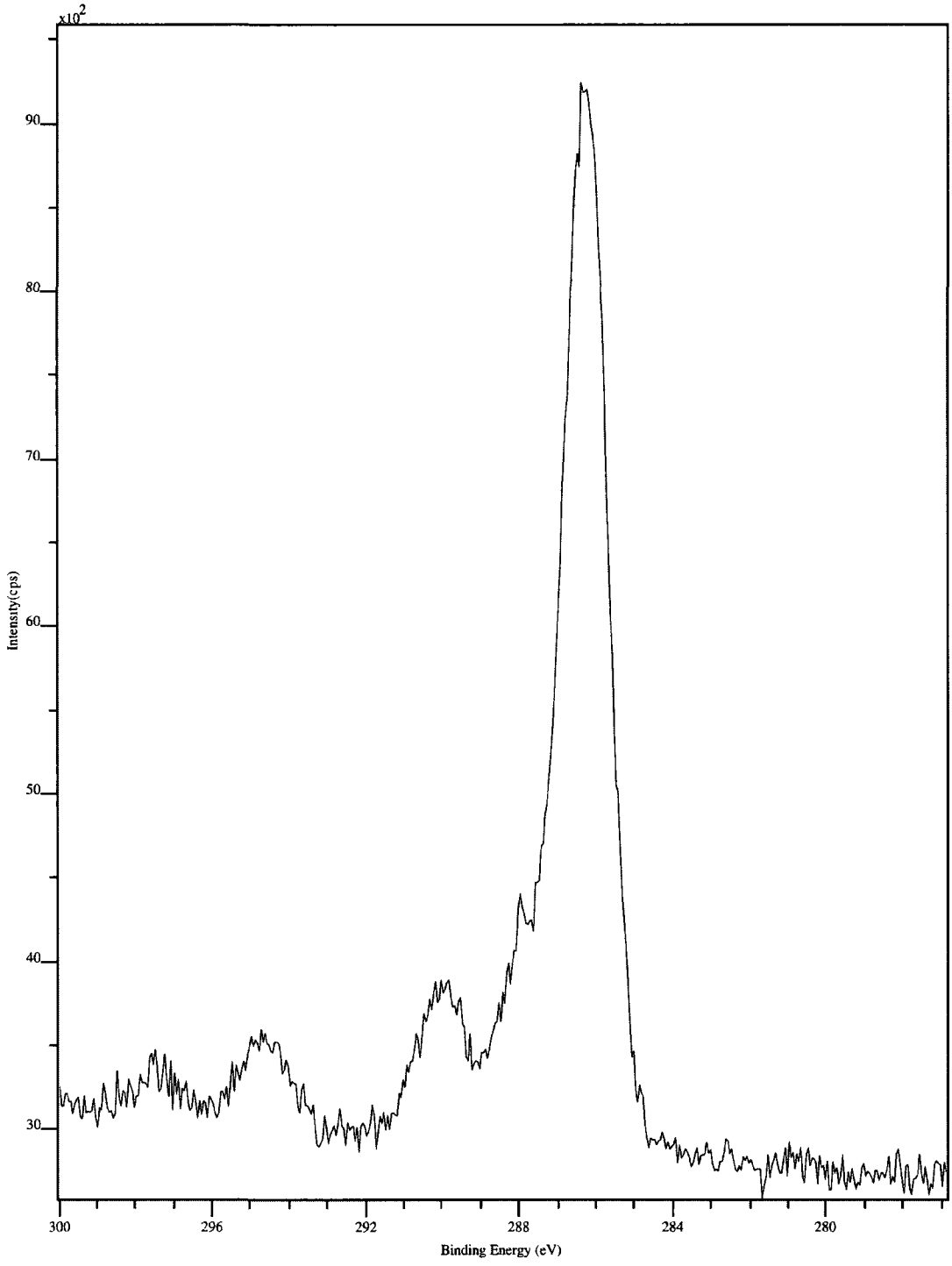

Figure 4 . 25 - XPS spectrum of the 1s peak of carbon from the AuNP sample prepared from 1.0 mM 1-azaxanthone in 17 mM CTAC. This peak is used as a reference for the XPS peak of the Au 4f peak.

4.6 References

1. Eustis, S., Krylova, G., Eremenko, A., Smirnova, N., Schill, A., El-Sayed, M., Growth and Fragmentation of Silver Nanoparticles in Their Synthesis with fs Laser and CW light by Photo-sensitization with Benzophenone. *Photochem. Photobiol. Sci.* **2005,** *4*, 154-159.

2. Eustis, S., Hsu, S.-Y., El-Sayed, M. A., Gold Nanoparticle Formation from Photochemical Reduction of Au3+ by Continuous Excitation in Colloidal Solutions. A Proposed Molecular Mechanism. *J. Phys. Chem. B* **2005,** *109*, 4811-4815.

3. Eustis, S., El-Sayed, M. A., Molecular Mechanism of the Photochemical Generation of Gold Nanoparticles in Ethylene Glycol: Support for the Disproportionation Mechanism. *J. Photochem. Photobiol. B.* **2006,** *110*, 14014-14019.

4. Korchev, A. S., Bozack, M. J., Slaten, B. L., Mills, G., Polymer-Initiated Photogeneration of Silver Nanoparticles in SPEEK/PVA Films: Direct Metal Photopatterning. *J. Am. Chem. Soc.* **2003,** *126*, 10-11.

5. Sakamoto, M., Tachikawa, T., Fujistuka, M., Majima, T., Two-color Two-laser Fabrication of Gold Nanoparticles in PVA Film. *Chem. Phys. Lett.* **2006,** *420*, 90-94.

6. Kapoor, S., Mukherjee, T., Photochemical Formation of Copper Nanoparticles in Poly(N-vinylpyrrolidone). *Chem. Phys. Lett.* **2003,** *370*, 83-87.

7. Scaiano, J. C., Intermolecular Photoreductions of Ketones. *J. Photochem.* **1973/74,** *2*, 81.

8. Turro, N. J.; Ramamurthy, V.; Scaiano, J. C., *Modern Molecular Photochemistry of Organic Molecules*. University Science Publishers: New York, N.Y., 2010; p 1100.

9. Wagner, P. J.; Truman, R. J.; Scaiano, J. C., Substituent Effects on Hydrogen Abstraction by Phenyl Ketone Triplets. *J. Am. Chem. Soc.* **1985,** *107* (24), 7093-7097.

10. Das, P. K.; Encinas, M. V.; Steenken, S.; Scaiano, J. C., Reaction of *tert*-Butoxy Radicals with Phenols. Comparison with the Reactions of Carbonyl Triplets. *J. Am. Chem. Soc.* **1981,** *103*, 4162-4166.

11. Scaiano, J. C., Aliaga, C., Maguire, S., Wong, D., Magnetic Field Control of Photoinduced Silver Nanoparticle Formation. *J. Phys. Chem. B.* **2006,** *110*, 12856-12859.

12. Marin, M. L., McGilvray, K. L., Scaiano, J. C., Photochemical Strategies for the Synthesis of Gold Nanoparticles from Au(III) and Au(I) Using Photoinduced Free Radical Generation. *J. Am. Chem. Soc.* **2008,** *130*, 16572-16585.

13. Gachard, E., Remita, H., Khatouri, J., Keita, B., Nadjo, L., Belloni, J., Radiation-induced and Chemical Formation of Gold Clusters. *New. J. Chem.* **1998**, 1257-1265.

14. Martinez, L. J.; Scaiano, J. C., The Photochemistry of 1-Azaxanthone in Aqueous Solutions and in Micellar Environments. *J. Phys. Chem. A* **1999,** *103* (1), 203-208.

15. Scaiano, J. C.; Weldon, D.; Pliva, C. N.; Martínez, L. J., Photochemistry and Photophysics of 1-Azaxanthone in Organic Solvents. *J. Phys. Chem.: A.* **1998,** *102* (35), 6898-6903.

16. Scaiano, J. C., Does Intersystem Crossing in Triplet Biradicals Generate Singlets with Conformational Memory? *Tetrahedron* **1982,** *38* (6), 819-824.

17. Yonezawa, Y., Sato, T., Kuroda, S., Photochemical Formation of Colloidal Silver: Peptizing Action of Acetone Ketyl Radical. *J. Chem. Soc. Faraday Trans.* **1991,** *87* (12), 1905-1910.

18. Kim, F., Song, J. H., Yang, P., Photochemical Synthesis of Gold Nanorods. *J. Am. Chem. Soc.* **2002,** *124*, 14316-14317.

19. Placido, T., Comparelli, R., Giannici, F., Cozzoli, P. D., Capatani, G., Striccoli, M., Agostano, A., Curri, M. L., Photochemical Synthesis of Water-Soluble Gold Nanorods: The Role of Silver in Assisting Anistotropic Growth. *Chem. Mater.* **2009,** *21*, 4192-4202.

20. Miranda, O. R., Ahmadi, T.S., Effects of Intensity and Energy of CW UV Light on the Growth of Gold Nanorods. *J. Phys. Chem. B.* **2005,** *109*, 15724-15734.

21. Dong, S.-A.; Zhou, S.-P., Photochemical Synthesis of Colloidal Gold Nanoparticles. *Mat. Sci. Eng. B* **2007,** *140*, 153-159.

22. Dong, S.; Tang, C.; Zhou, H.; Zhao, H., Photochemical Synthesis of Gold Nanoparticles by the Sunlight Radiation using a Seeding Approach. *Gold Bull.* **2004,** *37* (3,4), 187-195.

23. Leigh, W. J., Scaiano, J. C., Photochemistry of Acetone in Surfactant Solutions. *J. Am .Chem. Soc.* **1983,** *105* (17), 5652.

24. Vogler, A., Kunkely, H., Photoreactivity of Gold Complexes. *Coordination Chemistry Reviews* **2001,** *219*, 489-507.

25. Kapoor, S., Preparation, Characterization, and Surface Modification of Silver Particles. *Langmuir* **1998,** *14*, 1021-1025.

26. Eustis, S., Krylova, G., Smirnova, N., Eremenko, A., Tabor, C., Huang, W., El-Sayed, M. A., Using Silica Films and Powders Modified with Benzophenone to Photoreduce Silver Nanoparticles. *J. Photochem. Photobiol. A* **2006,** *181*, 385-393.

27. Kapoor, S., Palit, D. K., Mukherjee, T., Preparation, Characterization and Surface Modification of Cu Metal Nanoparticles. *Chem. Phys. Lett.* **2002,** *355*, 383-387.

28. Scaiano, J. C.; Abuin, E. B.; Stewart, L. C., Photochemistry of Benzophenone in Micelles. Formation and Decay of Radical Pairs. *J. Am. Chem. Soc.* **1982,** *104* (21), 5673-5679.

29. Kometani, N., Doi, H., Asami, K., Yonezawa, Y., Laser Flash Photolysis Study of the Photochemical Formation of Colloidal Ag Nanoparticles in the Presence of Benzophenone. *Phys. Chem. Chem. Phys.* **2002,** *4*, 5142-5147.

30. Maguire, S. Magnetic Field Control of Silver Nanoparticle Formation. Master, University of Ottawa, Ottawa, 2006.

31. Paul, H., Small, R. D., Scaiano, J. C., Hydrogen Abstraction by tert-Butoxy Radicals. A Laser Photolysis and Electron Spin Resonance Study. *J. Am .Chem. Soc.* **1978,** *100*, 4520-4527.

32. Griller, D., Howard, J. A., Marriot, P. R., Scaiano, J. C., Absolute Rate Constants for the Reactions of tert-Butoxyl, tert-butylperoxyl, and Benzophenone Triplet with Amines; The Importance of a Stereospecific Effect. *J. Am .Chem. Soc.* **1981,** *103*, 619-623.

33. Arimitsu, S., Laser Flash Photolysis Studies on Quenching Processes of Triplet Benzophenone by Amines in Fluid Solution. *J. Phys. Chem.* **1975,** *79*, 1255-1259.

34. Cohen, S. G., Chao, H. M., Photoreduction of Aromatic Ketones by Amines. Studies of Quantum Yields and Mechanism. *J. Am .Chem. Soc.* **1968,** *90*, 165-173.

35. Cohen, P., A., Parsons, G., Photoreduction by Amines. *Chem. Rev.* **1973,** *73* (141-161).

36. Lissi, E. A., Encinas, M. V., *Representative Kinetic Behaviour of Selected Reaction Intermediates: Triplet States* CRC Press: Boca Raton, 1989; Vol. II, p 481.

37. Scaiano, J. C., Solvent Effects in the Photochemistry of Xanthone. *J. Am. Chem. Soc.* **1980,** *102* (26), 7747-7753.

38. Mohtat, N.; Cozens, F. L.; Scaiano, J. C., Multistage Exit of Excited Xanthone from Micelles. *J. Phys. Chem.: B* **1998,** *102* (39), 7557-7562.

39. Bond, G. C., Sermon, P. A., Gold Catalysis for Olefin Hydrogenations. Transmutation of Catalytic Properties. *Gold Bull.* **1973,** *6*, 102-105.

40. Ferreira, G. C., Schmitt, C. C., Neumann, M. G., Dependence of the Thioxanthone Triplet-Triplet Absorption Spectrum with Solvent Polarity and Aromatic Ring Substitution. *J. Braz. Chem. Soc.* **2006,** *17* (5), 905-909.

41. Lai, T., Lim, E. C., Time-Resolved Fluorescence Spectra and Energy-Resolved Decays of Vibronically Coupled Electronic States: Effects of Solvent Relaxation of the Excited-State Dynamics of Thioxanthone. *Chem. Phys. Lett.* **1981,** *84* (2), 303-307.

42. Timpe, H.-J., Kronfeld, K.-P., Light-induced Polymer and Polymerization Reactions XXXIII: Direct Photoinitiation of Methyl Methacrylate Polymerization by Excited States of Ketones. *J. Photochem. Photobiol. A.* **1989,** *46*, 253-267.

43. Corrent, S., Martinez, L. J., Scaiano, J. C., Intrazeolite Photochemistry. Photochemistry of 1-Azaxanthone in Zeolites in the Presence of Hydrogen Donors, Electron Donors, and Energy Acceptors. *J. Phys. Chem. B.* **1999,** *103*, 8097-8103.

44. Coenjarts, C., Scaiano, J. C., Reaction Pathways Involved in Quenching of the Photoactivated Aromatic Ketones Xanthone and 1-Azaxanthone by Polyalkylbenzenes. *J. Am .Chem. Soc.* **2000,** *122*, 3635-3641.

Chapter 5

Nanoparticle Synthesis via Photoexcitation of $HAuCl_4$

5.1 Introduction

Investigations discussed up to this point have dealt with the synthesis of metal nanoparticles through a photochemical approach to generating reducing transients from organic chromophores. The work presented in this chapter uncovers the capability of a photochemical reduction via the photophysics of inorganic metal complexes, with metal chloride salts in particular.

The spectroscopic properties of several gold complexes have been studied extensively, and the absorption properties of $HAuCl_4$ at 323 nm (ε = 5800 $M^{-1}cm^{-1}$) have been attributed to the ligand-to-metal charge transfer (LMCT).[1] In aqueous media, the acid complex dissociates to a proton and the square planar complex. The Au-Cl bond dissociation energy has been reported as 60.3 kcal/mol for $AuCl_4^-$, and 53.7 kcal/mol for $Au(H_2O)Cl_3$.[2] As outlined in previous chapters, a one electron reducing agent such as a ketyl radical or a α-aminoalkyl radical initially reduces Au^{3+} to Au^{2+}, but the complexation of the metal species is often overlooked. In other words, while the fate of the chloride ions are known to dissociate in thermal reactions, excitation of the square planar complex to its excited state leads to an assisted reduction in the presence of a reducing agent through hemolytic cleavage of the Au-Cl bond. The mechanism for photochemical reduction is thought to occur through the following pathway, as outlined in Scheme 5.1.

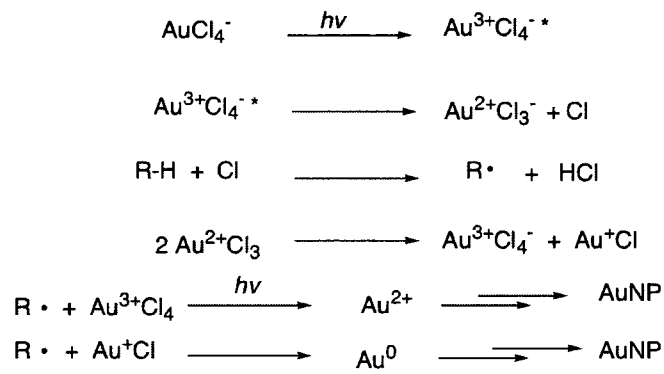

Scheme 5 . 1 - Photochemical reduction of $HAuCl_4$

Chlorine atom chemistry is known for its powerful additions to olefins, electron transfer and hydrogen abstraction reactivity.[3-7] In well-cited literature, high energy direct photolysis of the salt, pulsed radiolysis in a microemulsion, as well as pulsed flash photolysis in a methanol solution have all resulted in $AuCl_4^-$ reduction to generate colloidal gold.[8, 9] Solvated electrons reacted with Au(III) to reduce it to the unstable Au(II), as well as dissociate H_2O to form H• and •OH. The latter abstracted a hydrogen from methanol to form $•CH_2OH$; a reducing agent for Au(III). Interestingly, the reactivity of the Cl atom towards hydrogen abstraction was overlooked.

The chlorine atom, in turn, is a powerful hydrogen abstractor from various donors and has been thoroughly studied in physical organic chemistry with fast time-resolved techniques.[5-7] Its ability to abstract hydrogen from alcohols such as methanol is very efficient with rate constants for the α-hydrogen abstraction reported as 5.2×10^9 $M^{-1}s^{-1}$ in dichloromethane, which was both a solvent and source of Cl atoms via two photon photolysis. In the same report, rate constants for hydrogen abstraction from a variety of alkanes and cycloalkanes were measured to range between $9.3 - 11.8 \times 10^9$ $M^{-1}s^{-1}$.[6] The results confirmed that chlorine preferred to abstract from the β-position in alcohols and acids, unlike hydroxyl radicals, which were more reactive towards α-abstraction.

In this chapter, the reactivity of the chlorine atom is considered in the reduction for the generation of gold nanoparticles. These investigations were prompted from observation of the reduction of $AuCl_4^-$ with 1,4-CHD in the absence of any additional hydrogen atom abstractor such as the excited states of a ketone, as previously discussed in Section 4.3. Additionally, we have synthesized metal nanoparticles by exploiting the chlorine atom reactivity with common organic hydrogen donors wherein hydrogen abstraction leads to the formation of free radical reducing agents. The synthesis of AuNP from hydrogen peroxide, tetrahydrofuran, and pyrrolidine will be discussed.

5.2 Hydrogen Abstraction from Hydrogen Peroxide

A novel method for the synthesis of gold nanoparticles is presented using a simple, quick and clean method from the photolysis of hydrogen peroxide and tetrachloroauric acid, where the photochemistry of $HAuCl_4$ has been utilized to generate spherical and anisotropic gold nanomaterials. Upon absorption of UV light, the excited state of the salt, $AuCl_4^{-*}$, dissociates homolytically under aqueous conditions to generate $AuCl_3^-$ and liberate Cl.

Irradiation of hydrogen peroxide in aqueous solutions results in cleavage of the weak O-O bond to yield two hydroxyl radicals. The reactive, unstable species can react with another molecule of H_2O_2 via hydrogen abstraction to generate H_2O and a HOO•.[10] The hydroperoxyl radical or its alkaline analogue superoxide, $O_2^{\bullet-}$, operate as efficient one electron reducing agents. HOO•, a weak acid, and its weak conjugate base, $O_2^{\bullet-}$, exist in a pH-dependent aqueous equilibrium.

$$HOO\bullet \rightleftharpoons H^+ + O_2^{\bullet-} \qquad pk_a = 4.69$$

Either species can serve as a reductant or oxidant. The standard reduction potentials for these species in water have been reported to be

$E^0(O_2/H^+/HOO\bullet)$= -0.05 V (vs. NHE; O_2 at 1 atm) and $E^0(O_2/O_2^{\bullet-})$= - 0.33 V (vs. NHE; O_2 at 1 atm).[11] These measurements underline superoxide as a stronger reducing agent than the hydroperoxyl radical. All together, both species possess less negative (weaker) reduction potentials relative to those of ketyl radicals, where $E^0((CH_3)_2CO/(CH_3)_2COH\bullet)$ = -1.8 V (vs. NHE) for the 2-hydroxy-2-propyl radical.[9]

Under the given reaction conditions in aqueous $HAuCl_4$ at pH 3.4, HOO• will be the dominant species in solution. Both HOO• and $O_2^{\bullet-}$ absorb in the UV; HOO• with λ_{max}= 230 nm (ε= 1400 $M^{-1}cm^{-1}$), and $O_2^{\bullet-}$ with λ_{max}= 244 nm (ε= 2380 $M^{-1}cm^{-1}$). Both of these peaks, however, are screened by the LMCT of $AuCl_4^-$ when it is present in solution. $AuCl_4^-$ also has a band at 225 nm, (ε= 6.05 x 10^5 $M^{-1}cm^{-1}$) corresponding to another LMCT.[12] Therefore, the absorbances for H_2O_2 are at higher energy with lower extinction coefficients, and UVA photolysis alone will not excite H_2O_2 in the presence of the gold salt.

Excitation of the tail of the LMCT band of $AuCl_4^-$ positioned at 320 nm via UVA photolysis promotes the metal complex to an excited state wherein facile dissociation of a chlorine atom can occur, leading to further reaction when in the presence of a strong hydrogen donor. Several kinetic studies have revealed the ease of hydrogen abstraction from the chlorine radical with rates at diffusion control, particularly in aqueous systems.[3-5]

Investigations by Gilbert *et al.* revealed the high reactivity and low selectivity of the chlorine atom in hydrogen abstraction reactions, with rate constants around 1.5 x 10^9 $M^{-1}s^{-1}$.[5] In the presence of ethanoic acid or *tert*-BuOH, Cl prefered to attack the O-H bond rather than the C-H bond, whereas reactive hydroxyl radicals were more selective and attacked C-H bonds. The preference for O-H bond scission was attributed to polar effects with an earlier transition state for the reaction with a presumed electron transfer pathway. Selective O-H homolytic cleavage was also documented by Litorja *et al.*, with hydrogen peroxide as a substrate. The bond energy of the H-OOH bond has been reported to be 87.0 kcal/mol, with HOO• generation via hydrogen abstraction from halide atoms.[10]

The hydroperoxyl radical can be produced through direct photolysis of the weak HO-OH bond to generate two hydroxyl radicals, yet the masked absorbance by the LMCT of the gold salt likely minimizes this process, as outlined in Scheme 5.2.

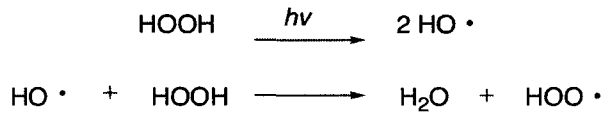

Scheme 5 . 2 - UV photolysis of hydrogen peroxide

Alternatively, Cl can form upon photoexcitation of $HAuCl_4$ and also abstract a hydrogen atom from H_2O_2 to form the hydroperoxyl reducing radical species. The multiple steps to AuNP synthesis occurs through a one electron reduction as well as by disproportion pathways. The processes are detailed in Scheme 5.3.

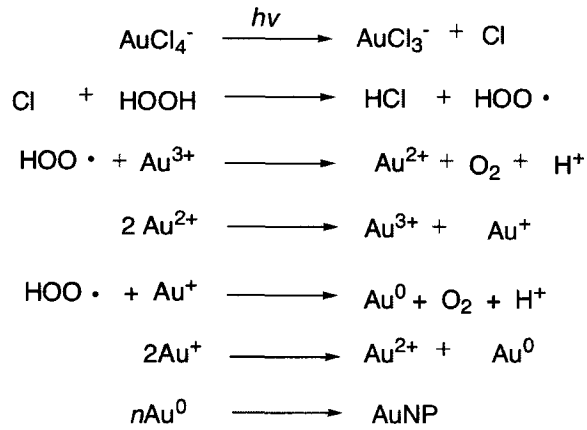

Scheme 5 . 3 - Proposed mechanism for the generation of AuNP by photolysis of hydrogen peroxide.

Nanoparticles were prepared by combining an aqueous solution of H_2O_2 and $HAuCl_4$ in a 1x1 cm quartz cuvette and irradiated for 30 minutes UVA photolysis in a photoreactor equipped with 14 lamps. A concentration study was performed to

optimize the synthesis of AuNP with this approach, and it was found that a concentration of 3.0 mM H_2O_2 was ideal in the presence of 0.33 mM $HAuCl_4$, at a ratio of 10:1 reducing agent: Au^{3+}. The spectra for the study are presented in Figure 5.1. At lower ratios, the SPB bandwidth was wider and less intense. The absorption at longer wavelength increased with H_2O_2, and is attributed to the longitudinal plasmon of anisotropic particles such as hexagonal and triangular prisms in addition to the growth of spherical particles. Both of these morphologies are identified in the SEM image in Figure 5.4.

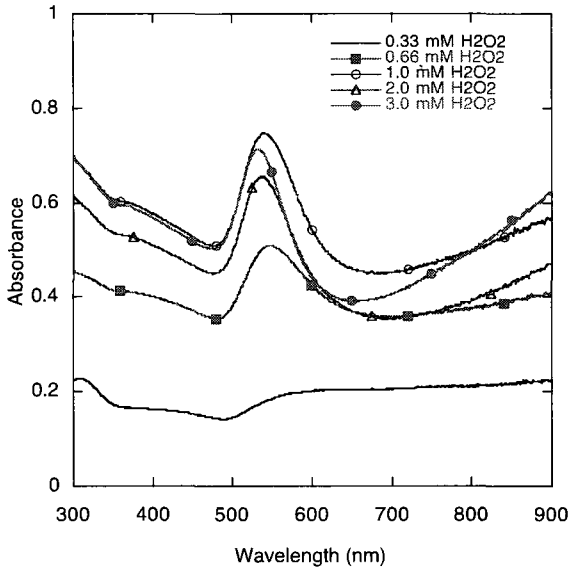

Figure 5 . 1 - Absorption spectra of AuNP prepared from 0.33 mM $HAuCl_4$ and various concentrations of H_2O_2 in air-saturated aqueous solutions following 30 minutes UVA photolysis.

One immediate observation is the difference in the colour and consequentially the UV-Vis absorption spectrum between AuNP prepared in this fashion and nanoparticles prepared from ketyl radicals. The colloidal solution displays a red/pink colour with a iridescent orange scatter, where the SPB is redshifted to approximately 530 nm with an increase in scatter at longer wavelength around 800 nm and into the NIR. This scatter can be present to different degrees and is not quantifiably

reproducible from samle to sample; a common challenge facing nanoparticle synthesis with weaker reducing agents.[13] Images of AuNP prepared under different conditions are included in Figure 5.2 to identify the scatter visible to the eye. The three vials contain AuNP that were prepared with 0.33 mM $HAuCl_4$ and at a low concentration of 0.33 mM H_2O_2, at 3.0 mM H_2O_2, and with 1.0 mM I-2959 for comparison, where the last sample is void of scatter.

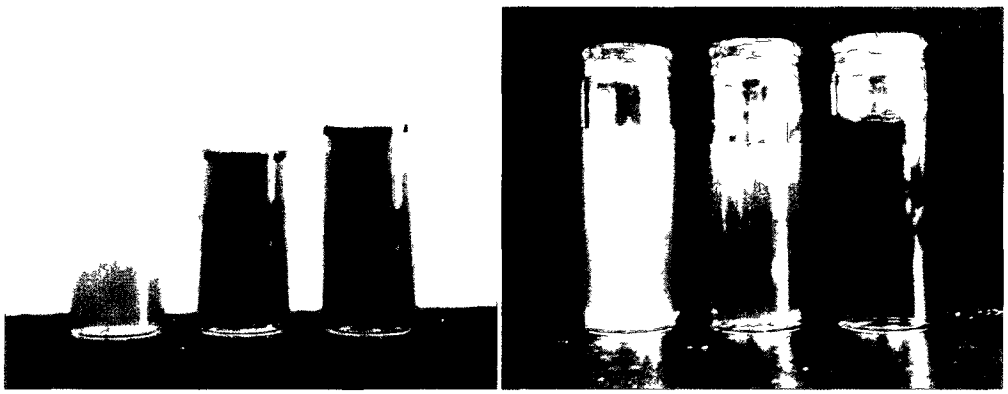

Figure 5 . 2 - Images of the turbidity of AuNP samples visualized with different backgrounds. Vials contain AuNP prepared from 0.33 mM $HAuCl_4$ with (left) 0.33 mM H_2O_2, (center) 3.0 mM H_2O_2 and (right) 1.0 mM I-2959 after 30 min UVA photolysis.

One advantage to this synthesis is the absorption at higher energy wavelength is observable, unlike the chemistry involving organic photoinitiators with the strong absorption of the ketones and photoproducts behaving as a UV screen. As such, the absorption band at 290 nm is attributed to the $AuCl_4^-$ species and its decay was monitored with time upon excitation. Samples were synthesized under both aerated and deareated conditions, and the growth of AuNP over time in both environments are presented in Figure 5.3.

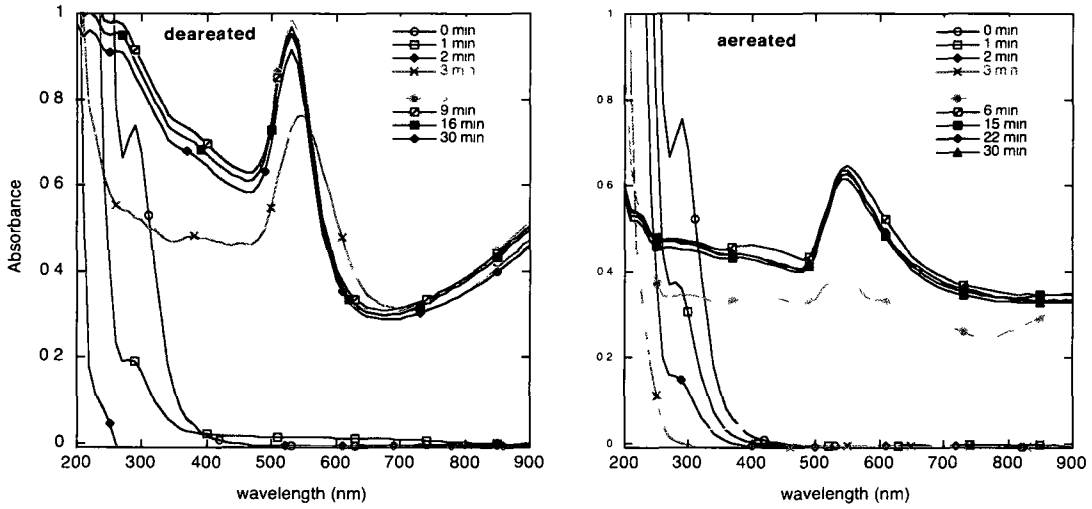

Figure 5 . 3 - Growth of AuNP over time prepared from UVA photolysis of a deareated solution (left) and air-saturated solution (right) of 0.33 mM $HAuCl_4$ and 3.0 mM H_2O_2.

In the deareated sample, the LMCT band disappeared in less than two minutes of irradiation, while the aerated sample required three minutes. The observed time between the complete loss of $AuCl_4^-$ and the commencement of observable AuNP formation is indicated to take less than 60 s, where the growth rate appeared to be greater for the deareated sample relative to the ambient sample.

Importantly, the procedure for purging samples necessitated modification from routine spectroscopic assays, as purging an aqueous solution containing $HAuCl_4$ and H_2O_2 with a stainless steel needle occasionally led to the formation of a pale blue/purple solution prior to any photolysis and in the absence of light. This reduction is attributed to the interaction of Fe^{2+} from the stainless steel, which can reduce Au^{3+}. This was later verified by addition of 0.1 mM $FeSO_4$ to a 0.33 mM $HAuCl_4$/3.0 mM H_2O_2 sample, where the solution transformed to a turbid pink/orange colour. Further purging was modified by adapting the stainless steel needle with a PTFE sleeve, such that only the Teflon tubing was in contact with the solution.

Air or argon atmospheres yielded similar absorbance spectra, but with different absorption intensities. A SEM investigation revealed essentially similar particles

with two distinct size populations; a mixture of prisms 237.9 ± 93.7 nm in diameter along with a larger abundance of smaller 48.9 ± 15.2 nm particles. Conveniently, the two sizes can be easily separated by centrifugation or filtration. Representative images of particles prepared under aerated and deareated conditions are shown in Figure 5.4 left and right, respectively.

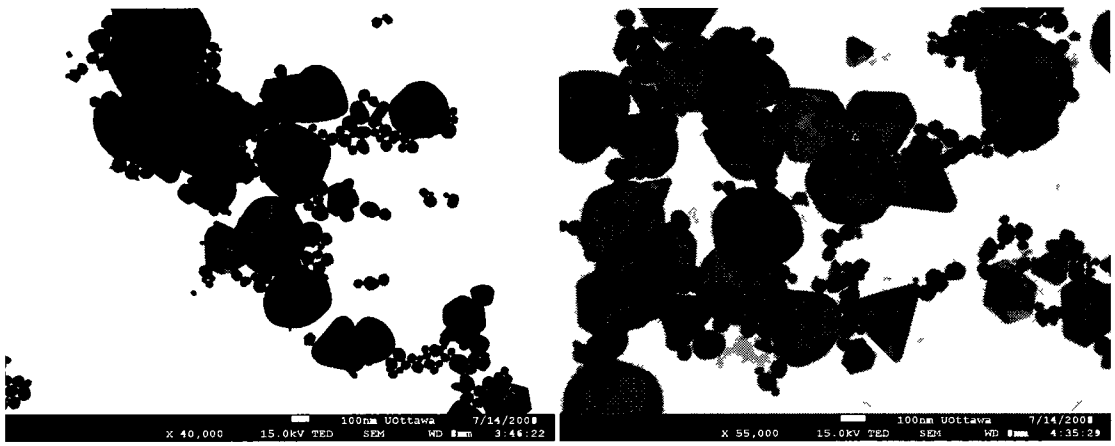

Figure 5 . 4 - SEM image of AuNP prepared from 0.33 mM $HAuCl_4$ and 3.0 mM H_2O_2 under air (left) and Ar-purged (right) conditions from 30 minutes 350 nm photolysis. The scale bars represent 100 nm.

If, however, an aqueous stabilizer is added during the synthesis, such as 4-hydroxyethoxy benzoic acid, 4-HEBA, platelet formation is significantly increased. 4-HEBA is the photoproduct stabilizing 10 nm AuNP when I-2959 is used as a photo-releasing reducing agent, as mentioned in Chapter 3. 4-hydroxyethoxy benzoic acid was synthesized according to a literature procedure[14] by Natalia Pacioni, a postdoctoral fellow in the group. It is noted that the AuNP synthesized in this experiment were prepared in a well plate, where the lower absorption intensity was the result of fewer UVA photons being absorbed relative to synthesis in a 1x1 quartz cuvette. In the presence of a stabilizer, the translational SPB for AuNP blueshifted to higher energy, while an increase in absorption beyond 800 nm was markedly observed. The significant differences in the absence and presence of 1.0 mM 4-HEBA resemble the absorption spectra of Figure 5.2; the generation of AuNP

in the presence and absence of oxygen, respectively. The absorption spectra for the 4-HEBA system is shown in Figure 5.5.

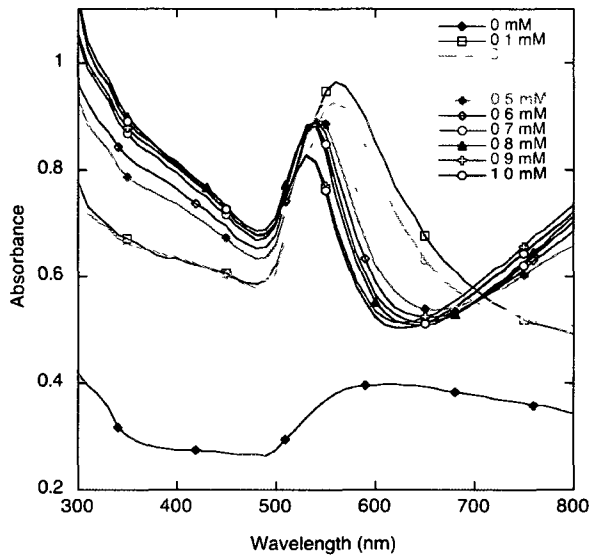

Figure 5 . 5 - AuNP prepared from 0.33 mM $HAuCl_4$ and 3.0 mM H_2O_2 in the presence of different concentrations of 4-hydroxyethoxy benzoic acid in aerated solutions from 30 minutes UVA photolysis.

As expected, no AuNP were formed from photolysis of 4-HEBA in the absence of H_2O_2. The trend toward narrower translational SPB and greater scatter with increasing 4-HEBA can be accounted for in the following way. When little or no ligand is present, a wider size distribution of spheres formed due to surface-catalyzed growth. When ligands are present and bound on the surface through physisorption as in the case of 1.0 mM 4-HEBA, a smaller initial size distribution in the presence was attained with the surface capped. Once the 4-HEBA was consumed through binding to the plethora of surface sites, remaining Au^0 and Au clusters grew slowly and anistropically to form platelets.

5.2.1 Surface-Catalyzed Growth Investigations

The growth behaviour of AuNP over time is depicted in Figure 5.3, and emphasizes an induction period (representative of the time required for nucleation and formation of small gold clusters prior to their growth into AuNP, at which time the surface plasmon energy shifts into the visible range). A rapid growth follows the induction period, completed by termination; a pattern characteristic of autocatalytic growth kinetics. The surface-catalyzed growth phenomenon was further investigated. In order to monitor the kinetics of AuNP more precisely, a Luzchem EXPO panel with five UVA lamps was mounted perpendicular to the sample compartment in the CARY spectrophotometer, with the details of the setup described in section 2.4.1. In these experiments, photolysis was arrested at the onset or during the burst in absorbance of the SPB. The results are presented in Figure 5.6.

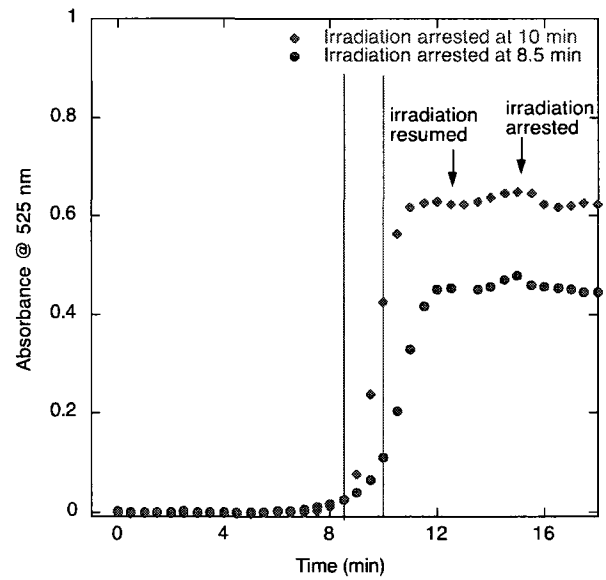

Figure 5 . 6 - Growth of AuNP SPB over time for two different samples when the lamps are turned off at 8.5 minutes and 10 minutes. The lamps are turned back on at 12.5 minutes for both samples, and turned off again at 15.5 minutes for both samples. Cuvettes contain 0.33 mM $HAuCl_4$ and 3.0 mM H_2O_2 in air-saturated solutions.

When the irradiation was arrested, the growth of AuNP was not inhibited, but terminated the earlier the photolysis was stopped. These results illustrate that both nucleation and growth processes are at play in solution when a continuous supply of reducing radical is removed. Nucleation continued as Au^+ was reduced to Au^0 *via* slow disproportionation in the absence of any reducing agent, and growth continued to form nanoparticles. The sooner the supply of reducing agent was cut off, the fewer AuNP were generated as less Au^+ was available, and the slower the growth as attributed by the smaller slope of the linear component of the s-shaped growth curve. Once the absorption of the SPB had reached a plateau, the lamps were turned back on. An increase in absorbance was observed within a minute, but the growth rate was much slower than the initial growth. This is interpreted as an increase in the reduction of surface stabilized Au^+ that will reduce quicker in the presence of HOO• and increase particle size. Once a second plateau period was established, the lamps were turned off again and the absorption intensity of both samples was seen to decrease for unknown reasons. It is worth emphasizing that the samples were irradiated separately, but still exhibited similar behaviour in the plateau areas at longer irradiation time. Furthermore, addition of H_2O_2 to a sample during the termination period resulted in minimal additional increase in the plasmon absorbance, confirming that Au^{3+} has been consumed within 30 minutes of photolysis. The invisible processes within the induction period can also be attributed to the presence of oxygen in solution. When the hydroperoxyl radical undergoes a redox reaction in the presence of $AuCl_4^-$, oxygen is generated.

This hypothesis was verified by measuring the change in pressure of a sealed sample vessel being irradiated in an equilibrated water tank relative to a foiled sample vessel on the same compostition. The samples were continuously shaken to ensure fast diffusion of oxygen inside the vessels. A detailed description of the instrument is given in Section 2.4. The sample and control were irradiated with the EXPO panel consistent of 5 UVA lamps positioned against a window to the equilibration tank, where photons penetrated through a thick 1 cm slab of glass and an aqueous chamber prior to reaching the sample. In other words, fewer photons reached the sample in comparison to photolysis in a photoreactor equipped with 14

lamps and within a quartz cuvette on a rotating carousel. Upon commencement of photolysis after five minutes of equilibration with the instrument, an increase in pressure was detected within seconds. The pressure increased steadily and leveled off momentarily. Following this, a second burst of O_2 was generated at twice the rate of the initial one. This oxygen evolution quickly subsided and followed with a decrease (or consumption) of oxygen. The data is shown in Figure 5.7.

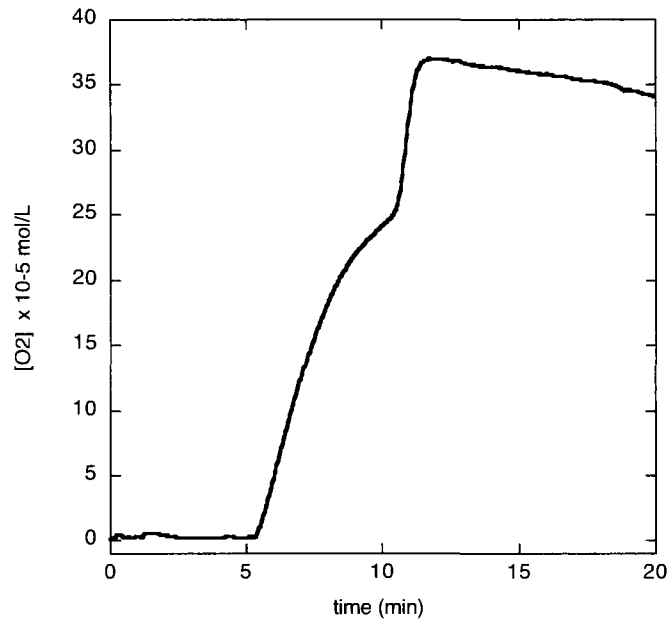

Figure 5 . 7 - Evolved oxygen pressure measured over time during gold nanoparticle synthesis via UVA photolysis of 0.33 mM $HAuCl_4$ and 3.0 mM H_2O_2. Photolysis commenced after five minutes.

These results can be interpreted in the following manner. The initial increase in oxygen resulted from the series of one-electron reduction steps and gradually decreased as the generation of nuclei resulted in consumption of H_2O_2 and fewer diffusion-controlled reduction events, with less oxygen released over time. Once stable gold clusters had formed, their reactive surfaces catalyzed the reduction of additional ions in solution, where particle size either increased or led to secondary nucleation and the slow formation of large prisms over time after irradiation was arrested. The burst resulted in a slope commencing after six minutes of photolysis

(12 minutes recording time, as indicated in Figure 5.7) that is greater than twice the slope of the initial oxygen generation. Finally, the decrease in oxygen pressure at longer reaction times has been rather interesting. Similar to the absorption measurements with arresting illumination during particle surface plasmon growth, identical procedures were applied to the oxygen evolution manifold, and it was found that in the absence of irradiation, the rate of oxygen produced also decreased, and recommenced when the lamps were turned on again, but the production was at a slower and slower rate. The process could be attributed to the oxidation of H_2O_2, however control experiments for oxygen evolution upon photolysis of hydrogen peroxide alone, or $HAuCl_4$ yielded negligible signal. Any oxidation taking place is thus likely catalyzed by the particle surface. A bar graph of the production rate of O_2 with time is presented in Figure 5.8.

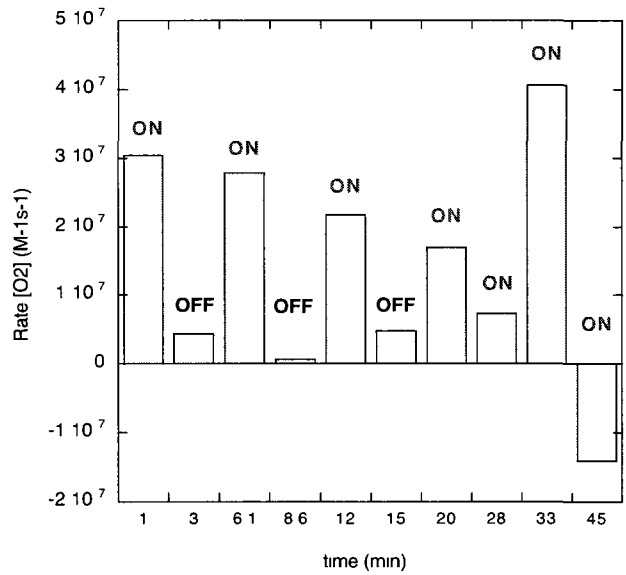

Figure 5 . 8 - Rate of O_2 generated during AuNP synthesis from H_2O_2 while UVA lamps are turned on/off. Aqueous sample contains 0.33 mM $HAuCl_4$, 3.0 mM H_2O_2 and has not been purged to remove oxygen.

For O_2 production following typical parabolic growth, the rate of production decreased with time, and the production while irradiation was off was much lower. Notably, a final decrease in oxygen pressure was also measured, which can be

correlated with a consumption as hypothesized with absorption observations stated above. This phenomenon has also been observed potentiometrically upon synthesis of gold nanoparticles from hydrogen peroxide under dark, alkaline conditions, and attributed to the formation of $O_2^{\bullet-}$ and identified by electron paramagnetic resonance studies.[15] The study neglected to address the size of AuNP resulting from the reduction, but described the solutions as purple and turbid brown for particles prepared at pH 7 and 13, respectively. From personal experience, these colours correlate with large agglomerates and micron-sized plates. Interestingly, the study focused on the reduction of $Au(OH)_2^-$ by $O_2^{\bullet-}$ in 0.1 M NaOH (after ligand exchange from $HAuCl_4$), and referred to the chloride ligands as nonreactive under the given (thermal) experimental conditions.

The role of photolysis in our study was assessed. It was observed that no dark reduction ensued below a pH of 5. At pH 1-2, Cl ligands are tightly bound to the metal center and do not readily dissociate as indicated by the lack of change in the absorption of the LMCT band. The pH of 0.33 mM $HAuCl_4$ dissolved in water is 2.91.[16] AuNP were prepared at several different pH as shown in Figure 5.9.

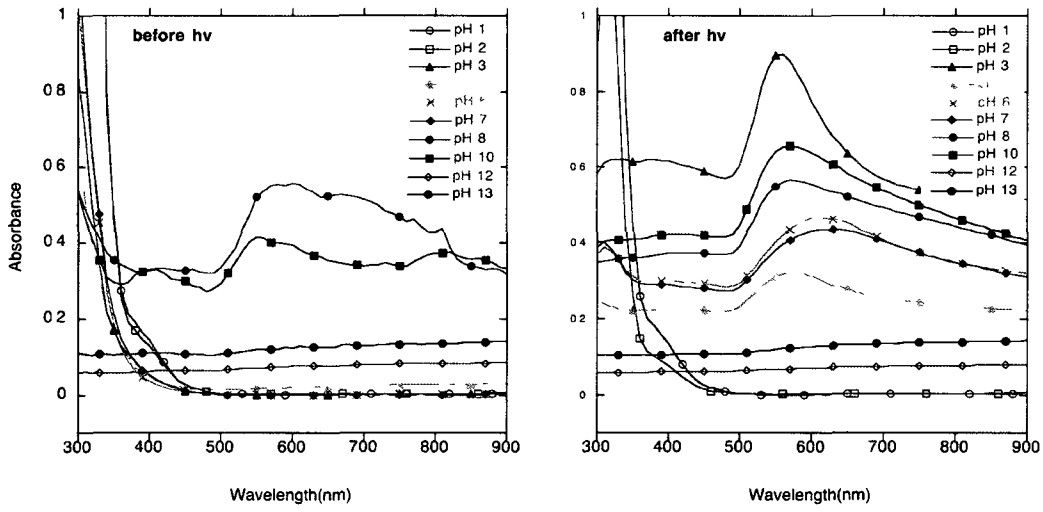

Figure 5 . 9 - Absorption of solutions before (left) and after (right) 30 minutes 350 nm photolysis. Samples prepared from 0.33 mM $HAuCl_4$ and 3.0 mM H_2O_2 in aqueous, aereated media where the pH was adjusted with HCl or NaOH. Samples were left to sit for 20 minutes prior to photolysis.

The pH of solutions was adjusted by addition of HCl or NaOH to distilled deionized water prior to addition of $HAuCl_4$, H_2O_2 and photolysis. In other experiments, the pH was adjusted with HCl/15 mM acetate buffers and 15 mM phosphate/NaOH, however the ionic strength of the buffers led to "scattered" and inconclusive results. As mentioned in Chapter 3, the synthesis of AuNP from I-2959 in the presence of buffers resulted in blue solutions (aggregated particles) when the phosphate buffer concentration was above 0.4 mM, which highlights the sensitivity of this photochemical method for charge-stabilized NP towards ionic strength.

At high pH, chlorine ions are exchanged for hydroxide ions and subsequently reduced by $O_2^{\bullet-}$, and the higher the pH, the faster this reaction occurs. This trend has been observed for the reduction of $HAuCl_4$ from other reducing agents such as ascorbic acid.[16] The scatter observed for samples at pH 12 and 13 are the result of an instant reduction to yielding blue/grey solutions. Interestingly, the samples at pH 7 and 8 also led to a thermal reduction with broad bands displayed in Figure 5.9, left. Photolysis, however, resulted in narrowing of the SPB. AuNP formed from photolysis at pH 3-7 with no dark reactions, yet an optimal SPB was disclosed at pH 3. It is evident than an increase in pH leads to a broadening and redshifting of AuNP SPB, which also correlates with an increase in $O_2^{\bullet-}$. From these results, it appears that the rate of AuNP is optimal and most stable at lower pH with higher [HOO•], where the reducing agent is under photochemical control.

5.2.2 Other Metal Chloride Salts

This preparation was also attempted with other metal chloride salts such as K_2PtCl_6, $RuCl_3$ and $RhCl_3$. While photolysis of $RuCl_3$ and $RhCl_3$ samples led to large aggregates as well as some nanoparticles, rather monodisperse platinum nanoparticles (PtNP) were achieved with this method. Platinum is more resistant to

oxidation relative to the other noble metals mentioned above. Figure 5.10 displays a SEM image of Pt prepared from hydrogen peroxide in water. The great monodispersity of the 16.2 ± 2.9 nm particles is impressive, for no synthesis of PtNP has yet been reported with such a simple system. The photochemical reduction of chloride metal salts has been reported for Au(III), Pt(IV), Rh(III) and Pd(II) by Borgarello *et al.*[17] whereby visible light photolysis of a solution containing the metal salt and TiO_2 (P25) was said to result from electron transfer from the excited semiconductor particles. While the report emphasizes the use of chloride salts, for other ligands such as cyanide were seen as ineffective, the photoreactivity of the chlorine atom was not addressed en lieu of the photocatalyst.

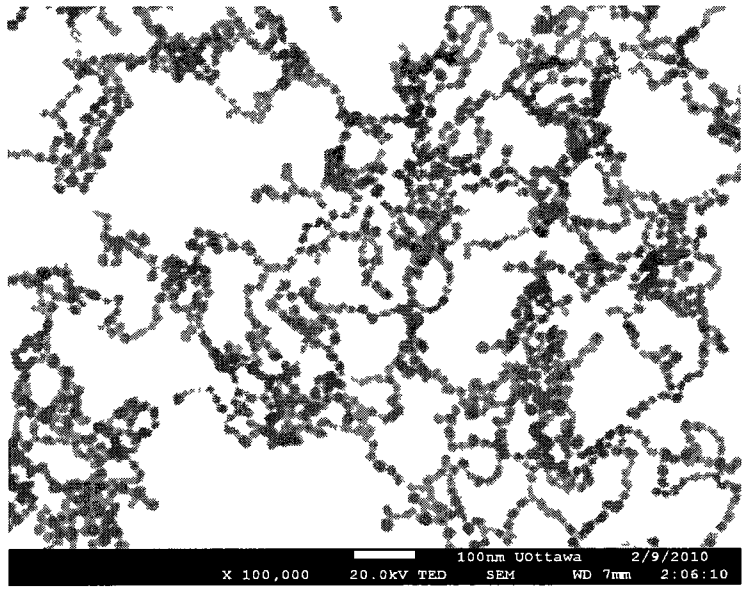

Figure 5 . 10 - SEM image of platinum nanoparticles prepared from 355 nm photolysis with 0.1 mM K_2PtCl_6, 3.0 mM H_2O_2 and 0.01 mM 4-HEBA. The scale bar represents 100 nm.

In our research, nanoparticles were formed from a solution composed of 0.1 mM K_2PtCl_6 and 3.0 mM H_2O_2 at pH 3. The spectra are presented in Figure 5.11. As PtNP do not possess a surface plasmon band in the visible range, a minor yellowing of the solution was observed after 30 minutes of photolysis, which is understood from the increase in the tail absorbance out to ca. 450 nm. Additionally, the LMCT

band for the platinum salt was seen to decrease at 289 nm. Much in the same way that 4-HEBA was observed to stabilize AuNP, the ligand was added at 0.01 mM concentration prior to photolysis. As a result, the absorbance of the shoulder around 325 nm decreased in comparison to the non-functionalied sample. While SEM images of the particles in the absence of stabilizer were unfortunately not acquired, the ligand assisted to produced PtNP in a clean synthesis, as seen in Figure 5.10. The pH of the aqueous synthesis of PtNP from H_2O_2 was also varied, and trend was also observed that thermal reduction was dominant above pH 5.

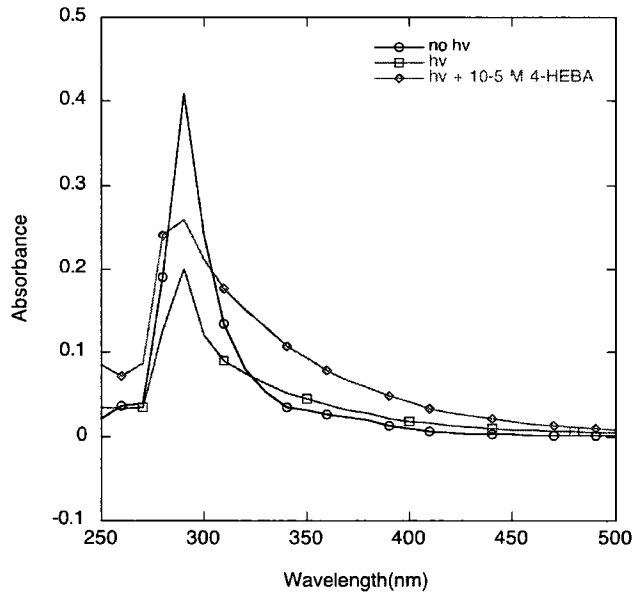

Figure 5 . 11 - Absorbance of solution containing 0.1 mM K_2PtCl_6, 3.0 mM H_2O_2 before and after exposure to UVA light for 30 minutes. Additional trace represents another identical sample containing 1.0 x 10^{-5}M 4-HEBA.

Some peculiarities presented themselves when nanoparticles were synthesized via hydrogen peroxide photolysis. Notably, the synthesis was ineffective in 17 mM CTAC, whereas several syntheses with organic free-radicals took place in this medium as presented in Chapters 3 and 4. The presence of an alkyl surfactant can likely be a preferred candidate for hydrogen abstraction over that of hydrogen peroxide given the high availability of C-H bonds in the long chain surfactants. Additionally, the synthesis of AuNP was not effective when $Au(OH)_3$ was used as a

starting material. The low solubility of the compound in water or 17 mM aqueous CTAC could be cause for poor reactivity, but the solution was clear throughout photolysis and thereafter. This emphasizes the facility of AuNP synthesis from $AuCl_4^-$ being in part due to the homolytic cleavage of Cl atoms to initiate the reduction process. When $AuBr_3$ was used as an alternate gold halide salt, photolysis did not yield nanoparticles either, despite similar absorbance at 350 nm. Bromine radicals have also been known to be less reactive in hydrogen abstraction reactions.[18] Finally, no nanoparticles were successfully prepared in acetonitrile, regardless of the presence of oxygen. There was a decay of the LMCT band for $AuCl_4^-$, yet no sequential generation of a surface plasmon band. The absorbance of irradiated $HAuCl_4$ in MeCN over time is displayed in Figure 5.12.

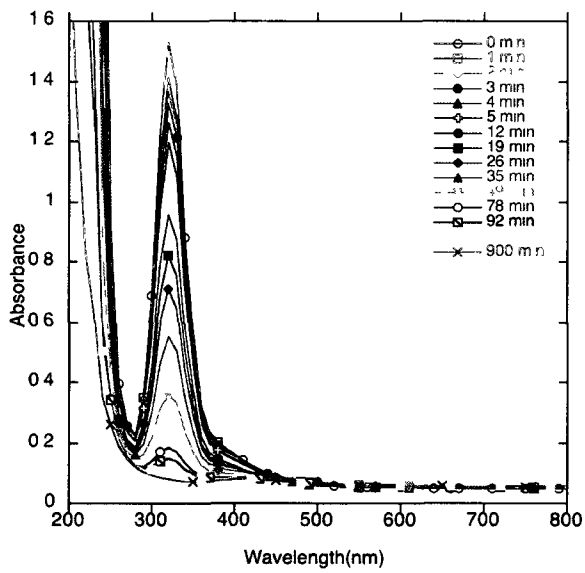

Figure 5 . 12 - Absorption spectrum for the photolysis of 0.33 mM $HAuCl_4$ and 3.0 mM H_2O_2 in ambient acetonitrile.

The same trend was observed in other non-protic solvents including DMSO and ethyl acetate. When tetrahydrofuran was employed, however, a faint purple solution formed, indicative of a reduction. This observation led to further studies with tetrahydrofuran.

5.3 Hydrogen Abstraction from Tetrahydrofuran

Tetrahydrofuran (THF) was also applied as a hydrogen donor via the synthesis of AuNP, where photolysis of $HAuCl_4$ in the presence of THF led to abstraction of a hydrogen and the onset of reduction via the produced radical with reduction properties. The synthesis of AuNP did not work effectively when 100% THF used as a solvent with 3.0 mM H_2O_2, as a dark blue solution formed from 30 minutes of photolysis. When the sample was prepared with 10% THF in water with 3.0 mM H_2O_2 however, nanoparticles did form. The resultant spectra are shown in Figure 5.13.

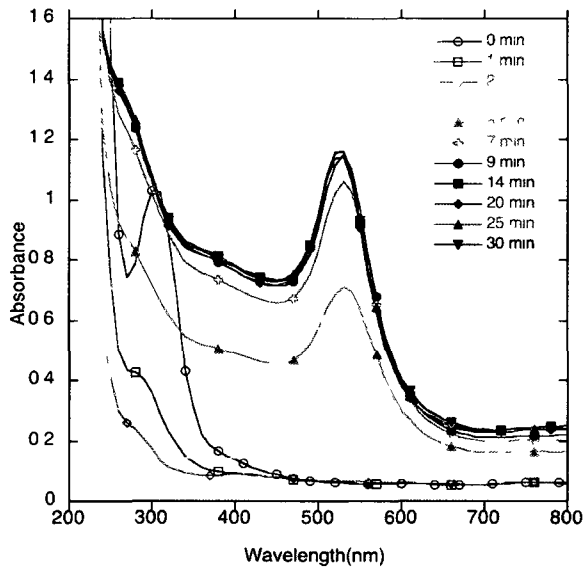

Figure 5 . 13 - UV-Vis absorbance during the growth of AuNP prepared from 10% THF in aqueous, deareated 0.33 mM $HAuCl_4$ and 1.0 mM H_2O_2 upon UVA photolysis.

Unlike H_2O_2 alone, the reduction occured successfully without the formation of significant scatter at longer wavelength. Tetrahydrofuran is an effective hydrogen donor, as underlined by previous studies where hydrogen atom transfer in the

presence of tert-butylperoxide as a scavenger formed the tert-butoxy radical with a rate constant of of 8.25 x 10^6 $M^{-1}s^{-1}$ in benzene.[19]

Hydrogen abstraction is favoured at the α-hydrogen, and a free radical is generated with a reduction potential of ~ -1.05 V vs. NHE.[20] Other photoproducts are likely generated, although no characterization was performed at the time. The reduction is proposed to follow the pathway shown in Scheme 5.4.

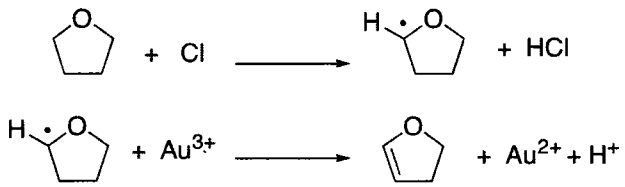

Scheme 5 . 4 - Hydrogen abstraction from tetrahydrofuran to yield a reducing radical.

The growth of AuNP over time was measured and is depicted in Figure 5.14. The spectra highlight the ability to monitor the dissapearance of $AuCl_4$ over time with another simple, common, and inexpensive reducing agent. The particles were surprisingly stable for weeks, possibly due to the ether functionality of the oxidized species, or THF iteself contributing to particle stabilization. A SEM image of the particles is shown in Figure 5.14. The sample is quite polydisperse and polyprismatic, however a facile method for generating AuNP of 20 nm is easily achieved from using a simple solvent as a reducing agent. Similar to reduction via H_2O_2 photolysis, large platelets and prisms can be removed via centrifugation or filtration with an inexpensive 0.1 μm PTFE filter. This THF route has yet to be further optimized for the generation of smaller and more monodisperse particles.

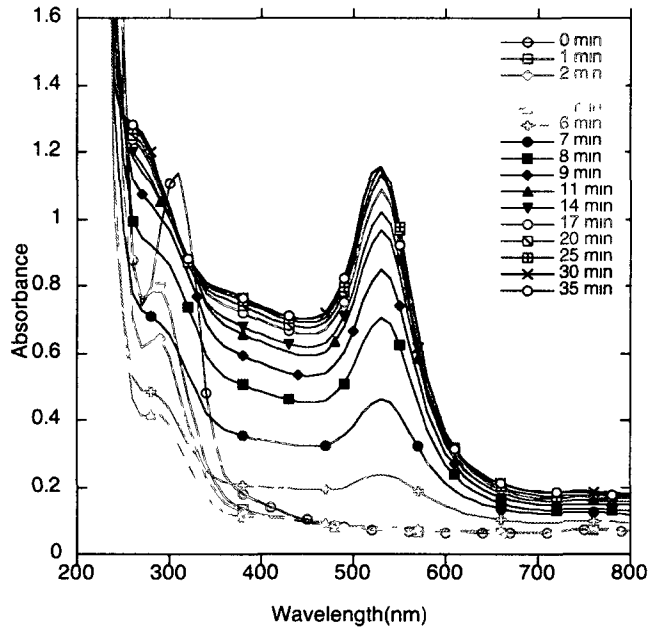

Figure 5 . 14 - UV-Vis absorbance during the growth of AuNP prepared from 10% THF in aqueous, deareated 0.33 mM $HAuCl_4$ upon UVA photolysis.

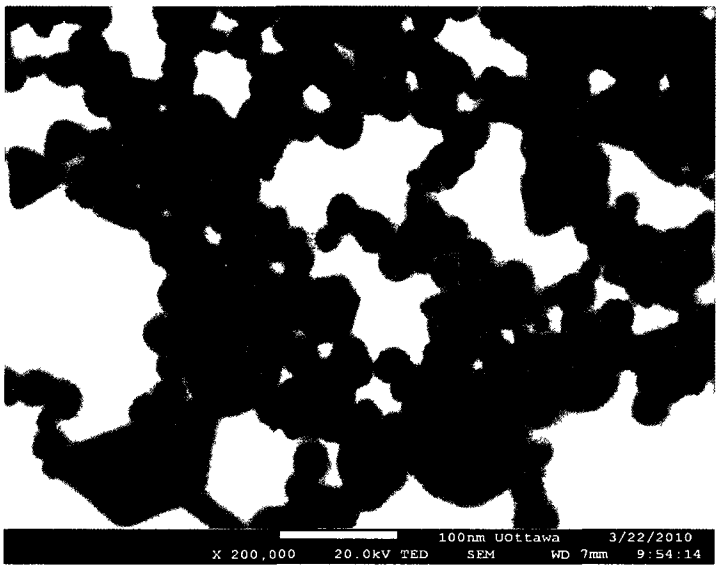

Figure 5 . 15 - SEM image of AuNP prepared from photolysis of THF in the presence of 0.33 mM $HAuCl_4$. The scale bar represents 100 nm.

AuNP generated in 10% THF were more stable (judging from the SPB) relative to those in pure THF, which could result from better charge stabilization in the more polar solvent. Notably, preparation of a 10% THF solution of 0.33 mM $HAuCl_4$ under dark conditions did not result in any AuNP generation. Given that THF does not absorb in the UV or Visible range of the spectrum, these findings are a proof of concept for facile reduction of metal salts from the photolytic production of transient free-radicals.

AuNP were also prepared by direct photolysis of thiols in the presence of $HAuCl_4$ in THF, inspired by previous work by Warren *et al.* In their report, the reduction potential of excited metal thiolate complexes were exploited for the formation of NP via visible light photolysis.[21] Bismuth, copper, lead and antimony nanoparticles were successfully prepared in dry THF from photolyis of metal salt complexes with dodecanethiol, carboxylates, or oleates of metal salts. Long irradiation times of 24 hours to two weeks under ambient led to excitation the MLCT within the metal thiolate complex, resulting in reduction and NP formation.

This concept was probed given the photochemical synthesis of AuNP with THF. Thiols such as 6-*n*-hexanethiol (6-SH), 16-*n*-hexadecylthiol (16-SH), and mercaptohexadecanoic acid (MHDA) at 1.0 mM concentrations were photolyzed with 0.33 mM $HAuCl_4$ in deareated THF. While 30 minutes photolysis with ligands did not lead to a blue solution as observed earlier in the absence of thiols, no colour change took place. 6 hours of UVA photolysis did, however, generate gold nanoparticles, owing to the red, pale pink and beige colours in solution for 6-SH, MHDA and 16-SH AuNP, respectively. Photolysis was continuted for 45 hours, however no significant change in absorbances were observed. The absorbance spectra and a photograph of the samples are presented in Figure 5.16. Among the different thiols employed, a trend of increased absorbance intensity and hyptochromic shift in SPB identified with a longer chain. Additionally, the superior SPB of MHDA over the other thiols likely relates to its greater solubility in THF over the aliphatic ligands. The resulting solutions were stable for a few days, until AuNP

precipitated from solution. A SEM image of 1.0 mM MHDA-AuNP is displayed in 5.17.

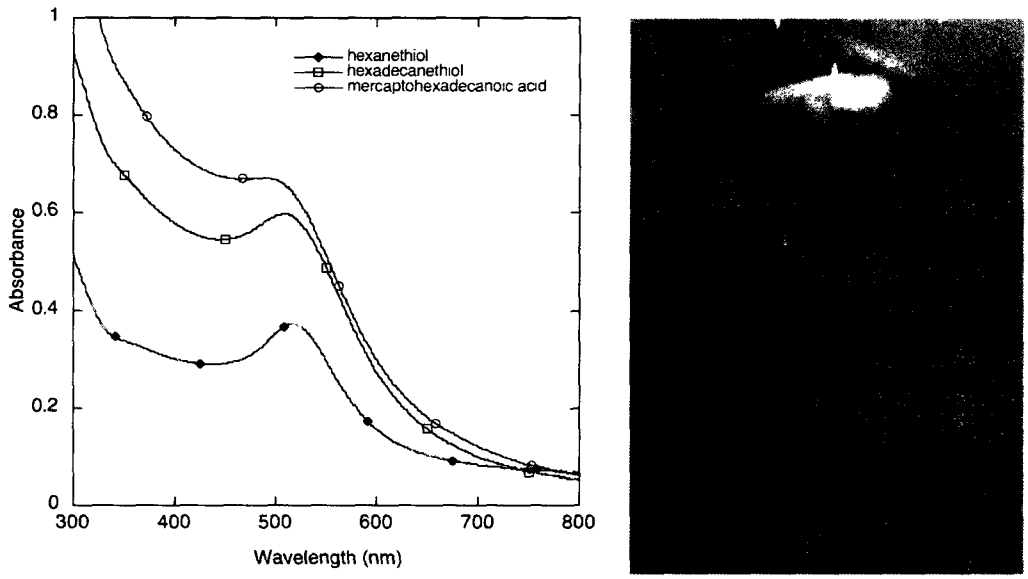

Figure 5 . 16 - (Left) Absorbance of AuNP synthesized via UVA photolysis of 0.33 mM $HAuCl_4$ and 1.0 mM thiol in THF for 6 hours using 6 lamps. (Right) Appearance of resulting colloid solutions. Hexanethiol, mercaptohexadecanoic acid and hexadecanethiol (left to right).

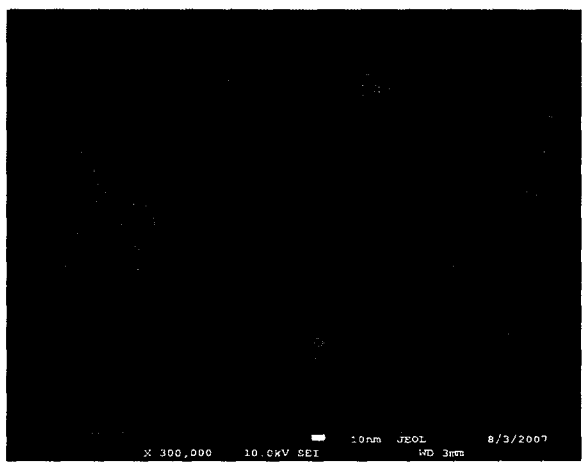

Figure 5 . 17 - SEM image of AuNP prepared from 45 hours 350 nm photolysis of 0.33 mM $HAuCl_4$ and 1.0 mM MHDA in THF. The scale bar represents 10 nm.

While the quality of the SEM image is poorer than that displayed in Figure 5.15, it is clear that there is a dramatic reduction in particle size when photolysis is performed in the presence of thiols.

Whether the photochemistry at play for the generation of AuNP in the thiol/THF systems is a consequence of photoexcited thiolates, generation of the tetrahydrofuranyl radical, or both, is unknown. It is possible that both contribute to the mechanism. The strong affinity for Au-S bonds leads to complexation to form a polymer-like Au(I)-S.[22] Reduction via the tetrahydrofuranyl radical alone may be inefficient, for its reduction potential of -1.05 V vs NHE is lower than that of the ketyl radicals studied herein , ~ -1.7 V vs NHE, and synthesis of AuNP in the presence of thiols proved rather ineffective with minimal SPB generation. No further product characterization studies were performed. While the redox potentials for the studied thiols were not investigated, it possible that similar photochemistry to that studied by Warren *et al.* took place. Further investigations with thiol derivitization are discussed in greater detail in Chapter 6.

5.4 Hydrogen Abstraction from Pyrrolidine

The same concept of hydrogen abstraction was also applied to pyrrolidine. Pyrrolidine loses the α-hydrogen adjacent to the nitrogen easily at a rate of 4.4×10^9 $M^{-1}s^{-1}$ by an abstractor such as benzophenone,[23] as mentioned in Chapter 4. This can also occur through charge transfer.[24, 25] In the same fashion that 1,4-CHD, H_2O_2, and THF can operate as hydrogen donors in the presence of an abstractor, radicals from pyrrolidine are capable of reducing the metal salt oxidation state to the atomic state. The reducing process for pyrrolidine is outlined in Scheme 5.5. α-Aminoalkyl radicals act as powerful reducing transients, as was demonstrated with the synthesis of AuNP from I-907 in Section 3.2. Similarly, pyrrolidine can reduce $HAuCl_4$ and generate gold nanoparticles.

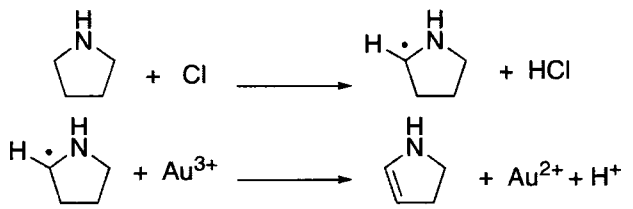

Scheme 5 . 5 - Proposed mechanism for the reduction of $HAuCl_4$ via pyrrolidine

The photochemical synthesis was carried out in deareated water, but the unstable product led to a fast precipitation and formation of a blue colloid. When 13.5 mM CTAC was replaced as the medium, nanoparticle synthesis occurred considerably faster (SPB plateau within three minutes). A dark blue solution formed with a bimodal SPB; a peak at 519 nm and a broad shoulder at 660 nm. With further irradiation, the longitudinal SPB diminished to yield a purple colloid after 15 minutes irradiation. Surprisingly, the sample appeared red 17 hours later, where the anisotropic SPB had completely diminished. The absorption spectra of the solutions are presented in Figure 5.18.

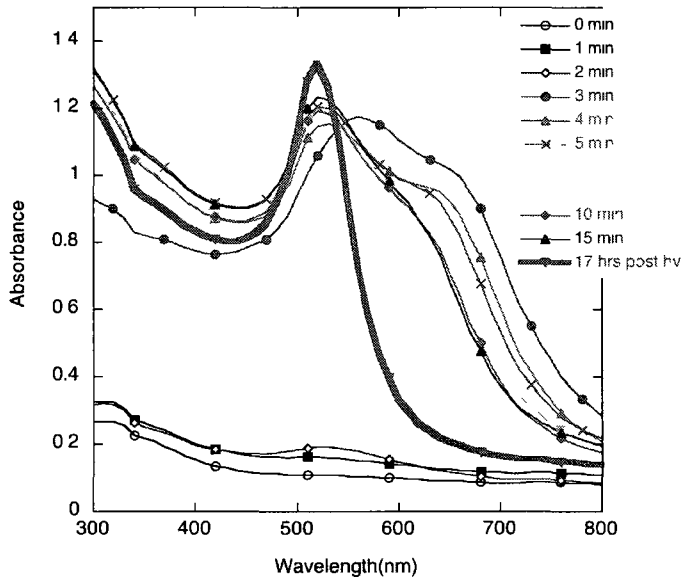

Figure 5 . 18 - Growth of AuNP over time with pyrrolidine as a hydrogen donor with UVA photolysis. Deareated solution contains 0.33 mM $HAuCl_4$, 10% v/v pyrrolidine in 13.5 mM CTAC.

An aliquot of the reaction mixture was removed for SEM immediately after photolysis, and after 17 hours. The particles of the "blue colloid" were irregular-shaped ellipses or cones in the presence of few spherical particles, whereas images of the final solution displayed perfect spheres of good monodispersity. SEM of the final solution is portrayed in Figure 5.19, left.

Control experiments were performed to assess the possibility of thermal reductions, as with many amine molecules, the alkalinity and high pk_a can be sufficient to cause reduction in the absence of photons.[26] Pyrrolidine has a pK_a of 11.35, and at the working concentration of 1.23 M (10% v/v), it can be oxidized thermally to form a radical cation with a reduction potential of + 1.4 V vs. Ag/TBAP.[27] When an identical sample was stored in the dark, no reduction was apparent after 30 minutes. Within two hours, however, the sample turned dark blue, and violet 30 minutes later. This finding supports the reduction through the radical species with the short timespan of the photochemical reaction. A SEM image of the colloid formed in the dark is shown in Figure 5.19, right, which is similar to the polymorphic prisms grown immediately after 15 minutes photolysis. Unlike the irradiated sample, however, the dark sample, when left on the bench with ambient room light alongside the photolysed sample, did not transform to red. The absorption spectrum of the dark sample is seen below in Figure 5.20.

The route to gold nanoparticle synthesis from pyrrolidine remains unclear, for it is uncertain whether reduction occurred from hydrogen abstraction or from the radical cation. Laser flash photolysis has been reported to detect the radical at 320 nm with an extinction coefficient of 510 $M^{-1}cm^{-1}$,[28] however this low absorption is screened by the LMCT of the metal salt complex, thus making the radical cation an unlikely reducing agent.

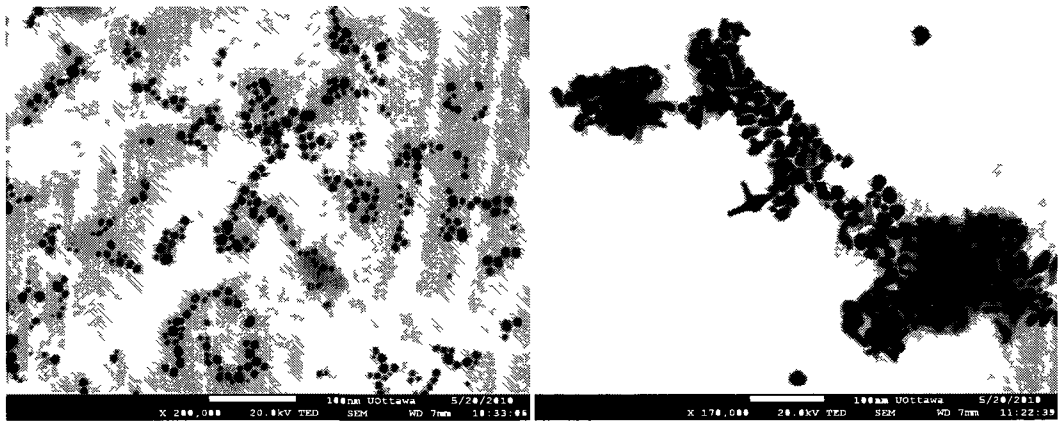

Figure 5 . 19 - SEM image of AuNP prepared from 0.33 mM $HAuCl_4$, 10% v/v pyrrolidine in 13.5 mM CTAC under (left) deareated and 15 minutes 350 nm irradiation after 17.5 hours, and (right) dark, air-saturated reaction after 17.5 hours.

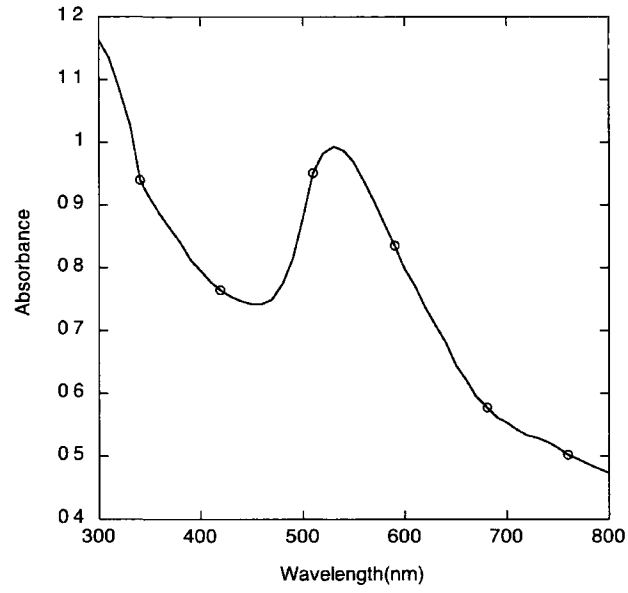

Figure 5 . 20 - Absorbance of AuNP formed under dark conditions from 0.33 mM $HAuCl_4$, 10% v/v pyrrolidine in air-saturated 13.5 mM CTAC.

The ability to generate AuNP from photolysis of pyrrolidine also sheds light on the unclear mechanism for $HAuCl_4$ reduction with poly(vinylpyrrolidone), where simple photolysis of the polymer led to nanoparticle formation as reported here and by others.[29] This was described in Section 3.5 6. In the case of work by Itakura *et al.*,

negligible reduction was observed with $AgClO_4$ and $Cu(ClO_4)_2$, but considerable reduction took place with the gold chloride salt. It can now be proposed that the reduction occurs through the abstraction of the α-hydrogen of the 5-membered ring via photoexcitation of $HAuCl_4$. In other words, it is likely the gold salt rather than the polymer that is excited, followed by generation of a reducing radical polymer due to the release of the reactive chlorine atom through photolysis.

5.5 Summary

The synthesis of metal nanoparticles can be easily achieved using photochemistry where the generation of excited state species can lead to colloidal nanoparticle solution for gold, but can be carried over to several other metals with cooperative reduction potentials. 1,4-cyclohexadiene, hydrogen peroxide, tetrahydrofuran and pyrrolidine were successfully used for the synthesis of gold nanoparticles. The generation of AuNP from H_2O_2 was tuned under photochemical and pH control. H_2O_2 was also briefly used for a novel method to synthesize platinum nanopartilces from its metal chloride salt. While the generation of AuNP with these methods yielded larger AuNP relative to synthetic methods involving ketyl radicals, the synthesis of larger particles presents another photochemical strategy nonetheless. Many of the experiments described in this chapter were simple proofs of concept, which could be optimized for facile synthesis of metal nanoparticles in future studies involving metal chloride salts.

5.6 References

1. Vogler, A., Kunkely, H., Photoreactivity of Gold Complexes. *Coord. Chem. Rev.* **2001,** *219*, 489-507.

2. Pichugina, D. A., Shestakov, A. F., Kuz'menko, N. E., Quantum Chemical Study of C-H Bond Activation in Methane Molecule by Au(III) Aqua Chloride Complexes. *Russian Chemical Bulletin, Int. Ed.* **2006,** *55* (2), 195-206.

3. Buxton, G. V., Bydder, M., Salmon, G. A., Reactivity of Chlorine Atoms in Aqueous Solution Part I. *J. Chem. Soc., Faraday Trans.* **1998,** *94* (5), 653-657.

4. Buxton, G. V., Bydder, M., Salmon, G. A., Williams, J. E., The Reactivity of Chlorine Atoms in Aqueous Solution Part III. The Reaction of Cl• with Solutes. *Phys. Chem. Chem. Phys.* **2000,** *2*, 237-245.

5. Gilbert, B. C., Stell, J. K., Peet, W. J., Radford, K. J., Generation and Reaction of the Chlorine Atom in Aqueous Solution. *J. Chem. Soc., Faraday Trans. I* **1988,** *84* (10), 3319-3330.

6. Sheps, L., Crowther, A. C., Elles, C. G., Crim, F. F., Recombination Dynamics and Hydrogen Abstraction Reactions of Chlorine Radicals in Solution. *J. Phys. Chem. A* **2005,** *109*, 4296-4302.

7. Sumiyoshi, T., Rate Constants for the Reactions of Benzene-Chlorine Atom π-complexes with Alcohols in Carbon Tetrachloride. *Radiat. Phys. Chem.* **1997,** *50* (5), 449-455.

8. Kurikara, K., Kizling, J., Stenius, P., Fendler, J. H., Laser and Pulse Radiolytically Induced Colloid Gold Formation in Water and in Water-in-oil Microemulsions. *J. Am .Chem. Soc.* **1983,** *105*, 2574-2579.

9. Gachard, E., Remita, H., Khatouri, J., Keita, B., Nadjo, L., Belloni, J., Radiation-induced and Chemical Formation of Gold Clusters. *New. J. Chem.* **1998**, 1257-1265.

10. Litorja, M., Ruscic, B., Ionization Study of the Hydroperoxyl Radical, HO2, and Hydrogen Peroxide, H2O2. *J. Elec. Spec. Rel. Phenom.* **1998,** *97*, 131-146.

11. Bielski, B. J. H., Cabelli, D. E., Highlights of current research involving superoside and perhydroxyl radicals in aqueous solutions. *Int. J. Radiat. Biol.* **1991,** *59* (2), 291-319.

12. Garza-Ortiz, A., den Dulk, H., Brouwer, J., Kooijman, H., Spek, A. L., Reedijk, J., The synthesis and biological properties of dichlorido(azpy)gold(III)chloride (azpy=2-(phenylazo)pyridine) and the gold-induced conversion of the azpy ligand to

the chloride of the novel tricyclic pyrido[2,1-c][1,2,4]benzotriazin-11-ium cation. *J. Inorg. Biochem.* **2007,** *101* (11-12), 1922-1930.

13. Daniel, M.-C., Arstruc, D., Gold Nanoparticles: Assembly, Supramolecular Chemistry, Quantum-Size-Related Properties, and Applications Toward Biology, Catalysis and Nanotechnology. *Chem. Rev.* **2004,** *104*, 293-346.

14. Meng, X., Natansohn, A., Barret, C., Rochon, P., Azo Polymers for Reversible Optical Storage. 10. Cooperative Motion of Polar Side Groups in Amorphous Polymers. *Macromolecules* **1996,** *29*, 946-952.

15. Paclawski, K., Fitzer, K., Kinetics of Reduction of Gold (III) Complexes Using H2O2. *Metall. Mater. Trans. B* **2006,** *37B*, 703-714.

16. Wang, S., Quain, K., Bi, X., Huang, W., Influence of Speciation of Aqueous HAuCl4 on the Synthesis, Structure, and Property of Au Colloids. *J. Phys. Chem. C.* **2009,** *113*, 6505-6510.

17. Borgarello, E., Serpone, N., Emo, G., Harris, R., Pelizzetti, E., Minero, C., Light-Induced Reduction of Rhodium(III) and Palladium(II) on Titanium Dioxide Dispersions and the Selective Photochemical Separation and Recovery of Gold(III), Platinum(IV), and Rhodium(III) in Chloride Media. *Inorg. Chem.* **1986,** *25*, 4499-4503.

18. Bottoni, A., Poggi, G. , An Ab Initio Study of Hydrogen Abstraction by Fluorine, Chlorine and Bromine Atoms from Ethane and Propane. *J. Molec. Structure (Theochem)* **1995,** *337*, 161-172.

19. Malatesta, V., Scaiano, J. C., Absolute Rate Constants for the Reactions of tert-butoxyl with Ethers: Importance of the Stereoelectronic Effect. *J. Org. Chem.* **1982,** *47*, 1455-1459.

20. Wayner, D. D. M., Griller, D., Oxidation and Reduction Potentials of Transient Free Radicals. *J. Am .Chem. Soc.* **1988,** *110*, 132-137.

21. Warren, S. C., Jackson, A. C., Cater-Cyker, Z. D., DiSalvo, F. J., Wiesner, U., Nanoparticle Synthesis via the Photchemical Polythiol Process. *J. Am. Chem. Soc.* **2007,** *129*, 10072-10073.

22. Corbierre, M. K., Lennox, R. B., Preparation of Thiol-Capped Gold Nanoparticles by Chemical Reduction of Soluble Au(I)-Thiolates. *Chem. Mater.* **2005,** *17*, 5691-5696.

23. Griller, D., Howard, J. A., Marriot, P. R., Scaiano, J. C., Absolute Rate Constants for the Reactions of tert-Butoxyl, tert-butylperoxyl, and Benzophenone Triplet with Amines; The Importance of a Stereospecific Effect. *J. Am .Chem. Soc.* **1981,** *103*, 619-623.

24. Cohen, P., A., Parsons, G., Photoreduction by Amines. *Chem. Rev.* **1973,** *73* (141-161).

25. Cohen, S. G., Litt, A. D., Rate Constants of Interaction of Benzophenone Triplet with Amines. *Tetrahedron Lett.* **1970**, 837-840.

26. Newman, J. D. S., Blanchard, G. J., Formation of Gold Nanoparticles Using Amine Reducing Agents. *Langmuir* **2006,** *22*, 5882-5887.

27. Bui, N.-N., Ho, X.-H., Mho, S., Jang, H.-Y., Organocatalyzed a-Oxyamination of Aldehydes Using Anodic Oxidation. *Eur. J. Org. Chem.* **2009**, 5309-5312.

28. Getoff, N., Schworer, F., Pulse Radiolysis of Pyrrolidine. *Radiation Research* **1970,** *41* (1), 1-14.

29. Itakura, T., Torigoe, K., Esumi, K., Preparation and Characterization of Ultrafine Metal Particles in Ethanol by UV Irradiation Using a Photoinitiator. *Langmuir* **1995,** *11*, 4129-4134.

Chapter 6

Surface Modification of Gold Nanoparticles

6.1 Introduction

The growth of research into nanomaterials in the past two decades has functioned as both cause and effect for the development of particles with a vast spread of applications in the fields of optical imaging and drug delivery. Within this branch of research, nanoparticles can be used as a sensor to monitor certain physical or biochemical transformations. As such, nanoparticles are labeled with a tethering molecule of interest prior to being introduced to the system under investigation.[1-3] An optimal size of AuNP for sensor applications falls in the 5-15 nm range; highlighting another advantage of I-2959 derived AuNP. In this research, the physical chemistry involved in labeling the particle surface has been investigated with photochemically-derived nanoparticles. The surface chemistry of gold nanoparticles generated via I-2959 synthesis has been studied extensively by derivatizing the particle surface with a number of different ligands with different functional groups. Additionally, further growth of nanoparticles has also been studied by exploiting the surface reactivity and catalysis of gold nanoparticles.

6.2 Seed-Mediated Growth of AuNP

Control over particle size and shape has frequently come at the expense of monodispersity, where a lack of uniformity of particle size decreases industrial appeal towards chemical catalysis or biological imaging and drug delivery.[4] Much success has been achieved for the synthesis of small nanoparticles in the 2-10 nm size range with reduction via $NaBH_4$ as a reducing agent and capping thiols to stabilize the particles. While narrow size distribution is obtained in the smaller particle size domain, this method suffers in monodispersity for larger particle sizes.[5] While reduction via the citrate method offers a good dispersity in the 5-20 nm range,

production of larger monodisperse particles using this method also presents challenges.[4, 6, 7]

In the last decade, Natan *et al.* devised a method to generate larger particles by a method termed seed-mediated growth.[8] This technique controls particle size by physically separating nucleation and growth periods by gradually enlarging particles through surface-catalyzed growth. In this approach, small metal particles are added to a solution of metal salt and mild reducing agent such that the metal particle surface catalyzes the reduction of metal salt on the particle surface via particle-mediated electron transfer. While the reduction potential of the Au_{atom}/Au^{+} (aqueous) is -1.5 V vs NHE, the ability of the particle surface to be sacrificially oxidized to reduce an adsorbed Au^{+} ion is in fact quite favourable, as indicated by the high reduction potential for the surface process; Au_{metal}/Au^{+} (aqueous) system is +1.68 V vs NHE.[9] Careful choice of a mild reducing agent is paramount to minimize the growth of new particle nucleation centers, also known as secondary nucleation. Ascorbic acid has been a common choice for many preparations, for the reduction potential of the weak acid is + 0.125 V vs. NHE and insufficient to reduce the aurous and auric species.[9] Other reducing agents such as hydrazine and hydroxylamine hydrochloride have also been explored as reducing agents in the growth solution, yet careful control of addition rate and order of addition must be exhaustively exercised to provide reproducible results.[10, 11]

Ascorbic acid has been used as a mild reducing agent in the growth solution in many seeding studies, but reports by several authors seem to give inconclusive results.[11-13] Essentially, the concentration of reagents, the nature of the solvent system, the presence of additives, and the order and rate of addition of reagents all play crucial roles in determining the feasibility and effectiveness of reduction. Particularly, Pal *et al.* reported that the reduction of $HAuCl_4$ in the presence of ascorbic acid alone did not lead to reduction due to its weak reduction potential in a solution of TX-100 surfactant,[12] whereas Jana *et al.* realized a strong reduction with the acid as a clear candidate for secondary nucleation.[9] Pal *et al.* were further able

to minimize the independent growth by slowing the addition of the acid, and finally by preparing seeded nanoparticles by sequential growth, where AuNP enlarged by seeded-growth acted as seeds for further growth. In another report, Cao *et al.* were able to control the generation of spherical particles by studying the order of addition of reagents.[11] They observed that adding $HAuCl_4$ to a growth solution of nanoparticle seed and reducing agent (hydroxylamine hydrochloride in this case) produced spheres predominantly, while addition of the reducing acid to a solution of seed and metal salt resulted in a mixture of anisotropic particles as well as spheres. They also observed that the rate of particle growth was entirely dependent on the concentration of hydroxylamine, where the concentration also determined the morphologies of the particles produced; higher hydroxylamine:Au^{3+} ratios resulted in more spherical particles. Their work also acknowledged the role of anion adsorption onto the surface with anisotropic growth, where they proposed that $AuCl_4^-$ adsorbed preferentially onto {111} surfaces where atoms are most densely packed in a face-centered cubic geometry. The rate of particle growth on the {111} face is much faster than the rate of growth on the {100} face, which accounts for the formation of nanoprisms and platelets. The growth of nanoprisms is not energetically favourable, for the surface energies of the crystallographic planes are in order of $\gamma\{111\} < \gamma\{100\} < \gamma\{110\}$ for face-centered cubic structures (fcc).[14] The growth of octahedral and truncated octahedral AuNP are more energetically favourable than the growth of cubic AuNP with {100} faces.[15] The {110} face is rarely observed due to its instability. Geometries of common polyhedra for gold nanoparticles are given in Scheme 6.1.

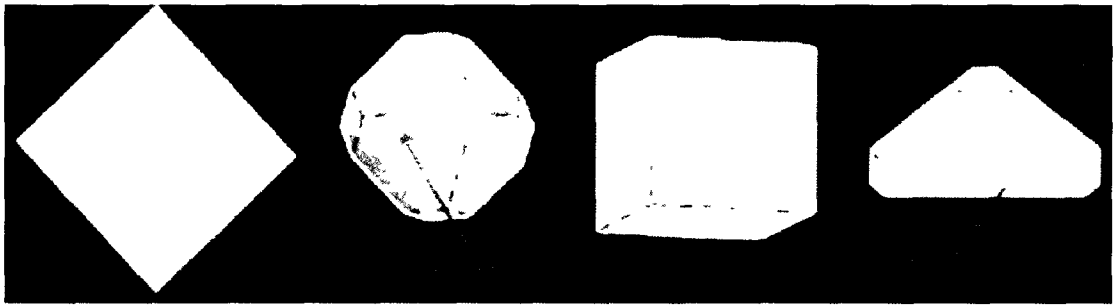

Scheme 6 . 1 - Representative polyhedra for gold nanoparticles with common fcc faces.

Herein, gold nanoparticles were grown via a seeding technique to assess the versatility of the photochemically generated particles towards this application. Aqueous gold nanoparticles synthesized using I-2959 as a reducing agent, as discussed thoroughly in Chapter 3, were used as seed particles for further growth. A selection of mild reducing agents were tested for AuNP growth *via* SPB appearance in the absence of added seed, and hydroxylamine hydrochloride was chosen as an ideal candidate with negligible particle formation. Under equivalent concentrations and conditions, however, ascorbic acid, sodium ascorbate, and hydroquinone all generated particles within 200 seconds. NH_2OH did cause a minimal reduction as determined by the growth of an SPB with low intensity, and was thus abandoned for its acidic counterpart; NH_2OH-HCl. The first procedure utilized NH_2OH-HCl as a mild reducing agent in the growth solution, where varying volumes of preformed, pre-irradiated AuNP of 10-12 nm diameter were added to a solution of 0.25 mM $HAuCl_4$ and 0.4 mM NH_2OH-HCl. The growth solution concentrations were adapted from work by Cal *et al.* who assessed the seed-mediated growth of citrate-capped nanoparticles with NH_2OH-HCl.[11] The reduction is thought to occur according to the following reaction.[16]

$$AuCl_4^- + NH_3OH^+ \longrightarrow Au^0 + 4HCl + NO \qquad (6.1)$$

Our initial work investigated the rate of reduction on the unprotected surface by varying the concentration of AuNP seed in a growth solution of constant concentration. Rachel Schwartz-Narbonne, an honours research student collaborating with the present work, investigated the kinetics of seeded growth, and found distinct differences in the rate of particle growth as well as the final morphology of particles produced with different concentrations of seed added. The details of her research are presented in her 2009 Undergraduate thesis.[17] The absorbance spectra of seeded-growth AuNP from different concentrations of AuNP seed are presented in Figure 6.1. It is clear that in the absence of seed, negligible AuNP growth took place after comparable time frame of 30-60 minutes. The results

in Figure 6.1 imply that lower seed concentration resulted in lower, broader SPB, indicative of larger AuNP.

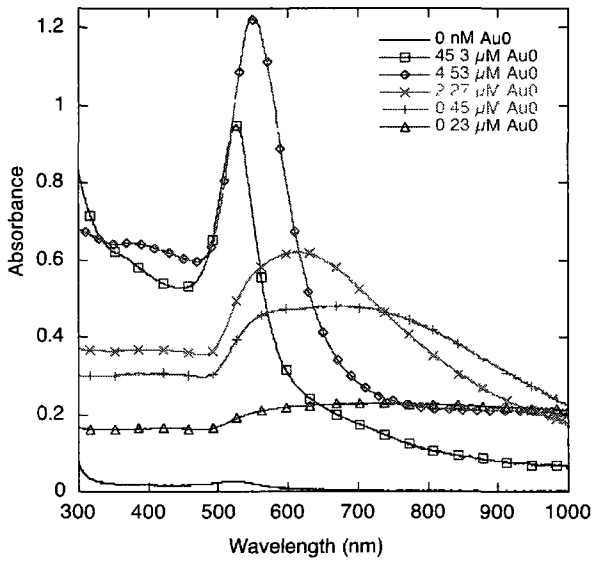

Figure 6 . 1 - Absorbance of AuNP prepared from a growth solution containg 0.25 mM $HAuCl_4$ and 0.4 mM NH_2OH-HCl upon addition of different concentrations of I-2959 AuNP seeds (10-12 nm), expressed in molarity of Au^0 added.

At high seed concentration, all of the $AuCl_4^-$ binds to the numerous surface sites of the many particles. Particles increase in size as layers of Au^0 are built up on the particle like layers on an onion. At low seed concentration, however, there are fewer surfaces in solution, and a high quantity of $AuCl_4^-$ is available to physisorb to the nanoparticle surface for reduction. As such, there is greater growth of particles as there is more $AuCl_4^-$ available per particle. This distinction in concentration is illustrated in Scheme 6.2.

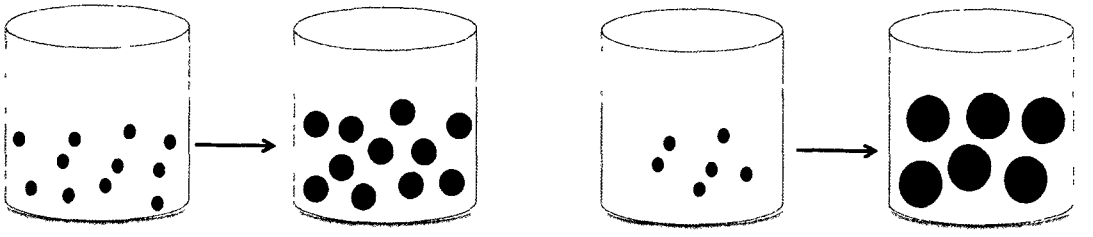

Scheme 6 . 2 - Seeded growth of colloidal gold nanoparticles. Higher concentrations of seed added to growth solution results in smaller nanoparticles in comparison to smaller seed concentration.

The seeded growth of nanoparticles displayed autocatalytic behaviour; similar to time-resolved growth studies for AuNP synthesized from photochemically-generated transient reducing agents in Chapters 3, 4 and 5. Autocatalytic growth is characterized by an induction period and a signature sigmoidal growth curve when analyzing the surface plasmon resonance absorbtion over time. The rate of growth of AuNP is a complex process with electron transfer, disproportionation, nuclei growth and surface catalyzed-reduction, as described in Chapter 1. In this research, the growth of AuNP has been analyzed by extracting the rate of autocatalytic growth from changes in SPB growth over time. The absorbance at the SPB maximum can be correlated with the yield of AuNP particles where a plot of $\ln\left(\frac{A_t}{A_f - A_t}\right)$ vs t generates a straight line with the slope equivalent to the observed rate of catalytic growth. This fit was applied to the "rapid growth" portion of the data, or the time between the induction period and the plateau period.

The time-resolved absorbance changes in the SPB of seeded-growth solutions with different concentrations of seed is given in Figure 6.2 (left), where a 100 µL aliquot of seeded AuNP was added to 1.5 mL distilled, deionized water. Plots of the change in absorbance at SPB over time are given in Figure 6.2 (right), where the slope of the line determined the growth rate as reported in Table 6.1. The particle diameters given in Table 6.1 were measured using SEM imaging analysis.

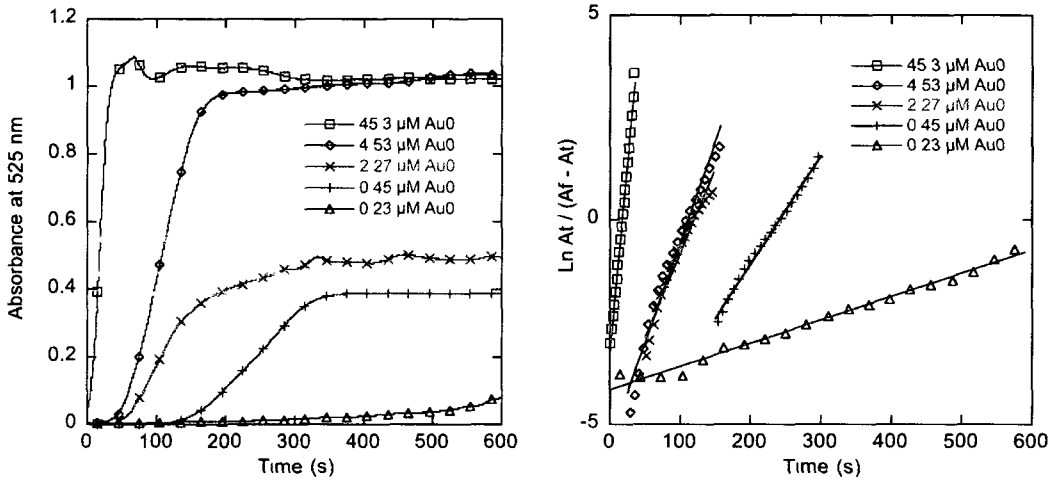

Figure 6 . 2 - Seed-mediated growth of AuNP at various concentrations of seed in 0.25 mM $HAuCl_4$ and 0.4 mM NH_2OH-HCl growth solution. (left) Growth of AuNP over time as monitored at 525 nm, and (right), linear analysis of the changes in absorbance from plots on the left.

It is clear from the spectra that the higher the concentration of seed, the faster the particle growth. The rates of particle growth were approximated by applying the linear fit for absorbance at 525 nm to determine the rate, *v*, and the data is compared in Table 6.1.

V_{seed} (µL)	C_{seed} (µM Au^0)	*v* (Ms^{-1})	Particle Size (nm)	
			Predicted	SEM
undiluted	135.9	N/A	N/A	10.3 ± 3.4
1000	45.3	0.1887	17.9	N/A
100	4.53	0.0488	39.7	36.4 ± 17
50	2.27	0.0410	50.0	N/A
10	0.45	0.0266	85.8	166.7 ± 45
5	0.27	0.0057	101.7	N/A

Table 6 . 1 - Variation in the observed rate constant with different concentration of seed added to growth solutions containing 0.26 mM $HAuCl_4$ and 0.40 mM NH_2OH-HCl.

Using the seeding approach, the size of the resulting particle, d_{final} can be calculated from the following equation adopted from work by Schmid *et al.*[18]

$$d_{final} = d_{seed}\sqrt[3]{[Au^0] + \frac{[Au^{3+}]}{[Au^0]}} \qquad (6.1)$$

Where d_{seed} is the diameter of the seed particle, $[Au^{3+}]$ is the concentration of the gold salt in the growth solution, and $[Au^0]$ is the concentration of gold atoms in solution. The concentration of gold atoms in solution was approximated using the molar extinction coefficient for 10 nm AuNP at 525 nm, intrapolated to be 2.5 x 10^8 $M^{-1}cm^{-1}$ from work by Jana *et al.*[4] Applying Beer's law given an absorbance of the AuNP seed solution of 1.2, the concentration of AuNP was determined to be 4.8 x 10^{-9} M particles. The number of gold atoms per particle, *N*, can be determined from the following equation[19]

$$N = \frac{\pi \rho D^3 N_A}{6M} \qquad (6.2)$$

where ρ is the packing density for gold, 19.3 g/cm^3, *D* is the nanoparticle diameter, N_A is Avogadro's number and *M* is the molecular weight of gold. Following this method, a concentration of 0.136 mM Au^0 was determined for a solution of 10 nm AuNP prepared under optimal I-2959 synthesis.

Because the particle surface itself is a site of reduction, the growth behaviour is intuitive in that new layers of particles form faster when more reducing agent is present as the concentration of $HAuCl_4$ is held constant. Additionally, the lesser the concentration of seed added, the larger particles result, as indicated by a greater absorbance bathochromic shift and broadening of the surface plasmon band.[20] The broadening of the resonance band is also indicative of particle agglomeration, which is surprisingly evident by SEM images as shown in Figure 6.3, center and right. The average particle size for AuNP prepared from 0.45 μM Au^0 measured 166.2 ± 44.5 nm, while particles prepared from 4.53 μM Au^0 were 36.4 ± 16.9 nm. While the

predicted particle diameter agreed well with the measured diameter from SEM measurements, the smaller seed concentration of 0.45 μM resulted in much larger particles. Interestingly, particles appear with dents and divets as though they resulted from the agglomeration of smaller particles onto larger particles. Other reports have observed similar structures for the generation of AuNP via seeded growth upon addition of $AgNO_3$ to form gold nanothorns, where lower concentrations of adsorbed ions induced a morphology changes from spherical to pseudo-spherical with several dents [21]

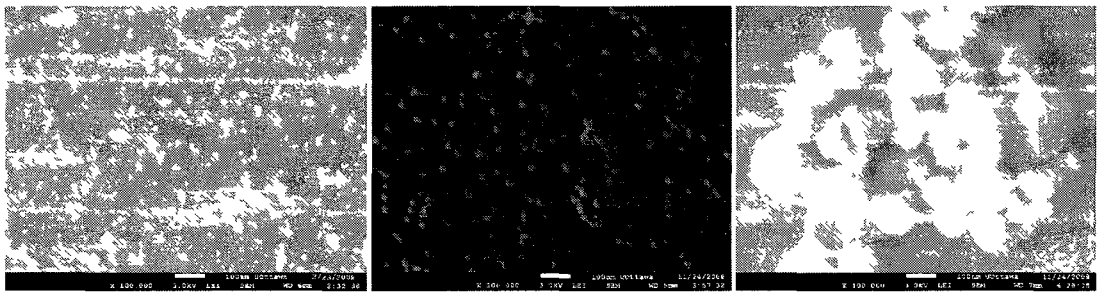

Figure 6 . 3 - SEM image of I-2959 synthesized seed(left) and seed-mediated AuNP prepared from (center) 4.53 μM Au^0 and (right) 0.45 μM Au^0 in 0.25 mM $HAuCl_4$ and 0.40 mM NH_2OH-HCl. All scale bars represent 100 nm.

In our research at low seed concentration, secondary nucleation within the growth solution is believed to play a role. The generation of anisotropic particles such as nanorods and triangular or hexagonal nanoprisms is also evident in the images, although low absorption at wavelengths > 800 nm do not indicate a sufficient population of these geometries. Other researchers have also observed the slight presence of anisotropic shapes within spherical nanoparticle synthesis.[8, 9 11 22] The prisms can be attributed to both the slow reduction of Au^{3+} and Au^{+} to Au^0, which desorb from the surface and slowly form clusters and single crystal prisms, as well as the blockage of surface sites by $AuCl_4^-$ ions such that growth occurs in the {111} direction to form single crystals as evidenced by others.[22] A recent report attributed the growth of anisotropic prisms to the addition of adatoms (or reduced Au^0 on the surfaces of seeds in this case) to twinned plane boundaries.[23] A pictoral description is provided in Scheme 6.3. The rapid photochemical synthesis of spherical

nanoparticles, on the other hand, produces polycrystalline particles with multiple crystal faces.

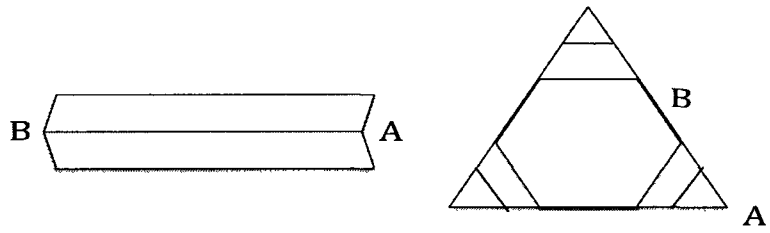

Scheme 6 . 3 – (left) Formation of twinned plane boundaries resulting in edges A and B with (111) directionality. Addition of adatoms to the A metal surface results in greater stabilization for adatom growth realative to surface B. (right) With extensive growth, large prisms are formed, as the (111) surface is consumed.

In search of greater control over particle size and monodispersity, the order of addition of reagents was tested to compare results for this method with previous studies. In this direction, hydroxylamine HCl was added to the growth solution containing the auric salt and the seed. Similar to experiments performed by Jana *et al.*,[9] a fresh solution of NH_2OH-HCl was added dropwise over the course of ten minutes to solutions of varied seed concentrations. As such, there was a much greater polydispersity observed, yet minimal differences in the absorbance spectra for the different seed concentrations are shown in Figure 6.4, left. SEM of the 0.33 μM Au^0 seeded sample revealed the presence of spheres of multiple sizes as well as rods and prisms, as displayed in Figure 6.4, right. The similarity in absorbance profile for all five concentrations suggests little variance from sample to sample and therefore identifies a lack of control with the dropwise addition method. With little variation in seed concentration, the rate of seed-mediated growth is dependent on the concentation and rate of addition of mild reducing agent. Slow addition of the mild reducing agent was the likely cause for the anisotropic prisms, and the greater concentration of seed led to a greater number of AuNP as implied by the greater absorption intensity. These results agree with work by Cao *et al.*, who observed significant growth of anisotropic particles when NH_2OH-HCl was added last, and the non-spherical growth was further intensified when the reducing agent was added slowly (dropwise).[11]

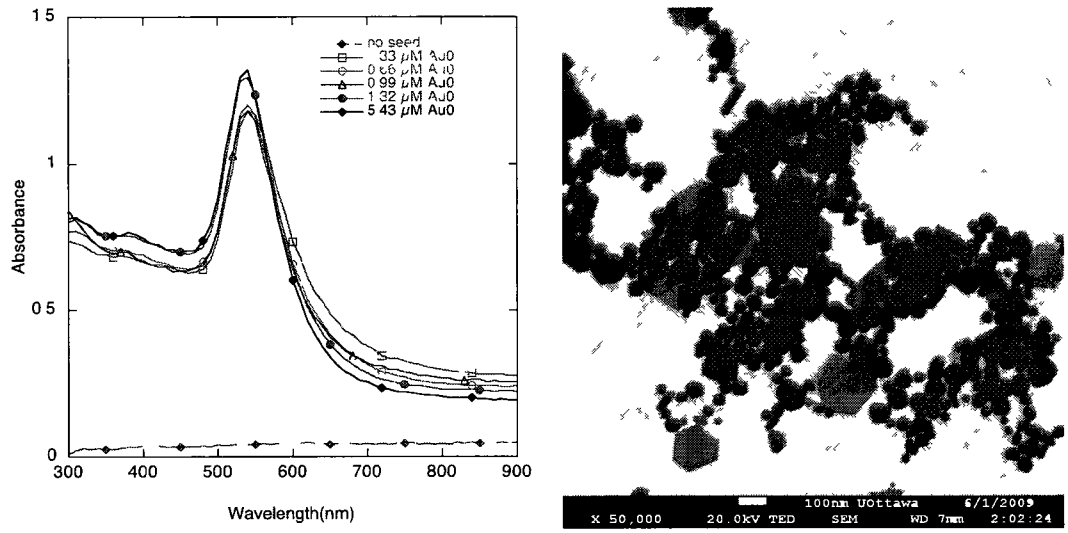

Figure 6 . 4 - (left) Absorption of seed-mediated growth AuNP for solutions of varied seed concentration in 0.25 mM $HAuCl_4$ upon slow dropwise addition of 0.40 mM NH_2OH-HCl. (Right) SEM image of AuNP corresponding to the absorbance of dropwise seeded AuNP from 0.33 μM Au^0. The scale bar represents 100 nm.

The generation of seeded particles using NH_2OH-HCl offered a very simple and quick method for generating a larger size of nanoparticles, where growth was often complete in a few minutes. The seeded particles were stable for 5 to 6 days, however the more anisotropic prisms suffered from precipitation within a couple of days of synthesis. While seeding with NH_2OH-HCl is not a novel technique, this research verified the applicability of this process to photochemically generated aqueous particles from I-2959, as well as allowed the investigation of the rate of growth on the unprotected surface.

Greater control over particle size, as well as morphology and size dispersity is needed for application, and this niche was assessed through a novel photochemical seeding approach.

6.3 Photoseeding

An alternative method was devised for better control of seeding wherein seeds were grown under photolytic conditions and added to a growth solution that was further irradiated. Carefully controlling the concentration of reducing agent, gold salt and metal particle allowed simple and reproducible growth of monodisperse nanoparticles to be achieved.

Previous work by Henglein *et al.* established an effective method for seed-mediated growth *via* γ-irradiation to generate the reductive hydroxymethyl radical, $\bullet CH_2OH$, from photolysis of N_2O and H_2O in methanol, and using citrate-stabilized 15 nm AuNP as a seed.[24] $Au(CN)_2$ was used as the metal salt for it dissociated at a slower rate and thus minimized secondary nucleation. Nevertheless, spherical and monodisperse particles were generated from 30 to 120 nm in diameter. A second report by the same authors furthered the investigation with reduction using the same $\bullet CH_2OH$ radical approach in solution containing PVP or PVA as stabilizers.[25] Their work used seeds 1.5-2.5 nm and profited from improved size control of smaller particles with the advantage of stabilizers for monodisperse particle size and morphology. In both cases, the reduction process was proposed as surface mediated catalysis whereby the reducing radical donates an electron to the already existing seed, and the stored electron reduces the Au^+ ions physisorbed to the surface. This method necessitated high energy radiolysis for the generation of $\bullet CH_2OH$, as well as long irradiation times on the order of several hours.

Given the success achieved in photochemical seeding with radical-mediated species, a similar approach was attempted using a less energetically exhaustive technique of UVA photolysis for the generation of reductive radicals. All photoseeding experiments were performed under aerated conditions.

6.3.1 I-2959

Initial attempts to grow AuNP by a photochemical seeding approach were executed by adding different concentrations of I-2959-generated AuNP to a growth solution containing $HAuCl_4$ and I-2959. The concentration of I-2959 needed to be low enough to minimize secondary nucleation and therefore needed to be well below the stoichiometric concentration for typical I-2959 particle synthesis. As such, the concentration was optimized at 0.5 mM I-2959. Samples were all irradiated for 30 minutes. Due to experimental challenges, the growth of AuNP over time measured spectrophotometricallly was not determined within the timescale of growth.

This photochemical technique offered improved monodispersity over equivalent concentrations of seed in comparison to the NH_2OH-HCl method. This is easily understood upon comparison of the SEM images of Figure 6.3 with Figure 6.6 at near equivalent seed concentrations. While there still remains to be some anisotropic growth of prisms at higher seed concentration, greater controlled growth of spherical particles has been attained at lower concentrations. A comparison of measured seeded particle diameters can also be made between the values in Table 6.1 and 6.2. The measured diameters via SEM are much closer to the predicted values when Equation 6.1 is applied. SEM of the I-2959 photoseeded AuNP are presented in Figure 6.6. The standard deviation is less for the photoseeded particles, which also decreases with increasing particle diameter. This has also been observed in the work by Henglein *et al.*[25]

V_{seed} (μL)	[Au^0] (μM)	Particle Diameter (nm)	
		Predicted	Measured (SEM)
200	6.61	33.6	47.9 ± 14.5
50	1.65	53.3	68.1 ± 15.6
10	0.33	91.2	98.1 ± 23.4

Table 6 . 2 - Comparison of AuNP seeded-growth diameters between the predicted diameter and the measured diameter via SEM.

Upon analysis of the absorbance spectra for the photoseeded-growth solutions in Figure 6.5, it is apparent that secondary nucleation is not a factor in this preparation when AuNP seeds are present, as concluded from the absence of particles in the 10 nm range.

In the absence of seed, however, the concentration of 0.25 mM I-2959 is sufficient to produce AuNP with a rather narrow SPB. The absorbance is unlike those presented in Chapter 3 for nanoparticles prepared from a 0.5:1 I-2959:$HAuCl_4$ ratio. While this result is surprising on its own, the preference for ketyl radicals to reduce surface-adsorbed Au^{3+} and Au^{+} is strong. The redshifting towards lower energy with decreased seed concentration follows the expected trend with increasing particle diameter.

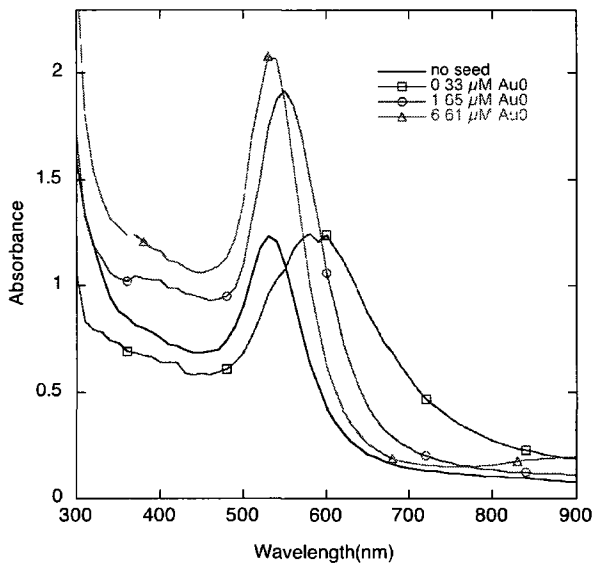

Figure 6 . 5 - Absorption spectrum of AuNP prepared from I-2959 seeding at different volumes of seed particle added to a growth solution containing 0.25 mM I-2959 and 0.4 mM $HAuCl_4$ following 30 minutes UVA photolysis.

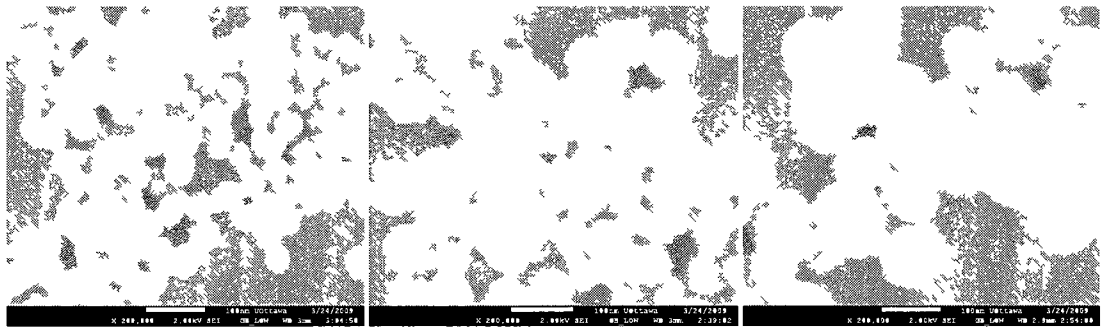

Figure 6 . 6 - SEM images of AuNP prepared via photochemical seeding with 0.25 mM I-2959 and 0.4 mM $HAuCl_4$ as the growth solution. Images reflect samples prepared from 6.61 µM I-2959-AuNP seeds (left), 1.65 µM seeds (center) and 0.33 µM seeds (right) following 30 minutes UVA photolysis. Scale bars all represent 100 nm.

The growth of photoseeded AuNP was slower relative to the growth using NH_2OH-HCl, where both methods have been performed under aereated conditions. After three minutes of photolysis, no increase in the absorbance solution had been identified for solutions containing the higher concentration of seed, whereas the reduction occurred essentially instantly with the amine. The rate of photoseeding could likely be accelerated in the absence of oxygen, based on growth experiments with ketyl radicals discussed in Chapters 3 and 4. The results in Section 6 2 using NH_2OH indicate that slow growth resulted in uniform, monodisperse seeded-particles, while fast growth afforded polydisperse spheres and anisotropic plates. The rate of growth was controlled by the concentration of seed added. With a photochemical approach, however, growth resulted in more monodisperse particles at all seed concentrations added, presumably through a more constant rate of formation of reducing agent, resulting in more uniform growth. Due to time constraints, no kinetic analysis of seeded growth was performed.

Careful control over surface growth was developed further by decreasing the concentration of the photoinitiator. Particularly, a subsequent seeding method was adopted. Herein, photochemically prepared seeds of 10-12 nm diameter were prepared from the I-2959 method and added to a growth solution containing 0.5 mM $HAuCl_4$ and 0.25 mM I-2959. The low concentration of reducing agent was devised to minimize secondary nucleation The solutions were prepared following a

sequential growth method by Henglein *et al.*[24] such that 1/8th the volume of seed solution was added to 7/8th volume of growth solution, irradiated for 15 minutes and ripened for 30 minutes. This sample was labeled A. Aliquots of A were subsequently added to another growth solution, B, of identical concentration followed with irradiation for 15 minutes, ripening and further subsequent seeding to C and then D. The procedure is illustrated in Scheme 6.4.

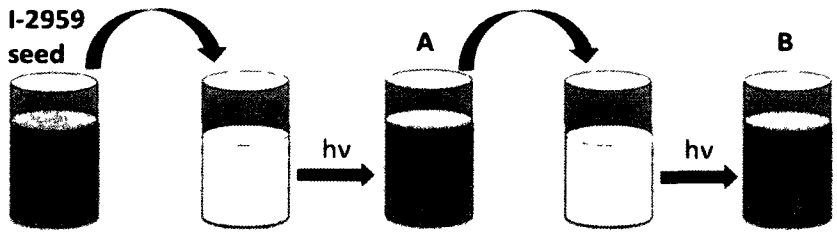

Scheme 6 . 4 - Subsequent photochemical seeding employing I-2959 or H_2O_2. An aliquot of I-2959-AuNP were used as seeds for addition to a growth solution, followed by UVA photolysis.

Further details for the method are available in Section 2.5.3. The irradiation time was held constant at 15 minutes in all cases. The SEM and corresponding absorption spectra are illustrated in Figure 6.7 and 6.8, respectively.

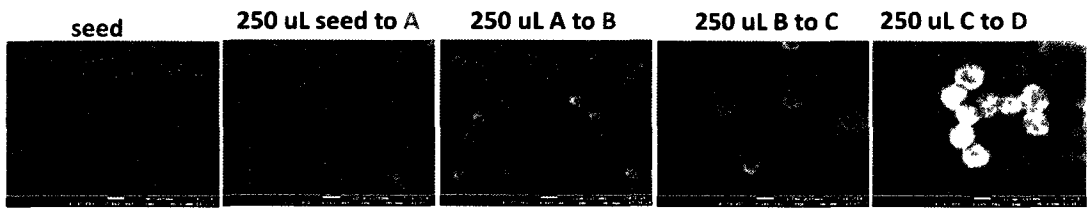

Figure 6 . 7 - SEM images of particles prepared from sequential seed-mediated growth with 0.25 $HAuCl_4$ and 0.13 mM I-2959 as the growth solution. The samples correspond to the absorbance spectra in Figure 6.8. The scale bars represent 100 nm in all images.

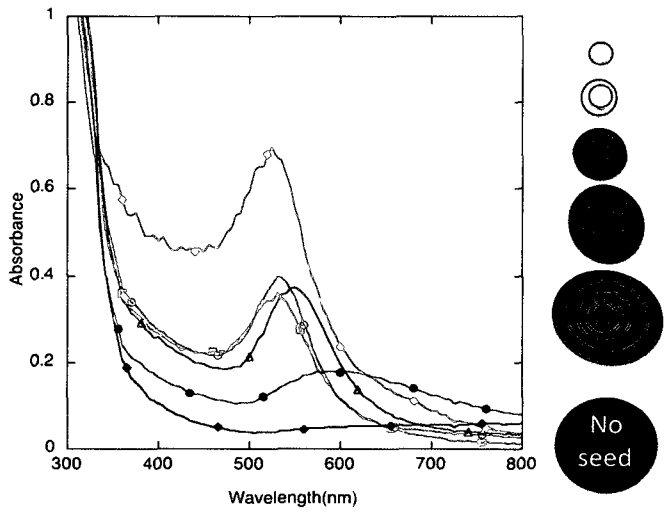

Figure 6 . 8 - UV-VIS absorption spectra of seed-mediated photochemical growth of AuNP prepared via photolysis of growth solution containing 0.5 mM $HAuCl_4$ and 0.13 mM I-2959. Each solution was composed of 1/8th seed volume and 7/8th growth solution volume. Each sample was photolyzed for 15 minutes and ripened for 30 minutes prior to further seeding.

In previous reports, similar methods for doubling of particle diameter were carried out with increasing irradiation time, ranging from 10 to 23 hours with γ radiolysis.[24, 25] It is worth emphasizing that UVA photolysis with an I-2959 system has proven successful with significantly less time. The absorption spectra of Figure 6.8 show a remarkable decrease in secondary nucleation in the absence of any seed. The absorption spectrum of the seeds is high as it was an undiluted sample. The initial aborbance for seeds A and B are lower than expected, and is a result of slower photochemical AuNP generation, for the irradiation time was decreased to 15 minutes relative to the spectra of Figure 6.5. At further seeding, however, the particle size nearly doubles, and the SPB redshifts for C and D. These absorbance bands are as expected. The latter samples do result in anisotropic particle growth where particles of 80-120 nm were prepared along with anisotropic plates of micron diameters.

It is worth repeating that the anisotropic growth is the result of an excess of $AuCl_4^-$ not reduced by catalytic surface sites on metal nanoparticles as there are fewer

nanoparticles per equal volume and fewer surface sites. Further studies were performed to improve the range over particle size, where a lower concentration of Au^0 was added to generate more monodisperse NP. The results are tabulated in Table 6.3.

Seed fraction	$[Au^0]$ (μM)	Irradiation time (min)	Particle diameter (nm)
seed	136	30	10
$1/10^{th}$	13.6	15	22.0 ± 5.3
$1/8^{th}$	17.0	15	28.7 ± 12.1
$1/10^{th}$ A'	13.5	15	41.3 ± 14.2
$1/8^{th}$ A	16.8	15	53.0 ± 12.3
$1/10^{th}$ B'	35.3	15	89.0 ± 14.2
$1/8^{th}$ B	44.2	15	103.0 ± 26.6 + plates
$1/8^{th}$ C	9.3	15	146.8 ± 18.7 + plates

Table 6 . 3 - Summary of subsequent photochemical seeding via I-2959 reduction. A = seeded AuNP at $1/8^{th}$ volume. B= seeded A at $1/8^{th}$ volume. C= seeded B at $1/8^{th}$ volume. A'= seeded AuNP at $1/10^{th}$ volume. B'= seeded A' at $1/10^{th}$ volume.

The concentration of Au^0 seed was calculated from the absorbance of the solution. For larger particles, however, larger molar extinction coefficients were approximated based on work by Jana *et al.*[4] with the absorbance of the seeded particles. The molar extinction coeffecient for 30 nm particles was $3.5 \times 10^9\ M^{-1}cm^{-1}$, and estimated at $2.2 \times 10^{10}\ M^{-1}cm^{-1}$ for 90 nm particles.

While seeding appeared to be effective for generation of particle diameters in the 20-80 nm range, seeding of larger particles tended to generate polymorphic samples with spherical particles aggregated together. We believe that further tuning of irradiation time and particle concentration will lead to a series of recipies for particles within a narrow diameter range.

6.3.2 H_2O_2

Gold nanoparticles have also been seeded with hydrogen peroxide as a reducing agent. H_2O_2 possesses a less negative reduction potential than the I-2959 ketyl

radical, and this deficiency can be advantageous with photochemical control over seed-mediated growth. Identical conditions were employed as those described in Section 6.3.1, except the concentration of H_2O_2 in the growth solution was increased to 0.5 mM for a 1:1 ratio of Au^{3+}: reducing agent in this method. The results are presented in Figure 6.9 with SEM images and corresponding absorption spectra. The images reveal a better control over particle size dispersity, yet a greater susceptibility to aggregation in the absence of stabilizing agents in comparison with the I-2959 photoseeding technique.

Additionally, the absorption spectra show greater absorption intensity as well as a greater distinction in SPB for each solution relative again to the I-2959 approach. These differences could result from greater Au^{3+} adsorption in the absence of physisorbed I-2959, photoproducts and thus more seeding. Furthermore, a greater control of particle size was also explored by differing seed ratios, and the results are tabulated in Table 6.4.

Seed fraction	$[Au^0]$ (μM)	Irradiation time (min)	Particle diameter (nm)
seed	136	30	10
$1/10^{th}$	13.6	15	28.9 ± 9.7
$1/8^{th}$	17.0	15	35.4 ± 10.0
$1/10^{th}$ A'	32.4	15	53.3 ± 15.4
$1/8^{th}$ A	40.6	15	62.3 ± 10.6
$1/10^{th}$ B'	34.3	15	83.6 ± 15.9
$1/8^{th}$ B	42.9	15	90.0 ± 34.1
$1/8^{th}$ C	13.8	15	156.2 ± 35 + plates

Table 6 . 4 - Summary of subsequent photochemical seeding via H_2O_2 reduction. A = seeded AuNP at $1/8^{th}$ volume. B= seeded A at $1/8^{th}$ volume. C= seeded B at $1/8^{th}$ volume. A'= seeded AuNP at $1/10^{th}$ volume. B'= seeded A' at $1/10^{th}$ volume.

The concentration of Au^0 was calculated in an identical procedure as described for I-2959 photoseeded AuNP.

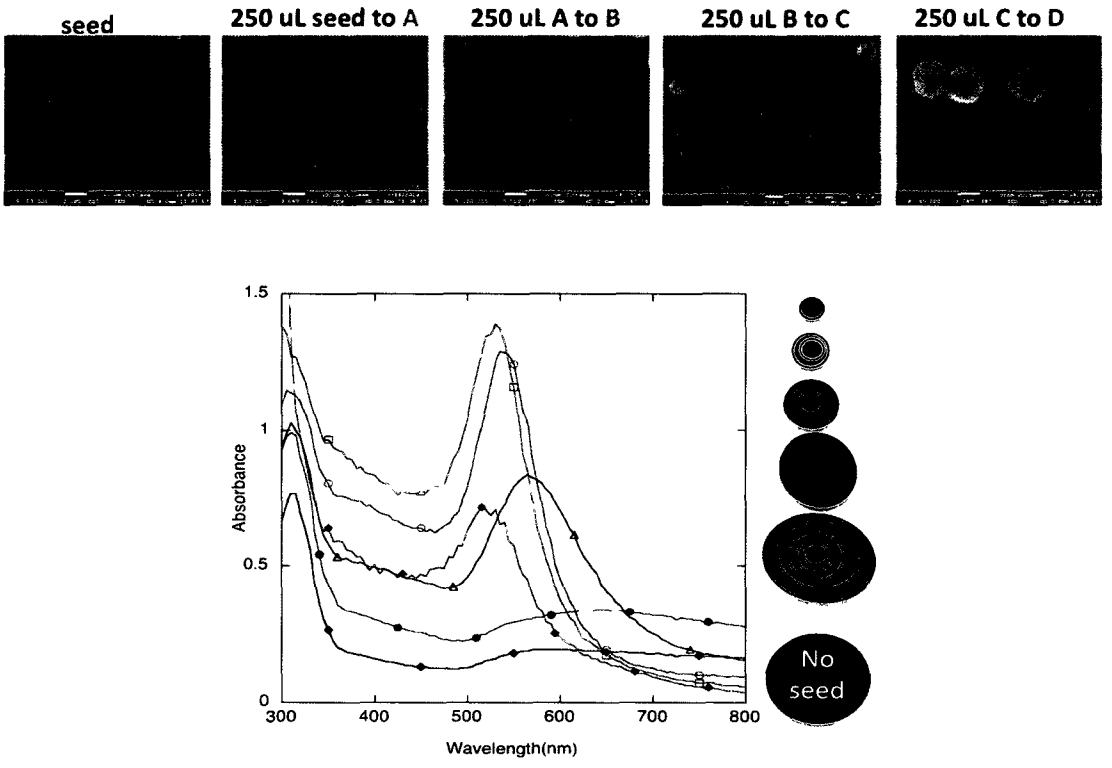

Figure 6 . 9 - SEM images and UV-VIS absorption spectra of seed-mediated photochemical growth of AuNP prepared via photolysis of growth solution containing 0.5 mM $HAuCl_4$ and 0.5 mM H_2O_2. Each solution was composed of $1/8^{th}$ seed volume and $7/8^{th}$ growth solution volume. Each sample was subjected to 15 min UVA followed by 30 min ripening. The scale bars for the SEM images each represent 100 nm.

With both the I-2959 and H_2O_2 systems, switching to $1/10^{th}$ seed volume, in other words decreasing the number of gold atoms in solution, decreased the particle size relative to the $1/8^{th}$ volume. These results are contrary to those obtained with the NH_2OH-HCl and other thermal seeding methods. This could be related to a significant change in kinetics. For the NH_2OH-HCl method, the autocatalytic growth is essentially diffusion controlled at high Au^0 concentration. Under these conditions, however, the rate of growth is regulated by the rate of ketyl radical formation and offers a new dimension of control over nanoparticle growth.

Overall, the particle growth via H_2O_2 offers higher seeded-AuNP yield but slightly larger AuNP with narrower size distribution as judged by absorption intensity and

SEM imaging relative to the I-2959 method. With the strong absorbance of AuNP in the UVA region, the photolysis of I-2959 was screened and the concentration of ketyl radicals decreased relative to a nucleated photochemical synthesis. The absorbance of $HAuCl_4$, however, was less inhibited as it has a greater absorbance in the UVA region. Recall the comparative absorbances from Figure 3.16. Both methods, nevertheless, outperform the NH_2OH-HCl at relatively comparable Au^0 concentrations, as indicated by the lesser secondary nucleation and narrowed particle size. Photochemical seeding is a useful method for enhancing particle growth with good monodispersity beyond the 20 nm size regime, where particle size is regulated by the rate of delivery of the reducing agent, and the power of the reducing agent is minimized by screened absorbance from AuNP. In order to stabilize the particles for better size distribution, 4-HEBA, the photoproduct responsible for I-2959 AuNP stabilization, was added *in-situ* to the growth solutions at 1.0 mM concentration. This allowed the particles to remain stable for an extened period of time; that is a couple of weeks instead of days.

The success of seed-mediated growth on the particle surface emphasizes the catalytic activity as a result of high surface energies in the nanoscale range. A similar photochemical technique has also been developed by others in the research group for bimetallic nanoparticle growth in the generation of core-shell gold/silver nanostructures.[26] Therein, gold nanoparticles were synthesized with photolysis of I-2959 in a CTAC system followed by subsequent photolysis of the AuNP seed in a growth solution of CTAC and $AgNO_3$.

Within this research, a monometallic theme was continued and research focused on the stabilization of gold nanoparticles. As such, surface-mediated growth was continued with the generation of a silica shell, and is discussed in Section 6.4.

6.4 Surface Modification With a Silica shell

The success of the photochemical generation of AuNP via photolysis of I-2959 was further exploited in this research where the particles were used as seeds for the growth of a silica shell on the particle surface. Modifying a synthetic technique by Liz-Marzan *et al.*, silica shells were grown in a simple aqueous environment.[27, 28] The general synthesis is illustrated in Scheme 6.5.

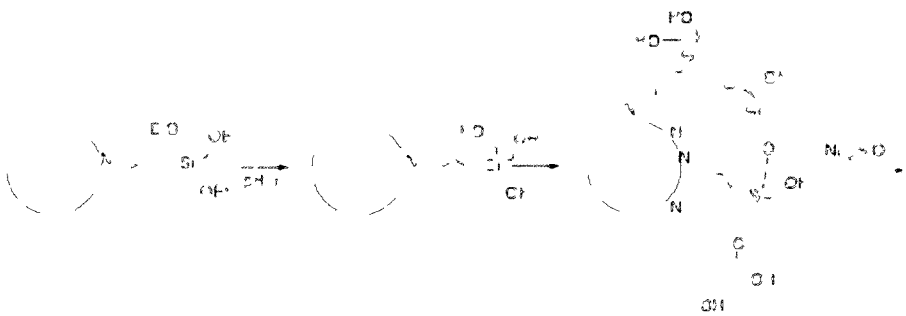

Scheme 6 . 5 - Synthesis of a SiO_2 shell on AuNP

In a typical experiment, 3-aminopropyltriethoxysilane (APTES) was added to an aqueous solution of colloidal gold nanoparticles to render the surface vitriophilic. Essentially, the amine group of the short alkyl chain binds to the gold surface while the silane moiety facilitates polymerization of silica upon addition of Na_3SiO_2. The details of the synthesis are included in Section 2.5.4.1. The solutions were left to grow a dense silica shell for a number of days, and the width of the shell ranged from 5-12 nm with time from two to six days. Particles were centrifuged to remove SiNP, and resuspended in distilled, deionized water or ethanol and displayed prolonged stability on the order of a couple of years.

As the shell is transparent, there are no changes in optical properties or the SPB of AuNP upon functionalization of the gold surface with a silica shell. SEM images of the particles grown after two days are displayed in Figure 6.10. Previous reports

have addressed the occurrence of multiple cores polymerized into one shell of SiO_2 in the formation of SiO_2 aggregates [29] While a small number of particles appear to be grouped together, this synthesis has largely generated individually functionalized seeds Notably, however, the aggregation of AuNP@SiO_2 particles on a dried copper grid is a poor interpretation of the separation and electrostatic forces in solution

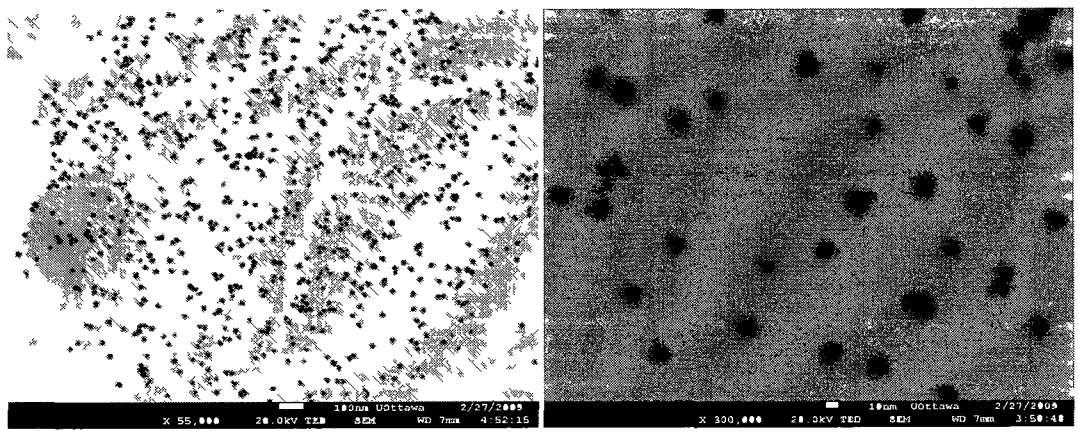

Figure 6 . 10 - SEM images of AuNP with a shell of amorphous silica grown for two days in aqueous solution The bar size represents 100 nm (left) and 10 nm (right).

Essentially, the shell functions as a protective but transparent shield that can be used to support AuNP in a variety of imaging, drug delivery and catalytic applications where harsh solution conditions could otherwise cause agglomeration and precipitation of the colloidal solution Within a silica shell, AuNP were stable in a variety of organic solvents such as toluene, dichloromethane and chloroform The modified particles also displayed profound stability under harsh pH condition in the range of pH 2-12, yet the absorbances redshifted at pH 1, and 13-14

One approach to test the strength of the silica shell was to expose the modified particles to caustic conditions In the presence of 0 1 M KCN and 1 0 M KOH, unprotected AuNP were dissolved and etched as KCN performed as an oxidizing agent The process occurred rather rapidly, and the dissapearance of the SPB of the spherical particles was monitored over time at 525 nm 500 µL aliquots of AuNP

were added to 2.5 mL etchant solution. The process was also replicated in the presence of a SiO_2 shell, and the results are compared in Figure 6.11. A resistance to corrosion was observed, but the shell did not provide complete protection against the harsh conditions of etching. In fact, the dense shell is a porous amorphous layer that allows for the transport of small molecules to the gold surface.[30] The shell merely delayed the attack of the etchant to the surface, as the rate of decrease is slower in the presence of the shell, yet the same loss of plasmon absorbance is attained overall when the absorption intensity are normalized. No SEM analysis of the etched particles was performed.

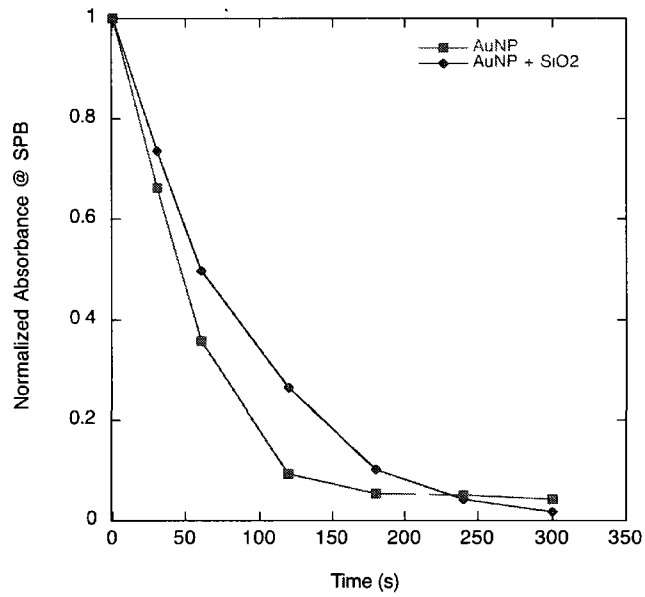

Figure 6 . 11 - Etching of AuNP over time with and without a SiO_2 shell in a solution of 0.1 M KCN in 1.0 M KOH. Shell size approximately 10 nm grown after four days.

Alternatively, the shell was also evaluated for protection of the catalytic gold surface against further gold seeding with the thermal hydroxylamine hydrochloride system discussed in Section 6.2. Interestingly, instead of preventing further particle growth, the new insulating surface acted as a new site for autocatalytic growth of new gold layer. The rates of growth were monitored with addition of different concentrations

of seed, and compared with the rates of seeding on a bare gold surface. The data is presented in Figure 6.12. At greater seed concentration, the rate of seeding is essentially similar and instantaneous as $AuCl_4^-$ is rapidly adsorbed to the surface followed by surface-catalyzed growth.

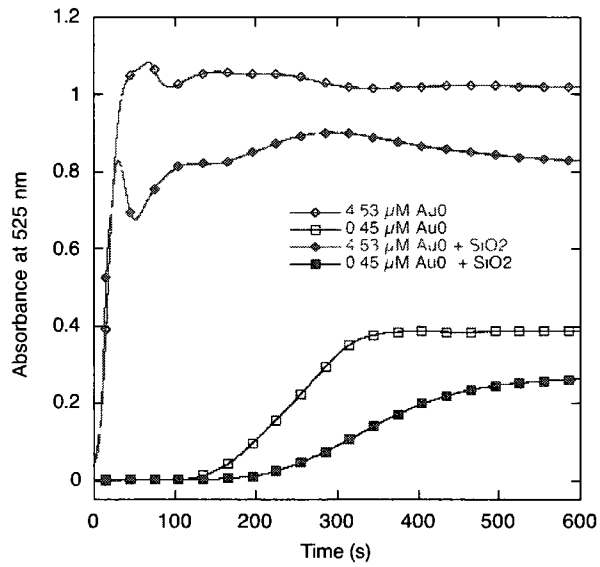

Figure 6 . 12 - Seed-mediated growth of Au layer on AuNP and Au/SiO2 over time. Growth solution contains 0.25 mM $HAuCl_4$ and 0.4 mM $HAuCl_4$.

pH studies on the silica-modified particles validate the stability and versatility of samples coated with a transparent layer of amorphous glass. The etching approach furthermore verifies the presence of a silica layer on the surface of gold nanoparticles, and seeding experiments identify similar reactive properties with the gold core.

6.5 Surface functionalization

The surfaces of AuNP prepared in a photochemical approach via I-2959 photolysis have been studied extensively for their ability to be functionalized with a variety of different ligands. The goal was to observe the effect of different functional groups

binding to the particle surface and to achieve stability of the resulting colloid for further potential applications. A selection of ligands was focused on water-soluble compounds possessing moieties favourable for further chemical modification.

Essentially, atoms possessing strong interactions with gold atoms were chosen as head groups, such as thiols and amines, which are both soft acids to complement the soft metal. The length and packing density was also varied in effort to further understand the dynamics of surface functionalization. Terminal groups of the molecule with alcohols or carboxylic acids were eagerly investigated owing to their ability for modification through common synthetic routes for further assembly and application. Linkage of AuNP to drugs, probes and biological molecules are common for designing diagnostic tools.[3]

Research commenced with hydrophilic molecules and progressed with simpler, longer alkyl chain derivatives. It is worth stating that a greater variety of ligands were probed for surface stabilization, however only a select few were chosen for further study and discussed in this thesis. Initial investigations were principally based on absorption spectroscopy due to availability of instrumentation at the time. A discussion in the remainder of the chapter will deal with multifunctional, hydrophilic ligands, followed by a comparison with primary aliphatic compounds.

6.5.1 Multifunctional ligands

The following ligands were used to modify the surface of gold nanoparticles: 3-mercaptopropane sulfonic acid sodium salt (MPSA), 16-mercaptohexadecanoic acid (MHDA), 4,4'-dithiodibutyric acid (DTBA), cysteine (CYS), 2-mercaptothazoline (MTHZ) and ethanolamine (ETHA). The structures of these compounds are given in Scheme 6.6.

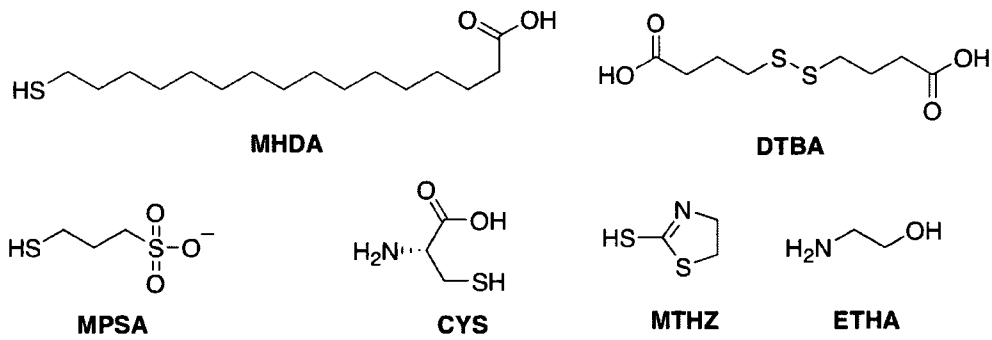

Scheme 6 . 6 - Various multifunctional ligands studied for surface functionalization of aqueous gold nanoparticles.

The procedure for ligand modification varied over the course of the research and with particular experiments, but can be generalized in the following way. AuNP were synthesized using I-2959 as previously outlined in Chapter 3. Briefly, nanoparticles were produced from photolysis of 0.33 mM $HAuCl_4$ and 1.0 mM I-2959 aqueous solution with 30 minutes irradiation using 14 UVA lamps. Further synthetic details are available is Section 2.5.4. Particles were left to "ripen" under dark conditions for 3-12 hours prior to further modification. This allowed complete growth of AuNP through the autocatalytic mechanism, where slow disproportionaition of remaining Au^+ after irradiation was arrested and led to further reduction and nanoparticle growth. The colloid was centrifuged and resuspended in either ddH_2O or 1.0 mM NaOH. This step removed residual photoproducts and HCl from the medium prior to further modification. Stock solutions of 10-50 mM ligand were prepared in water for MPSA, CYS, MTHA and ETHA, while ethanol or 1.0 mM NaOH was necessary to dissolve MHDA or DTBA. Ligands were added at various concentrations and/or pH to study the stability of the resulting colloid. The functionalization step took place either under static conditions in a well plate, or in a polycarbonate centrifuge tube under moderate shaking for a minimum of 24 hours. AuNP were then centrifuged to remove residual and unbound molecules, and resuspended in distilled, deionized water, 1.0 mM NaOH, or 1:1 H_2O:EtOH depending on the solubility of the functional tail groups of the ligands.

Upon AuNP functionalization, the position and breadth of the surface plasmon band indicated the degree of particle flocculation. The term flocculation has been previously defined and adopted to vaguely describe particles that have either agglomerated in a loose but reversible fashion, as well as particles that have aggregated with a dense and irreversible process. Identifying which state the organization is in remains a challenge with UV-VIS spectroscopy alone.[31]

In this research, AuNP showed strong sensitivity to many of the ligands studied. IR and NMR studies of ligand-nanoparticle characterization proved challenging due to the low concentration of ligands bound to the particle surface. Given the concentration of NP in solution along with the number of atoms per 10 nm particle derived from Equation 6.2, and calculating the number of surface atoms per particle based on the gold atomic radius of 144 pm, an upper limit for a monolayer concentration was determined to be 18 μM such that every surface atom would be tethered to a ligand. Practically speaking, bound ligand concentrations are lower due to other physisorbed ligands, or steric interactions, and the concentration of ligands on the nanoparticle surface after centrifugation is too low for the sensitivity of these techniques. For this reason, the sensitivity of the SPB and absorbance spectroscopy was used as a main tool for characterizing colloidal nanoparticle interactions.

Early surface modifications performed in water led to strong redshifts in the SPB and frequent precipitation of particles from solution at mM ligand concentration. At one point, a number of ligands were probed in a variety of buffers, particularly 7.5 mM phosphate buffer. Ligand chemisorption was questioned, however, as negligible change in the surface plasmon occurred in the presence of up to 10 mM thiol in some cases. Given the charge-stabilized nature of the colloid, the lack of a visible change in the SPB decreased the sensor properties of the material. For this reason, much work has been performed in aqueous media or in solutions of various pH, adjusted upon addition of HCl or NaOH.

6.5.1.1 3-Mercaptopropane Sulfonic Acid Sodium Salt

This ligand was selected as an ideal candidate for particle stabilization based on its hydrophilicity and ability to bind to citrate-stabilized AuNP through ligand exchange.[31, 32] Our initial functionalization experiments started with this ligand, and soon branched off to other ligands. Initially, AuNP were prepared with a range of concentrations of 0 – 1.2 mM MPSA, and the absorbance properties of the solutions disclosed remarkable differences as shown in Figure 6.13. At small concentrations such as 0.09 mM MPSA, a shift in the SPB and growth of a shoulder at longer wavelength was readily apparent.

Further additions of MPSA resulted in the growth of a second plasmon band characteristic of anisotropic geometries, as adsorption of MPSA onto specific facets of spherical AuNP could have resulted in directional agglomeration. Further addition of MPSA beyond 0.33 mM led to a decrease in the absorbance, where both peaks decreased in absorbance. Essentially, the plasmon band shift is a result of a reduction in electrostatic forces brought on by introduction of the MPSA ligand. Adsorption of a neutral ligand onto the particle surface caused a decrease in the electrostatic repulsive forces needed to balance the attractive Van der Waals forces between nanospheres. As a result, the interparticle distance decreased and resulted in a redshift or broadening of the SPB. In contrast, deposition of a silica shell of AuNP, as described in Section 6.4, resulted in a negligible redshift of the SPB upon deposition of a silica shell with negatively charged surface groups.

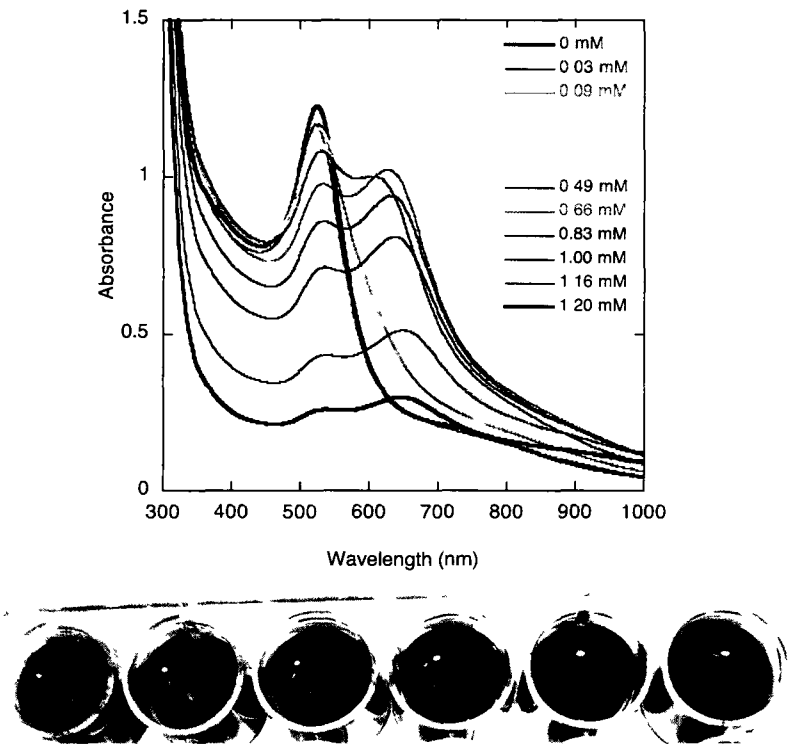

Figure 6 . 13 - (Top) Absorbance of MPSA-functionalized AuNP at different concentrations in aqueous solution. AuNP prepared from 0.33 mM $HAuCl_4$ and 1.0 mM I-2959 with 30 minutes photolysis. Particles were not centrifuged prior to MPSA addition. (Bottom) Photograph of AuNP contaning (left to right) 0 mM, 0.03 mM, 0.09 mM, 0.17 mM, 0.23 mM and 0.33 mM MPSA. Solutions at higher [MPSA] all appeared dark blue.

To assess whether the agglomeration was a result of an increase in the ionic strength of the medium (if the MPSA was instead in the sulfonate form), control experiments were performed with addition of 1.0 mM of an ionic salt to the solution of AuNP. The comparison is presented in Figure 6.14. As such, it is clear that only samples containing neutral MPSA resulted in a spectra change, thus confirming that the MPSA is in the neutral form.

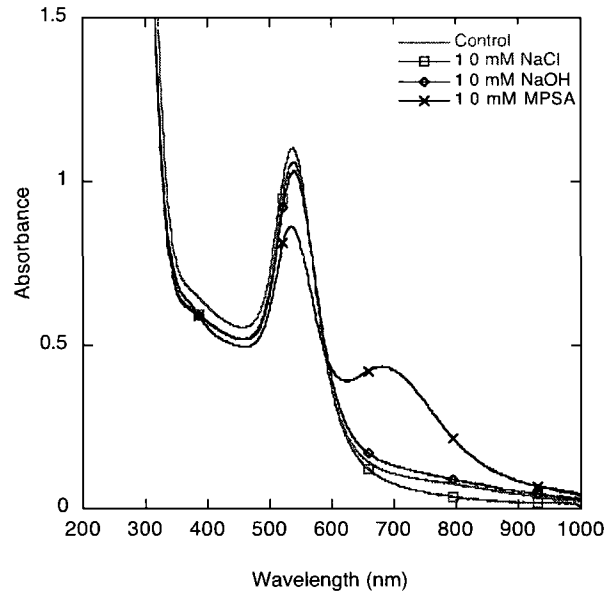

Figure 6 . 14 - Absorbance of AuNP (0.33 mM $HAuCl_4$, 1.0 mM I-2959, 30 min UVA) in the presence of equimolar salts to assess the effect of ionic strength on AuNP plasmon band. AuNP were not centrifuged prior to salt addition.

Another approach was taken to functionalized AuNP with MPSA *in-situ* such that the ligand could bind to particles during photolysis and arrest the growth to afford smaller particles. A range of 0.33 - 1.65 mM MPSA was added to solution at different times during particle growth, in a well plate under aerated conditions. The sooner the thiol was added, the lower the resulting SPB intensity. Additionally, the greater the concentration of thiol added at initial times, the less AuNP were formed. Consistently, 0.5 mM MPSA added prior to irradiation caused the colloid to develop a pale pink/peach colour indicative of a slower synthesis and lower yield of particles, compared to the vibrant cherry red of AuNP solutions formed in the absence of additives. After one day, all samples treated with MPSA had all become violet with a longitudinal SPB band.

MPSA was also added in effort to stabilize AuNP prepared under deareated conditions to prevent agglomeration in the absence of oxidation photoproducts. MPSA was added to Ar-purged AuNP samples as soon as the growth of the SPB

had subsided (8 minutes). Similar to the aerated samples prepared in a well plate, the particles were unstable with 1:1 Au^{3+}:MPSA. The absorbance redshifted by 25 nm after a day, and AuNP precipitated from solution within two days. The AuNP SPB was very sensitive to concentration of MPSA, where significant shifts and growths were greater on some days than others. Functionalization with this small aqueous ligand became difficult owing to irreproducibilities.

While previously mentioned absorption studies in aqueous solution affirmed the presence of the neutral form of MPSA in solution, whether it was actually bound to the particle surface remained unanswered. To resolve this issue, a series of experiments were undertaken to probe the surface chemistry. As such, NH_2OH-HCl seeded-growth, as discussed in Section 6.2, was a valuable tool to determine surface reactivity.

Samples of AuNP were functionalized with the ligand for a minimum of 24 hours, followed by centrifugation at a slower speed than non-functionalized AuNP to minimize aggregation if particles were not sufficiently covered with a monolayer. AuNP were seeded such that MPSA-AuNP were added last to a growth solution containing 0.25 mM $HAuCl_4$ and 0.4 mM NH_2OH-HCl. The optical changes in the colloid were monitored over time to extract kinetics of particle growth. Seeded growth of unprotected AuNP resulted in a rapid increase in the translational SPB as well as a redshift of absorbance as the particle size increased. The absorbance spectra in Figure 6.15, left, emphasize these changes, and underline the fact that growth was complete within 90 seconds.

When particles were derivatized with 1.0 mM MPSA, obvious changes to seeded growth were observed. A decreased growth rate was observed, where almost negligible changes in optical density were observed after the equivalent 90 seconds and the growth ceased after 12 minutes. The final absorbance, or more importantly the change in absorbance was significantly lower than the seeded non-functionalized AuNP. Within the first 240 s, the absorbance of MPSA-AuNP seeds

increased by a factor of 1.5 (or by 2.8 overall) relative to an increase of 5.5 for non-functionalized AuNP. The rate for seeded-growth was extracted by plotting $\ln(A_t/(A_f-A_t)$ vs time, where v = 0.0043 Ms^{-1} and 0.105 Ms^{-1} represent seeding with 0.5 mM MPSA-AuNP and non-functionalized, respectively. The shape of the plasmon and their rates of changes are clear indications that the surfaces of I-2959-synthesized AuNP have been modified. These results are seen below in Figure 6.15, right.

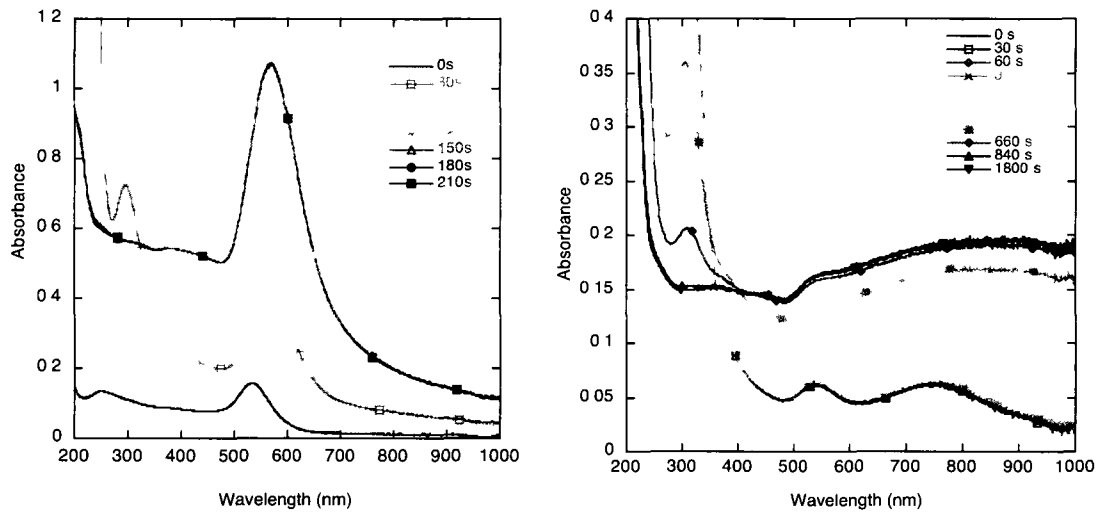

Figure 6 . 15 - Seed-mediated growth of (left) non-functionalized AuNP and (right) 0.5 mM MPSA-functionalized AuNP in the presence of a growth solution containing 0.26 mM $HAuCl_4$ and 0.4 mM NH_2OH-HCl. 100 µL seed added.

In another approach, derivatized AuNP were also subjected to etching such that organic ligands would protect or delay the corrosive destruction of gold nanoparticles. An aliquot of MPSA-AuNP was added to a basic solution containing 0.1 M KCN in 1.0 M KOH, and the optical changes were monitored over time *via* UV-VIS absorption. Despite the same concentration of 0.5 mM MPSA used in the experiment, the absorbance of the MPSA-AuNP is different, which emphasizes the sensitivity of the particles to ligand attachment with this molecule. Nevertheless, the experiments are reproducible and show a decreased rate of etching relative to non-functionalized AuNP. Results are summarized in Figures 6.16, left and right.

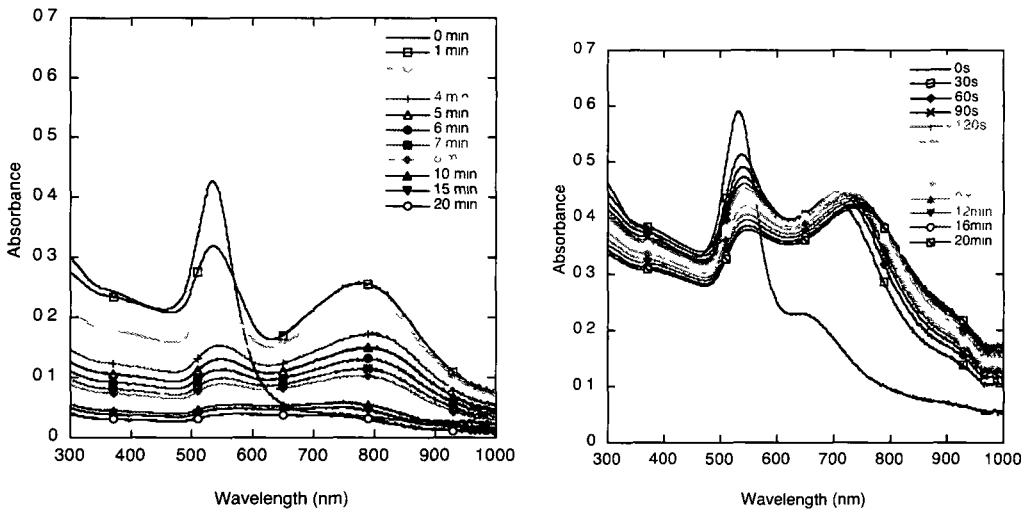

Figure 6 . 16 - AuNP SPB decay over time of (left) non-functionalized AuNP, and (right) 0.5 mM MPSA-functionalized AuNP exposed to etchant solution containing 0.1 M KCN in 1.0 M KOH. 500 µL AuNP added to solution.

These surface studies on MPSA-AuNP confirm the presence of the ligand on the particle surface. As the molecule attached to the particle surface, its presence at unmodified pH resulted in agglomeration and precipitation of AuNP via charge neutralization. Given the sensitivity of I-2959-synthesized AuNP toward MPSA, other aqueous multi-functional ligands were explored.

6.5.1.2 Cysteine

L-Cysteine-HCl (CYS) was also added in an attempt to stabilize AuNP, but the AuNP SPB was also responsive to ligand addition, as the colour shifted from red to blue immediately and precipitated within a day. A SEM image of the resulting particles appears in Figure 6.17, where it is clear that particles have flocculated without agglomeration. These results agree with those for AuNP bound to positively-charged thiols such as cysteamine in previous studies.[33]

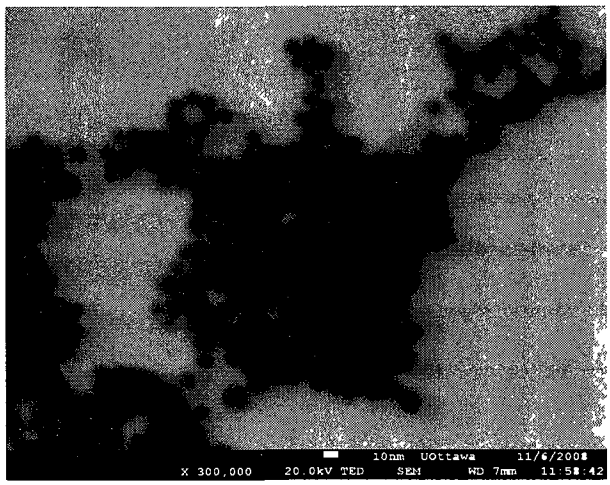

Figure 6 . 17 - SEM image of AuNP functionalized with 1.0 mM cysteine at pH 7. The scale bar represents 10 nm.

Concentration studies determined 1.0 mM cysteine to be the ideal concentration such that minimal flocculation was observed without noticeable precipitation. CYS-AuNP solutions were also evaluated in seeding and etching experiments to probe the degree of surface functionalization.

For seeding experiments, aliquots of AuNP-CYS were added to a fresh growth solution containing 0.25 mM $HAuCl_4$ and 0.4 mM NH_2OH-HCl, and the absorption was monitored over time. The results for CYS-modified AuNP at various concentrations are displayed in Figure 6.18, where the changes in absorbance at the SPB maximum are normalized to the initial absorbance of non-functionalized AuNP. The rate constants for seeded growth decreased with increased cysteine, such that the catalytic growth rate measured 0.012, 0.002 and 0.002 Ms^{-1} for 0.1, 0.5 and 1.0 mM CYS, respectively. The rates of growth for the higher concentrations of cysteine were essentially negligible beyond 30 s, and the fitting of data was thus rather difficult. Almost identical kinetics for 0.5 mM and 1.0 mM cysteine samples further imply that the particle surface was passivated at a lower concentration to form a monolayer.

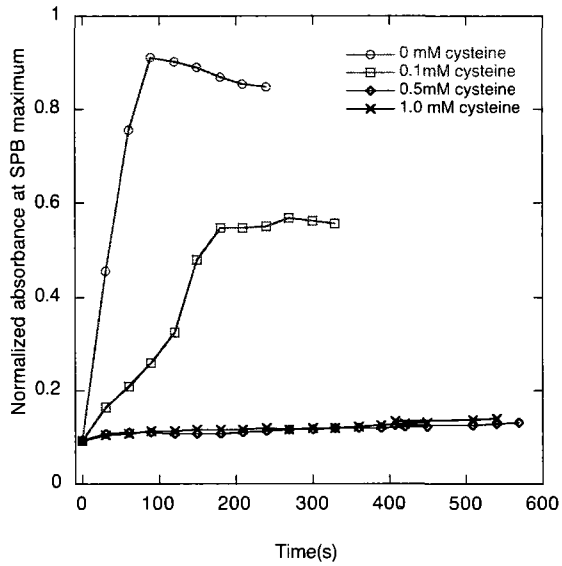

Figure 6 . 18 - Seed-mediated growth of cysteine-functionalized AuNP in a growth solution containing 0.25 mM $HAuCl_4$ and 0.4 mM NH_2OH-HCl. 100 µL seed added to 2.9 mL growth solution.

Etching experiments further confirmed a decrease in surface reactivity. The decay of 0.5 mM CYS-modified AuNP over time is shown in Figure 6.19, (left), and the decay over time is compared to other concentrations (right). The results are similar for all three different cysteine concentrations. Under basic conditions, cysteine is in the anionic form, and the negative charges on the ligands could cause repulsion towards degradation of gold by other anionic etchants such that low concentrations are sufficient for protection.

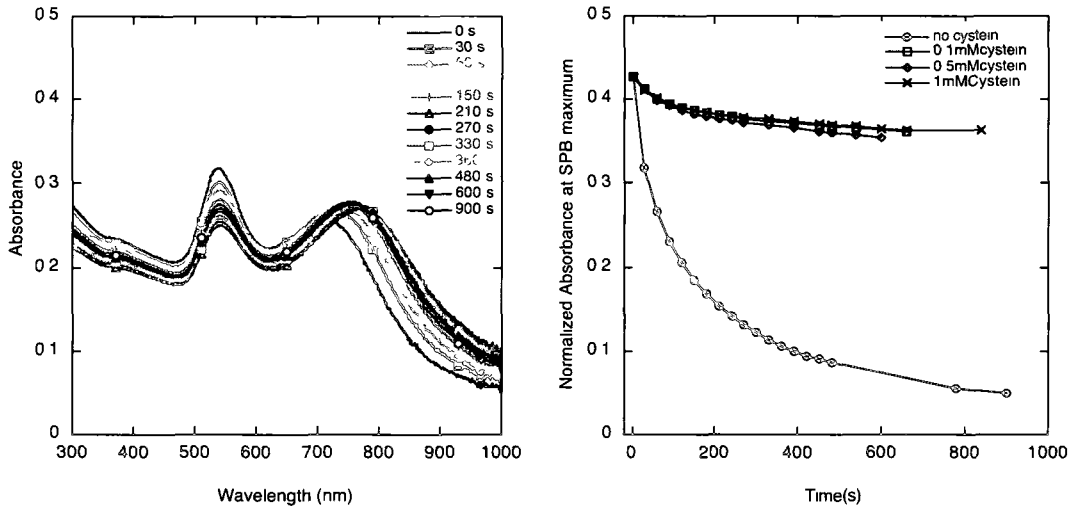

Figure 6 . 19 - (Left) Etching of 0.5 mM CYS-modified AuNP in the presence of 0.1 M KCN in 1.0 M KOH. (Right) Decay of AuNP SPB over time upon addition of 0 - 1.0 mM CYS-AuNP.500 µL NP added to etchant 2.5 mL etchant solution. Decay is normalized to the initial absorbance of the non-functionalized AuNP.

IR studies were also conducted to evaluate the attachment of the ligand to the particle surface. Key features observed for the CYS-AuNP can be identified by the broad N-H stretch at 3500 cm^{-1}, which is stronger in intensity but nevertheless overlaps with the O-H stretch for adsorbed water in the pellet, as well as the tail primary alcohol on the physisorbed photoproduct. Secondly, the small peak at 2900 and 2850 cm^{-1} for the non-functionalized AuNP representative of the methylene C-H symmetric and asymmetric stretches of the tail of the photoproduct, and are essentially absent in the CYS-AuNP spectrum. The comparison of CYS-AuNP and non-functionalized AuNP is given in Figure 6.20.

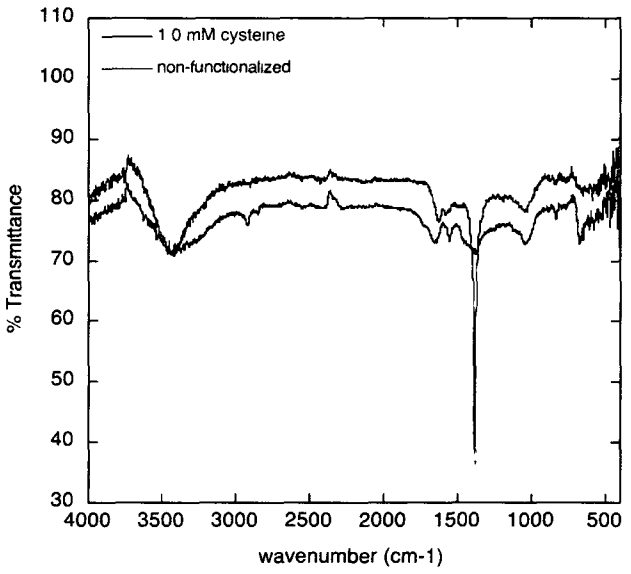

Figure 6 . 20 - IR spectra of 1.0 mM cysteine and non-functionalized AuNP.

Importantly, the small peak at 1560 cm^{-1}, characteristic of the O=C-O stretch of the carboxylate salt, is present for the non-functionalized AuNP yet absent for CYS-AuNP as the ligand is in the neutral form at pH 5. For CYS-AuNP, The sharp peak at 1380 cm^{-1} is characteristic of the symmetric O-C-O.[34] While it is also present in the non-functionalized AuNP sample, the stronger signal could be a result of the protonated form for cysteine. The peak at 1050 cm^{-1} is present in both samples as a result of the C-H bend. Importantly, the characterisitic medium-strength signal for the S-H stretch found in the 2600-2540 cm^{-1} region is absent, which supports the ligand being bound to the particle surface.[35] The C-S stretch, which is known to be weak and often absent, is also missing in the 560 cm^{-1} region, where signal characterization is generally unreliable.

The sensitivity of the AuNP plasmon, as well as seeding, etching and IR studies affirm the presence of cysteine on the surface of AuNP. The stability of the particles in aqueous suspension with cysteine as a surface modifier, however, is poor as the particles crashed out of solution within a matter of hours.

6.5.1.3 Mercaptohexadecanoic acid

This alkyl thiol with a carboxylic acid functional group has several advantages when used for partcle modification. Its long alkyl chain allows for dense packing of the linear molecule to the surface. Whitesides *et al*. studied the packing density of gold films modified with MHDA and realized that the chains anchor at an angle of 30° to minimize changes in entropy at high monolayer concentration.[31] At lower MHDA concentration, the long chains are assumed to rest on the surface. Additionally, the carboxylic acid presents a versatile functional group that can easily be manipulated for tether of biological molecules for imaging and drug delivery.

Various experiments were conducted with this ligand and the concentration of varied over a few orders of magnitude. The majority of the work was performed at 1.0 mM, however some seeding experiments were performed at 10 μM in comparative studies with other ligands. At 10 μM MHDA, the pH of the solution was varied to observe differences towards flocculation. From the results shown in Figure 6.21, the SPB of AuNP is most stable at higher pH, yet broadened and decreased around pH 3 and 5. Given that the pK_a for most carboxylic acids is approximately 4-5, the state of the carboxylic acid moiety around and below this pH value is in the neutral form. Insufficient electrostatic repulsion occurs between nanoparticle surfaces and the interparticle distance likely decreased, leading to SPB red-shifting to longer wavelengths and band broadening.

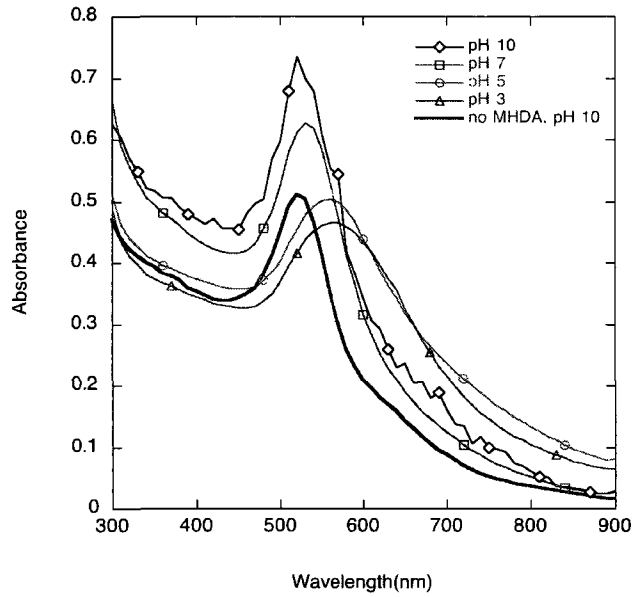

Figure 6 . 21 - AuNP funtionalized with 10^{-5} M MHDA in 1:1 H_2O:EtOH and added to solutions of various pH. pH was adjusted by addition of HCl or NaOH.

A SEM of AuNP functionalized with 10 μM MHDA at pH 10 is shown in Figure 6.22. Even after drying the colloid onto a copper grid, the stability of the particles through ligand functionalization and repulsive particle-particle interactions is easily visulalized and AuNP appear more separated relative to non-functionalized particles of smililar concentration and deposition volume. (Compare to Figure 3.18)

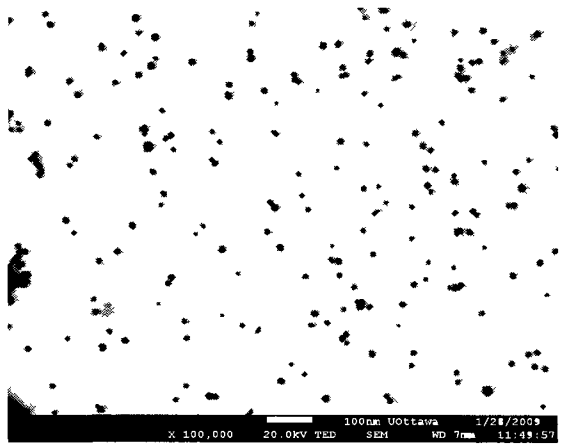

Figure 6 . 22 - SEM of AuNP functionalized with 10^{-6} M MHDA in 1.0 mM NaOH. The size bar represents 100 nm.

At higher MHDA concentrations, AuNP required functionalized in 1:1 H_2O:EtOH cosolvent due to poor aqueous solubility from the long alkyl chain. The sample changed colour from red to magenta over time, indicative of flocculation at that pH. Within 24 hours, a thick, light purple agglomerate was suspended in the clear, colourless solvent. Gentle shaking resuspended the precipitate, which eventually separated from solution once more. Centrifugation of the sample and resuspension in acetonitrile or ethanol led to a stable colloid. This observation further confirmed the passivation of the gold particle surface as the tail end of the acid displayed limited solubility in aqueous media. As the concentration of acid increased in separate samples, the absorption of the resuspended AuNP also increased. The comparison is illustrated in Figure 6.23.

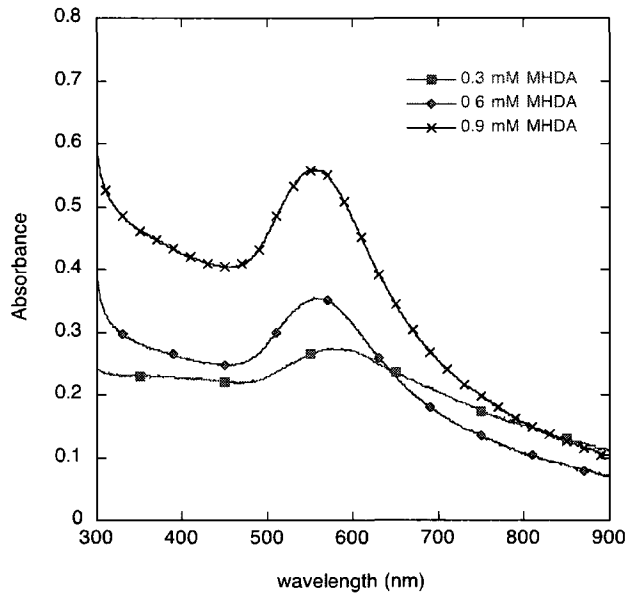

Figure 6 . 23 - Absorption of MHDA-functionalized AuNP at various concentrations in MeCN. AuNP were derivatized in 1:1 H_2O:EtOH for 16 hours, centrifuged and resuspended in the MeCN.

The zeta potential of 10^{-5} M MHDA-AuNP post centrifugation was measured to be - 6.24 mV; a value significantly higher than - 24.5 mV for unfunctionalized AuNP and lower than the potential of the ligand alone of - 2.46 mV.

Seeding experiments were also conducted with AuNP modified with either 10 μM or 0.5 mM MHDA. A primary investigation with 0.5 mM MHDA monitored the rate of seeded growth over time upon addition of 100 μL of seed (3.3 μM Au^0) added to a fresh growth solution containing 0.25 mM $HAuCl_4$ and 0.4 mM NH_2OH-HCl. The changes in optical properties of the colloid are visualized in Figure 6.24. Upon addition of the seed to the growth solution, minimal growth of the SPB was observed with slight redshifting, while the absorbance of the LMCT for $AuCl_4^-$ decreased over the course of the reaction. This salt was consumed by the slow reduction of Au^{3+} by hydroxylamine with the slow generation of anistropic structures, as evidenced by SEM images in Figure 6.26. Kinetics of the control experiments in the absence of

any seed showed a very minor increase in absorbance, but the presence of MHDA-modified AuNP disclosed a slightly greater increase in absorbance than the control. The rate of growth for the unimolecular autocatalytic seeded-growth was measured to be 0.0023 Ms^{-1} for 0.5 mM MHDA-AuNP; significantly lower than 0.105 Ms^{-1} obtained for non-functionalized AuNP. For clarification, a rate of v = 0.0004 Ms^{-1} was measured for the growth solution in the absence of seed. These results confirm the presence of a passivated monolayer of MHDA on the particle surface.

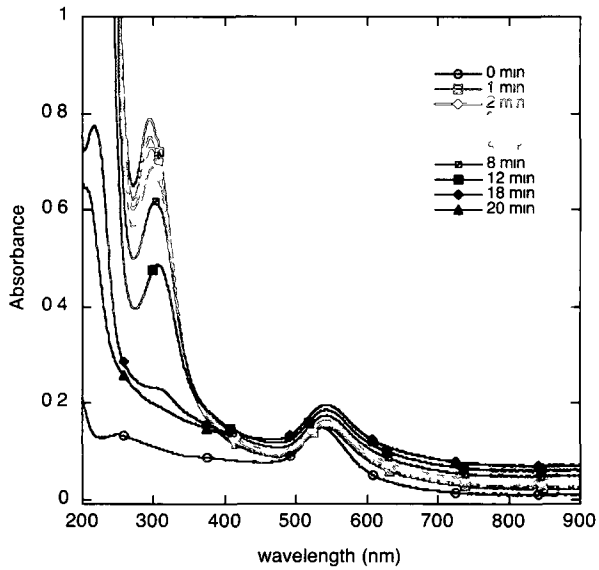

Figure 6 . 24 - Growth of AuNP over time via seeding of 0.5 mM MHDA-functionalized AuNP in the presence of 0.25 mM $HAuCl_4$ and 0.4 mM NH_2OH-HCl. 100 µL seed (3.3 µM Au^0) added to growth solution.

Further seeding studies investigated the effect of the concentration of MHDA-modified seed particles on the size and morphology of the resulting particles. The volume of seed added to an identical growth solution as in the previous study ranged from 5-200 µL, or 0.15 µM to 6.61 µM Au^0. It can be recalled from results in previous studies with non-functionalized seeds that the greater the amount of seed, the faster the growth and the greater the increase in absorbance at the translational SPB maximum, while the lower concentrations resulted in a slower and redshifted

increase in absorbance. The results from the seeding study with MHDA-modified AuNP are presented in Figure 6.25.

Interestingly, these spectra show an opposite trend to that expected, where larger seed volumes generated a significant scatter at longer wavelength, while smaller particle additions led to a redshifted increase in absorbance. The high absorbance is the result of the high degree of scatter in solution from the generation of large prisms and plates.

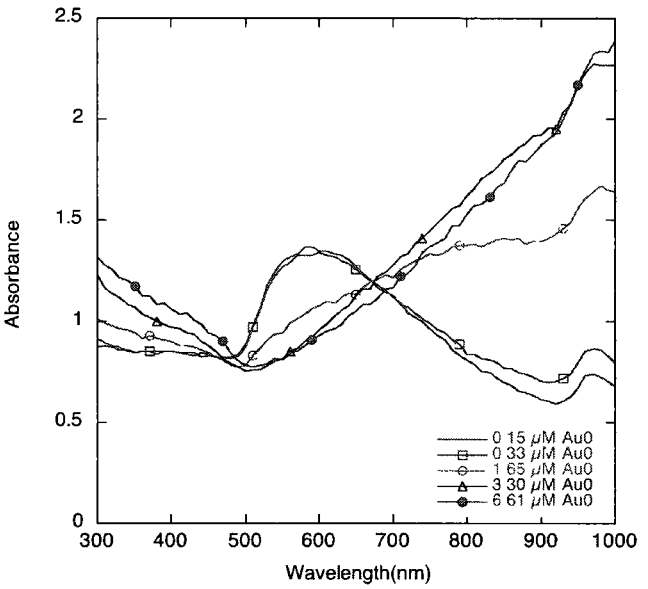

Figure 6 . 25 - Absorption of 10^{-5} M MHDA-functionalized AuNP used as seeds in growth solutions containing 0.25 mM $HAuCl_4$ and 0.4 mM NH_2OH-HCl. Volumes of seed added to growth solution ranged from 5-200 µL (0.15 µM- 6.61 µM).

SEM images of the particles were taken to assess the difference in size and morphology from the mentioned experiment, and are presented in Figure 6.27. Unmodified particles increased in size from 10 nm to roughly 60 nm with spherical geometries. In addition, small plates and triangular prisms were also produced, which are similar to results with the hydroxylamine seeding system as previously discussed in Section 6.2. For AuNP modified with 10 µM MHDA, the resulting nanoparticles emerged with two distinct populations; 1) small, spherical AuNP of

essentially 10 nm remained, implying a high surface passivation of the ligand, and 2) large plates and prisms with triangular, hexagonal and "snowflake" geometries. The plates resulted from either slow growth in the absence of seed, or growth from unpassivated crystal faces. Judging from SEM images of seeding studies in Section 6.2, where very few micron-sized prisms took form, the new growth of "nano-snowflakes" supports the argument of seeded-growth from non-passivated crystal faces

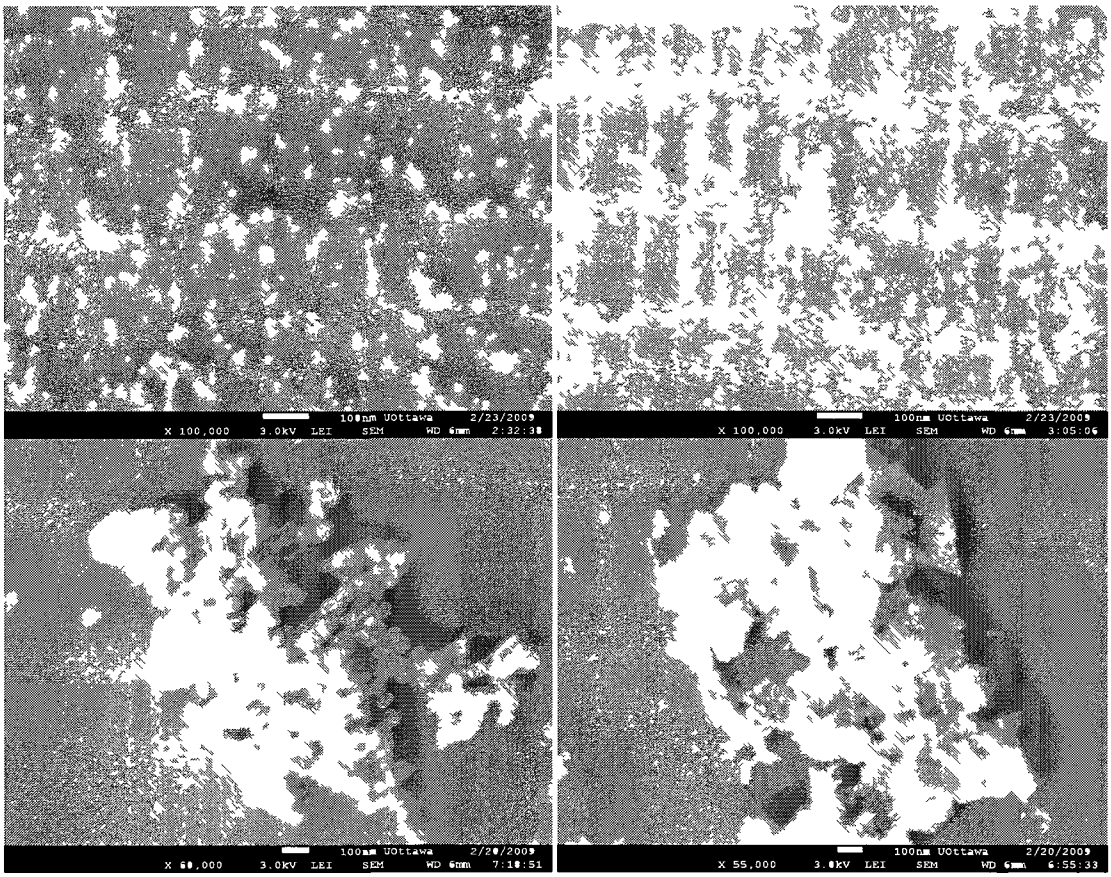

Figure 6 . 26 - SEM image of AuNP from seed-mediated growth experiments. (top left) Non-functionalized AuNP seeds and (top right) 10^{-5} M MHDA-functionalized seeds. (Bottom left) Resulting AuNP grown upon addition of 200 µL (6.61 µM Au^0) non-functioalized seeds and (bottom right) 200 µL (6.61 µM Au^0) 10^{-5} M MHDA-seeds to a solution containing 0.25 mM $HAuCl_4$ and 0.4 mM NH_2OH-HCl. The scale bars in all images represent 100 nm.

In addition to seeding experiments, etching was also performed with the MHDA-modified particles. 500 µL of modified AuNP were added to a caustic solution of 0.1 M KCN in 1.0 M KOH, and the absorbance was monitored over time. The results are displayed in Figure 6.27. The initial absorbance was measured separately, for the rapid decrease in absorbance within the first minute is significant but reproducible among comparative studies. In comparison to studies performed with non-functionalized seeds, the MHDA monolayer functions as an effective barrier. While a fully passivating monolayer would be expected to prevent any degradation, similar studies in previous reports have also noted a rapid initial decrease in absorbance intensity.[31]

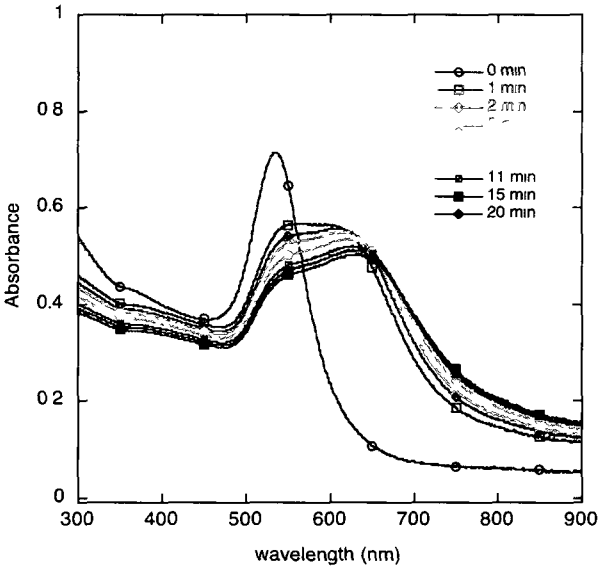

Figure 6 . 27 - Absorbance over time of 0.5 mM MHDA-functionalized AuNP exposed to etchant solution containing 0.1 M KCN in 1.0 M KOH. 500 µL AuNP added to solution.

To investigate the chemistry on the particle surface, infrared spectroscopy was performed. Details of the sample preparation are given in Section 2.1.7. The spectra for MHDA are displayed in Figure 6.28.

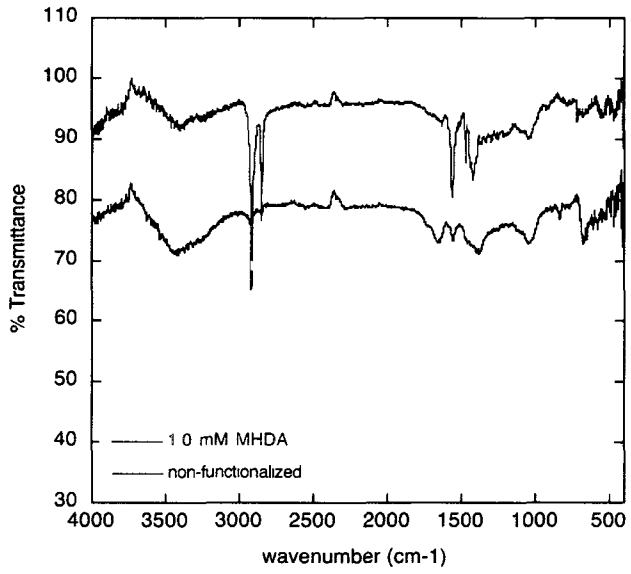

Figure 6 . 28 - IR spectra of 1.0 mM MHDA-AuNP and non-functionalized AuNP.

Confirmation of surface modification rests in the strong peaks at 2910 and 2850 cm^{-1}, representative of the symmetric and anti-symmetric C-H stretches for aliphatic CH_2 in the long alkyl chains. The peaks at 1560 cm^{-1} and 1380 cm^{-1} are also a clear indication of the symmetric and antisymmetric O-C-O stretches for carboxylate salts, respectively. Importantly, the peak for S-H stretch is missing, indicative of the chemisorption of the thiolate to the particle surface.

6.5.1.4 4,4'-Dithiodibutyric acid

Along with thiols, dialkanethiols and dialkanedisulfides have also gained interest in gold nanoparticle functionalization.[36, 37] A water-soluble disulfide, 4,4'-dithiodibutyric acid, DTBA, was investigated. Experiments over the course of this research were conducted at either 10 μM or 1.0 mM concentration. The pH of the system was also varied to determine the range for the most stable particles at pH 10, similar to the

monothiol acid, MHDA. The absorbance of AuNP colloids at various pH are displayed in Figure 6.29.

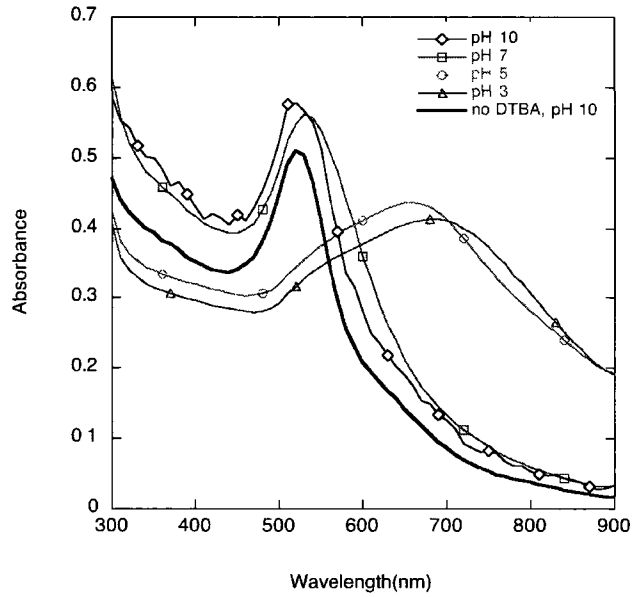

Figure 6 . 29 - Absorbance of AuNP functionalized with 10^{-5} M DTBA at various pH, in the absence of buffer. pH was adjusted by addition of HCl or NaOH.

The pK_a for DTBA has been reported to be 4-5 on par with most carboxylic acids, and thus the same observations for particle stabilization were noted as with MHDA. At pH 5 and below, the carboxylic acids are neutralized and reduce the ionic sphere around individual nanoparticles, promoting flocculation. Relative to MHDA, a greater band broadening and redshift is observed, and could be attributed to the doubled decrease in ionic strength at lower pH for the same molar concentration of ligand. DTBA-modified AuNP showed ideal particle stability in solution at 10 μM, and their SEM is presented below in Figure 6.30.

To determine the effectiveness of ligand binding to the surface, seeding experiments were conducted in a parallel fashion to those for MHDA-modified AuNP. The results for the growth of seeded DTBA-modified AuNP over time upon addition of 100 μL seed are presented in Figure 6.49 in Section 6.5.3.2, and show decreased resistance to the seeded growth relative to the non-functionalized AuNP, however

much greater growth relative to other modified AuNPs such as those with MHDA or MTHZ (*vide infra*) for equivalent 1.0 mM concentration. The rate of particle growth was calculated to be 0.012 Ms^{-1}; sixfold faster than the long chain thiol.

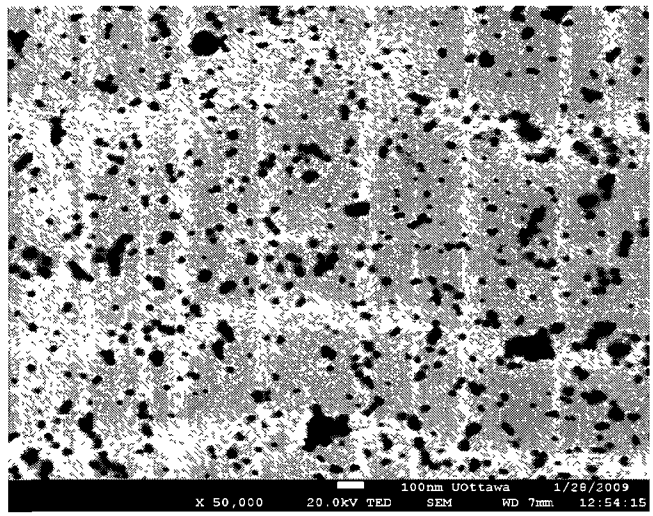

Figure 6 . 30 - SEM image of AuNP functionalized with 10^{-6} M DTBA at pH 10. The scale bar represents 100 nm.

Following this, varied concentrations of 10 μM DTBA-AuNP seed were added to a NH_2OH-HCl/$HAuCl_4$ growth solution. Unlike MTHZ and MHDA, particles derivatized with DTBA displayed a strong increase in the translational SPB absorbance for almost all concentrations save the lowest amount of seed added. These spectra are essentially identical to the observations for parallel reactions with unmodified seed. The spectra are shown in Figure 6.31.

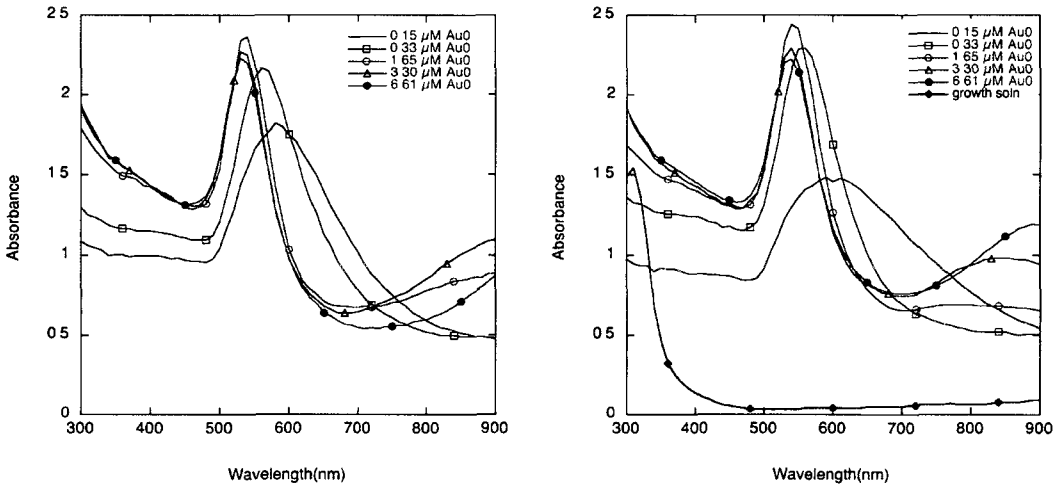

Figure 6 . 31 - (left) Seeding of non-functionalized AuNP and (right) 10^{-5}M DTBA-AuNP at different seed concentrations in the presence of 0.25 mM $HAuCl_4$ and 0.4 mM NH_2OH-HCl growth solution.

Following these results, samples of the 6.6 μM DTBA-Au^0 addition were run for SEM, and the images indicate polydispersity similar to non-functionalized particles. The SEM micrographs are depicted in Figure 6.32. The majority of particles are spheres of varied diameter with a rough average diameter of 40 - 60 nm along with the generation of small plates and prisms.

Both IR and ^1H NMR were performed for DTBA-AuNP in D_2O after centrifugation, however the spectra were essentially void of any signal other than the few small peaks also present in the IR and ^1H NMR of centrifuged non-functionalized seeds.

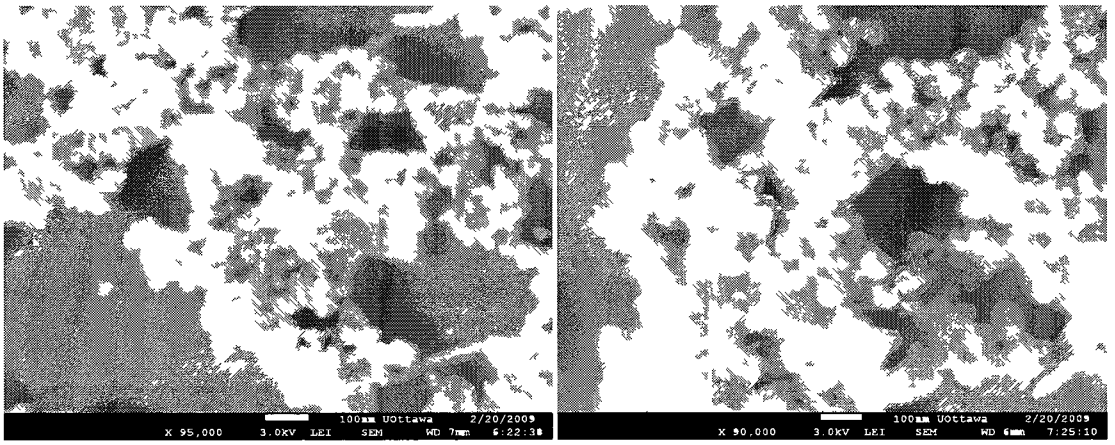

Figure 6 . 32 - SEM image of (left) non-functionalized AuNP and (right) 10^{-5} M DTBA-functionalized AuNP used as seeds in the growth of AuNP in a solution of 0.25 mM $HAuCl_4$ and 0.4 mM NH_2OH-HCl. 200 µL seed added (6.6 µM Au^0) . The scale bars represent 100 nm.

In these comparative experiments, it seems evident that the disulfide was not effectively bound prior to centrifugation at equivalent speeds as the other systems. Compared to MHDA and MTHZ, DTBA still allows for particle growth The decreased passivation is likely a result of poor disulfide binding to the AuNP surface. Unlike previous reports from our lab describing strong binding of disulfides to CdSe quantum dots under deareated conditions in toluene after seven hours of derivatization,[38] 40 hours of disulfide funtionalization with mild shaking did not appear to tether the thiols to the particle surface. Disulfides have been observed to show a weaker affinity to the metal particle surface relative to thiolates. This difference has been noted for AuNP prepared and stabilized in the Brust-Schiffrin method, where alkanethiol surface ligands on 2-5 nm AuNP undergo oxidation to form disulfides under ambient conditions, resulting in particle agglomeration as a consequence of ligand dissociation.[39]

6.5.1.5 Mercaptothiazoline

AuNP were also prepared with 2-mercaptothiazoline. This ligand was chosen based on its water solubility and its known affinity for adsorption onto metal surfaces. In

particular, MTHZ belongs to an organic class of metal corrosion inhibitors that participate as key ingredients in the chemical decontamination of nuclear power reactors.[40]

Similar to procedures performed with other ligands, a concentration study revealed a high sensitivity of the surface plasmon band of gold nanoparticles to low concentrations of MTHZ in aqueous solutions. In parallel experiments with MHDA and DTBA, similar pH stability tests were conducted. The results for 10^{-5} M MTHZ are displayed in Figure 6.33, where it is clear from the redshifted SPB that AuNP have flocculated at all pH tested. The pK_a for MTHZ has been reported to be 11,[40] which explains the AuNP destabilization with the neutral ligand.

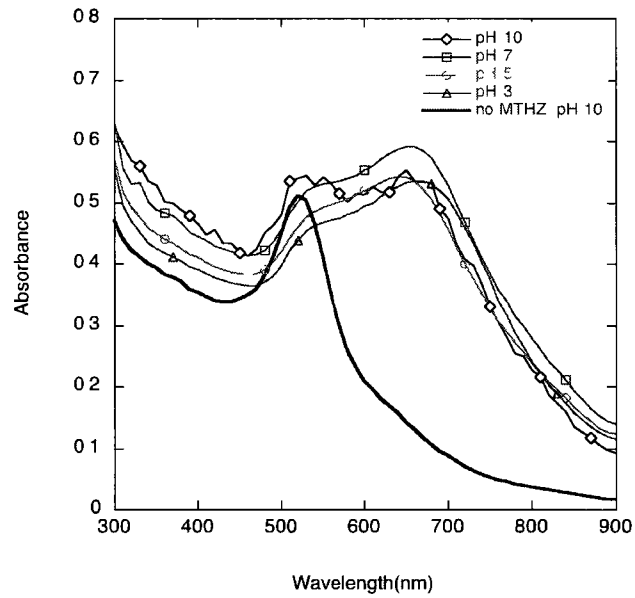

Figure 6 . 33 - Absorbance of AuNP functionalized with 10^{-5} M MTHZ at different pH in the absence of buffer.

Taking advantage of the strong sensitivity of AuNP toward the molecule, MTHZ was also added to aqueous solutions for derivatization of AuNP *in-situ* during the I-2959 photolysis generation of AuNP. The thiol was added at 1.0 mM concentrations to different wells at different times during the irradiation process, and the results are

illustrated in the absorption spectra of Figure 6.34. The traces for samples with additives are all lower (thus representing a lower yield of AuNP) than non-functionalized AuNP. It is well known that thiols can form a Au^{+} polymer-like complex with thiols.[41, 42] When the thiol was added before the 3 minute mark, insufficient nucleation had taken place to allow for the growth of clusters and small particles. The optimal time, however, seemed to be at the 5 min irradiation mark, such that thiols adsorbed to already-formed small AuNP and clusters. Beyond the 5 minute point, however, the addition of MTHZ led to a strong agglomeration and dampening of the surface band, and the increasing time yielded an increased quantity of flocculated particles with a grey/blue colour.

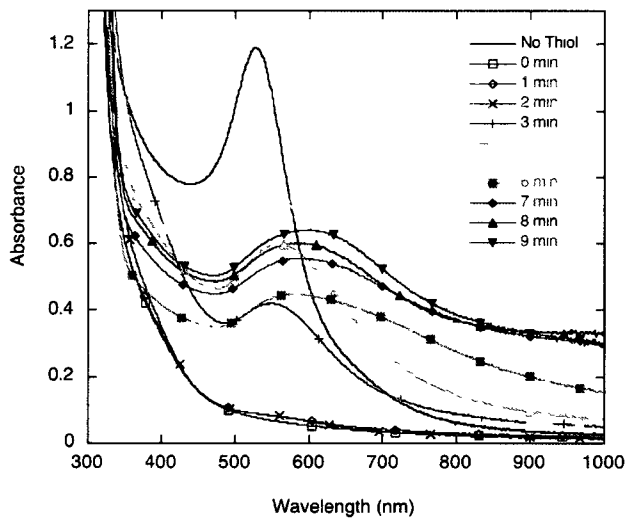

Figure 6 . 34 - Absorbance of AuNP synthesized upon addition of 1.0 mM MTHZ at different times during 30 minutes UVA photolysis. 0.33 mM $HAuCl_4$ and 1.0 mM I-2959 for synthesis of AuNP.

The redox chemistry of MTHZ could also be a factor involving the yield of AuNP. Studies by Mahal *et al.* acknowledged an inability of the 2-hydroxy propyl radical with a redox potentiao of E^0 = -1.39 V vs. NHE, to reduce MTHZ, and measured the redox potential of MTHZ at pH 7 to be -1.6 V vs NHE.[40] Despite the favourable reduction potential, control experiments revealed an inability of MTHZ (10 μM to 1.0

mM) alone to generate AuNP under dark or UVA conditions; likely a result of a Au(I)-MTHZ complex formed with a new peak around 400 nm instantly formed upon mixing. Furthermore, the decreased yield could be attributed to the decreased amount of ketyl radicals as a result of the reducing radicals being reduced themselves by the MTHZ transient species. For this reason, functionalization was continued as a subsequent process. When MTHZ was added at later irradiation times, the ligand tethered to the already-formed AuNP and induced particle flocculation, thus redshifting the absorbance maximum.

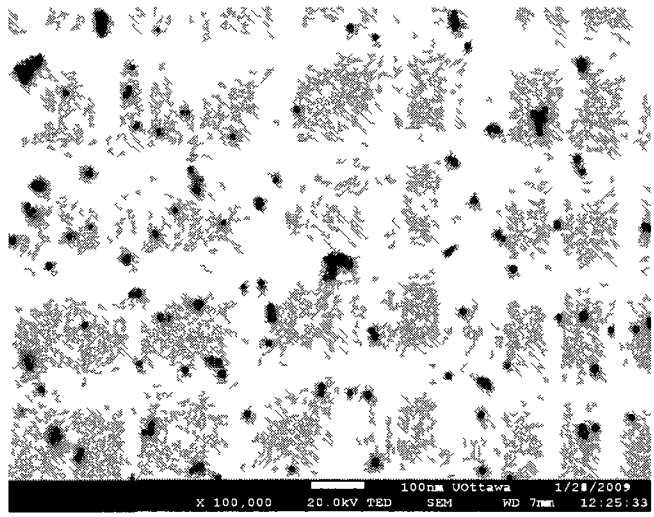

Figure 6 . 35 - SEM of 10^{-5} M MTHZ-functionalized AuNP at pH 10. The size bar represents 100 nm.

AuNP were easily stabilized at a concentration of 10^{-5} M MTHZ, and the particles are displayed in the SEM image in Figure 6.35, above. Despite the large redshifts and broadening of the SPB shown in Figure 6.33, the particles of the pH 10 sample appear small and well dispersed. At higher concentrations such as 1.0 mM, AuNP were stable for approximately a day while particles at the 10^{-5} M range were stable for almost a week prior to precipitation out of solution Others have attributed this precipitation as a consequence of the functionalized AuNP no longer soluble in aqueous conditions [43]

Along the same lines as the seeding experiments performed with MHDA and DTBA as ligands, MTHZ was also evaluated for particle passivation with NH_2OH-HCl seeded growth. Upon examination of Figure 6.36, a similar trend appears as that with MHDA in Figure 6.25. Particularly, the absorbance at 530 nm is essentially featureless for greater seed volumes, and the increase in absorbance at longer wavelength is attributed to the growth of plates and prisms. At smaller seed concentration, the absorbance is clearly redshifted relative to non-functionalized seeds.

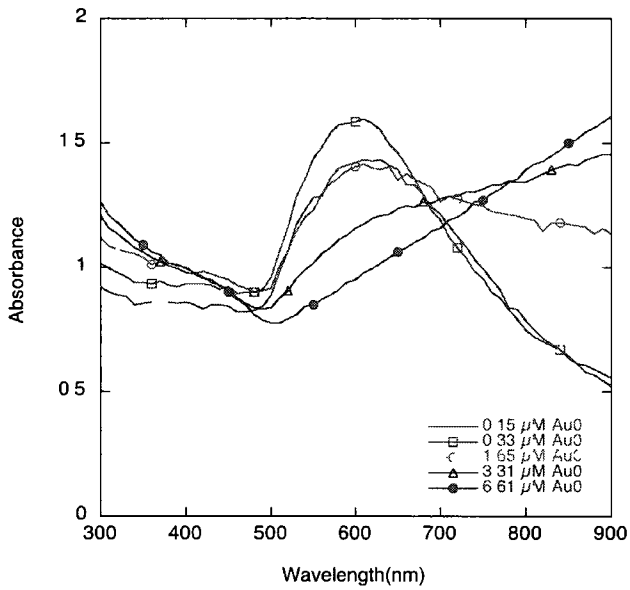

Figure 6 . 36 - Absorbance of seed-mediated growth of 10^{-5} M MTHZ-functionalized AuNP at different concentrations in the presence of 0.25 mM $HAuCl_4$ and 0.4 mM NH_2OH-HCl.

Additionally, SEM images of the larger quantity of MTHZ-AuNP seeds yielded particles with interesting morphologies similar to those achieved with MHDA-AuNP. These particles are presented in Figure 6.37. Their similarity to the images of MHDA particles suggests that MTHZ also performs as an excellent stabilizer through adsorption onto the particles surface. Two morphologies are imaged; 1) small 10 nm range AuNP with no additional growth as a result of surface passivation, and 2) "nano-snowflakes" of large plates and prisms where growth likely occurred along non-passivated facets on the spherical seeds. There is a dramatic difference in

morphology in comparison with non-functionalized seeds of the same added seed concentration. A comparison can be made between Figure 6 32 (left) and Figure 6.37.

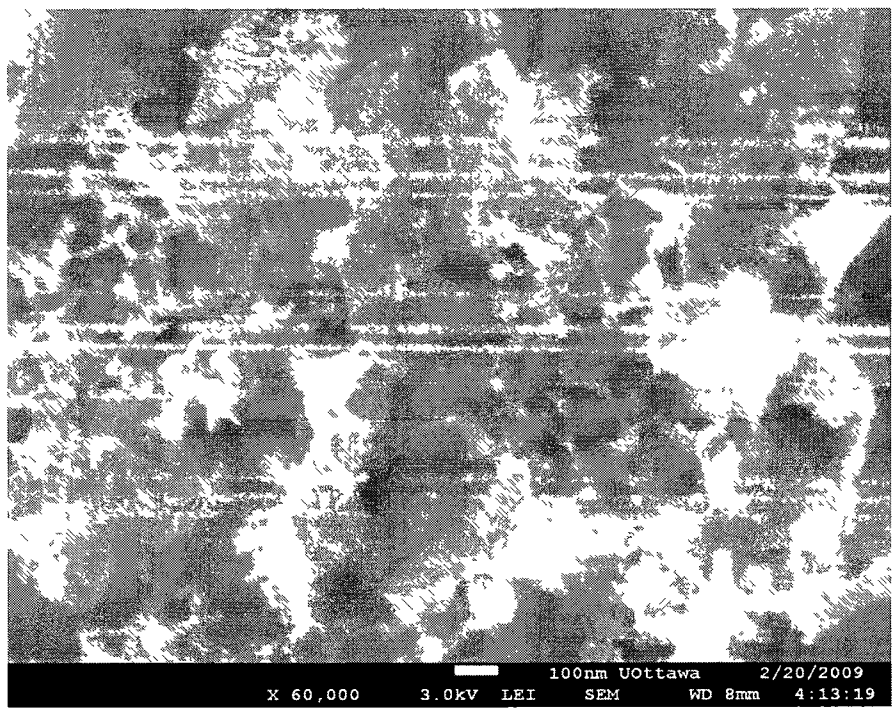

Figure 6 . 37 - SEM of seeded AuNP upon addition of 6.61 µM 10^{-5} M MTHZ-AuNP to growth solutions containing 0.25 mM $HAuCl_4$ and 0.4 mM NH_2OH-HCl. The scale bar represents 100 nm.

The zeta potential of AuNP derivatized with 10^{-5} M MTHZ was recorded, and measured – 8.33 mV in comparison with a value of -24.5 mV for unprotected AuNP and – 4.78 mV for a solution of 10^{-6} M MTHZ alone. These results imply that the particle surface is stabilized with the thiolate ligand. It is apparent that the MTHZ-AuNP have a more negative surface charge in comparison with the value of - 6.24 mV for the MHDA-Au surface, which relates to more MTHZ ligands with neutral charge on the particle surface due to their higher pK_a, relative to MHDA. From visual inspection through SEM, there seems to be a much greater population of "untouched" small, spherical particles for the MTHZ sample in comparison with

MHDA-AuNP. These two observations suggest that the ligand manages to protect the surface; likely a result of steric hindrance of the cyclic backbone of the ligand.

Given this successful protection of particles from surface growth, the next step was to demonstrate the ability to functionalize the surface after particle growth. As with all colloids, particle stability depends on the balance of intermolecular forces and decreases in surface energy with increase in particle size. AuNP were prepared via photoseeding through reduction via H_2O_2 as discussed in Section 6.2. Subsequent particle growth took place, and particles were derivatized with MTHZ after the first, A and second generation, B had formed. The procedure is depicted in Scheme 6.7.

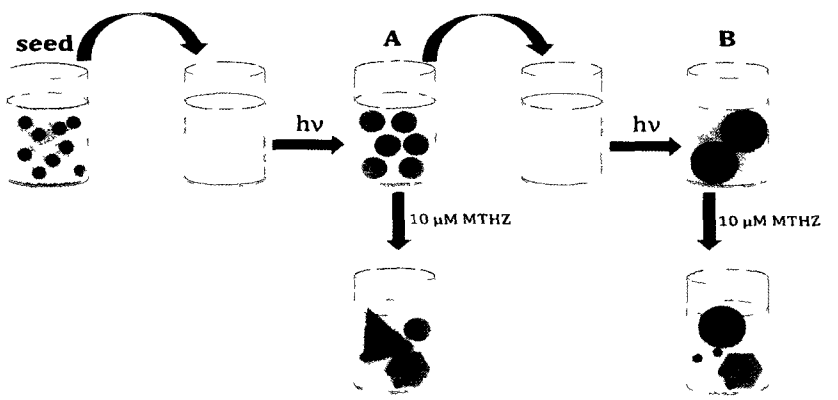

Scheme 6 . 7 - Post-derivitization of photochemically seeded I-2959-AuNP were seeded in a growth solution of 0.5 mM $HAuCl_4$ and 0.5 mM H_2O_2 with 30 minutes UVA photolysis.

In these experiments, particles were not centrifuged prior to functionalization with 10 μM MTHZ. Particles grew accordingly with results discussed in Section 6.2, and SEM images were captured to compare the particles in the presence and absence of MTHZ at different generations. The results are summarized in Figure 6.38.

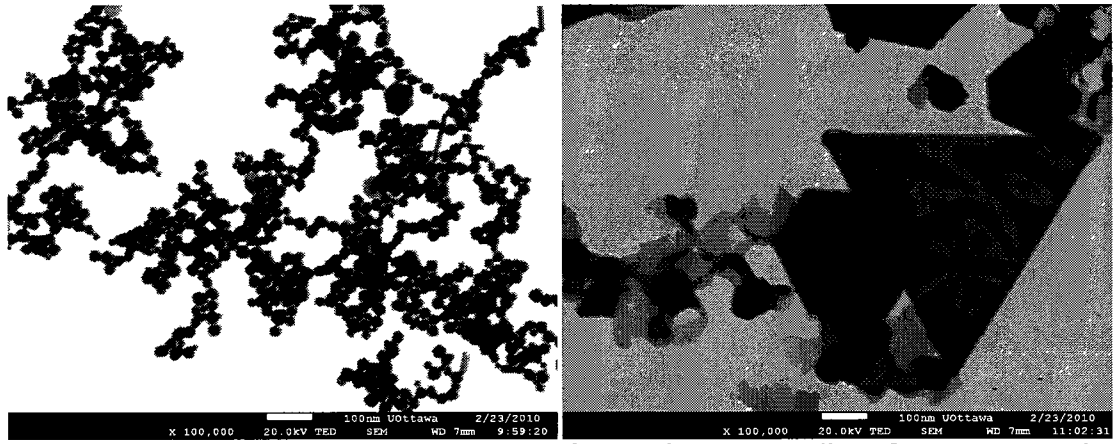

Figure 6 . 38 - SEM images of AuNP produced from H_2O_2 photoseeding after one generation from 50 µL seed addition. Growth solution contained 0.5 mM $HAuCl_4$and 0.5 mM H_2O_2. (left) in the absence and (right) in the presence of 10^{-5} M MTHZ added after 30 minutes of photoseeding. The scale bars represent 100 nm.

Addition of MTHZ after seeding seems to have induced further anisotropic growth of AuNP. The presence of large anisotropic particles in solution was surprising, and could be rationalized in the following way. The high pK_a of the ligand functioned to increase the pH of the uncentrifuged reaction mixture to 6.5. The reduction potential of MTHZ, being similar to that of aromatic ketyl radicals, could have induced a slow reduction for the formation of plates and prisms. Testing 10 µM MTHZ as a reducing agent with 0.25 mM $HAuCl_4$ upon addition of 0.33 µM to 6.61 µM Au^0 as seeds did not, however, lead to seeded-growth.

The formation of prisms is identified in both the first and second generation of MTHZ-Au, while substantially less in the non-functionalized generations. Most interesting, however, was the additional generation of small 3-5 nm AuNP on the surface of the AuNP, which are identifiable by SEM. Significantly fewer small AuNP are observable independent of large prisms. Whether these particles were formed in solution and adhered to the MTHZ surface after, or were reduced on the AuNP surface still remains unclear. There appears to be greater generation of prisms and decreased population of new, small AuNP for the first generation AuNP relative to the second, attributed to the decreased surface reactivity of larger particles.

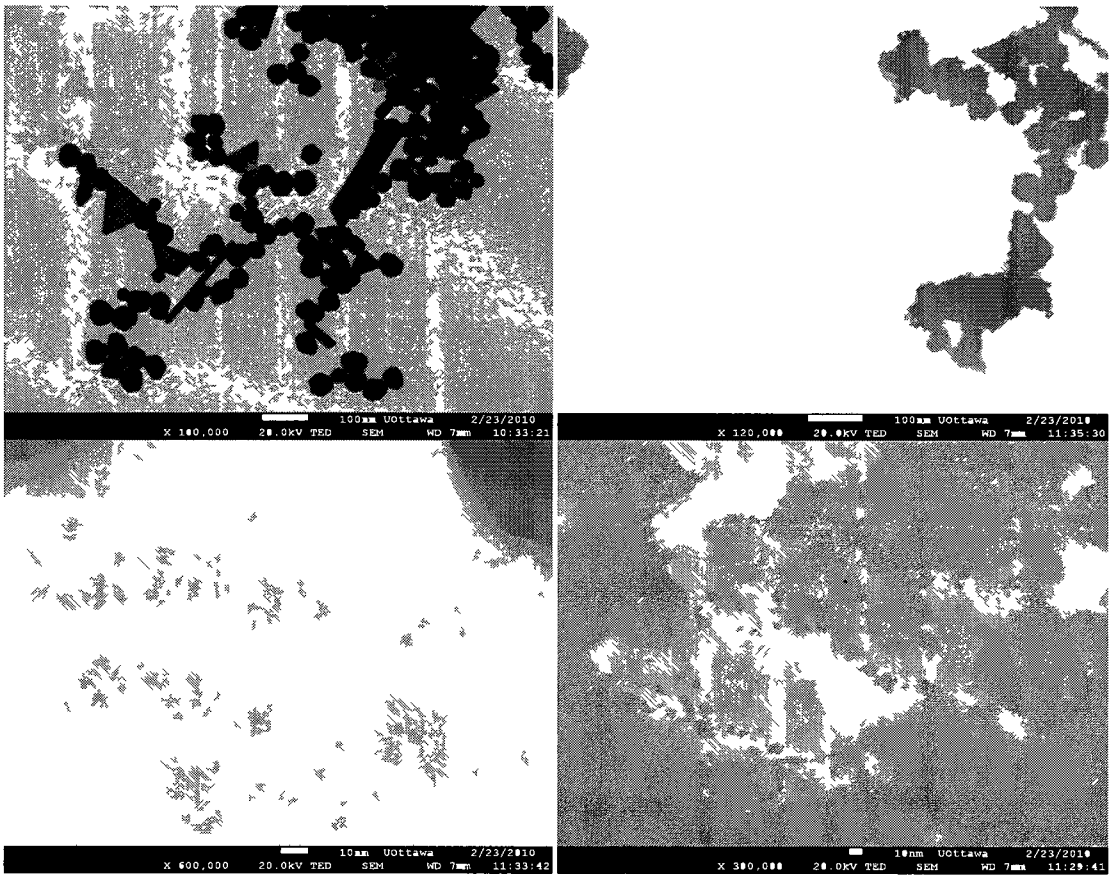

Figure 6 . 39 - SEM images of AuNP produced from H_2O_2 photoseeding after two generations from 50 µL seed addition of the first generation. Growth solution contained 0.5 mM $HAuCl_4$ and 0.5 mM H_2O_2. (top left) in the absence and (top right, bottom left and right) in the presence of 10^{-5} M MTHZ added after 30 minutes of photoseeding. Bottom left and right reveal presence of 3-5 nm AuNP. Top scale bars represent 100 nm. Bottom scale bars represent 10 nm.

For the same concentration of MTHZ added, the smaller, first generation particles will have better surface coverage compared to the larger particles. Secondly, the larger, second generation particles will have a lower surface energy and adsorption would likely be weaker in comparison.[44] These facts account for why there is a greater additional anisotropic growth for the first generation. Upon inspection of the second generation of MTHZ-AuNP in Figure 6 41, the average particle size does appear to have increased upon addition of the thiol. In comparison with the 10 nm AuNPs, which were well passivated in earlier experiments, these 40 nm particles are less covered for equivalent ligand concentration. Additional growth and seeding on

the surface also triggered secondary nucleation, where new, smaller particles with much higher surface energies were trapped at early growth diameters by the MTHZ ligand.

Functionalization with MTHZ provides a new method for the generation of small, stable and aqueous AuNP. While synthesized in solution with larger anisotropic varieties, simple centrifugation could easily separate the smaller particles for further applications. The larger seeded particles, with highly faceted snowflake geometries could be excellent candidates for SERS studies.

6.5.1.6 Ethanolamine

Acknowledging that multifunctional ligands with thiols could function to derivatize AuNP, another approach was to probe the possibility with multifunctional amines. The ligand of choice was ethanolamine, due to its water-solubility, its availability and, importantly, its inability to reduce $HAuCl_4$ in a thermal fashion. Several amines, particularly secondary and tertiary amines, have been noted to generate AuNP.[45-47] For ethanolamine, a pH study was performed to determine ideal conditions for successful functionalization, but unlike the multifunctional thiol ligands, AuNP did not display a similar sensitivity to ETHA. Ethanolamine has a pK_a of 9.5, and should certainly be in a neutral form at pH 3, 5, and 7. At these pH, however, 1.0 mM ETHA does not induce any agglomeration to reduce particle-particle distance. The absorbance spectra for the amine at various pH is displayed in Figure 6.40.

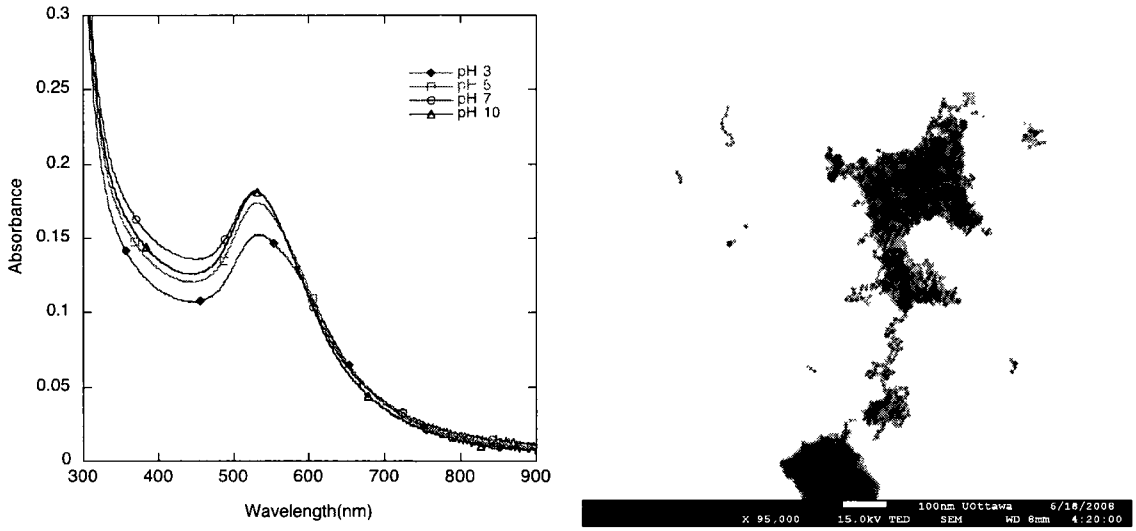

Figure 6 . 40 - (left) Absorbance of AuNP in the presence of 1.0 mM ETHA at various pH. pH varied upon addition of HCl or NaOH to H_2O. (Right) SEM image of ETHA-AuNP at pH 10.

No significant change in SPB absorbance was observed for ETHA-AuNP up to 10 mM, however centrifugation of 10 mM ETHA-AuNP at 6000 rpm for 15 minutes resulted in partial agglomeration. This is indicative of weak amine- gold nanoparticle interaction. AuNP were also prepared such that EDTA was added to different samples during the first ten minutes of the 30 minutes photochemical synthesis, where it was realized that the earlier the addition, the greater the broadening of the SPB around 700 nm. The spectra for the different samples are presented in Figure 6.41, below.

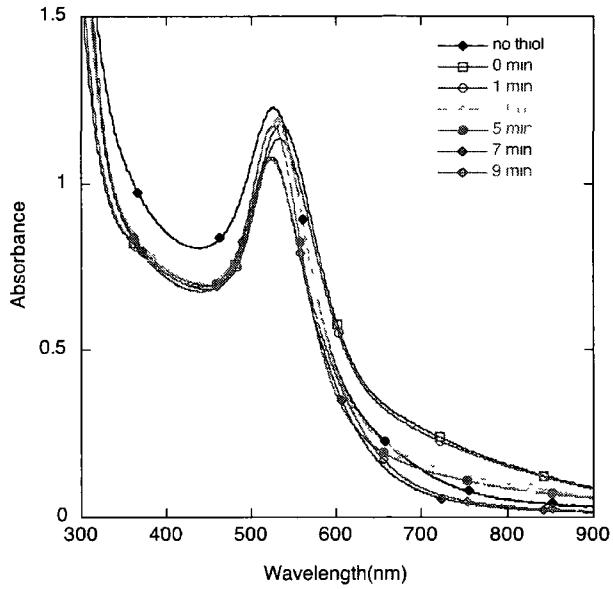

Figure 6 . 41 - Absorbance of AuNP prepared from 355 nm photolysis of 0.33 mM $HAuCl_4$ and 1.0 mM I-2959 with 1.0 mM ETHA added at different irradiation times during the 30 min UVAsynthesis. All of the spectra were acquired after the 30 minute synthesis was complete.

The results in these spectra are in contrast to observations of the identical synthesis using MTHZ, and indicate that ETHA does not bind to small, growing AuNP in the same manner as MTHZ, which agrees with previous reports stating a reduced binding for Au-NH_2 relative to Au-S, where the gold-primary amine bond has been described as weakly covalent, at best.[48]

To verify attachment of ETHA to the AuNP surface, IR and ^1H NMR of AuNP-ETHA were aquired, but no signal was present in the spectra beyond the small noise already present for the photoproducts of I-2959, similar to Figure 3.33 for centrifuged but non-functionalized AuNP. The absence of characteristic peaks for ETHA further affirms the absence of a covalent interaction of ETHA to the AuNP surface.

6.5.2 Primary Aliphatic Ligands

To facilitate the investigation of ligand adsorption, simple aliphatic thiols and amines were probed for their ability to bind to the particle surface. The ligands studied are summarized in Scheme 6.8, below.

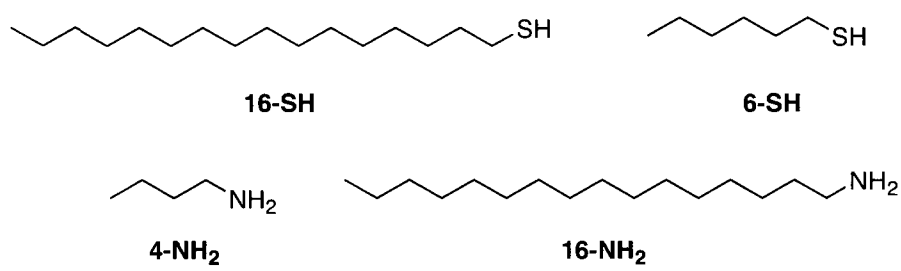

Scheme 6 . 8 - Primary aliphatic amines and thiols analyzed in this work for surface functionalization.

Short and long-chain alkyl amines and thiols were both utilized to compare the adsorption properties with other ligands in this study.

6.5.2.1 Primary amines

Both n-butylamine and hexadecylamine were employed as surface modifiers and were analyzed by absorbance spectroscopy. Fresh 50 mM stock solutions of the ligands in ethanol were prepared prior to their addition to 1:1 H_2O:EtOH AuNP solutions for a final concentration of 1.0 mM. When 4-n-butylamine was added to the red colloidal solution at pH 5, the colour transformed instantly to blue. This could be a sign of either agglomeration or larger particles, as the blue solution was stable for over a month. The blue colour can be assigned to the decreased interparticle distance with neutral, short-chained ligands that have displaced anionic ligands. In the preparation of hexadecylamine, addition of the ligand solution along the same preparatory way led to a minor shift in the SPB towards longer wavelength. The

longer chain length leads to a greater interparticle distance with equally neutral ligands replacing charged species. The pK_a values for *n*-butylamine and hexadecylamine are reported both reported around 10.6.[49, 50] These ligands are both believed to bind through the lone pair of electrons on the nitrogen, with no loss of protons.[51] The absorbance spectra for 1.0 mM amine-AuNP are both presented in Figure 6.42.

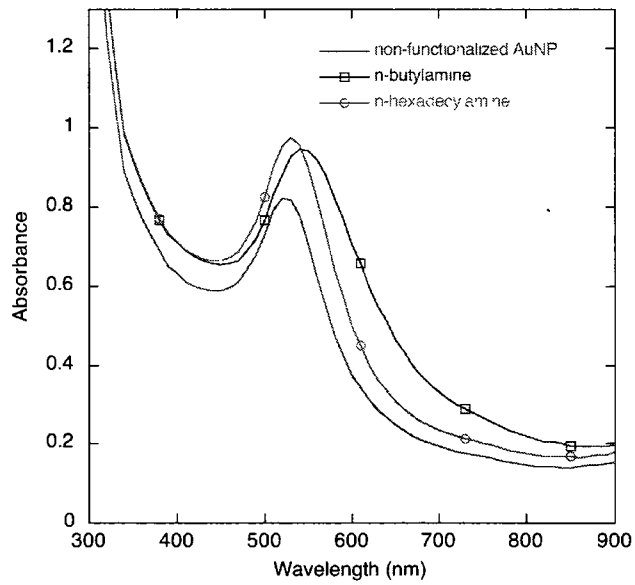

Figure 6 . 42 - Absorption spectrum of AuNP prepared via I-2959 and modified with 1.0 mM ligand. AuNPs in 2:1 H_2O:Ethanol.

Similar to experimental procedures for validating ligand attachment with multifunctional ligands, amine-AuNP were also subjected to identical seeding experiments using the NH_2OH-HCl approach. The kinetic growth of seeded AuNP are presented in Figure 6.43.

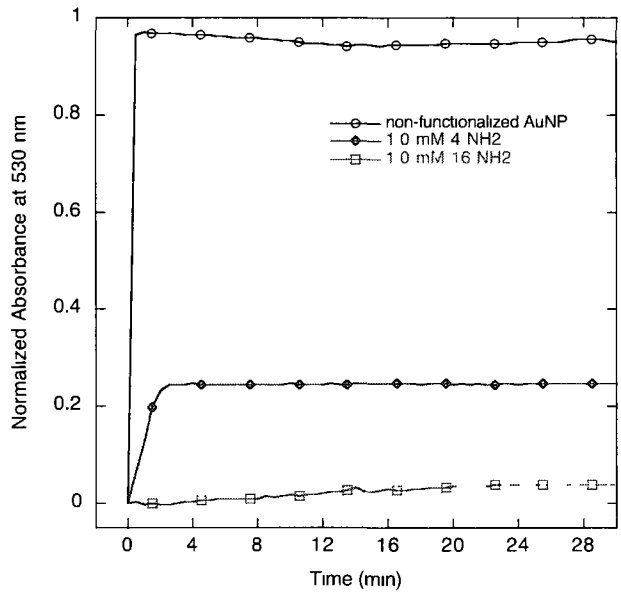

Figure 6 . 43 - Seeded growth over time of AuNP functionalized with 1.0 mM ligand. 100 µL seed added to growth solution containing 0.25 mM $HAuCl_4$ and 0.4 mM NH_2OH-HCl.

From the data, it is observed that both ligands construct a barrier to seeding, over non-functionalized AuNP, suggesting that the amines are tethered covalently to the nanoparticle surface. Between the two ligands, the shorter chained amine-AuNP underwent significant seeding relative to hexadecylamine-AuNP, albeit at a slower rate than non-functionalized AuNP. The lower plateau aborbance intensity is a result of the blue 4-NH_2-colloid possessing a lower absorbance intensity at 530 nm. The red-pink 16-NH_2-AuNP, however, possess a robust protection layer to autocatalytic seeding. The measured rates for both systems are 0.35 Ms^{-1} and 0.01 Ms^{-1} for 4-NH_2-AuNP and 16-NH_2-AuNP, respectively. The difference in behaviour is attributed to the difference in chain length, for the short-chain amine provided insufficient protection as a result of low packing density and lower Van der Waals forces between the neighbouring chains needed to construct the barrier. The longer chains of 16-NH_2, however, provided better protection through either a simple surface converage, or more dense packing at high monolayer concentration, for

long-chain amines have been known to stabilize AuNP in various synthetic preparations.[47]

6.5.2.2 Alkanethiols

The mechanism for adsorption of thiols on gold was probed by Whitesides *et al.*, who concluded that the thiols were adsorbed with liberation of H_2,[31] as opposed to release of H^+ via oxidation of a thiolate as proposed earlier by Henglein *et al.*[52] Whitesides proved that the latter proposal failed due to observations that rates of flocculation of AuNP increased with increasing chain length of alkyl thiols. The rate of flocculation was determined by redshifting of the colloidal absorbance, which could be interpreted as the rate of thiol binding to the surface with a decrease in charge and stabilization of interparticle electrostatics. Flocculation could also be caused by precipitation of chemisorbed thiols on the particle surface, as the AuNP functionalized with alkyl groups are less soluble in aqueous media. The argument of thiol binding via surface oxidation fell through for the rate of oxidation would have had to have increased faster as a thicker alkane barrier was in place. Additionally, no change in the rate of flocculation was apparent in deareated or O_2 purged samples.

In this work, AuNP were also functionalized with simple alkanethiols such as hexanethiol and hexadecanethiol. Their poor solubility in aqueous solvent necessitated aqueous AuNP to be resuspended in acetonitrile or ethanol, followed by ligand addition. The concentration of ligand added varied in several experiments. Below are the absorption spectra for AuNP functionalized with high concentrations well above the monolayer limit of the short and long alkanethiol, presented in Figure 6.44. The differences between the SPB imply that 1) addition of the R-SH neutralizes the surface charge resulting in flocculation, evident from the redshift and band broadening relative to bare AuNP in acetonitrile. 2) the degree of band

broadening of 16-SH AuNP is lower than that of 6-SH, likely due to the increased chain length for increased interparticle distance.

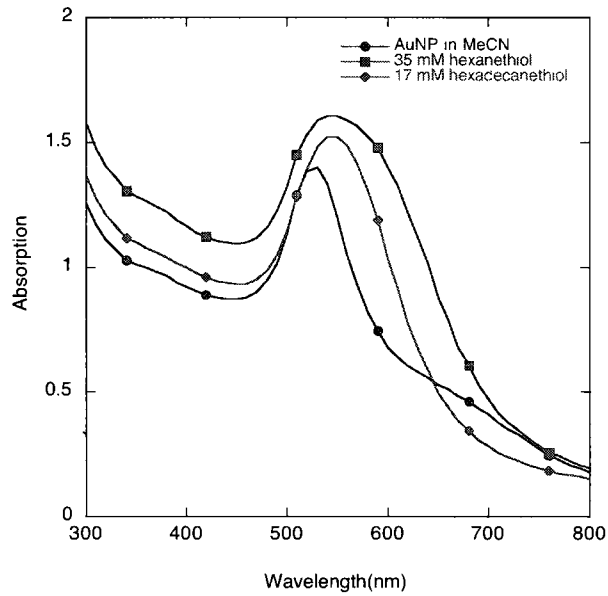

Figure 6 . 44 - Absorption of AuNP functionalized with different alkanethiols at different concentrations in acetonitrile.

Seeding was also performed *via* the NH_2OH-HCl method with AuNP functionalized under identical conditions to those of the primary amine study, where derivatized AuNP seeds were in a solvent of 1:1 H_2O:EtOH prior to addition to the aqueous growth solution, and monitored for 30 minutes. Similar to the amines, the thiol ligands also provided a passivation layer to particle modification. Unlike the amines studied, however, the thiols displayed rather similar reactivity. Both short and long-chained thiols provided a barrier to seeded growth for the first ten minutes, but both systems displayed eventual growth with prolonged measurement. 6-SH-AuNP were susceptible to seeded-growth at a shorter time of 12 minutes, while 16-SH-AuNP possessed an induction period of approximately 20 minutes. These results are displayed in Figure 6.45, where all initial absorbances are normalized to zero.

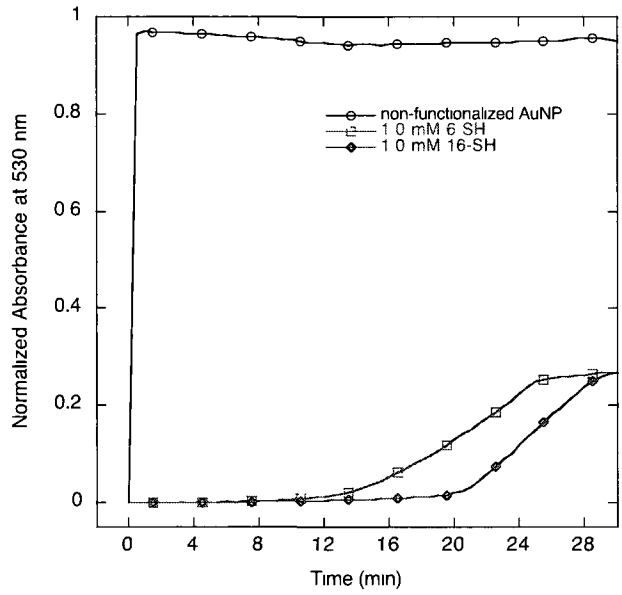

Figure 6 . 45 - Seeded growth over time of AuNP functionalized with 1.0 mM ligand. 100 µL seed added to growth solution containing 0.25 mM $HAuCl_4$ and 0.4 mM NH_2OH-HCl.

The occurrence of seeded-growth after long induction periods can be understood by recalling that the samples were seeded under aereated conditions. As discussed in Section 6.5.1.4, alkanethiols are susceptible to oxidation to form dialkyldisulfides, and dialkyldisulfides have been observed in previous reports to dissociate from AuNP surfaces, resulting in AuNP aggregation.[39] While the alkanethiol-AuNP in these experiments had been aged for approximately two weeks under ambient conditions, introduction of additional $AuCl_4^-$ could initiate oxidation of the thiols. It is known that $K_3Fe(CN)_6$ has been used as an oxidizing agent to oxidize octanethiol monolayers to its disulfide at millimolar concentrations,[53] and with $AuCl_4^-$ (E^0 = +0.99 vs NHE) possessing a more positive reduction potential that that of $Fe(CN)_6^{3+}$ (E^0 = +0.459 vs NHE)[54], the oxidation of thiol-bound AuNP by Au^{3+} is a possibility. While the mechanism for desorption in the presence of growth solution is currently unknown to us, it is noted that this chemistry did not occur for MHDA. The longer induction period for seeding by 16-SH relative to 6-SH is attributed to a longer chain length with the same argument of packing density as presented for hexadecylamine.

An explanation for the trend was previously targeted at the existence of an energy barrier for the detangling of the methylene chains and disruption of hydrogen bonding of the terminal carboxylate moieties. An energy value of roughly 3-6 kcal/mol was allotted to the process of separating linear alkanethiol chains, and the collective interactions allude to a densely-packed surface for chain lengths beyond ten methylene groups.[31]

6.5.3 Comparative Analysis

Over the course of this doctoral research, several seeding experiments have been performed to assess the covalent intereactions between the ligands and gold nanoparticle surfaces. They are presented collectively in this section for a clear comparison between ligands with different chain lengths, different tethering groups, and different pK_a. Given the aqueous nature of these colloidal studies, the pK_a of the molecules has proven to offer a useful reference point for the behaviour of nanoparticle interactions in solution. The pH of the as-synthesized AuNP has been measured to be 5.2 after ripening, where the particles are charge stabilized by 4-HEBA, which has a pK_a of 4.45. When the pH of the solution is above the pK_a of the molecule, the molecule will be in the dissociated form, hence 4-HEBA stabilizing AuNP in the anionic form. Given the proximity of the pK_a to the pH of the solution, the percentage of dissociated species in solution was approximated to be 17.8 using the following equation 6.6.

$$pH = pK_a + \log\left[\frac{A^-}{HA}\right] \qquad (6.3)$$

With an average quantum yield for photodissociation of 0.3 and the assumption that all of the benzoyl radicals are oxidized to the carboxylate, an upper limit on the concentration of 4-HEBA in solution then becomes 6.6 μM. At this concentration, AuNP have been charge-stabilized for over four years with optimal stability. Addition

of neutral or negatively-charged ligands to this system resulted in different spectral shifts obvious to the naked eye.

In the case of negatively-charged ligands such as MPSA and CYS in pH 5 solutions, and MHDA and DTBA at pH 7 and 10 conditions, different behaviour was observed which was attributed to the surface adsorption interactions. The short-chained thiol groups of MPSA and CYS lead to a reduction in ligand surface packing density as well as interparticle distance. As a result, both of these groups displayed red-shifted absorbance spectra with increasing ligand concentration. The seed particles of MPSA and CYS both possessed a longitudinal peak implying irregular or rod-like shape, yet electron imaging neglected to display particles with longitudinal features. CYS-stabilized AuNP have been known to display agglomeration as a result of the attractive forces between carboxylate and amine groups on neighbouring particles.[55] These flocculation observations are in contrast to the narrow absorbance band for MHDA-AuNP at alkaline pH, for the longer chain length and better packing density of the molecule allows for a greater interparticle distance.[56] A number of the ligands studied were present in solution in their neutral form, as a result of their higher pK_as. A summary of the pK_a for the ligands studied in this research is presented in Table 6.5.

Ligand		pK_a
MPSA	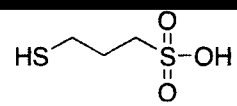	3.6
CYS	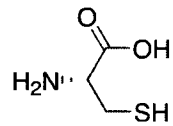	2.05 (COOH) 8.0 (SH) 10.2 (NH_2)
MHDA	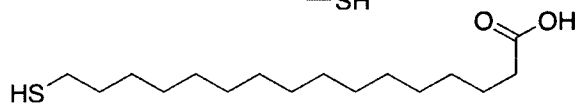	4-5
DTBA	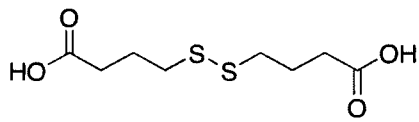	4-5
6-SH	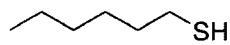	10.3
4-NH_2	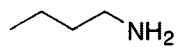	10.6
16-NH_2	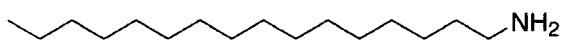	10.6
16-SH	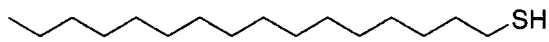	10.8
MTHZ	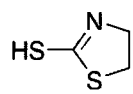	11.0

Table 6 . 5 - pK_a values for the ligands studied in this work.

Among the studied neutral molecules, *n*-butylamine displayed the greatest spectral shift in the shortest time, where the solution instantly turned to a deep blue upon addition, while *n*-hexanethiol afforded a lilac purple colour gradually over approximately 5 minutes. While both molecules are shorter chains, the extra two carbons on 6-SH account for better chain particle packing and greater Van der Waals attractive interactions. The direct comparisons between 4-NH_2 and 16-NH_2, as well as 6-SH with 16-SH display a decrease in SPB redshift with increasing chain-length as a result of increased interparticle distance induced by the ligand length. MTHZ, like 4-NH_2, is a short and water-soluble ligand. Unlike the amine, however, the SPB for this multifunctional ligand displayed a purple/blue colour. This difference could be attributed to an increase in interparticle distance as a result of

steric hindrance afforded by the heteroatomic ring. The different absorbance properties of some functionalized AuNP are presented in the photograph in Figure 6.46. It is worth emphasizing that all AuNP were synthesized from the same batch, underlining the change in SPB with identical particle size and differing interparticle distance.

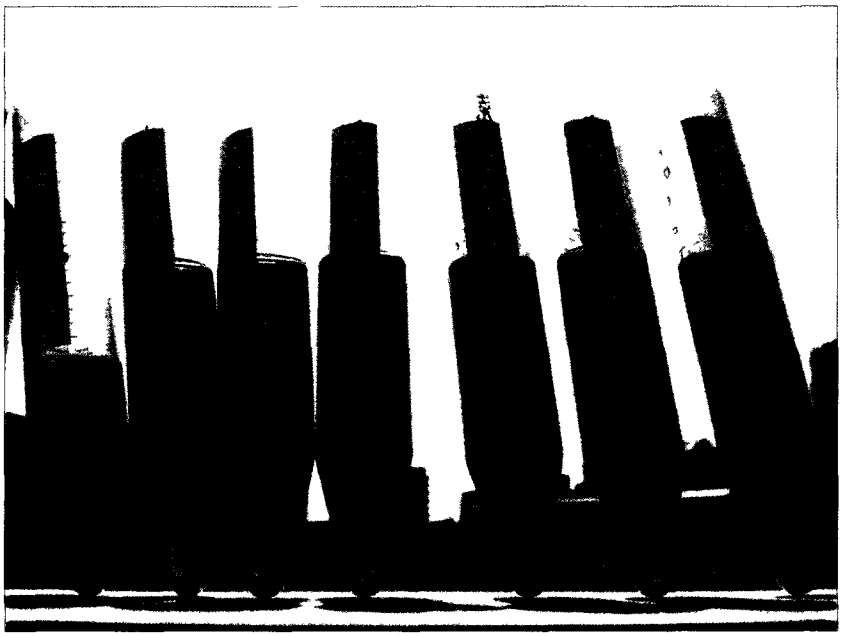

Figure 6 . 46 - Photograph displaying the spectra sensitivity of AuNP. (left to right) non-functionalized AuNP, 16-NH_2-AuNP, MHDA-AuNP, 6-SH-AuNP, 16-SH-AuNP, MTHZ-AuNP, 4-NH_2-AuNP. All AuNP are functionalized at 1.0 mM ligand in 1:1 H_2O:EtOH.

In addition to the different spectral properties of the ligands studied, further distinctions can be made by analysis of the functionalized AuNP in etching and seeding experiments.

6.5.3.1 Etching

When discussing the etching studies with various ligands, it was helpful to compare the decay rates of these processes. Essentially, the absorbance of the translational SBP shifted to longer wavelength followed by nanoparticle decomposition. In the

absence of any ligand, nanoparticles decomposed and precipitated out of solution, while the presence of MPSA, MHDA and CYS at 0.5 mM concentrations provided a passivation layer for which the process was minimized. The normalized decays are presented in Figure 6.47.

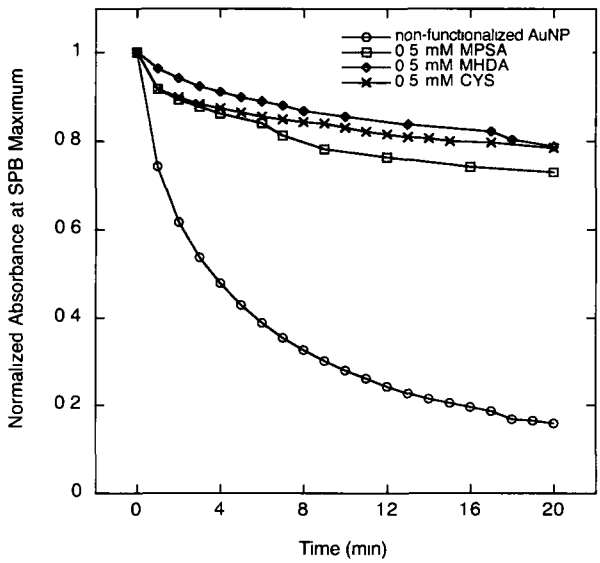

Figure 6 . 47 - Etching of AuNP functionalized with 0.1 mM different ligands upon exposure to etching solution containing 0.1 M KCN in 1.0 M KOH. 500 µL seed added to etching solution.

The resulting surface plasmon bands displayed both a translational and longitudinal band, suggesting that some agglomeration took place. This behaviour has also been observed by others, and suggests that the surface of the particles aren't fully passivated by thiol ligands.[32] Among the three thiols evaluated, MPSA offered the least protection, followed by CYS, with MHDA displaying the strongest passivation. This trend can be attributed to the size and structure of the ligand, where long, linear chains such as MHDA pack better to build strong monolayers, while shorter ligands provide less dense packing and a shorter barrier for the etchant to penetrate through. This resistance of MHDA could also be the result of the decreased solubility of the ligand in aqueous solutions, relative to the aqueous ligands. The pK_a for the studied groups are approximately 4.5 for MHDA, 3.6 for MPSA and 2.05 for the carboxylate group of CYS. The clear trend in resistance with pK_a under strongly

basic conditions suggests that ligands behaving as stronger bases show a better ability to minimize the etching of the gold surface, likely through electrostatic repulsion of the incoming anionic base to the anionic surface shield.

In these experiments, the shape of the surface plasmon band changed significantly with a growth appearing around 750 nm which redshifts with time. While no SEM or TEM images have been taken of the functionalized but etched particles, it is likely that this process involves coagulation of the surfaces of the gold nanoparticles that weren't passivated by thiol. The KCN could have stripped off the stabilizing Au^{+}, Cl^{-} and other ions on the surface, which led to flocculation.

6.5.3.2 Seeding

When nanoparticles were functionalized with MHDA, cysteine or MPSA, the seeding appeared to be arrested, relative to non-functionalized AuNP. The comparison is made in Figure 6.47. Nevertheless, among the three ligands, MPSA displayed weaker resistance, while CYS and MHDA displayed a more robust barrier to the growth. Notably, the increase in the SPB of a growth solution is also displayed for comparison. This order of ligands is in agreement with the etching experiments discussed in the previous section. The strong resistance to CYS AuNP can also be attributed to the agglomeration of amino-acid residues on the surface, despite its short and flexible chain, relative to MHDA.

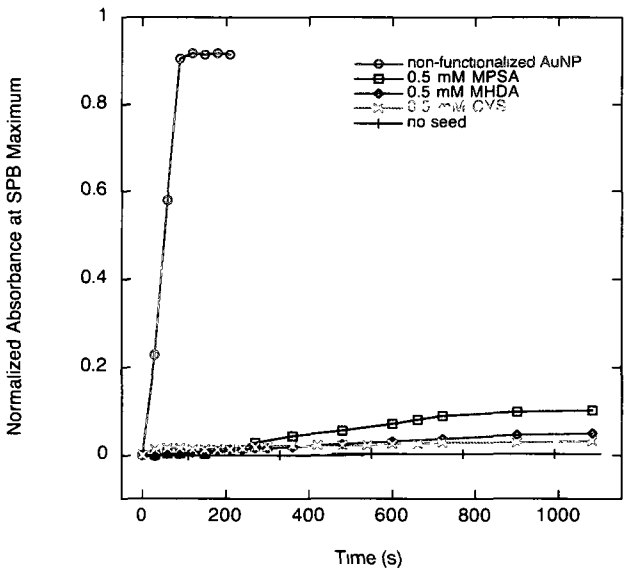

Figure 6 . 48 - Absorbance of SPB of AuNP functionalized with 05 mM various ligands and added to growth solution containing 0.25 mM $HAuCl_4$ and 0.4 mM NH_2OH-HCl. 3.3 µM seed added.

Other seeding studies were performed with MHDA, MHTZ and DTBA, where the kinetics of seeded growth with a 3.31 µM aliquot of functionalized seed were monitored over time in an identical hydroxylamine seeding system. These results are also compared and presented in Figure 6.48. MHDA is presented to act as a reference for the degree of protection that the ligands displayed in the separate experiments. It is immediately clear that MTHZ is as strong as MHDA in preventing seeded growth, while the disulfide DTBA was rather ineffective. With the argument of pK_a, MTHZ is known to be a much stronger base than the two carboxylic acids, yet both MHDA and MTHZ performed equally as well while DTBA provided poor surface protection. The rates for seeded growth were calculated to be 0.012 Ms^{-1}, 0.004 Ms^{-1} and 0.002 Ms^{-1} for DTBA, MTHZ and MHDA, respectively. The rates for all of the AuNP-functionalized seeded growth experiments are summarized in Table 6.6.

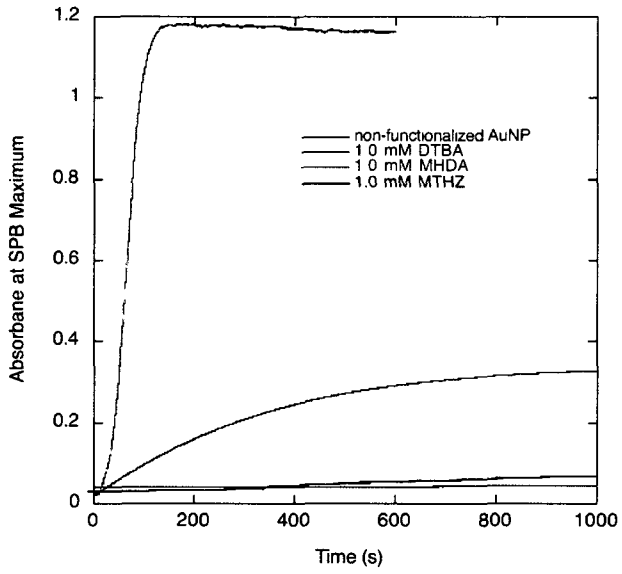

Figure 6 . 49 - Seed-mediated growth of functionalized AuNP over time in the presence of 0.25 mM $HAuCl_4$ and 0.4 mM NH_2OH-HCl. 3.31 µM seed functionalized with 1.0 mM ligand.

The seeding results for MHDA and DTBA, in agreement with SEM images of the seeding experiments, emphasize that the prevention of seeding is not merely a result of electrostatic repulsion between the mild reducing agent and ligands with negatively-charged end groups in solution, but in fact proves that the thiol ligands are bound to the surface. Otherwise, DTBA and MHDA, with essentially identical pK_a, would have displayed the same resistance to seeded growth.

A final seeding comparison analyzed the effects of primary alkyl stabilizers against seeded growth under similar conditions as the previous ones, except for the concentration of ligand was doubled to 1.0 mM. In the presence of simple alkane ligands, where the pK_a are all essentially equivalent at 10, a true understanding of the effects of binding group and chain length can be understood. The comparison of aliphatic derivatized seeded-growth is found in Figure 6.50, where seeding is expected to arise on the (111) surfaces of the dodecahedral particles, as described in earlier sections.

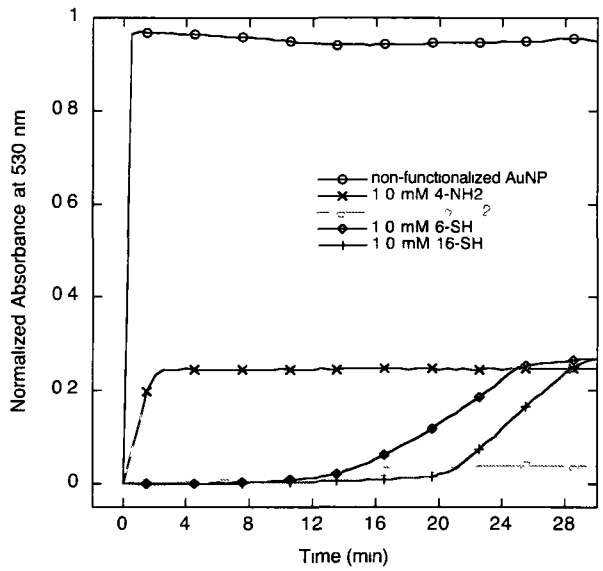

Figure 6 . 50 - Seeded growth over time of AuNP functionalized with 1.0 mM ligand. 3.31 μM seed added to growth solution containing 0.25 mM $HAuCl_4$ and 0.4 mM NH_2OH-HCl.

Functional Ligand	Ligand Concentration (mM)	v (Ms^{-1})
No ligand	N/A	0.105
4-NH_2	1.0	0.035
DTBA	1.0	0.012
CYS	0.1	0.012
16-SH	1.0	0.010
6-SH	1.0	0.008
MPSA	0.5	0.005
MTHZ	1.0	0.004
16-NH_2	1.0	0.003
CYS	0.5	0.002
CYS	1.0	0.002
MHDA	0.5	0.002
No AuNP seed	N/A	0.0004

Table 6 . 6 - Summary of rates for the autocatalytic seed-mediated growth of functionalized AuNP under aereated conditions in 0.25 $HAuCl_4$ and 0.4 mM NH_2OH-HCl growth solution.

The poor seeding protection displayed by 4-NH_2 relative to 16-NH_2 is purely a consequence of chainlength, and is attributed to low packing density of the alkyl chains, as discussed in the previous section. The two thiols displayed strong resistance, yet eventual seeding took place after long induction periods. The seeding is thought to be a consequence of surface oxidation of thiols to disulfides, potentially induced by $HAuCl_4$ in the growth solution. Notably, 16-NH_2 provided strong protection against seeding and without ligand desorption.

The chemistry involved in tethering organic molecules to the surface of photochemically generated aqueous gold nanoparticles has been studied with a number of molecules such that the results contribute to the greater understanding of chemisorption and physisorption on the nanoparticle surface.

6.5.4 DNA

Substantial research has gone into derivatizing gold nanoparticles with DNA and using plasmon sensitivity as a probe for biological sensing.[57-59] In this research, we experimented with the synthesis of AuNP *in-situ* single and double-stranded DNA *via* the I-2959 method for facile surface modification using low energy UVA irradiation.

Double stranded calf-thymus DNA was utilized as a biological surface modifier due to its availability in the lab. DNA was prepared in 0.5 to 0.25 mg/mL concentrations, which were shaken lightly to dissolve the viscous biopolymer. The samples were prepared fresh but kept at 4°C and stored in the refrigerator until added to the samples. Additionally, single-stranded DNA was prepared by simply denaturing the polymer, which was achieved by boiling the DNA in a water bath for five minutes.

AuNP prepared *in-situ* appear smaller in size according the SEM presented in Figure 6.51, where a large population of particles 3-5 nm in size is present in

addition to 10 nm particles. The two size populations could be separated through careful centrifugation. Particles prepared with double-stranded DNA gave an average hydrodynamic radius of 16.3 nm, while samples prepared with single-stranded DNA were on average of 5.1 nm. SEM images reveal the presence of 10 nm particles in both samples, yet a greater population using the double stranded DNA sample. This difference in hydrodynamic radius could also relate to the decrease in viscosity of the single-stranded DNA as a result of boiling and thus allow for more binding with the particle surface.

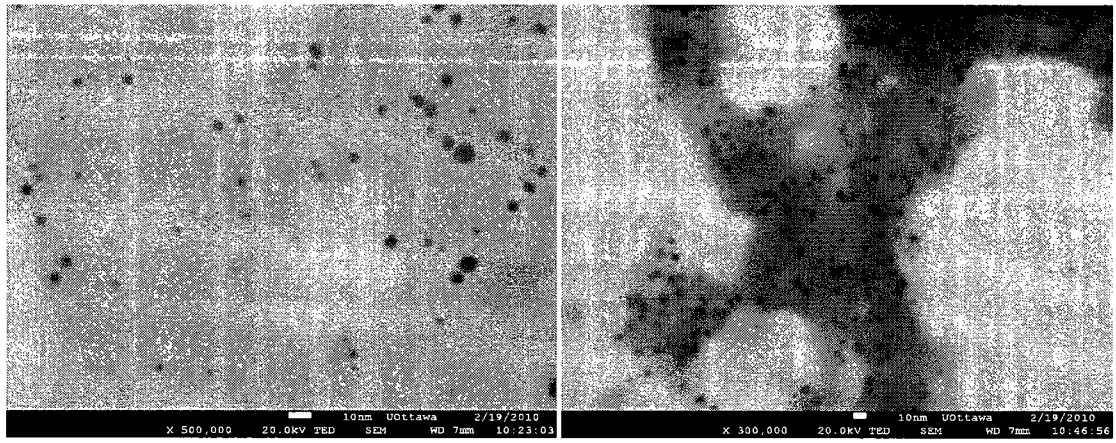

Figure 6 . 51 - SEM image of AuNP prepared *in-situ* with single-stranded calf thymus DNA before (left) and after (right) centrifugation. The scale bars both prepresent 10 nm.

Seeding of calf thymus single-stranded DNA on AuNP was also executed, where low resistance was observed in comparison with other seeding studies compared in Section 6.5.3. A rate constant for the autocatalytic seeded-growth was determined to be 0.012 Ms^{-1} after a 4 minute induction period. The growth of the AuNP SPB over time is presented in Figure 6.52. The biological material provided a greater delay over the commencement of seeding compared to 4-*n*-butylamine, cysteine or DTBA, and this could be attributed to the DNA acting as an anionic polymeric barrier through which the reducing agent and gold salt diffused. Once the seeding reagents diffused through, however, the degree of seeded growth increased to a larger

intensity, likely due to the lack of specific adsorption of any base-pairs to the particle surface.

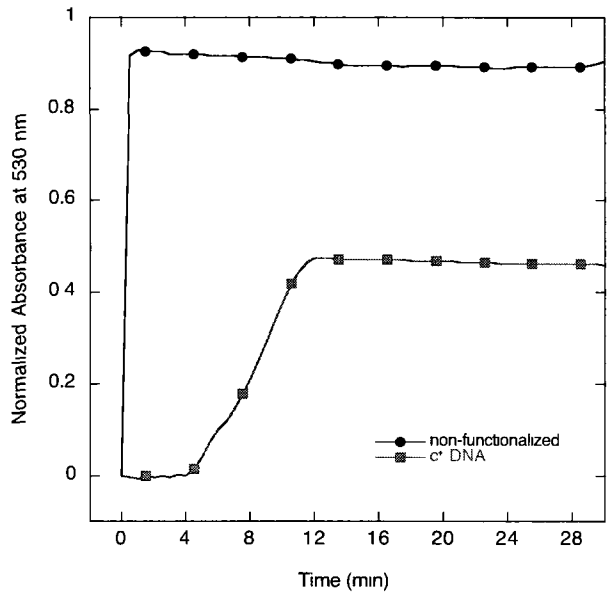

Figure 6 . 52 - Seed-mediated growth of AuNP over time of AuNP functionalized with various ligands. 100 µL seed added to growth solution containing 0.25 mM $HAuCl_4$ and 0.4 mM NH_2OH-HCl.

With these results in mind, this partial protection could provide perfect conditions for catalytic biological reactions on the gold nanoparticle surface. In such situations, the particle would maintain an ideal interparticle distance without a shift or loss of surface plasmon absorbance, yet still be an ideal candidate for plasmon-assisted catalysis.

6.7 Summary

The surface reactivity of photochemically prepared AuNP from I-2959 has been investigated through seed-mediated growth and surface modification with a silica shell as well as various organic ligands. The enlargement of AuNP through seeding

was studied with a NH_2OH-HCl system, where the rate of seeded growth increased with increased seed concentration, while the size of resulting particles increased with decreased seed concentration. A sequential photochemical seeding technique was devised using both I-2959 and H_2O_2 as separate reducing agents, and the monodispersity of resulting larger particles improved relative to NH_2OH-HCl, where the size of resulting particles was observed to increase with increased seed concentration with respect to identical "generations". The photochemical seeding approach offers an additional strategy for careful increase of particle size. AuNP modified with a silica shell displayed improved stability to etchant solutions, organic solvents and aqueous solution in the 2-12 pH range, relative to non-functionalized AuNP.

Gold nanoparticles were derivatized with a variety of different ligands, where long chain thiols and amines provided denser monolayers relative to shorter chained molecules. Binding of small ligands such as MPSA, CYS and MTHZ resulted in strong redshifts in SPB absorbance, while ETHA did not. Seeding and etching experiments validated the surface coverage by the ligands, and the rates of seeded growth were compared. MHDA, MYHZ and 16-NH_2 provided strong resistance to seeded growth. AuNP were also prepared with highly polymerized calf thymus DNA to afford small ~3-5 nm AuNP. These findings highlight the versatility of photochemically generated AuNP, where the photoproduct functions as a physisorbed stabilizer, and can easily be exchanged for several different ligands.

6.8 References

1. Han, G., Ghosh, P., Rotello, V., Special Focus: Advances in Nanomedicine Symposium- Review. *Nanomedicine* **2007,** *2* (1), 113-123.

2. Chithrani, B. D., Ghazani, A. A., Chan, W. C. W., Determining the Size and Shape Dependence of Gold Nanoparticle Uptake in Mammalian Cells. *Nano Lett.* **2006,** *6*, 662-668.

3. Gosh, P., Han, G., De, M., Kim, C. K., Rotelo, V. M., Gold Nanoparticles in Drug Delivery Applications. *Adv. Drug Delivery Rev.* **2008,** *60*, 1307-1315.

4. Jana, N. R.; Gearheart, L.; Murphy, C. J., Seeding Growth for Size Control of 5-40 nm Diameter Gold Nanoparticles. *Langmuir* **2001,** *17* (22), 6782-6786.

5. Hostetler, M. J., Wingate, J. E., Zhong, C.-J., Harris, J. E., Vachet, R. W., Clark, M. R., Londono, D., Green, S. J., Stokes, J. J., Wingall, G. D., Glish, G. L., Porter, M. D., Evans, N. D., Murray, R. W., Alkanethiolate Gold Cluster Molecules with Core Diameters from 1.5 to 5.2: Core and Monolayer Properties as a Function of Core Size. *Langmuir* **1998,** *14*, 17-30.

6. Meltzer, S.; Resch, R.; Koel, B. E.; Thompson, M. E.; Madhukar, A.; Requicha, A. A. G.; Will, P., Fabrication of Nanostructures by Hydroxylamine Seeding of Gold Nanoparticle Templates. *Langmuir* **2001,** *17* (5), 1713-1718.

7. Dong, S.; Tang, C.; Zhou, H.; Zhao, H., Photochemical Synthesis of Gold Nanoparticles by the Sunlight Radiation using a Seeding Approach. *Gold Bull.* **2004,** *37* (3,4), 187-195.

8. Brown, K. R.; Walter, D. G.; Natan, M. J., Seeding of colloidal Au nanoparticle solutions. 2. Improved control of particle size and shape. *Chem. Mater.* **2000,** *12* (2), 306-313.

9. Jana, N. R., Gearheart, L., Murphy, C. J., Evidence For Seed-Mediated Nucleation in the Chemical Reduction of Gold Salts to Gold Nanoparticles. *Chem. Mater.* **2001,** *13*, 2313-2322.

10. Chen, D.-H., Chen, C.-J., Formation and Characterization of Au-Ag Bimetallic Nanoparticles in Water-in-Oil Microemulsions. *J. Mater. Chem.* **2002,** *12* (1557-1562).

11. Cao, L., Zhu, T., Liu, Z., Formation Mechanism of Nonspherical Gold Nanoparicles During Seeding Growth: Roles of Anion Adsorption and Reducing Rate. *J. Colloid. Interface Science* **2006,** *293*, 69-76.

12. Sau, T. K., Pal, A., Jana, N. R., Wang, Z. L., Pal, T., Size Controlled Synthesis of Gold Nanoparticles Using Photochemically Prepared Seed Particles. *J. Nanoparticle Res.* **2001,** *3*, 257-261.

13. Jana, N. R., Gearheart, L., Murphy, C. J., Seed-Mediated Growth Approach for Shape -Controlled Synthesis of Spheroidal and Rod-like Gold Nanoparticles Using a Surfactant Template. *Adv. Mater.* **2001,** *13*, 1389-1393.

14. Wang, Z. L., Gao, R. P., Nikoobakht, B., El-Sayed, M. A., Surface Reconstruction of the Unstable {110} Surface in Gold Nanorods. *J. Phys. Chem. B.* **2000,** *104*, 5417-5420.

15. Elechiguerra, J. L., Reyes-Gasga, J., Yacaman, M. J., The Role of Twinning in Shape Evolution of Anisotropic Noble Metal Nanostructures. *J. Mater. Chem.* **2006,** *16*, 3906-3919.

16. Zou, X., Ying, E., Dong, S., Seed-Mediated Synthesis of Branched Gold Nanoparticles With the Assistance of Citrate and Their Surface-Enhanced Raman Scattering Properties. *Nantechnology* **2006,** *17*, 4758-4764.

17. Schwartz-Narbonne, R. Investigations into Seeding Growth of Photochemically Produced Gold Nanoparticles. Undergraduate, University of Ottawa, Ottawa, 2009.

18. Schmid, G., Clusters and Colloids- Metals in the Embryonic State. *Chem. Rev.* **1992,** *92*, 1709-1727.

19. Liu, X., Atwater, M., Wang, J., Huo, Q., Extinction Coefficient of Gold Nanopartciels with Different Sizes and Different Capping Ligands. *Coll. Surf. B. Biointerfaces* **2006,** *58*, 3-7.

20. Link, K., El-Sayed, M. A., Size and Temperature Dependence of the Plasmon Absorption of Colloidal Gold Nanoparticles. *J. Phys. Chem. B.* **1999,** *103*, 4212-4217.

21. Yuan, H., Ma, W., Chen, C., Zhao, J., Liu, J., Zhu, H., Gao, X., Shape and SPR Evolution of Thorny Gold Nanoparticles Promoted by Silver Ions. *Chem. Mater.* **2007,** *19*, 1592-1600.

22. Millstone, J. E., Metraux, G. S., Mirkin, C. A. , Controlling the Edge Length of Gold Nanoprisms via a Seed-Mediated Approach. *Adv. Mater.* **2006,** *16*, 1209-1214.

23. Lofton, C., Sigmund, W., Mechanisms Controlling Crystal Habits of Gold and Silver Colloids. *Adv. Funct. Mater.* **2005,** *15*, 1197-1208.

24. Henglein, A., Meisel, D., Radiolytic Control of the Size of Colloidal Gold Nanoparticles. *Langmuir* **1998,** *14*, 7392-7396.

25. Henglein, A., Giersig, M., Formation of Colloidal Silver Nanoparticles: Capping Action of Citrate. *J. Phys. Chem. B.* **1999,** *103*, 9533-9539.

26. Gonzalez, C. M.; Scaiano, J. C., Photochemical Strategies for the Facile Synthesis of Gold-Silver Alloy and Core-Shell Bimetallic Nanoparticles. *J. Phys. Chem. C.* **2009,** *113* (27), 11861-11867.

27. Ung, T., Liz-Marsan, L. M., Mulvaney, P., Controlled Method for Silica Coating of Silver Colloids, Influence of Coating on the Rate of Chemical Reactions. *Langmuir* **1998,** *14*, 3740-3748.

28. Liz-Marzan, L. M., Geirsig, M., Mulvaney, P., Synthesis of Nanosized Gold-Silica Core-Shell Particles. *Langmuir* **1996,** *12*, 4329-4335.

29. Xu, J., Perry, C. C., A Novel Approach to Au@SiO2 Core-Shell Spheres. *J. Non-Crystalline Solids* **2007,** *353*, 1212-1215.

30. Lee, J., Park, C., Bang, J. U., Song, H., Precise Tuning of Porosity and Surface Functionality in Au@SiO2 Nanoreactors for High Catalytic Efficiency. *Chem. Mater.* **2008,** *20*, 5839-5844.

31. Weisbecker, C. S., Merritt, M. V., Whitesides, G. M., Molecular Self-Assembly of Aliphatic Thiols on Gold Colloids. *Langmuir* **1996,** *12*, 3763-3772.

32. Zhu, T., Vasilev, K., Kreiter, M., Mittler, S., Knoll, W., Surface Modification of Citrate-Reduced Colloidal Gold Nanoparticles with 2-Mercaptosuccinic Acid. *Langmuir* **2003,** *19*, 9518-9525.

33. Chen, S.-J., Chang, H.-T., Nile Red-Adsorbed Gold Nanoparticles for Selective Determination of Thiols Based on Energy Transfer and Aggregation. *Anal. Chem.* **2004,** *76*, 3727-3734.

34. Pawlukojc, A., Leciejewicz, J., Ramirez-Cuesta, A.J., Nowicka-Scheibe, J., L-Cysteine: Neutron Spectroscopy, Raman, IR and ab initio Study. *Spectrochimica Acta Part A* **2005,** *61*, 2474-2481.

35. Aryal, S., Remant, B. K. C., Dharmaraj, N, Bhattarai, N., Kim, C. H., Kim, H. Y., Spectroscopic Identification of S-Au interaction in Cysteine Capped Gold Nanoparticles. *Spectrochimica Acta Part A* **2006,** *63*, 160-163.

36. Hasan, M., Bethell, D., Brust, M., The Fate of Sulfur-Bound Hydrogen on Formation of Self-Assembled Thiol Monolayers on Gold: 1H NHR Spectroscopic Evidence from Solutions of Gold Clusters. *J. Am .Chem. Soc.* **2002,** *124*, 1132-1133.

37. Porter, L. A., Ji, D., Westcott, S. J., Graupe, M., Czernuszewics, R. S., Halas, N. J., Lee, T. R., Gold and Silver Nanoparticles Functionalized by the Adsorption of Dialkyl Disulfides. *Langmuir* **1998,** *14*, 7378-7386.

38. Billone, P., Maretti, L., Maurel, V., Scaiano, J. C., Dynamics of the Dissociation of a Disulfide Biradical on a CdSe Nanoparticle Surface. *J. Am .Chem. Soc.* **2007,** *129*, 14150-14151.

39. Dasog, M., Scott, R. W. J., Understanding the Oxidative Stability of Gold-Nanoparticle Monolayer-Protected Clusters in the Presence of Halide Ions under Ambient Conditions. *Langmuir* **2007,** *23*, 3381-3387.

40. Mahal, H. S., Mukherjee, T., Kinetic and Spectroscopic Properties of Intermediates Formed in the Reaction of Some Oxidizing and Reducing Radicals with 2-mercaptothiazoline (2-MT) in Aqueous Solutions. *Radiation Physics and Chemsitry* **1999,** *54*, 29-37.

41. Jin, R., Quantum Sized, Thiolate-Protected Gold Nanoclusters. *Nanoscale* **2010,** *2*, 343-362.

42. Corbierre, M. K., Lennox, R. B., Preparation of Thiol-Capped Gold Nanoparticles by Chemical Reduction of Soluble Au(I)-Thiolates. *Chem. Mater.* **2005,** *17*, 5691-5696.

43. Ackerson, C. J., Jadzinsky, P. D., Kornberg, R. D., Thiolate Ligands for Synthesis of Water-Soluble Gold Clusters. *J. Am .Chem. Soc.* **2005,** *127*, 6550-6551.

44. Burda, C., Chen, X., Narayanan, R., El-Sayed, M. A., Chemistry and Properties of Nanocrystals of Different Shapes. *Chem. Rev.* **2005,** *105*, 1025-1102.

45. Newman, J. D. S., Blanchard, G. J., Formation of Gold Nanoparticles Using Amine Reducing Agents. *Langmuir* **2006,** *22*, 5882-5887.

46. Gandubert, V. F., Lennox, R. B., Assessment of 4-(Dimethylamino)pyridine as a Capping Agent for Gold Nanoparticles. *Langmuir* **2005,** *21*, 6532-6539.

47. Aslam, M., Fu, L., Su, M., Dravid, V. P., Novel One-step Synthesis of Amine-stabilized Aqueous Colloidal Gold Nanoparticles. *J. Mater. Chem.* **2004,** *14*, 1795-1797.

48. Chen, F., Li, X., Hihath, J., Huang, Z., Tao, N., Effect of Anchoring Groups on Single-Molecule Conductance: Comparitive Study of Thiol-, Amine-, and Carboxylic-Acid-Terminated Molecules. *J. Am .Chem. Soc.* **2006,** *128*, 15874-15881.

49. Hayashi, M., Kobayashi, T., Seimiya, T, Muramatsu, T., Hara, I., Ionic Properties of Phospholipids at the Oil/Water Interface. *Chem. Phys. Lipids.* **1980**, 1-8.

50. Simanek, E. E., Abdou, H., Lalwani, S., Lim, J., Mintzer, M., Venditto, V. J., Vittur, B., The 8 Year Thicket of Triazine Dendrimers: Strategies, Targets and Applications. *Proc. R. Soc. A.* **2009**.

51. Stolberg, L., Lipkowski, J., Irish, D. E., Adsorption of Pyridine at the Au(110)-Solution Interface. *J. Electroanal. Chem.* **1990,** *296*, 171-189.

52. Linnert, T., Mulvanney, P., Henglein, A., Surface Chemistry of Colloidal Silver: Surface Plasmon Dampening by Chemisorbed Iodide, Hydrosulfide (SH-) and phenylthiolate. *J. Phys. Chem.* **1993,** *97*, 679-682.

53. Ahmad, J., Astin, K. B., Reactions in Monolayers: The Oxidation of Thiols to Disulfides. *Coll. Surf* **1990,** *49*, 281-287.

54. Das, T. N., Dhanasekaran, T., Alfassi, Z. B., Neta, P., Reduction Potential of the tert-Butylperoxyl Radical in Aqueous Solutions. *J. Phys. Chem. A* **1998,** *102*, 280-284.

55. Li, P. Z., Duan, X. R., Liu, C. H., Du, B. A., Selective Determination of Cysteine by Resonanace Light Scattering Technique Based on Self-Assembly of Gold Nanoparticles. *Anal. Biochem.* **2006,** *351*, 18-25.

56. Ulman, A., Formation and Structure of Self-Assembled Monolayers. *Chem. Rev.* **1996,** *96*, 1533-1554.

57. Elghanian, R., Storhoff, J., Mucic, R. C., Letsinger, R. L., Mirkin, C. A., Selective Colorimetric Detection of Polynucleotides Based on the Distance-Dependent Optical Properties of AuNP. *Science* **1997,** *277*, 1078-1081.

58. Liu, T., Tang, J., Zhao, H., Deng, Y., Jiang, L., Particle Size Effect on the DNA Sensor Amplified with Gold Nanoparticles. *Langmuir* **2002,** *18*, 5624-5626.

59. Liu, J., Lu, Y., Adenosine-Dependent Assembly of Aptazyme-Functionalized Gold Nanoparticles and Its Application as a Colorimetric Biosensor. *Anal. Chem.* **2004,** *76*, 1627-1632.

Chapter 7

Applications, Conclusions and Future Directions

7.1 Investigating AuNP in Sensor Applications

This thesis highlights several photochemical routes to the generation of gold nanoparticles. These AuNP exhibit profound stability, where I-2959-derived AuNP in particular have been stable for over four years. The aqueous colloids are largely unprotected, however maintain stability through charge stabilization of physisorbed 4-hydroxyethoxy benzoic acid, which can be exchanged with a variety of different ligands for facile and custom derivatization. Tethering AuNP to selected molecules opens the door to a multitude of applications where the nanoparticles can be exploited as sensors.

7.1.1 AuNP for Surface-Enhanced Raman Scattering (SERS)

Harnessing the optical properties of these materials, novel investigations have commenced wherein molecule-nanoparticle interactions are being probed with fluorescence spectroscopy. In addition, the nanoparticles themselves are currently being evaluated as probes in a collaborative effort with the research group of Hanan Anis to identify Surface-Enhanced Raman Scattering of small organic molecules in the presence of a gold surface. With I-2959-derived AuNP derivatized with a number of ligands presented in Chapter 6, the Raman signal can potentially be amplified in the presence of metal nanoparticles 10^{15}-10^{14} times relative to the signal of the molecules alone.[1] The signal is proportional to the square of the electric dipole moment of the compounds, which is enhanced as a result of both the enhanced polarizability and the strong electric field in the presence of the metal's plasmon.

7.1.2 Investigating Surface Functionalization with Fluorescent Probes

A variety of fluorescent dyes have been synthesized in order to explore interactions with the gold nanoparticle surface. In particular, boron-dipyrromethene (BODIPY) dyes offer several advantages over other organic fluorescence dyes. A high extinction coefficient and fluorescence quantum yield, a strong photostability, and a diverse solubility in a number of polar and organic solvent were key highlights for their use in probing interactions between flurescence dyes on the metal nanoparticle surface. In this research, BODIPY dyes derivatized with a thiol or disulfide moiety were synthesized by Marta Liras, a postdoctoral fellow, such that a short spacer between the fluorophore and the interacting sulfur varied. Three dyes were prepared, namely BODIPY-ph-SH, the disulfide $(BODIPY\text{-}ph\text{-}S)_2$- and the short alkyl chain thiol, and are illustrated below in Scheme 7.1. The dyes were prepared according to a literature preparation.[2, 3]

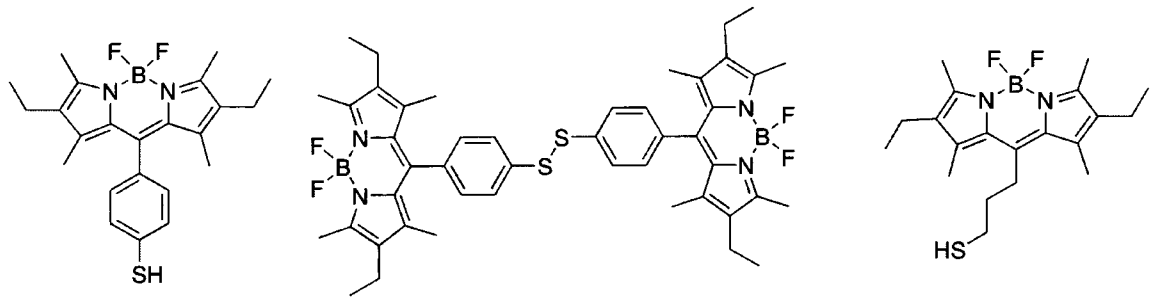

BODIPY-ph-SH **(BODISPY-ph-S)-2** **BODIPY-C_3-SH**

Scheme 7 . 1 - Modified BODIPY dyes investigated in this study.

In the unbound form, the free thiol or disulfide expresses strong fluorescence at 534 nm in acetonitrile, characteristic of the pink dye colour for numerous BODIPY probes. When the proton is lost through covalent interaction with other molecules or in this case metal nanoparticles, the bound sulfide loses its fluorescence. Upon

introduction of a different ligand, the chromophores are liberated from the surface and the fluorescence is restored. In this fashion, addition of different ligands to different AuNP-fluorophore substrates allows for the investigation of kinetics of both fluorescence quenching and enhancement. A description of the interactions is presented in Scheme 7.2, below.

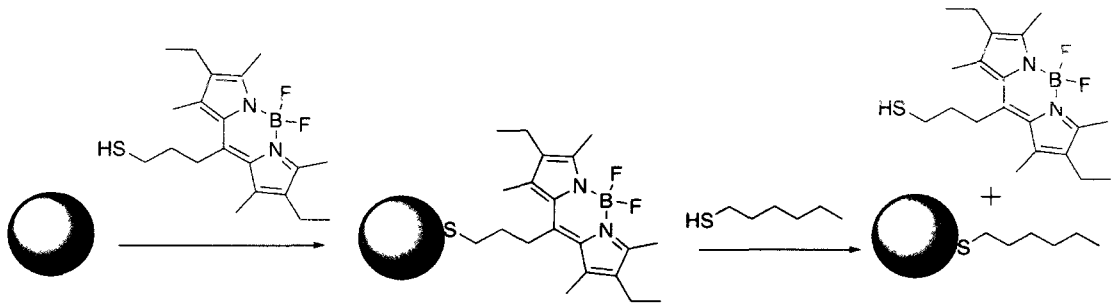

Scheme 7 . 2 - Molecular interactions between modified BODIPY dyes and gold nanoparticles

Gold nanoparticles were synthesized via the I-2959 photo-reduction approach. Due to the extremely low fluorescence quantum yield in aqueous solutions, sensor studies were performed in acetonitrile. Particles were centrifuged and resuspended in acetonitrile to afford a bright red and slightly blueshifted absorbance spectrum. The particles were stable for approximately 4-5 days when stored in the dark, yet developed a pink/orange turbidity with prolonged storage as a result of the formation of anisotropic prisms. As such, AuNP investigations with AuNP in acetonitrile were performed within a day or two of solvent resuspension. Particles were derivatized with the three different BODIPY dyes in acetonitrile solutions at a concentration of 1.0 μM for 16 hours prior to ligand exchange studies. To solutions of fluorophore-bound AuNP, hexanethiol was added and the changes in fluorescence were monitored over time. Addition of 3.3 μM Au^0 AuNP to solutions of the dye molecules resulted in a quenching of fluorescence as the intensity decreased by 80%, 81% and 62% for BODIPY-ph-SH, BODIPY-C_3-SH and (BODIPY-S)$_2$, respectively after 16 hrs of monolayer formation.

The increase in fluorescence intensity upon addition of 3.0 μM hexanethiol (6-SH) was recorded and expressed in Figure 7.1, below. From the quenched fluorescence intensity, the fluorescence had recovered by 55%, 49% and 6% for BODIPY-ph-SH, BODIPY-C_3-SH and (BODIPY-S)$_2$, respectively after 3.5 hours.

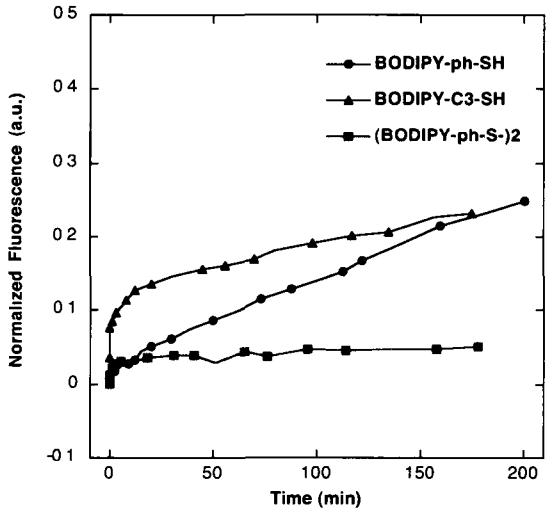

Figure 7 . 1 - Normalized fluorescence enhancement over time upon addition of hexanethiol to 1.0 μM solution of various BODIPY dyes. Fluorescence is normalized relative to the intensity at time of addition of thiol ligand.

The low fluorescence recovery can be a result of the sensitivity of the fluorophores to metal nanoparticles in solution, for quenching is strongly dependent on the distance to the metal particle surface, as efficient quenching is still sensed 50 nm away from the particle.[3]

The rates and degree of fluorescence recovery varied with the exiting fluorophore, where BODIPY-C_3-SH showed the fastest release, followed by a steady release by BODIPY-ph-SH and an immediate but smaller change for the disulphide. A note on the latter sulfide is that the initial fluorescence quenching by the disulfide was also essentially negligible and attributed to poor binding of the thiols to the gold surface over the course of 16 hours. This poor binding observation is in agreement with

results with DTBA discussed in Chapter 6. The comparative behaviour of the short chain dye with the phenyl chain dye can be attributed to electronic interactions, for the mild electron donor properties of the phenyl group of BODIPY-ph-SH could be attributed to the slower release relative to the short alkyl chain of BODIPY-C_3-SH.

Control experiments were performed to ensure that the fluorescence enhancement was not attributed to interactions with the metal salt as well as from solvent interactions with the dyes alone that could be the result of dimerization. While 0.33 mM $HAuCl_4$ quenched the dye fluorescence, no fluorescene increase was observed. Interestingly, the optical properties of the nanoparticles were altered upon incorporation of the fluorescent dyes. Both of the thiol dyes caused a redshift of the particle absorbance from a red to a violet solution, while the disulfide dye did not induce any such transformation. The redshifting of the absorbance spectrum of the AuNP solution was fortuitous due to less screening at 560 nm by the BODIPY chromophore. This attribute further clarifies interactions occurring between the nanoparticle and fluorescent probe for the monothiolate probes.

While this preliminary work has been built on AuNP-BODIPY fluorophores in similar previous studies,[2-4] future work includes utilizing the BODIPY dyes to probe the surface binding of different ligands, in particular the MHTZ, DTBA as well as alkylthiols and amines presented in Chapter 6. Synthesis of different dyes such as derivatized coumarins could also offer a unique probe to monitor interactions such that the absorbance and fluorescence wavelengths of the dye are within a window of minimal AuNP particle absorbance, and could thus also function to probe ligand interactions.

7.1.3 Plasmon-assisted Enhancement of Photophysical Interactions

Apart from exploiting the optical properties of AuNP in colloidal systems, the enhanced surface energy and high electron density have been explored to assess the catalytic properties of the metal nanoparticles that have been synthesized using a photochemical approach. AuNP have been used as probes by using the photophysics of dyes to understand the enhancement of molecular interactions.

Plasmon sensing with colloidal gold has been revamped by harnessing the optical properties of the sol. Excitation of the surface plasmon of metal nanoparticles such as silver and gold increases the surface energy of the particles dramatically such that the temperature of the particle surface has been found to melt ice and PEG polymer matrices.[5] 50 nm particles have been found to display a heat flux intensity of 9.6 μW under 532 nm irradiation with 5.0 mW power.[6] This increase in temperature allows for AuNP to be exploited as nanoscopic heaters for a multitude of endothermic organic reactions simply by photolysis in the visible range of the spectrum.

Initial investigations have been conducted in collaboration with postdoctoral fellows Natalia Pacioni, María González-Béjar and Emilio Alarcón, where the photophysics of methylene blue (MB) were altered in the presence of excited AuNP.[7] Thus, the chromophore was irradiated at 650 nm in the proximity of a gold nanoparticle, and the triplet energy of the dye was measured via laser flash photolysis absorption spectroscopy. The process is analogous to transmitter/receiver interactions with antennae

AuNP were synthesized in water according to the I-2959 photoreduction approach presented in Chapter 3 to afford monodisperse 15 nm particles. Aliquots of AuNP were added to deareated aqueous solutions of MB. $^3MB^*$ displays a signal at 420 nm, while the excited singlet decays rapidly with a lifetime of ~380 ps before rapid intersystem crossing (ISC) to the triplet, $^3MB^*$, which decays at 420 nm. The lifetime

of the triplet in the presence and absence of 1.2 nM AuNP was measured to be 11.8 and 82 µs, respectively, which corresponds to a quenching rate constant of 6.4 x 10^{13} $M^{-1}s^{-1}$ by AuNP. The kinetic treatment is presented below in Figure 7.2.

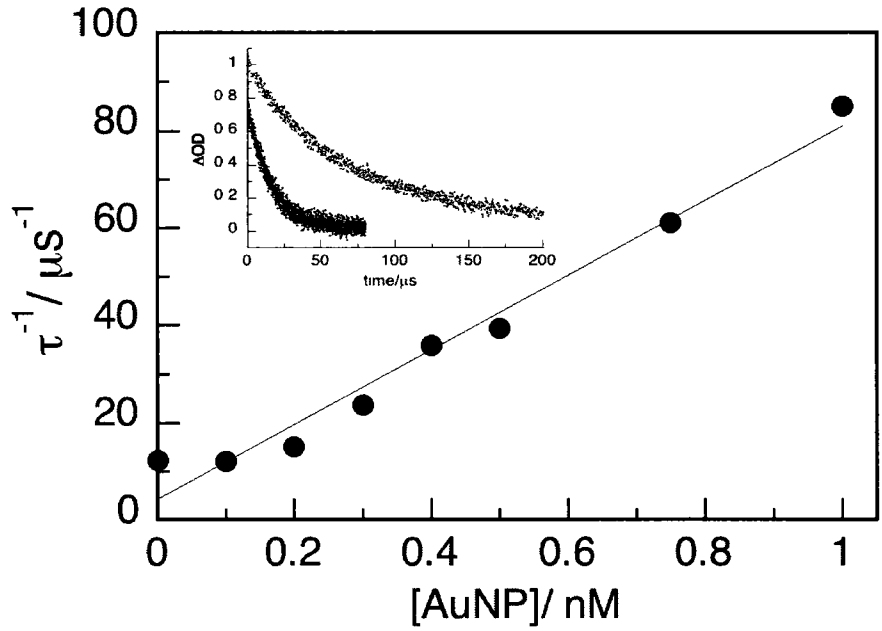

Figure 7 . 2 - Quenching of MB triplet (monitored at 420 nm) following 650 nm laser excitation; the slope of this plot is the bimolecular rate constant for triplet quenching by AuNP. Inset: MB triplet decay in the absence and presence (shorter decay) of 1.2 nM AuNP, monitored at 420 nm.

An analysis of decay kinetics revealed that the MB alone could be fit to a single exponential, while decay of $^3MB^*$ in the presence of AuNP resulted in an initial rapid decay followed by a slow decay and required a biexponential fit. This fast decay was observed at all AuNP concentrations, and is ascribed to static quenching (as well as self-quenching) of MB molecules in the proximity of the AuNP surface at the time of excitation. The occupation of surface sites by MB was further affirmed by zeta-potential measurements, where an essential neutral potential was produced upon interaction of the cationic dye with a colloid possessing a independent zeta-potential of approximately -24 mV. It is envisaged that the majority of the MB is

associated on the surface by charge stabilization, otherwise the quenching would have been much faster. Meanwhile, the high triplet quenching rate constant, which can be expressed with a diffusional rate constant on the order of 10^{11} $M^{-1}s^{-1}$ according to Debye theory, and taking the difference in mass between the large nanoparticle and the small dye. While the high rate constant is inconsistent with diffusional quenching in homogeneous systems, the fast process in this case is attributed to a large buildup of $^3MB^*$ in the vicinity of AuNP as a result of plasmon enhancement. As such, the transient absorbance of $^3MB^*$ increased by a factor of 2.2 upon introduction of AuNP.

The interactions of MB with the particle surface as measured by triplet quenching overlap remarkably well with the electrostatic double-layer Debye model for charge-stabilized colloids, and illustrate how plasmon excitation operates as a strategic tool to monitor molecular interactions in the surface vicinity. Ongoing work with plasmon catalysis is in progress with aqueous AuNP of varied sizes to establish the effects of particle size with surface reactivity and MB triplet enhancement.

7.2 Photochemicallly Generated AuNP Applied to Catalysis

In the past few decades, an abundant amount of research has transpired regarding the application of gold nanoparticles towards catalysis, despite the historical inertness of the bulk metal.[8, 9] Gold metal earned its ranking among one of the noble metals for its exceptional resistance to oxidation, and has often been excluded from organometallic catalysis chemistry. With a high ionization potential and an inability to adsorb hydrogen or oxygen onto the planar surface, bulk gold was deemed inactive for hydrogenation and oxidation reactions.[10] It wasn't until the 1970s that Bond *et al.*, and later Parravano *et al.* discovered catalytic activity of supported Au towards hydrogenation,[11] and oxygen and hydrogen transfer reactions,[12] respectively. A decade later, Haruta *et al.* discovered that small 1-3 nm

hemi-spherical AuNP loaded on metal oxide supports exerted catalytic activity in the oxidation of carbon monoxide.[13] Since then, an explosion of investigations have probed the catalytic activity of gold nanoparticles on various supports as well as in solution, and have revealed that AuNP have a niche for various oxidation, epoxidation and some aromatic reduction reactions.[14]

7.2.2 Supported AuNP Catalysis

Synthesizing AuNP on solid supports opens the doors to several advantages common to heterogeneous catalysis such as facile separation and high turnover frequency for greater, greener industrial appeal.[15] In general, the catalytic activity of gold nanoparticles depends on the surface reactivity, and the catalytic behaviour decreases with increasing particle size. Particularly, some reviews regarding oxidation reactions have established that AuNP with sizes greater than 5 nm do not display catalytic properties.[10, 16, 17] In other studies, particles of 15-50 nm have been found to also exhibit catalytic activity.[18-20] The role of the support can easily be assigned to particle stabilization, for adsorption onto the medium minimizes agglomeration and controls monodispersity and thus particle reactivity. Furthermore, several researchers have also established a synergistic effect on the added catalytic activity of the combination of nanoparticle and the solid support, where reactants can easily adsorb onto the support as well as onto the surface of the metal nanoparticle.[8, 21-23] The support reactivity will depend on the number of surface hydroxyl sites, the amount of surface defects as well as the crystal phase upon which reagents and Au will adsorb.

Within the field of metal nanoparticles on solid supports, and gold nanoparticles in particular, there is a plethora of variables governing successful catalysis. Regarding catalytic activity, high selectivity, large rates of conversion, and efficient catalyst reusability are all strongly desired. Catalytic activity is dependent on the size of the nanoparticle, the type of support and the deposition method.

Our desire was to design a photochemical method for the preparation of AuNP on supports with catalytic activity using the I-2959 photo-reduction method. Two traditional deposition methods have been used in numerous reports, and these include impregnation and deposition precipitation.[14] The impregnation method refers to a solution-based synthesis where $HAuCl_4$ is mixed with the support under aqueous conditions, and then subsequently dried prior to reduction. When the solvent volume is minimized to the volume of the pores in mesoporous supports, this approach is referred to as incipient wetness impregnation. It can be advantageous as an approach to ensure pore coverage and minimize reagent loss. The dry material can either be reintroduced into a solution for reduction via formate,[24] or is often dried and calcined at temperatures above 473 K, and finally exposed to a stream of dilute H_2 in He for reduction to form nanoparticles.[25] This method suffers from AuNP aggregation as a result of poor fixation of the salt complex to the support surface with many supports. This can be overcome by selecting a support with an appropriate surface charge, which can be approximated at a given pH if its isoelectric point (IEP) is known. The IEP of a material is the pH in solution at which a zero point charge is acquired. Essentially, anionic $AuCl_4^-$ will preferentially adsorb to cationic surface sites when the pH of the solution is below that of the IEP. Reports have suggested that aggregation was also enhanced due to the presence of Cl^-, where the preparation typically generated particles of 30 nm in diameter.[10] Rigorous washing of the supports is a requirement for halide ion removal.

Deposition-precipitation is the most common technique and has earned significant success from CO oxidation chemistry. A solution of $HAuCl_4$ is converted to $Au(OH)_3$ upon addition of NaOH so that the hydroxyl groups bind to the material for the salt reduction to occur directly on the surface. Above a pH of 9, $Au(OH)_3$ precipitates and deposits on the support surface. The solids are calcined around 773 K, followed by reduction. In the context of mesoporous supports, the method suffers from rapid and inhomogeneous alkalination such that the precipitate cannot enter the pores, leaving metal hydroxides to be reduced on the surface alone. More recently, the problem has been overcome using urea for a more gradual increase of

pH and thus slower prepicipitation.[23, 26] The resulting solids are commonly reduced with a H_2 stream to yield AuNP in the 2-3 nm range.

7.2.2.1 Preparation of Supported AuNP

Approaching the field of nanocatalysis with inexperience and ignorance, our choice of support was defined from literature reviews as well as materials available in collaborations with others. Introductory work was conducted on a research collaboration abroad in Valencia, Spain under the supervision of Hermenegildo Garcia and Avelino Corma at the Universidad Politécnica Valencia (UPV). Over the course of two months, research had been exercised on mesoporous SBA-15 silicate molecular sieves, as well as with TiO_2 (P25).

SBA-15 is a well-ordered structure with hexagonal silicate pores with variable pore diameter, depending on the synthesis.[27] The material was synthesized by Maria Teresa Navarro, a research associate at the UPV, and the diameter of the pores were 2 nm and 6 nm in separate samples. The appeal of the mesoporous channels was to confine the growth of nanoparticles to the diameter of the pores and potentially generate nanorods with unique optical and catalytic properties. The molecular sieves were calcined prior to use in order to remove residual template surfactants and dried under vacuum. The support was modified with addition of 3-aminopropyltriethoxysilane (APTES) to enhance coordination of the gold salt to the pores of the solid. 100 mg of the support was added to a solution of 2.0 mM APTES in methanol with stirring for 18 hours. The solid was washed with water and acetone and dried overnight at 100°C for 20 hours, following a similar literature method.[28] Incipient wetness impregnation was chosen as the method to load the starting materials. $HAuCl_4$ and I-2959 with a minimum solvent volume of approximately 100-200 µL to attain uniform pore coverage, and the samples were mixed manually via a mortar and pestle to dryness, followed by drying in a dessicator overnight. The materials were not calcined, as initial attempts resulted in a thermal cleavage of I-

2959 and reduction of $HAuCl_4$, as the complex is reduced above 60°C. This property has acted as a significant challenge to minimize particle size, for calcination has shown proven ability to anneal the metal salt to the surface, thus profoundly minimizing agglomeration and particle size. Nevertheless, the unannealed resulting yellow powder was irradiated in a Rayonet photoreactor with six lamps for 15 hours with periodic stirring to expose new powder. With this procedure, a variety of Au@SBA-15 supports were prepared, with the gold loading ranging from 2-5% and the ratio of I-2959· Au from 5·1-3·1 to afford powders ranging in colour from violet to magenta. A TEM image of the sample is presented below in Figure 7.3.

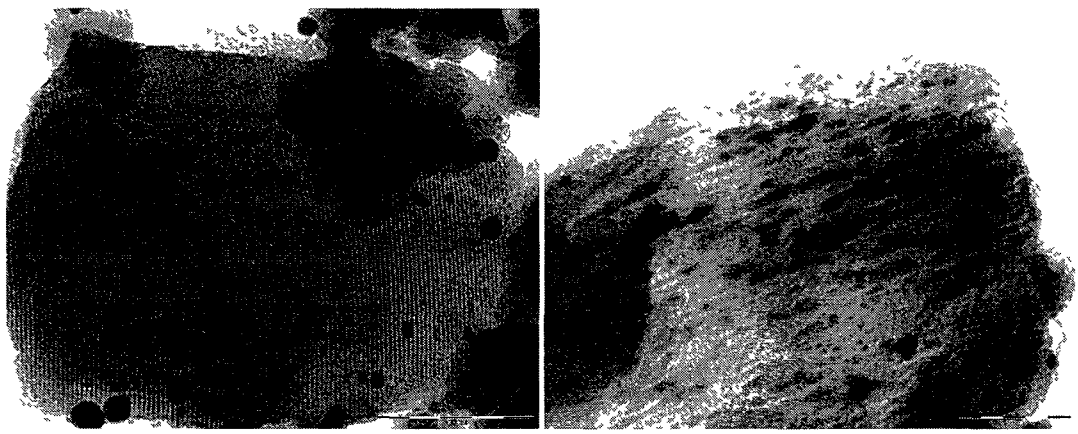

Figure 7 . 3 - TEM image of SBA-15 with 2 nm pores (left) and 6 nm pores (right) modified with APTES, loaded with 2.5% Au at 4:1 I-2959:$HAuCl_4$ and irradiated for 15 hours. The scale bars represent 100 m (left) and 250 nm (right).

The materials were not rinsed with water to remove halide ions or non-adsorbed AuNP prior to imaging, essentially due to naivety. In the TEM image for the SBA-15 with 2 nm pore size, it is clear that AuNP of approximately 10-15 nm in size along with aggregates were deposited solely on the exterior of the support, despite derivatization with the aminosilane. The 6 nm pores, on the other hand, appear to contain AuNP within the channels, where there is additional reduced Au on the exterior of the unwashed support as well. The 6 nm pore size sample was tested for catalytic activity in nitroaromatic reductions, however the material exhibited no such

increase in reactivity, presumably a consequence of the unwashed material and the unknown poisonous effect of residual chlorine ions at the time. No further research was performed on these materials within the time constrains; however the knowledge and the concepts for advanced material synthesis were applied to other systems.

AuNP were also prepared on P25 TiO_2 following a similar incipient wetness impregnation approach. The solid composed of approximately 20 nm metal oxide nanoparticles was dried at 373 K for 16 hours prior to incipient wetness impregnation of 2.5% $HAuCl_4$ and a 4:1 ratio of I-2959:$HAuCl_4$. The solid was then irradiated with periodic mixing over the course of 15 hours. The powder appeared blue-violet within a few minutes, and this is attributed to the materials absorption of UVA light, thus enhancing the photochemical reaction. While a control reaction of photolysis of $HAuCl_4$ and TiO_2 alone revealed the redox ability of the semiconductor material, a greater purple tinge was developed for the powder irradiated with the photoinitiator, indicating smaller particles with a blue-shifted SPB. A TEM image of the I-2959 AuNP is presented below in Figure 7.4. Similar to Au@SBA-15 samples, these solids were not rinsed to remove excess AuNP. A mixture of large 15-30 nm AuNP seem to be present along with significantly smaller 2-4 nm particles.

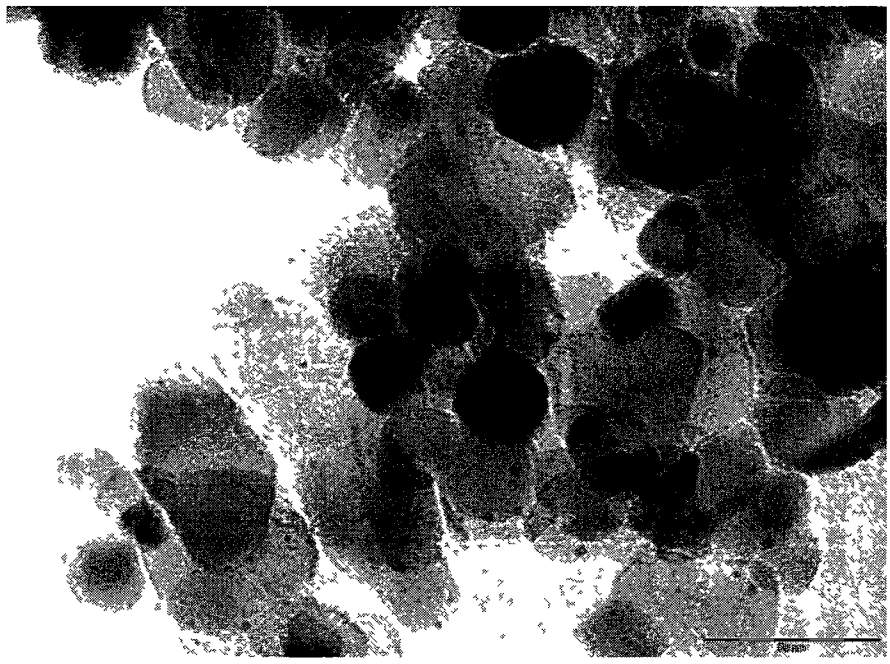

Figure 7 . 4 - TEM image of $Au@TiO_2$ prepared via photolysis of 2.5% $HAuCl_4$ and 4:1 I-2959:$HAuCl_4$ for 15 hours under 355 nm irradiation. Sample not washed prior to imaging. The scale bar represents 50 nm.

A modified deposition-precipitation approach was applied to the $Au@TiO_2$ synthesis, whereby the pH of an aqueous solution of $HAuCl_4$ and TiO_2 was increased upon addition of urea. A 2% wt Au sample and 100 mg TiO_2 was combined with 0.42 M urea and stirred vigorously at 353 K for four hours, following a literature procedure.[29] The materials was washed with a minimum of 1L of water after precipitation of $Au(OH)_3$ on the surface and prior to addition of I-2959 via incipient wetness impregnation and subsequent UVA photolysis for 16 hours. The resulting sample turned from a pale orange to a dark purple powder after irradiation. TEM images of the urea-modified support also reveal the presence of small 4 nm AuNP, however fewer AuNP are present, which could be attributed to copious washing after irradiation. Also due to time constrains, no catalytic testing was performed on the materials.

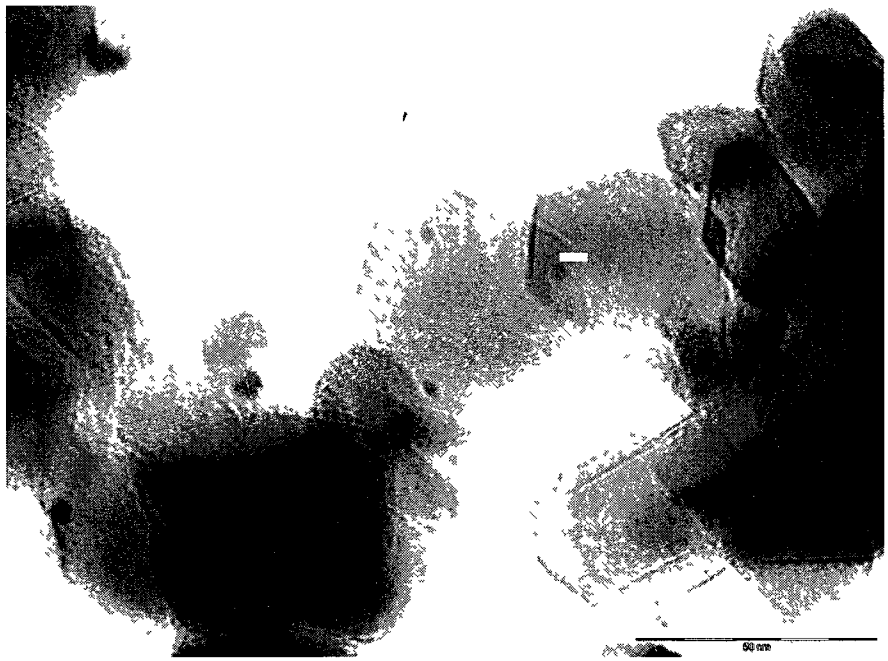

Figure 7 . 5 - TEM image of Au@TiO_2 prepared from modified urea deposition-precipitation of 2% wt Au with subsequent photolysis of 4:1 I-2959:$HAuCl_4$ via 16 hours UVA. Sample washed with 1-1.5 L water prior to imaging. Scale bar represents 50 nm.

The preparation of Au@TiO_2 and Au@SBA-15 reveal the diversity of the I-2959 approach to nanoparticle synthesis and its entrance into advanced materials synthesis. Further work with support preparation has been continued and modified with more precise purification steps in collaboration with Geneice Hallet-Tapley, a postdoctoral fellow and Charles-Oneil Crites as part of his undergraduate research project.

Briefly, Au@support were synthesized on a number of different supports, with notable success among metal oxides TiO_2 P25 and γ-Al_2O_3, as well as with hydrotalcite (HT); a common zeolite. The materials were prepared by stirring a slurry of $HAuCl_4$, I-2959 and the support in acetonitrile for 2-3 hours to allow sufficient time for Au salt to adsorb onto the support, which was verified by UV-VIS absorbance of the mother liquor. The powders were dried under rotory evaporation, high vacuum and placed in glass vials for photolysis. The samples were irradiated with a home-built system consisting of a Luzchem EXPO panel with 5 UVA lamps

(65 W/m^2) placed directly overtop of a sample turning board devised from a commercial hot dog cooker. The vials were lined horizontally on the rolling pins, which turned at a frequency of 3 rpm to ensure optimal homogeneous photolysis conditions, and irradiated for 8-12 hours until a uniform colour change was achieved. The powders were subsequently purified via washing though Soxlet extraction with acetonitrile for 48-72 hours to remove any unreacted $HAuCl_4$, organic photoproducts as well as poorly adsorbed AuNP.

A diffuse reflectance spectrum of the prepared materials at 1% Au loading is shown in Figure 7.6, and highlights the differences in particle size with support. The supports can be characterized and compared with their isoelectric points, where the isoelectric points for TiO_2, γ-Al_2O_3, and HT are approximately 6, 8 and 10, respectively. The greater the IEP, the greater the ability of anionic structures such as $AuCl_4^-$ to adsorb onto the metal oxide surface in acetonitrile solutions where the pH was typically 4. The results in Figure 7.6 identify a correlation of greater blueshifted SPB maximum with greater IEP, and this could be attributed to a lesser tendency for agglomeration of AuNP during photolysis if the gold salts are better adsorbed.

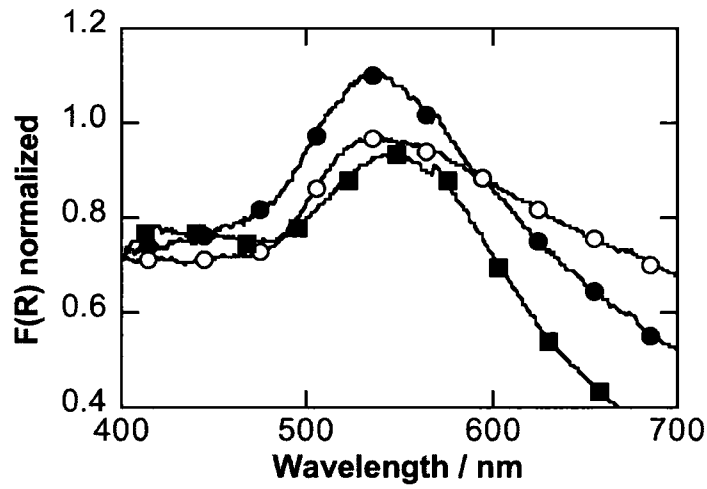

Figure 7 . 6 - Diffuse Reflectance Spectra of 1% Au on (●) HT, (O) γ-Al_2O_3 and (■) TiO_2.

Electron microscopy confirmed the size of Au on the supports for the three metal oxides at both 1% and 5% Au loading, however lack of transmission from the support remained a challenge even as samples were sonicated for several minutes (to loosen up the powders) in dichloromethane prior to deposition and drying on the copper grids. A summary of particle sizes is highlighted below in Table 7.3. The correlation between increased isoelectric point and decreased particle size is further validated in the measurements obtained from TEM analysis, and emphasizes the importance of metal precursor adsorption for support preparation.

Support	% wt Au	Particle size (nm)	PDI
TiO_2	1	33	1.20
	5	142	1.26
γ-Al_2O_3	1	30	1.14
	5	112	1.22
HT	1	21	1.24
	5	47	1.31

Table 7 . 1 - Average size and polydispersity index (PDI) of the supported AuNP.

The powders were further characterized by XRD and XPS to reveal that metallic gold was readily formed on the supports. Due to the sensitivity of the techniques and the low concentrations with nanomaterials, 5% Au was required to complete the characterization. The fingerprint peaks for face-centered cubic gold are Au(III), Au(200), Au(220) and Au(311), which appeared at 38.2°, 44.5° 64.6° and 77.6°, respectively. XPS analysis revealed the oxidation state of the AuNP as predominantly Au^0 owing to the signal for the Au $4f_{5/2}$ and $4f_{7/2}$ peaks at 87 and 84 eV, respectively. These results highlight the effectiveness of the novel synthesis and purification method via Soxlet extraction, for non-purified samples displayed additional Au^{3+} peaks at 88.5 and 85 eV.

7.2.2.2 Catalytic Activity of supported AuNP

The catalytic activity of the prepared materials was assessed initially with a common reaction. The reduction of nitroarenes, with the reduction of 4-nitrophenolate to 4-aminophenolate in particular, have been studied extensively and served as a strategic method to compare the catalytic activity among the supports prepared within the research group and with others.[20] Additionally, the reaction success can be monitored spectrophotometrically by the decay of the 4-nitrophenolate absorbance at 400 nm with the growth of the 4-aminophenolate species at 290 nm, and proved to be a strategic method to screen successful catalytic candidates.

The catalysis was evaluated by addition of a fresh solution of $NaBH_4$ (36.6 mM) to an aqueous solution containing 3.76 mM 4-nitrophenolate and 1-2 mg catalyst, followed by monitoring the kinetics of the decay of the peak at 400 nm over time. The spectra are presented in Figure 7.7, below. For clarity, a summary of the first-order decay reaction kinetics is also presented in Table 7.4

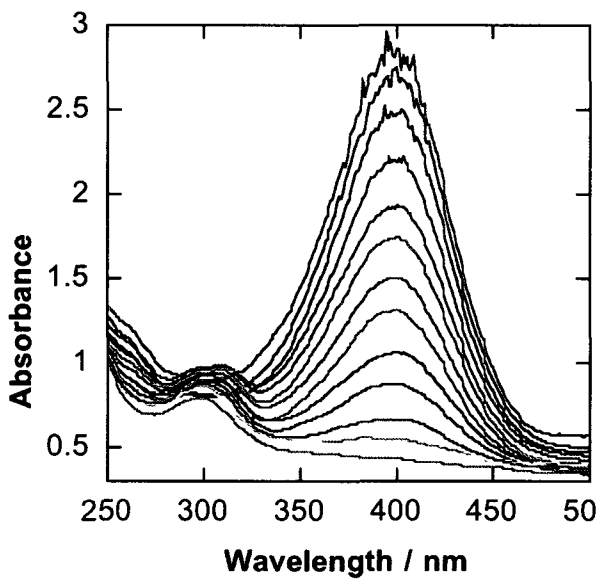

Figure 7 . 7 – UV-Visible absorption spectra for the reduction of 4-nitrophenolate catalyzed by 1% Au on HT in an aqueous solution of 3.76 mM p-nitrophenolate and 36.6 mM $NaBH_4$.

Support	% wt Au	Particle size (nm)	k_{decay} at 390 nm (min^{-1})
TiO_2	1	33	0.12 ± 0.01
	5	142	0.16 ± 0.05
γ-Al_2O_3	1	30	0.45 ± 0.01
	5	112	1.9 ± 0.20
HT	1	21	0.6 ± 0.01
	5	47	2.2 ± 0.20

Table 7 . 2 – Rate constants for the decay of 4-nitrophenolate using supported AuNP as catalysts.

The kinetic results show a correlation between isoelectric point of the support and rate of reaction, where the higher isoelectric point led to a faster rate of conversion of nitrophenolate to aminophenolate. Secondly, a higher gold loading also increased the rate of the reaction. A higher loading resulted in larger AuNP and greater polydispersity, which is synonymous with general heterogeneous catalysis findings. The higher loaded samples, despite their decreased surface energy of resulting larger particles, produced more AuNP total surface area and thus resulted in faster reaction rates. The correlation between isoelectric point and catalytic activity could be the result of smaller particles from improved adsorption of the metal salt, as well as adsorption of the anionic reagent 4-nitrophenolate where the support would play a role in the catalysis as well. Notably, no catalysis was observed when supported Au was absent from the system. These results clearly demonstrate the catalytic ability of AuNP prepared on TiO_2, γ-Al_2O_3 and hydrotalcite with a novel impregnation and purification approach.

Research with these supports and this method are ongoing, where the catalysts are currently being evaluated in alcohol oxidation reaction and epoxidation chemistry. Future directions also include modifying the support preparation by adapting the deposition/precipitation method with urea to adsorb $Au(OH)_3$ onto the support surface, followed by impregnation with I-2959 and MeCN, and the established photolysis and purification. Combining the two traditional methods with the photochemical method could minimize particle size and thus increase catalytic activity. Investigations in the heterogeneous catalysis domain have only just begun

within the research group, and application of the I-2959 method to support preparation can be spread to preparation of a large variety of supports and catalytic reactions.

7.3 Other Future Directions

7.3.1 Photochemically-induced reduction of metal nanoparticles

The work that commenced with developing photochemical techniques for the generation of colloidal gold nanoparticles has been expanded to several other metals, where research projects by other group members have flourished using the I-2959 approach. Synthesis of silver, copper, platinum, cobalt, ruthenium and bimetallic systems have been achieved with the aforementioned photoinitiator as well as with I-907 in non-aqueous systems.

Future work building on these pioneering investigations will include optimization of nanoparticle synthesis with other commercial photoinitiators such as Irgacure 184 and Irgacure 127, where their molecular structures are shown in Scheme 7.3. Both of these compounds will work in organic systems, where the latter photo-releases two 1-hydroxymethylethyl radicals and one larger photoproduct for steric stabilization, and thus has potential to improve synthesis. I-127 could offer advantages in comparison with I-2959, where the two-for-one ketyl radicals do not come at the expense of doubled absorbance (and hence screening) of the metal salt by the photoinitiator.

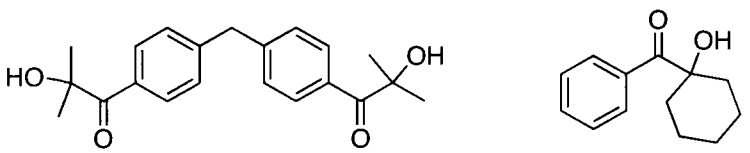

I-127 I-184

Scheme 7 . 3 - Other photoinitiators succeptible to Norrish I α-cleavage; Irgacure-127 and Irgacure 1-184.

The technique of photochemically seeded growth has been developed in our group, and can be continued for the growth of various metal nanoparticles. In particular, exciting research with plasmon-assisted seeded growth of silver nanoparticles, whereby a solution containing small, spherical AgNP in an $AgNO_3$ solution has been irradiated with light emitting diodes at the SPB wavelength for silver as well as longer wavelengths. As a result, plasmon excitation has initiated growth of larger particles with distinct geometries depending on the wavelength of irradiation used.[30] With this idea in mind, photolysis of the AuNP SPB with visible light could offer a remarkably simple maneuver for the synthesis of larger AuNP.

7.3.2 Other Photochemical Approaches to Heterogeneous Catalyst Design

While the modified impregantion/photolysis/purification method for metal@support has been focused on the synthesis of supported AuNP, the technique has also been recently applied to Ag@supports. Other photochemical approaches can also be applied to the design of solid support catalysts, where calcination can take place to better adhere the gold deposits prior to reduction. Reduction could be executed using I-2959 after impregnation, or in the presence of THF as a solvent in photolyzing a slurry in the rotating vial apparatus. Furthermore, given the cationic nature of a variety of supports studied, photochemical generation of AuNP from

H_2O_2 has potential, where the IEP would disfavour thermal reduction by $O_2^{\bullet-}$, and the support could function to better stabilize the generated species, thus minimizing platelet formation.

7.3.3 Probing Molecular Interactions

As presented in Chapters 4 and 5, the synthesis of AuNP from both H_2O_2 and THF yields a mixture of small nanoparticles as well as larger plates. Centrifugation will separate the two species easily, and the isolated plates can be functionalized with ligands and investigated for SERS enhancement, as large silver and gold triangular prisms have been reported to induce a greater signal enhancement relative to smaller spherical particles.

On a grander scale, both small spherical AuNP and larger prisms could be directed to signaling various types of interactions with attachment of the right molecules. Various studies have attached specifically sequenced single-stranded DNA to the particle surface for probing a multitude of biochemical interactions.[31] Given the success of synthesizing AuNP in the presence of DNA, future work can be directed to synthesis with different types of DNA and different strands for a variety of interactions. Interestingly, any DNA damage resulting from UVA photolysis during AuNP preparation could also be probed with fluorescent studies involving thiazole orange, as doctoral research from previous grad student Larisa Mikelsons specialized in developing a fluorescent approach to studying any defects through dye intercalation between complimentary DNA strands.[32]

Finally, solution-based heterogeneous catalysis could be further evaluated beyond AuNP prepared from I-2959 photoreduction. Specifically, AuNP synthesized from AuNP as well as xanthones led to the formation of remarkably small 3-5 nm particles. These particles are stabilized loosely in either a weakly adsorbed

polyelectrolyte or micellar environment, respectively, and could thus allow for catalytic activity on the surface of reactive small particles.

7.4 Conclusions

The focus of this research has been on developing photochemical strategies for the optimal synthesis of gold nanoparticles, where a few key principles can be applied to a spread of metal and bimetallic materials. This chemistry has dealt with two general synthetic pathways for the generation of transient species with reducing character, and their application to nanoparticle assembly.

From a photochemical perspective, precursors with sufficient extinction coefficients at the wavelength of excitation are necessary which absorb at low energies for the synthesis to be environmentally feasible. As such, aromatic ketones have operated as ideal candidates for excitation of their tail absorbance in the low energy region of the UV spectrum. In one approach, the reducing agent has been generated through an intramolecular bond cleavage to photo-release the desired species. This has been achieved through careful selection of precursors with short triplet lifetimes to minimize competitive quenching processes and the ability to undergo homolytic cleavage. Another tactic has harnessed the character of the excited state transitions of the chromophores in an intermolecular approach to the formation of reducing free radicals, whereby chromophores with n,π^* character undergo hydrogen atom transfer with faster rates relative to compounds with π,π^* character. Aromatic ketones, with their non-bonding states, have been an ideal choice of precursor with their tendency to form ketyl radicals for this reason.

Throughout this thesis, the selection of reducing agent has been governed by photophysical absorption properties as well as the reactivity of the free-radical. Additionally, redox potentials of the reactive intermediates have been considered, highlighting the thermodynamic contribution toward the kinetically-driven metal salt

reduction process. A selection of reactants and their reduction potentials are summarized in Table 7.3.

Redox Couple	Reduction Potential E^0 (V vs NHE)
$AuCl / Au^0$	+ 1.11
$AuCl_4^- / Au^0$	+0.99
$O_2 + H / HOO\bullet$	-0.05
$O_2 / O_2^{-\bullet}$	-0.33
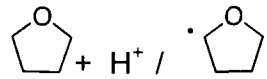	-1.05
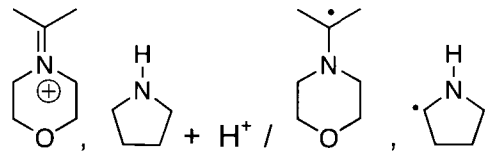	(-1.47)
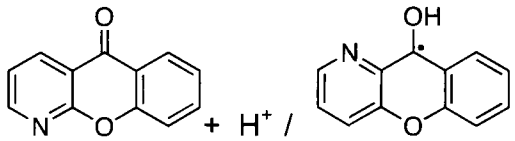	-1.48
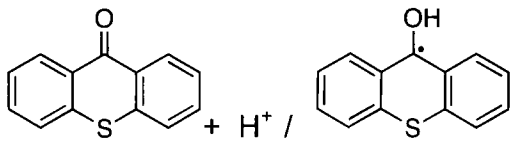	-1.62
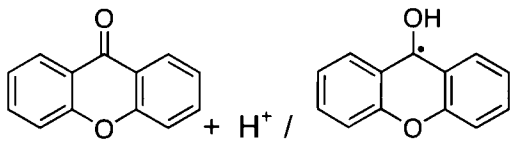	-1.65
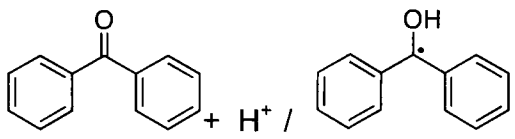	-1.72
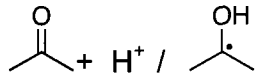	-1.80

Table 7 . 3 – Summary of redox couples exploited in the photochemical synthesis of gold nanoparticles in this research.

In a novel direction, the excited state chemistry of $HAuCl_4$ has been studied to investigate the reactive Cl atom and exploit its hydrogen atom abstraction properties for the generation of other reductive transients with few photophysical properties, such as the hydroperoxyl radical as well as the tetrahydrofuranyl radical. This work has exemplified the beauty of a photochemical understanding, such that nanomaterials can be generated from cheap, clean and inexpensive precursors (noble metal salts not withstanding).

The growth of gold nanoparticles has been further pursued through traditional seeding techniques and the development of a photochemical seeding approach. The photochemical advantages of spatial-temporal control were perfectly exploited in this application for the careful delivery of low amount of reducing agent to overcome secondary nucleation.

Photochemically generated AuNP have been derivatized with a number of ligands to assess the surface reactivity of the particles as well as to observe the effects of different functional groups on the binding properties of compounds to a charge-stabilized colloid. In particular, ligands such as mercaptohexadecanoic acid, mercaptothiazoline and hexadecylamine have displayed strong binding behaviour. These investigations have set the stage for various applications where particles can be exploited as sensors for their optical properties.

Finally, the photochemical approach to generating nanomaterials has also been applied to the synthesis of gold nanoparticles on various supports with a unique deposition method, and materials have been screened for catalytic activity using a facile reaction of nitrophenolate reduction in the presence of $NaBH_4$. These preliminary support development and heterogeneous catalysis investigations have laid the foundation for a new and exciting direction of research within the Scaiano group, where novel practices have already flourished into interesting results.

7.5 Claims to Original Research

1. A photochemical method has been developed for the synthesis of metal nanoparticles where photolysis of a water-soluble α-hydroxy ketone in the presence of a metal salt has resulted in the monodisperse generation of gold nanoparticle, which have been stable for over four years. This method has been applied to the synthesis of other metallic and bimetallic syntheses.

2. A photochemical method has been developed for the synthesis of metal nanoparticles via the generation of α-aminoalkyl radicals from a commercial photoinitiator ketone. This method has been applied to the synthesis of both gold and copper nanoparticles.

3. While others have synthesized nanomaterials from hydrogen atom abstraction pathways with aromatic ketones, novel work has been presented herein for generating reducing species from xanthone derivatives.

4. The photochemical lability of the Au-Cl bond in the starting material has been acknowledged in previous reports, however the reactivity of the Cl atom towards hydrogen atom abstraction has been evidenced and exploited in trivial syntheses for the generation of gold nanoparticles from simple organic and inorganic compounds.

5. Photochemically derived gold nanoparticles have been enlarged via a photochemical seeding technique for size selective synthesis of relatively monodisperse particles.

6. A unique photochemical approach has been applied to the design of inorganic supports for heterogeneous catalysis studies for gold nanoparticles, and has also been applied to silver and cobalt systems.

7.6 Publications

7.6.1 Publications Resulting From Work Presented in This Thesis

1. McGilvray, K. L., Decan, M. R., Wang, D., Scaiano, J. C., Facile Photochemical Synthesis of Unprotected Aqueous Gold Nanoparticles, *J. Am. Chem. Soc.*, **2006**, *128*, 15980-15981.

2. Marin, M. L., McGilvray, K. L., Scaiano, J. C., Photochemical Strategies for the Synthesis of Gold Nanoparticles from Au(III) and Au(I) Using Photoinduced Free Radical Generation, *J. Am. Chem. Soc.*, **2008**, *130*, 16572-16585.

3. Scaiano, J. C., Billone, P. S., Gonzalez, C. M., Maretti, L., Marin, M. L., McGilvray, K. L., Yuan, N., Photochemical Routes to Silver and Gold Nanoparticles, *Pure. Appl. Chem.*, **2009**, *81*, 4, 635-647.

4. McGilvray, K. L., Scaiano, J. C., Directed Photochemical Control as an Advantage in Metal Nanoparticle Synthesis, CRC Handbook of Organic Photochemistry and Photobiology, 3rd Edition, Taylor & Francis Group, *in press*.

5. McGilvray, K. L., Liu, Y, Holt, J., Correia, M., Banks, J. T., Scaiano, J. C., Opportunistic Use of Tetrachloroaurate Photolysis in the Generation of Reductive Species for the Production of Gold Nanostructures, *in preparation.*

6. McGilvray, K. L., Schwartz-Narbonne, R. Yuan, N., Scaiano, J. C., Surface Derivitization of Photochemically-Generated Aqueous Gold Nanoparticles, *in preparation.*

7. McGilvray, K. L., Scaiano, J. C., Photochemical Seed-mediated Growth of Gold Nanoparticles, *in preparation.*

7.6.2 Publications Resulting From Work Not Presented in This Thesis

1. McGilvray, K., Chretien, M. N., Lukeman, M., Scaiano, J. C., A Simple and Smart Oxygen Sensor Based on Intrazeolite Reactions of a Substituted Anthraquinone. *Chem. Commun.*, **2006**, 4401-4403.

2. Pacioni, N. L., Pardoe, A., McGilvray, K. L., Chretien, M. N., Scaiano, J. C., Synthesis of Copper Nanoparticles Mediated by Photogenerated Free Radicals: Catalytic Role of Chloride Anions, *Photochem. Photobiol. Sci.,* **2010**, *9*, 766-774.

3. Pacioni, N. L., Gonzalez-Bejar, M., Alarcon, E., McGilvray, K. L., Scaiano, J. C., Surface Plasmons Control the Dynamics of Excited Triplet States in the Presence of Gold Nanoparticles, *J. Am. Chem. Soc.,* **2010**, *132*, 6298-6299.

4. Hallet-Tapley, G. L., Crites, C.-O., Gonzalez-Bejar, M., McGilvray, K. L., Netto-Ferreira, J.-C., Scaiano, J. C., Dry Photochemical Synthesis of Supported Gold Nanoparticles on Hydrotalcite, γ-Al_2O_3 and TiO_2: Potential Applications as Heterogeneous Catalysts, *submitted*.

7.7 References

1. Ulman, A., Formation and Structure of Self-Assembled Monolayers. *Chem. Rev.* **1996,** *96*, 1533-1554.

2. Rohr, H., Trieflinger, C., Rurack, K., Daub, J., Proton- and Redox-Controlled Switching of Photo- and Electrochemiluminescence in Thiophenyl-Substituted Boron Dipyrromethene Dyes. *Chem. Eur. J.* **2006,** *12*, 689-700.

3. Shepherd, J. L., Kell, A., Chung, E., Sinclar, C. W., Workentin, M. S., Bizzotto, D., Selective Reductive Desorption of a SAM-Coated Gold Electrode Revealed Using Fluorescence Microscopy. *J. Am .Chem. Soc.* **2004,** *126*, 8329-8335.

4. Hong, R., Fernandez, J. M., Nakade, H., Arvizo, R., Emrick, T., Rotello, V. M., In Situ Observation of Place Exchange Reactions of Gold Nanoparticles. Correlation of Monolayer Structure and Stability. *Chem. Commun.* **2006**, 2347-2349.

5. Govonov, A. O., Zhang, W., Skeini, T., Richardson, H., Lee, J., Kotov, N. A., Gold Nanoparticle Ensembles as Heaters and Actuators: Melting and Collective Plasmon Resonances. *Nanoscale Res. Lett.* **2006,** *1*, 84-90.

6. Richardson, H. H., Hickman, Z. N., Govorov, A. O., Thomas, A. C., Zhang, W., Kordesch, M. E., Thermooptical Properties of Gold Nanoparticles Embedded in Ice: Characterization of Heat Generation and Melting. *Nano Lett.* **2006,** *4*, 783-788.

7. Pacioni, N. L., Gonzalez-Bejar, M., Alarcon, E., McGilvray, K. L., Scaiano, J.C., Surface Plasmons Control the Dynamics of Excited Triplet States in the Prescence of Gold Nanoparticles. *J. Am .Chem. Soc.* **2010,** *132*, 6298-6299.

8. Grisel, R., Weststrate, K.-J., Gluhoi, A., Nieuwenhuys, B. E., Catalysis by Gold Nanoparticles. *Gold Bull.* **2002,** *35*, 39-45.

9. Haruta, M., Date, M., Advances in the catalysis of Au nanoparticles. *Applied Catalysis A: General* **2001,** *222*, 427-437.

10. Haruta, M., Catalysis of Gold Nanoparticles Deposited on Metal Oxides. *Cattech* **2002,** *6* (2), 102-115.

11. Bond, G. C., Sermon, P. A., Gold Catalysis for Olefin Hydrogenations. Transmutation of Catalytic Properties. *Gold Bull.* **1973,** *6*, 102-105.

12. Galvano, S., Parravano, G., *J. Catal.* **1978,** *55*, 178.

13. Haruta, M., Yamada, N., Kobayashi, T., Iijima, S., Gold Catalysis Prepared by Coprecipitation for Low-Temperature Oxidation of Hydroge and of Carbon Monoxide. *J. CAtal.* **1989,** *115*, 301-309.

14. Corma, A., Garcia, H., Supported Gold Nanoparticles as Catalysts for Organic Reactions. *Chem. Soc. Rev.* **2008,** *37*, 2096-2126.

15. Astruc, D., Lu, F., Aranzeas, J. R., Nanoparticles as Recyclable Catalysts: The Frontier Between Homogeneous and Heterogeneous Catalysis. *Angew. Chem. Int. Ed.* **2005,** *44*, 7852-7872.

16. Sinha, A. K., Seelan, S., Tsubota, S., Haruta, M., Catalysis by Gold Nanoparticles: Epoxidation of Propene. *Topics in Catalysis* **2004,** *29*, 95-102.

17. Horvath, D., Toth, L., Guczi, L., Gold Nanoparticles: Effect of Treatment on Structure and Catalytic Activity of Au/Fe2O3 Catalyst Prepared by Co-Precipitation. *Catal. Lett.* **2000,** *67*, 117-128.

18. Kim, S., Bae, S. W., Lee, J. S., Park, J., Recyclable Gold Nanoparticle Catalyst of the Aerobic Alcohol Oxidation and C-C Bond Forming Reaction Between Primary Alcohols and Ketones Under Ambient Conditions *Tetrahedron* **2009,** *65*, 1461-1466.

19. Safavi, A., Absalan, G., Bamdad, F., Effect of Gold Nanoparticle as a Novel Nanocatalyst on Lumino-Hydrazine Chemiluminescence System and its Analytical Application. *Anal. Chimica Acta* **2008,** *610*, 243-248.

20. Lee, J., Park, C., Bang, J. U., Song, H., Precise Tuning of Porosity and Surface Functionality in Au@SiO2 Nanoreactors for High Catalytic Efficiency. *Chem. Mater.* **2008,** *20*, 5839-5844.

21. Zhou, Y., Wang, S., Ding, B., Yang, Z., Catalytic Oxidation of Polyethylene Glycol Dodecyl Ether to Corresponding Carboxylic Acid by Gold, Palladium (Mono and Bimettalic) Nanoparticles Supported on Carbon. *Catal. Lett.* **2007,** *118*, 86-90.

22. Sinha, A. K., Seelan, S., Tsubota, S., Haruta, M., A Three-Dimensional Mesoporous Titanosilicate Support for Gold Nanoparticles: Vapor-Phase Epoxidation of Propene with High Conversion. *Angew. Chem.* **2004,** *116*, 1572-1574.

23. Zanella, R., Giorgio, S., Henry, C. R., Louis, C., Alternative Methods for the Preparation of Gold Nanoparticles Supported on TiO2. *J. Phys. Chem. B* **2002,** *106*, 7634-7642.

24. Prati, L., Rossi, M., Gold on Carbon as a New Catalyst for Selective Liquid Phase Oxidation of Diols. *J. Catal.* **1998,** *176*, 552-560.

25. Pinna, F., Supported Metal Catalysts Preparation. *Cat. Today* **1998,** *41*, 129-137.

26. Zanella, R., Giorgio, S., Shin, C.-H., Henry, C. R., Louis, C., Characterization and Reactivity in CO Oxidation of Gold Nanoparticles Supported on TiO2 Prepared by Deposition-Precipitation with NaOH and Urea. *J. Catal.* **2004,** *222*, 357-367.

27. Zhao, D., Feng, J., Huo, Q., Melosh, N., Fredrickson, G. H., Chmelka, B. F., Stucky, G., Triblock Copolymer Synthesese of Mesoporous Silica with Periodic 50 to 300 Angstrom Pores. *Science* **1998,** *279*, 548-552.

28. Gosh, A., Patra, C. R., Mukherjee, P., Sastry, M., Kumar, R., Preparation and Stabilization of Gold Nanoparticles Formed by in-situ Reduction of Aqueous Chloroaurate Ions Within Surface-modified Mesoporous Silica. *Micro. Meso. Mater.* **2003,** *58*, 201-211.

29. Xu, J., Zhao, Y., Chen, C., Jiang, Z., Photocatalytic Inactivation Effect of Gold-Doped TiO2(Au/TiO2) Nanocomposites on Human Colon Carcinoma LoVo Cells. *Int. J. Photoenergy* **2007,** *97308.*

30. Stamplecoskie, K. G.; Scaiano, J. C., Light Emitting Diode Irradiation Can Control the Morphology and Optical Properties of Silver Nanoparticles. *J. Am. Chem. Soc.* **2010,** *132* (6), 1825-1827.

31. Kang, B., Mackey, M. A., El-Sayed, M. A., Nuclear Targeting of Gold Nanoparticles in Cancer Cells Induces DNA Damage, Causing Cytokinesis Arrest and Apoptosis. *J. Am .Chem. Soc.* **2010,** *132*, 1517-1519.

32. Mikelsons, L. Experimental and Computational Studies of the Interactions of Cyanine Dyes with DNA. Doctoral, University of Ottawa, Ottawa, 2007.